



Delft University of Technology

Natural Fracture Network Characterisation Numerical modelling, outcrop analysis and subsurface data

Boersma, Q.D.

DOI

[10.4233/uuid:25049b8f-f663-490c-b50a-80a9278dec54](https://doi.org/10.4233/uuid:25049b8f-f663-490c-b50a-80a9278dec54)

Publication date

2020

Document Version

Final published version

Citation (APA)

Boersma, Q. D. (2020). *Natural Fracture Network Characterisation: Numerical modelling, outcrop analysis and subsurface data*. [Dissertation (TU Delft), Delft University of Technology]. Delft University Publishers. <https://doi.org/10.4233/uuid:25049b8f-f663-490c-b50a-80a9278dec54>

Important note

To cite this publication, please use the final published version (if applicable).
Please check the document version above.

Copyright

Other than for strictly personal use, it is not permitted to download, forward or distribute the text or part of it, without the consent of the author(s) and/or copyright holder(s), unless the work is under an open content license such as Creative Commons.

Takedown policy

Please contact us and provide details if you believe this document breaches copyrights.
We will remove access to the work immediately and investigate your claim.

NATURAL FRACTURE NETWORK CHARACTERISATION

NUMERICAL MODELLING, OUTCROP ANALYSIS AND
SUBSURFACE DATA

NATURAL FRACTURE NETWORK CHARACTERISATION

NUMERICAL MODELLING, OUTCROP ANALYSIS AND
SUBSURFACE DATA

Proefschrift

ter verkrijging van de graad van doctor
aan de Technische Universiteit Delft,
op gezag van de Rector Magnificus prof. dr. ir. T.H.J.J. van der Hagen,
voorzitter van het College voor Promoties,
in het openbaar te verdedigen op vrijdag 20 november 2020 om 15:00 uur

door

Quinten Diede BOERSMA

Master of Science in Earth Sciences,
aan de Universiteit Utrecht, Nederland
geboren te Utrecht, Nederland.

Dit proefschrift is goedgekeurd door de

promotor: Prof. dr. G. Bertotti
copromotor: dr. A. Barnhoorn

Samenstelling promotiecommissie:

Rector Magnificus,	voorzitter
Prof. dr. G. Bertotti,	Technische Universiteit Delft
Dr. A. Barnhoorn,	Technische Universiteit Delft

Onafhankelijke leden:

Dr. T. Finkbeiner,	King Abdullah University of Science and Technology
Prof. dr. H. de Bresser	Universiteit Utrecht
Dr. D. Voskov,	Technische Universiteit Delft
Dr. N. Hardebol,	Staats Toezicht op de Mijnen
Prof. dr. D. Bruhn	Technische Universiteit Delft, GFZ Potsdam

Reserve lid:

Prof. dr. W.R. Rossen	Technische Universiteit Delft
-----------------------	-------------------------------

Prof. dr. G. Bertotti, dr. N. Hardebol en dr. A. Barnhoorn hebben in belangrijke mate aan de totstandkoming van het proefschrift bijgedragen.



Keywords: Natural Fractures, Mechanical Modelling, Drone Imagery, Geothermal Energy, Fluid flow Modelling

Printed by: Gildeprint

Front & Back: 2D drone image of the Brejoes pavement outcrop that illustrates a beautiful example of an hierarchical fracture network.

Copyright © 2020 by Q. Boersma

ISBN 978-94-6366-320-5

An electronic version of this dissertation is available at
<http://repository.tudelft.nl/>.

CONTENTS

Summary	xi
Samenvatting	xiii
1 Introduction	1
1.1 Rationale: why and how do we study natural fractures?	2
1.2 Thesis outline	5
1.3 Note to the reader of this thesis	5
1.4 Data availability	6
2 Mechanical factors controlling the development of orthogonal fracture network geometries	7
2.1 Introduction	8
2.2 Model design and fundamental framework	9
2.2.1 Model setup	9
2.2.2 Brittle failure and sources of tensile stresses in subsurface	11
2.3 Modelling Strategy	11
2.3.1 From local effective stresses to a theoretical sub critical fracture propagation rate	11
2.3.2 A step-by-step modelling approach: Developing an orthogonal network under fixed remote stress conditions	13
2.4 Modelling results: saturated network geometries as a function of the remote stress state and Poisson's ratio	14
2.5 Discussion	16
2.5.1 Modelling effective tensile stresses: can boundary tensile stresses replace internal fluid pressure?	16
2.5.2 Linking network geometries to remote stress, local perturbations and material conditions	18
2.5.3 Implications for field geology and subsurface reservoirs	20
2.6 conclusions	21
3 Mechanical controls on the development and saturation of conjugate shear fracture networks	23
3.1 Introduction	24
3.2 Modelling strategy	25
3.2.1 Initial model geometry and boundary conditions	25
3.2.2 Calculating stress intensity and theoretical fracture propagation	25
3.2.3 Sub critical crack growth in static finite element models	28
3.2.4 Modelling scenarios and procedure	29

3.3	Results	30
3.3.1	Developing a connected conjugate network under sub-critical stress conditions	30
3.3.2	Conjugate network geometries and characteristics as a function of the applied boundary conditions	31
3.4	Discussion	34
3.4.1	Will continued fracture infill result in a saturated network geometry?	34
3.4.2	Similarities and differences between numerically-derived conjugate - and orthogonal fracture networks	35
3.4.3	Implications of the main modelling assumptions	35
3.5	Conclusions	37
4	Mechanical controls on stress and fracture behaviour in layered rocks	39
4.1	Introduction	40
4.2	Model set-up and numerical procedure	41
4.2.1	Model design and material parameters	41
4.2.2	Performed numerical experiments	42
4.3	Modelling results and sensitivity analysis	43
4.3.1	Model validation	43
4.3.2	Local stresses as a function of contrasting elastic parameters	44
4.3.3	Impact friction between layers	45
4.3.4	Impact of the confining pressure	46
4.4	Discussion	48
4.4.1	Mechanical factors controlling fracture behaviour in layered materials	48
4.4.2	Are the modelled tensile stresses high enough to cause tensile failure?	49
4.4.3	Implications for subsurface reservoir studies	52
4.4.4	Implications for field geology	55
4.5	Conclusions	55
5	Linking natural fractures to karst cave development	57
5.1	Introduction	58
5.2	Geological background and study area	59
5.2.1	Tectonic setting	59
5.2.2	Stratigraphy	59
5.2.3	Study area	59
5.3	Methods: Outcrop Interpretation and Modelling Workflow	59
5.3.1	Digital outcrop acquisition and interpretation (steps 1.1 and 1.2)	61
5.3.2	Meshing and stress modelling using FEM (Steps 2.1 and 2.2)	62
5.3.3	Stress induced aperture calculations (Step 2.3)	62
5.3.4	Constant aperture in fluid flow models (Step 2.3)	64
5.3.5	Power law aperture scaling derived from vein analysis (Step 2.3)	64
5.3.6	Fluid flow modelling (Steps 3.1 and 3.2)	66
5.3.7	Cave map digitization and interpretation	66

5.4	Results: Structural data analysis	66
5.4.1	Field data analysis	66
5.4.2	Structural interpretation of the acquired drone images and cave system	68
5.5	Results: Fracture aperture and fluid flow modelling	70
5.5.1	Modelling scenario 1: Stress sensitive fracture aperture and fluid flow	72
5.5.2	Modelling scenario 2: Fluid flow modelling assuming constant fracture aperture	74
5.5.3	Modelling scenario 3: Fluid flow modelling assuming power-law aperture scaling	76
5.5.4	Impact of the implemented matrix permeability	76
5.6	Discussion	77
5.6.1	Lessons for reservoir modelling	77
5.6.2	Link between the tectonics, fractures and the cave network geometry	78
5.6.3	Implications of the chosen aperture model and matrix permeability	78
5.6.4	Implications of the main assumptions	79
5.7	Conclusions	79
6	FracSim2D: A new methodology for generating geological constrained 2D discrete fracture networks	81
6.1	Introduction	82
6.2	Design of the algorithm	83
6.2.1	The workflow of the algorithm	84
6.2.2	The input file	84
6.3	Results	88
6.3.1	Case study: Brejoes fractured pavement	88
6.3.2	Simulations of other natural examples	91
6.3.3	The importance of geological constraints: Implications for fluid flow	93
6.4	Discussion	95
6.4.1	An open source code for creating statistically or geologically constraint 2D DFN's	95
6.4.2	Main limitations of the current version of the code	97
6.4.3	Potential applications for field and reservoir studies	98
6.5	Conclusions	98
7	The impact of fractures on heat extraction from tight Triassic reservoirs in the West Netherlands Basin	101
7.1	Introduction	103
7.2	Geological setting and geothermal energy within study area	105
7.2.1	Present-day geometry of the West Netherlands Basin (WNB)	105
7.2.2	Stratigraphy and diagenesis of the Main Buntsandstein Subgroup (Early-Triassic) in the WNB	105
7.2.3	Previous reporting on the data extracted by NLW-GT-01	106

7.2.4	Other mentions of natural fractures within the Lower-Triassic formations of the WNB	107
7.3	Data and methods	107
7.3.1	The dataset, velocity model and 2D modelling domain	107
7.3.2	General workflow	108
7.3.3	Petrophysical analysis	108
7.3.4	Geostatistical inversion and property modelling.	109
7.3.5	Borehole image log and core interpretation and fracture characterisation	110
7.3.6	Seismic discontinuity analysis	111
7.3.7	Discrete Fracture Network (DFN), aperture and permeability modelling.	112
7.3.8	Fluid-flow/temperature modelling.	113
7.4	Results: Petrophysical analysis, geostatistical inversion, and property computations in the modelling domain.	115
7.4.1	Petrophysical analysis of the NLW-GT-01 well	115
7.4.2	Geostatistical inversion and property modelling.	115
7.5	Results: Fracture and fault network characterisation	117
7.5.1	FMI and core interpretation and fracture analysis	117
7.5.2	Automated fault extraction and characterisation.	120
7.6	Results: DFN modelling, aperture computations, permeability upscaling and fluid flow and temperature simulations	121
7.6.1	A Reservoir scale DFN	121
7.6.2	Aperture and upscaled permeability results	123
7.6.3	Fluid flow and temperature modelling.	126
7.7	Discussion	129
7.7.1	Impact of natural fractures and faults on heat production from the Main Buntsandstein Subgroup near the NLW-GT-01 well	129
7.7.2	Potential implications of the dataset and workflow for future geothermal energy development in the WNB	130
7.7.3	Potential improvements to the modelling workflow	130
7.8	Conclusions.	131
8	Conclusions and recommendations	133
8.1	Synopsis	134
8.1.1	Mechanical and tectonic controls on natural fracture network development and characteristics	134
8.1.2	Characterization of natural fracture network patterns using outcrop analogues.	135
8.1.3	The impact of natural fractures on heat extraction from low-permeability reservoirs	135
8.2	Outlook and recommendations for future work.	136
8.2.1	Placing the key findings in a broader conceptual understanding.	136
8.2.2	Numerical techniques for modelling the development of a natural fracture networks	137
8.2.3	Future of drone imagery in outcrop analogue studies	137

8.2.4	Using FracSim2D as input for MPS models.	138
8.2.5	Basin scale seismic reservoir characterization for the purpose of geothermal energy exploration.	138
A	Interactive python script for estimating stylolite depth of formation	139
B	Scripts for extracting 2D and 3D data from ABAQUS database files	147
C	Acquired drone data and natural fracture interpretations	151
	Bibliography	157
	References	157
	Acknowledgements	173
	Curriculum Vitae	175
	List of Publications	177

SUMMARY

Responsibly using the subsurface for geo-energy extraction or storage requires an accurate understanding of the static and dynamic behaviour of the targeted reservoirs. While mostly dependent on intrinsic rock properties (e.g. porosity and permeability), this behaviour is also believed to be significantly impacted by the presence of natural fractures. For example, depending on their opening, connectivity, intensity or cement infill, natural fractures can both channel or inhibit fluid flow, thereby causing significant local flow heterogeneities which can both increase or decrease geo-energy production values. Therefore, assessing the possible characteristics of natural fractures has become an integral component in complex reservoir studies.

The characterization of natural fractures in the subsurface is often done using a multitude of scales, tools and data-types. For example, larger structural features such as faults ranging from tens to several hundreds of meters in length are often characterized and mapped using high-quality data. However, smaller fractures (e.g. metre scale joints) mostly fall below the seismic resolution, and can therefore only be detected and characterized using image log and core data. Although wells hold valuable information on fracture characteristics such as aperture, orientation or structural style, the extracted data is constrained to location of the well. Further, wells only provide 1D insights in to a 3D problem. This implies that inter-well interpolation for the purpose of reservoir scale fracture prediction is susceptible to uncertainties caused by the lack of quantitative data points. Therefore, in this Thesis, we aim to better characterize natural fracture networks and assess their impact on fluid flow and geo-energy extraction, so that the uncertainties related to fracture prediction are reduced. This is done using numerical modelling, outcrop analogues and subsurface data.

Using a numerical modelling procedure expanded upon previous literature studies, we investigate the development of natural fracture networks. Our work shows that the characteristics of the numerically-acquired networks are mostly controlled by the interplay between the applied stress conditions and Linear Elastic Fracture Mechanics. For instance, we show that mode I fracture networks reach a saturated state, where further fracture infill is inhibited, because of local tensile driving stress reductions (chapter 2). Depending on the applied tensile stress conditions and Poisson's ratio, saturated network geometries range from close spaced parallel fractures to orthogonal nested arrangements. Mode II conjugate fractures form in response to compressive differential stresses and reach a 'saturated' state via stress localization, with numerically derived geometries being resembled out of conjugate fractures having coeval abutment relations (chapter 3). Here the network characteristics such as intensity or porosity are dependent on the applied differential stresses.

Natural fractures are also influenced by the mechanical stratigraphy (chapter 4). We show that differences in elastic properties result in significant local stress changes and tensile stresses developing in the stiffer layers. Our results also show that these local

stress changes can explain the differences in fracture behaviour commonly observed in laboratory experiments and outcrop examples. Finally, implementing low inter-facial frictions and/or high confining pressures negate the observed effects caused by contrasting layer properties.

In chapter 5, we present an outcrop analogue study which highlights clear correlations between natural fractures, compressive far-field stresses and a large underlying cave system. The acquired drone imagery and on-site investigations indicate a large and connected fracture network which most likely formed due to two compressive deformation events. Further, field evidence, geometrical data and fluid-flow simulations portray a clear correlation between the observed fractures and cave tunnels. Because of this correlation, we believe that the observed fractures acted as conduits for fluid-flow, which given enough time, resulted in the development of the large underlying cave-system.

Our and other outcrop examples indicate that natural fracture network arrangements generally have distinct hierarchical, spacing and topological relationships. In chapter 6, we present FracSim2D, a open-source and python-based 2D discrete fracture network (DFN) simulator which incorporates these characteristics by introducing user-defined placement rules. By doing so, geological observations made on outcrop analogues can be adequately captured by the simulated DFN's.

In chapter 7, we investigate the potential impact of natural fractures on geothermal heat extraction from tight reservoirs, by performing a subsurface case study which presents a multi-scale and data-driven workflow of 1) image-log and core-data analysis, 2) seismic reservoir characterization and 3) DFN - and temperature modelling. The results show that the studied Triassic reservoir is significantly fractured and faulted, with the analysed fractures being hydraulically conductive. Further, the DFN - and temperature models indicate that if open, the observed natural fractures significantly increase the effective permeability of the reservoir, thereby making fluid-flow and heat production possible.

The results presented in this Thesis further illustrate the mechanical and tectonic controls on fracture network development and saturation, as well as, the impact that these structural features have on the effective permeability, fluid flow and geo-energy production. While some important processes and uncertainties are not fully addressed, we believe that the results and workflows presented in this Thesis provide a framework which can help in better characterizing natural fracture networks on outcrops and in subsurface reservoirs. However, it should be noted that the prediction and characterization of natural fractures in subsurface reservoirs remains an relatively uncertain process.

SAMENVATTING

Het verantwoordelijk gebruik van de ondergrond met betrekking tot energie exploitatie of opslag vereist een goed begrip van statisch en dynamisch gedrag van het betreffende reservoirgesteente. Dit gedrag is voornamelijk afhankelijk van de eigenschappen van de steen in kwestie (bv. permeabiliteit en porositeit). Echter, onderzoek laat ook zien dat het statisch en dynamisch gedrag van reservoirgesteente erg wordt beïnvloed door de aanwezigheid van natuurlijke breuken. Of deze beïnvloeding positief of negatief is, is afhankelijk van de gemeten breuk eigenschappen. Bijvoorbeeld, open breuk netwerken kunnen energie exploitatie bevorderen. Daarentegen, gesloten of gecementeerde breuk netwerken hebben voornamelijk een negatief effect. Het in kaart brengen van mogelijke ondergrondse breuk patronen is dan ook een belangrijk onderdeel bij studies die complex reservoir gesteende onderzoeken.

Het karakteriseren van ondergrondse breuk patronen wordt voornamelijk gedaan op verschillende schalen en met behulp van meerdere hulpmiddelen en datasets. Bijvoorbeeld, grotere structuren met lengtes die variëren tussen de tien en enkele honderden meters worden hoofdzakelijk in kaart gebracht door middel van seismische data. Kleinere structuren (bv. Breuken van enkele meters in lengte), vallen onder de seismische resolutie en kunnen daarom alleen worden gedetecteerd middels aangeboorde put data. Hoewel putten waardevolle informatie kunnen bevatten betreffende de karakteristieken van ondergrondse breuken, deze data is beperkt tot de locatie van de put. Verder, geeft put data enkel 1D informatie binnen een 3D probleem. Door deze gebrekkige informatie kan het in kaart brengen van natuurlijke breuk patronen in de ondergrond een onzeker proces. Daarom proberen we in deze Thesis natuurlijk breuk patronen en hun invloed op vloeistof patronen en ondergrondse energy exploitatie beter te karakteriseren, zodat de onzekerheden betreffende natuurlijke breuk voorspellingen worden verminderd. Dit doen we middels numeriek modelleren, het besturen van natuurlijk dagzoom patronen en ondergrondse reservoir data.

Middels een numerieke werkwijze welke gebaseerd is op eerder gepubliceerd werk laten onze resultaten zien dat de vorming en saturatie van natuurlijke breuk netwerken voornamelijk wordt beïnvloed door de wisselwerking tussen de mate van deformatie en Lineair Elastische Breuk Mechanica. Ons werk toont ook aan dat mode I breuk netwerken een gesatureerde staat bereiken doordat nieuwgevormde breuken de benodigde spanning lokaal verlagen (hoofdstuk 2). Verder laten onze modellen zien dat de geometrie van de gesatureerde netwerken afhankelijk is van de toegepaste deformatie en materiaaleigenschappen. De gemodelleerde netwerken variëren tussen dicht uit elkaar geplaatste parallelle breuken tot complexe orthogonale netwerken. Ons werk laat ook zien dat mode II netwerken zich vormen door middel van het toepassen van compressie en dat deze netwerken en gesatureerde staat bereiken doordat de benodigde deformatie zich steeds verder lokaliseert (hoofdstuk 3). De numeriek verkregen netwerken bestaan uit conjugate breuken waarvan de lokale breuk intensiteit en opening sterk afhankelijk

is van de toegepaste deformatie.

Natuurlijke breuken worden ook beïnvloed door mechanische eigenschappen van gelaagde gesteente pakketten (hoofdstuk 4). Ons werk laat zien dat contrasten tussen de elastische eigenschappen van stenen ervoor zorgt dat significante veranderingen ontstaan in de gemodelleerde deformatie. De verkregen numerieke resultaten kunnen helpen met het beschrijven van natuurlijke breuk patronen die worden geobserveerd in laboratoriumexperimenten of op dagzoompakketten. Tot slot laten we zien dat het invoegen van lage frictie parameters en/of een hoge horizontale compressie waardes ervoor zorgt dat de effecten veroorzaakt door de contrasten in mechanische eigenschappen worden geminimaliseerd.

In hoofdstuk 5, presenteren we een onderzoek van een natuurlijk dagzoom patroon dat een correlatie laat zien tussen natuurlijke breuken, regionale deformatie en een groot grotten systeem. De verkregen drone fotografie en veld data laten een groot en verbonden breuk netwerk zien, welke zich waarschijnlijk vormde middels twee verschillende tektonische compressie richtingen. Verder laten de verkregen veld - en numerieke resultaten een duidelijke correlatie zien tussen de geïnterpreteerde breuken en grottunnels. Vanwege deze correlatie denken wij dat het geobserveerde breuk netwerk werd gebruikt als een soort van leiding voor vloeistof transport wat, gegeven genoeg tijd, resulteerde in het vormen van het onderliggende grotten systeem.

Onze en andere bestudeerde dagzoom studies laten duidelijk zien dat natuurlijke breuk netwerken zich voornamelijk geordend organiseren middels een duidelijke hiërarchie, spatiëring en topologie. In hoofdstuk 6 presenteren wij FracSim2D, een nieuwe open-source en python-based Discrete Fracture Network (DFN) simulator die deze organisatorische regels implementeert door het introduceren van plaatsingsregels gedefinieerd door de gebruiker. Doordat we dit doen, kunnen geologische observaties gemaakt op natuurlijk dagzoom patronen goed worden beschreven door de gesimuleerde DFN's.

In hoofdstuk 7 bestuderen we de impact van natuurlijke breuk netwerken op geothermische energie exploitatie vanuit impermeabel reservoir gesteende. Dit doen we middels een casestudie met een geïntegreerde en data gedreven werkwijze van 1) put - en kern data-analyse, 2) seismische reservoir karakterisatie en 3) DFN - en temperatuur modellen. Onze resultaten laten zien dat het bestudeerde reservoirgesteente veel natuurlijke breuken bevat die hydraulisch doorlaatbaar zijn. Verder laten onze DFN - en temperatuur modellen duidelijk zien dat als deze breuken opening vertonen, ze een significante impact hebben de reservoir permeabiliteit, vloeistof patronen en geothermische productie.

De in deze Thesis gepresenteerde resultaten geven een verdere beschrijving van de mechanische en tektonische invloed op de vorming en saturatie van natuurlijk breuk netwerken, als mede van de impact die breuken kunnen hebben op reservoir permeabiliteit, vloeistof patronen en geo-energie exploitatie. Hoewel niet alle belangrijke processen en onzekerheden volledig zijn behandeld, geloven wij dat de gepresenteerde resultaten en werkwijze een platform kunnen bieden die kan helpen bij het beter karakteriseren van natuurlijke breuk netwerken op dagzomen en in de ondergrond. Dat gezegd hebbende, moet men niet vergeten dat het karakteriseren en voorspellen van natuurlijke breuken in de ondergrond een onzeker proces blijft.

1

INTRODUCTION

1.1 Rationale: why and how do we study natural fractures?

Natural fractures generally form as result of brittle deformation caused by stresses and strain applied on the rock matrix and are commonly observed on outcrops [Bai et al., 2002, Bertotti et al., 2017, Boersma et al., 2019b, Fossen, 2010, Hardebol et al., 2015] and subsurface reservoirs [Holdsworth et al., 2019, Maerten et al., 2006, Teufel and Clark, 1984, Toubanc et al., 2005, Vidal and Genter, 2018, Williams et al., 2017]. These structural features are believed to highly influence the overall rock strength and the effective permeability [Ferrill et al., 2017a, Gale et al., 2014]. For instance, studies addressing hydraulic stimulation of tight reservoirs show that natural fractures greatly influence the characteristics and geometry of the hydraulically induced fractures [Gale et al., 2007, Wang et al., 2019]. Furthermore, multiple subsurface studies show that open natural fractures highly influence fluid flow patterns and production for hydrocarbon and geothermal reservoirs having a low matrix permeability [Holdsworth et al., 2019, Rijken, 2005, Toubanc et al., 2005, Vidal and Genter, 2018]. However, when closed or cemented, fractures are believed negatively influence fluid flow and production, since they tend to form fluid flow barriers [Bisdom, 2016, Gale et al., 2007]. Therefore, optimized development of a naturally fracture reservoir requires an in-depth understanding of the fracture presence, extend, 3D distribution, geometrical characteristics, and connectivity [Maerten et al., 2006, Olson et al., 2009, Toubanc et al., 2005, Williams et al., 2017].

The characterization of natural fractures in the subsurface is often done different using data-types on a variety of scales [Freeman et al., 2015, Quinn et al., 2014, Williams et al., 2017]. For example, larger structural features such as faults with dimensions ranging from several - to hundreds of meters are often characterized using seismic data [Maerten et al., 2006] (Figure 1.1a). Smaller features such as meter scale joints generally fall below the seismic resolution (Figure 1.1a-b). Therefore, these features are often interpreted using well data. However, well data only provides local information at and around the well (Figure 1.1a-b). This implies that, sub-surface characterization of small natural fractures requires inter-well interpolation which can introduce significant uncertainties due to the lack of quantitative data points [Bisdom et al., 2017a, Laubach et al., 2019, Maerten et al., 2006, Toubanc et al., 2005, Williams et al., 2017] (Figure 1.1a-b).

In the case of high quality data, seismic attributes can help in identifying zones of intensive fracturing and faulting [Bounaim et al., 2019, Hale, 2013, Jaglan and Qayyum, 2015, Williams et al., 2017]. For instance, applying edge enhancement filters (e.g. fault likelihood filter), allows for the automatic detection and extraction of large fault networks [Boe, 2012, Boersma et al., 2019a, Hale, 2013, Jaglan and Qayyum, 2015]. Additionally attributes such as curvature, amplitude contrast, coherency and/or similarity can be used for identifying areas which show a discontinuous seismic signal, thereby highlighting fault zones and/or significantly fractured areas (e.g. Jaglan and Qayyum [2015]). Therefore, seismic attributes can be used for reducing potential uncertainties regarding fracture network prediction in the sub-surface.

Another way of reducing the uncertainties involved in natural fracture prediction is by using numerical forward modelling. Here, studies generally assess relations between different fracture network geometries, alternating layer properties and applied stress and strain conditions, assuming theories such as Linear Elasticity (Hooke's law), Linear Elastic Fracture Mechanics (LEFM) [Griffith, 1921, Irwin, 1957] and Sub Critical

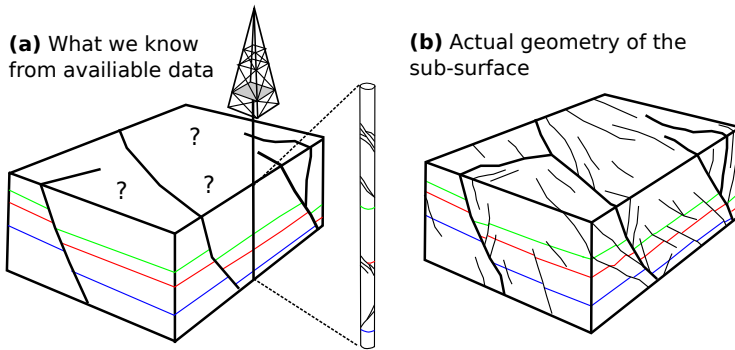


Figure 1.1: The subsurface problem. a) The available data we have from fractured and faulted reservoirs in the subsurface. b) The actual geometry of the subsurface. Figure is modified after [Maerten et al. \[2006\]](#)

Crack Growth (SCCG) [[Atkinson, 1984](#)] (Figure 1.2a-b). These studies commonly show that because of local stress perturbations and driving stress reductions caused by LEFM, numerically derived fracture network geometries can reach saturated states at which further fracturing is inhibited [[Bai et al., 2002](#), [Boersma et al., 2018a](#), [Olson, 2007](#), [Rijken, 2005](#)] (Figure 1.2a). These saturated geometries show predictable characteristics and a clear correlation with the applied mechanical and boundary conditions [[Bai et al., 2002](#), [Olson, 2007](#), [Rijken, 2005](#)]. Apart from local stress changes caused by LEFM, natural fractures are also believed to be influenced by local stress perturbations caused by alternating layer properties and inter-facial frictions (Figure 1.2b). For example, numerical studies addressing this issue generally show that, due to local stress changes, fractures mainly concentrate in the stiffer layers [[Bourne, 2003](#), [Cooke and Underwood, 2001](#), [Laubach et al., 2009](#), [Roche and van der Baan, 2015](#)]. Because of these observed correlations, numerical modelling is often used for creating mechanically constrained descriptions of sub-seismic features in structurally complex reservoirs [[Boersma et al., 2019a](#), [Maerten et al., 2006, 2019, 2016](#)].

Outcrop analogues can also help in the prediction of natural fracture networks in the subsurface [[Bertotti et al., 2017](#), [Bisdorn et al., 2017a](#), [Bruna et al., 2019](#), [Hardebol and Bertotti, 2013](#), [Olson et al., 2009](#)]. For instance, outcrops often provide descriptions of geometrical properties such as, fracture length, topology, connectivity and spatial variability [[Bisdorn, 2016](#), [Prabhakaran et al., 2019](#)] (Figure 1.3a). Furthermore, some outcrops provide detailed and large fracture network descriptions, and place them in the context of large scale deformation, such as faulting or folding [[Bertotti et al., 2017](#), [Boersma et al., 2019b](#), [Hardebol et al., 2015](#), [Maerten et al., 2016](#)]. Additionally, network geometries observed on outcrops can help assessing the impact of different fracture network characteristics (e.g. connectivity and topology) on fluid flow and the effective permeability (Figure 1.3b-c). While, outcrops description contain a lot of data, they are not always a direct proxy for their subsurface counter parts [[Li et al., 2018](#)]. For instance, the geometry and characteristics fractures present on outcrops have generally been influenced by surface processes such as exhumation, stress relaxation and weathering [[Fos-](#)

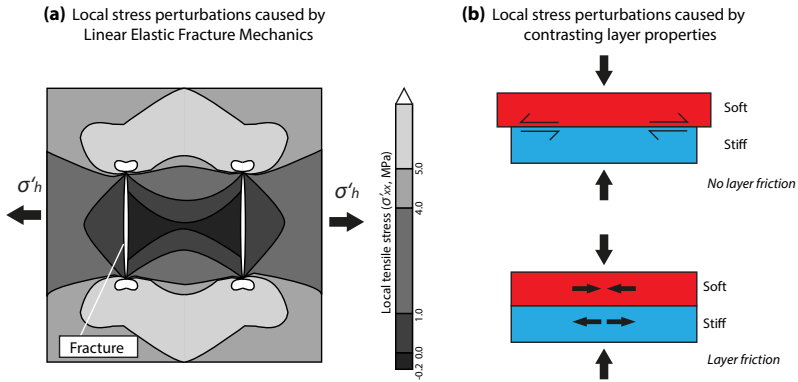


Figure 1.2: Numerical modelling of natural fractures and alternating layer properties. a) The local tensile stress field surrounding two closely spaced mode I fractures. b) Local stress perturbations caused by alternating layer properties and inter-facial frictions. The figures are modified after Boersma et al. [2018a], Bourne [2003]

sen, 2010]. These surface processes need to be accounted for in order to use outcrop data for the purpose of subsurface fracture prediction [Bisdom, 2016, McGinnis et al., 2015]. That being said, if analysed correctly, outcrops can help increasing our conceptual understanding of the relation between large scale tectonics, mechanical properties and fracture network geometries and characteristics.

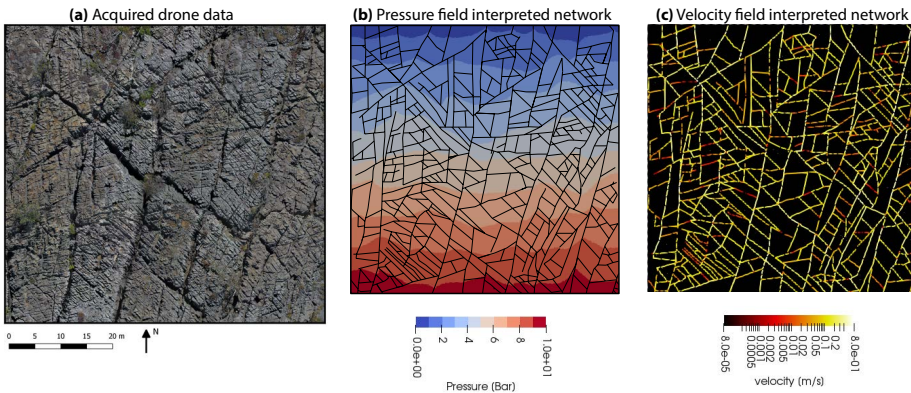


Figure 1.3: Fluid flow modelling experiment done on a natural fracture network acquired from an outcrop analogue (Brejoes, Brazil). Interpretation is done by Boersma et al. [2019b] a) Drone data of the Brejoes pavement outcrop. b) Modelled fluid pressure field through the interpreted fracture network. c) Velocity field of the modelled fluids. Fluid flow experiments have been performed using AD-GPRS (Stanford University's Automatic Differentiation based General Purpose Research Simulator)

In this thesis, we expand upon the above described methodologies with the aim of better characterizing natural fracture networks on outcrops and in the subsurface. First, we present a new numerical methodology and derive the different mechanical and tec-

tonic controls on the development, characteristics and saturation of naturally occurring fracture network arrangements. Here, we assume that fractures perturb the elastic rock matrix following LEFM and can propagate under sub critical stress conditions, both of which are widely used approaches in modelling the development of fracture networks [Ko and Kemeny, 2011, Olson et al., 2009, Rijken, 2005, Shen and Rinne, 2007]. Second, newly acquired drone imagery of a previously uninvestigated pavement outcrop located in Brazil is presented. Using the acquired 3D outcrop models we assess: 1) the natural network geometry and characteristics, 2) the relationship with tectonic drivers and larger structural features, 3) the spatial variabilities and 4) the impact that fractures have on fluid flow and the effective permeability. Third, we present an open source 2D Discrete Fracture Network simulator which incorporates distinct fracture characteristics commonly observed on outcrop analogues. Finally, we perform a sub-surface case study which assesses the impact of natural fractures on geothermal heat extraction from low permeability Hot Sedimentary Aquifers (HSA).

1.2 Thesis outline

This thesis starts with three numerical modelling studies which assess the mechanical controls on natural fracture network development, saturation and characteristics. In chapters 2 and 3 we derive and quantify the mechanical and tectonic controls on the development and saturation of mode I orthogonal - and mode II conjugate fracture networks. Chapter 4 goes in the third dimension, and addresses the question on how alternating layer properties influence fracture behaviour in layered materials.

The second part of this thesis consists of two chapters which characterize natural fracture data from outcrop analogues. In chapter 5, we present a 3D outcrop model of a large fractured pavement in Brejoes (Brazil) and discuss the link between the observed fractures, the tectonic history and a large underlying cave system. In addition, we address the impact of the observed fractures on fluid flow, the effective permeability and karstification and cave development, using different aperture models and a methodology previously developed by Bisdorn [2016]. In chapter 6 we present FracSim2D, a new and open source 2D DFN simulator which is able to generate geologically constrained network geometries, by incorporating fracture characteristics such as hierarchy, topology and spacing in to the simulation workflow.

Finally, in chapter 7 we present subsurface case study where we assess the potential impact of open natural fractures on geothermal heat extraction from low permeability Triassic sandstones in the West Netherlands Basin. This is done using a multi-scale workflow of 1) reservoir property characterisation using petrophysical-analysis and geostatistical-inversion, 2) image log- and core interpretation, 3) large-scale seismic fault extraction and characterisation, 4) Discrete Fracture Network (DFN) modelling and permeability upscaling, and 5) fluid-flow - and temperature modelling.

1.3 Note to the reader of this thesis

The different chapters in this thesis should be seen and read as individual studies that are part of a larger research project (natural fracture network characterization on a variety of scales). This implies that each chapter can be read individually. However, this also implies that there may be some overlap in the explained methodologies and equations.

Further, it should also be noted that in chapter 2, we use the engineering sign convention for depicting stress and strain results, making tensile stresses positive and compressive stresses negative. In all other chapters we use the geological sign convention (i.e. tension is negative and compression is positive). Additionally, it is assumed that the basics regarding Fracture Mechanics and Structural Geology are known by the reader.

1.4 Data availability

Most of the results, methods, python scripts, and interpretations presented in this Thesis are publicly available using the 4TU data-service (<https://researchdata.4tu.nl/en/>). For each chapter and appendix, a separate DOI has been generated. These DOI's can be found in the respective data availability sections.

2

MECHANICAL FACTORS CONTROLLING THE DEVELOPMENT OF ORTHOGONAL FRACTURE NETWORK GEOMETRIES

Orthogonal fracture networks are generally composed of open and well-connected fractures which have perpendicular - and sometimes show coeval abutment relations. Previous modelling studies have shown that the networks can form response to local stress perturbations rather than a complete rotation in remote stress field. In this study, we expand on the implications of these local stress perturbations using a static finite element approach. The derived stress field is examined to assess the development of implemented microfractures. The results show that the continuous infill of fractures leads to a gradual decrease in the local tensile driving stresses, and, therefore, results in the development of a saturated network, at which further fracture placement is inhibited. The geometry of this fully developed network is dependent on the remote effective stresses and partly on the material properties. Saturated networks range from: 1) a set of closely spaced parallel fractures, 2) a ladder-like geometry, and 3) an interconnected nested arrangement. Finally, we show that our modelling results at which we apply effective tension, are equivalent to having a uniformly distributed internal pore fluid pressure, when assuming static steady state conditions and no dynamic fluid behaviour.

Parts of this chapter have been published in *Rock Mechanics and Engineering* **51**, 11 (2018). [Boersma et al. \[2018a\]](#)

2.1 Introduction

Orthogonal fracture networks are an arrangement of mode I fractures, which generally consist of two fracture sets orientated perpendicular to each other [Bai et al., 2002, Gross, 1993, Olson, 2007, Rives et al., 1992, Ruf et al., 1998] (Figure 2.1). If hydraulically open under the in-situ stress conditions, these features may provide pathways for fluid flow [Bai and Pollard, 2001], thereby significantly enhancing effective permeabilities particularly in case of tight reservoir rock [Bisdom et al., 2016c, Houben et al., 2017]. The opening of these Mode I fractures is controlled by the local stress field, and this implies that the understanding fracture enhanced effective permeabilities requires knowledge of the local stress field and its effect on the local fracture behaviour [Bai et al., 2002, Gale et al., 2014, Hardebol et al., 2015].

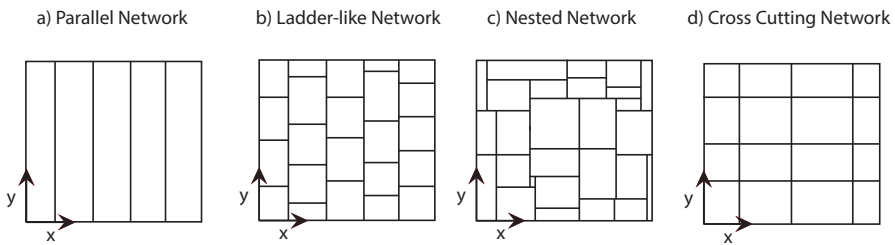


Figure 2.1: Four naturally occurring mode I fracture arrangements. a) A system of closely spaced parallel fractures. b) A ladder-like network depicting both parallel and orthogonal fractures. c) A nested network geometry at which both orthogonal and parallel fractures abut against each other. d) A cross cutting fracture network

In linear elastic fracture mechanics (LEFM), mode I fractures align parallel to σ'_1 and perpendicular to σ'_3 . Therefore, an orthogonal or nested fracture network geometry such as shown in Figure 1b, c requires a rotation of the principal driving stresses. Numerical models developed by Bai et al. [2002] showed that when both in plane principal stresses (σ'_H, σ'_h) are in effective tension, the formation of orthogonal cross fractures can be explained by a local stress switch. These authors suggested that the formation of orthogonal fractures is driven by local deviations in the stress field and requires no regional stress rotation. They showed that this change in orientation occurs because of the reduction in effective stresses (σ'_h) assigned perpendicular to the strike of the implemented fractures.

The reduction of the effective tensile stress caused by fracture opening is called the stress shadowing effect (Figure 2.2) [Bai and Pollard, 2000, Schöpfer et al., 2011, Tang et al., 2008]. Following from LEFM, the opening of a fracture highly perturbs the local stress field. Here, tensile stresses are being concentrated around the crack tip, resulting in local tensile stress reductions at the fracture walls (Figure 2.2a). As two closely spaced layer-bounded fractures interact, the two regions of local stress perturbations interfere and the effective tensile stresses in the x-direction (driving stresses) reach 0.0 MPa (Figures 2.2b, c). The spacing at which these effective tensile conditions reach 0.0 MPa is called the critical spacing [Bai and Pollard, 2000]. Consequently, due to the absence of local tensile stresses (Figure 2.2c), further fracture infill below this critical spacing becomes highly improbable. Therefore, the two interacting fractures have reached

a saturated state. Bai et al. [2002] showed that under bi-axial tension, applied tensile tangential stresses (parallel to the fracture wall) (σ'_y) were less affected by stress shadowing, resulting in a local stress switch ($\sigma'_y > \sigma'_x$). These authors argued that this effective stress switch could explain the occurrence of orthogonal fractures in between two mode I fractures. Olson [2007], Olson et al. [2009] used these bi-axial tensile stress conditions to systematically develop mode I orthogonal fracture networks, and argued that these network geometries could develop in one single deformation phase.

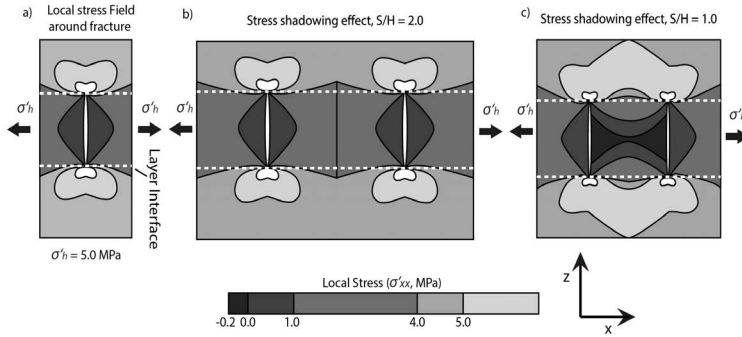


Figure 2.2: Local stress perturbations as a result of LEFM and the concept of stress shadowing. It should be noted that tensional stresses are positive and that all layers have the same material properties. a) Local stress perturbation due to the opening of single crack. b) Stress shadowing effect due to two closely spaced opening fractures. c) Two critically spaced opening fractures. Local stresses in between reach compression

The aim of this study is to simulate the feasibility of the development of a saturated orthogonal fracture network under one constant remote stress regime, using a relation between LEFM and sub critical crack growth, which is used in several other modelling studies [Ko and Kemeny, 2011, Olson, 2007, Pollard and Segall, 1987, Shen and Rinne, 2007]. We will focus on how an orthogonal fracture network shapes and is shaped by the regional applied effective tensile stresses and material conditions. Further, we compare how the numerically derived fracture network geometries correlate to published field studies. Finally, we test the feasibility of replacing effective tension caused by fluid over pressures ($\sigma'_z > P_f > \sigma'_H \geq \sigma'_h$) with tension assigned to model boundaries and discuss whether mode I fracture networks can be present within the subsurface.

2.2 Model design and fundamental framework

2.2.1 Model setup

In our 3D mechanical simulations, we will mimic the effective tensile stress state by directly applying tensile stresses in both horizontal directions (σ'_H, σ'_h). Furthermore, because we work mainly in the tensile stress domain, the presented results follow the engineering sign convention so that tension is positive and compression is negative.

The largest effective tensile stress is σ'_h and corresponds to the smallest principle compressive stress plus the pore pressure ($\sigma'_h = \sigma_3 + P_f$). The second horizontal stress is σ'_H and corresponds to ($\sigma'_H = \sigma_2 + P_f$). Throughout this study, the effective horizontal

tensile stress conditions are mostly referred to using the applied stress ratio (i.e. $\frac{\sigma'_H}{\sigma'_h}$). This ratio can range from near isotropic conditions (e.g. $\sigma'_h = 5.0$ MPa and $\sigma'_H = 4.5$ MPa ($\frac{\sigma'_H}{\sigma'_h} = 0.9$)) to a more heterogeneous tensile stress field (e.g. $\sigma'_h = 5.0$ MPa and $\sigma'_H = 0.5$ MPa ($\frac{\sigma'_H}{\sigma'_h} = 0.1$))

The meshing and calculation of the local stresses and strains is done using the ABAQUS finite element software. Here, fractures are represented by rectangular crack seam planes which have duplicate nodes on both opposite walls, allowing them to separate. These features can therefore slip or open following LEFM [Irwin, 1957]. Meshing of the fracture networks done using tetrahedral elements, and this allows us to change the aspect ratio (L/H), spacing over height ratio (S/H) or orientation of the individual fracture planes. The model domain has a linear elastic rock matrix which follows Hooke's law. For the material we assume isotropic conditions, so that the rock matrix is defined by a constant elastic Young's modulus (E) and Poisson's ratio (ν). To prevent any rotation or translation of the model, the corners of the bottom plane are fixed in any of the free directions ($x, y, z = \text{fixed}$) (Figure 2.3a). Further, the bottom surface in the z -direction to counter the overburden stress (Figure 2.3a).

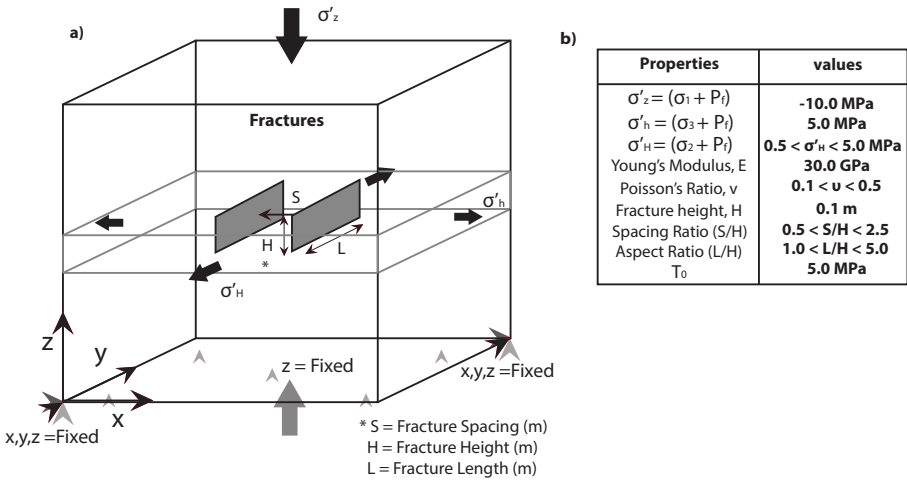


Figure 2.3: Model setup and parameter list. a) Model setup, where fractures are placed within the centre layer and extruded in the z -direction. The triangles represent the fixing boundary condition which prevents rotation and translation ($x = 0$ $y = 0$ and $z = 0$). The arrows represent the applied stresses in the horizontal and vertical directions. b) List of model parameters used in this study

In our models tension is assigned in both horizontal directions at the side walls, where σ'_h and σ'_H will represent the regional tensile stress in the x - and y -directions, respectively (Figures 2.3a, b). The vertical stress (σ'_z) corresponds to the effective over-

burden stress (Figures 2.3a, b). We assume that our model is placed at 1.0 km depth, assuming a typical layer cake type of geological basin. The tensile rock strength (T_0) (Figure 2.3b), is set equal to the maximum applied remote tensile stress ($\sigma'_h = 5.0$ MPa) and will remain constant in all models. In this study, the Poisson's ratio (ν), horizontal stress ratio ($\frac{\sigma'_H}{\sigma'_h}$) are changed in order to test how these parameters influence the local stress state and ultimately the saturated network geometry. The list of materials properties, assigned stresses and their respective ranges in magnitude are summarized in Figure 2.3b.

2.2.2 Brittle failure and sources of tensile stresses in subsurface

Mode I fracturing occurs when the tensile rock strength T_0 is overcome. However, in general, principal stresses in the subsurface are compressive due to the overburden, Poisson's and superimposed tectonic stresses. This implies that for mode I failure to occur in the sub-surface, additional tensile stresses are necessary. In geology, these extra stresses can be explained by a variety of processes such as, 1) local extension in a folding layer [Liu et al., 2016], 2) exhumation and the resulting thermal expansion [Fossen, 2010] or 3) an alteration of softer and stiffer layers and the coinciding stress perturbations [Boersma et al., 2020, Bourne, 2003, Guo et al., 2017].

Uniformly distributed pore fluid pressures are also regarded to be an important source of effective tension within the subsurface [Olson, 1993, Philipp et al., 2013]. Here, internal fluid pressures take part of the total stress that acts on the porous rock, thereby leading to a less compressive, more tensile effective stress state [Fossen, 2010]. In case of a fully connected pore volume of the stratified rock column, pore pressures follow the hydrostatic depth curve. However, under a variety of geological scenarios, such as hydrocarbon generation in rocks with low matrix permeabilities or disequilibrium compaction, pore fluids within rocks can reach significant overpressures [Emery, 2016, Hantschel and Kauerauf, 2009, Ouraga et al., 2018, Tingay et al., 2008]. These overpressures form a possible explanation for effective tensile stresses in overburdened compressed rock layers [Gale et al., 2010, Germanovich and Astakhov, 2004]. In Figure 2.4, this change in the effective stress state due to pore fluid pressures is depicted in Mohr space. The implemented fluid pressures can shift the Mohr circle potentially into the tensile domain until tensile failure occurs ($\sigma'_h = T_0$).

2.3 Modelling Strategy

2.3.1 From local effective stresses to a theoretical sub critical fracture propagation rate

While the formation of mode I fractures driven by effective stresses that reach the tensile rock strength (T_0) is understood (Figure 2.4), describing closely spaced mode I fractures is more difficult, since local tensile driving stresses in between a set of parallel mode I fractures get greatly reduced [Bai and Pollard, 2000] (Figure 2.2). This implies that the development of closely spaced mode I fractures and therefore orthogonal networks often occurs under sub critical stress conditions, because the theoretical rock strength is never overcome. Therefore, in geology, rock failure under these sub critical stresses is often described using the empirical theory of Sub Critical Crack Growth (SCCG) [Atkinson,

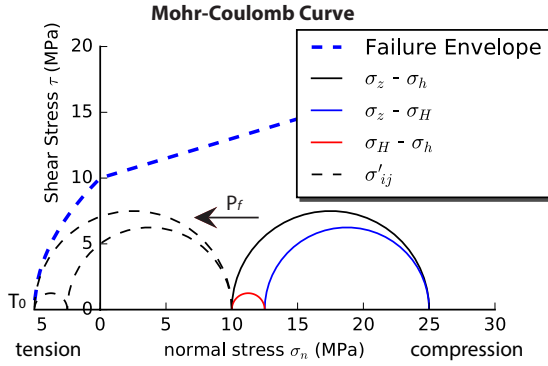


Figure 2.4: Regional stress state depicted in Mohr–Coulomb and the modelled effective regional stress state caused by fluid pressures

1984]. This theory is based on the relation between stress intensity (K_i), fracture toughness (K_{ic}) and measured fracture propagation rates, and postulates that fracture growth does not halt but slows when local stress intensity factors fall below the critical value (i.e. $K_i < K_{ic}$ and $\sigma'_h < T_0$ [Atkinson, 1984, Nara et al., 2012, Olson, 2007]).

Our study uses LEFM to incorporate SCCG in to our static models. This is done by calculating the stress intensity (K_i) on the implemented micro cracks, using the modelled crack opening and the LEFM relations first described by Pollard and Segall [1987]. These authors showed that the local stress intensity can be calculated using Eq. (2.1)

$$K_{tip} = Y \frac{\sqrt{\pi} E}{4(1 - \nu^2)\sqrt{a}} C_{open} \quad (2.1)$$

where E is the Young’s modulus of the matrix, ν is the Poisson’s ratio, Y is a geometrical factor (set at 1 in this modelling study), a is half the crack length and C_{open} is the maximum opening on a crack plane. The calculated stress intensity on each crack tip can then be related to a sub critical propagation rate using the stress corrosion cracking power–law [Atkinson, 1984]. This power–law relation is shown by Eq. (2.2) and is used in multiple lab an modelling studies describing SCCG [Atkinson, 1984, Ko and Kemeny, 2011, Nara et al., 2012, Olson et al., 2009, Shen and Rinne, 2007]:

$$v = v_{max} \left(\frac{K_{tip}}{K_{ic}} \right)^n, \text{ if: } K_i < K_{ic} \quad (2.2)$$

where v is theoretical sub critical growth rate (m/s), v_{max} is the maximum crack propagation rate, K_{tip} is the stress intensity on the crack tip, K_{ic} is the mode I fracture toughness (material property) and n is the sub critical crack growth index. We assume that K_{ic} can be related to the tensile rock strength and an initial crack length ($K_{ic} = Y T_0 \sqrt{a_{initial}}$, where $a_{initial} = 0.0125$ m), and the magnitudes of n and v_{max} are set to 35 and 100 (m/s), respectively, which is similar to other modelling studies [Olson, 2007, Olson et al., 2009, Shen and Rinne, 2007]. The implemented SCCG approach states that low local tensile stresses result in low stress intensities on the crack tip and therefore low calculated fracture propagation velocities. This implies that the reduction of effective stresses (Figure

2.2) would result in a saturated network at which no implemented fractures will grow. In this study we will not focus on the impact of changing the sub critical crack growth index (n), which is known to have a significant impact on the fracture spacing in mode I fracture networks [Olson, 2007, 2004].

2.3.2 A step-by-step modelling approach: Developing an orthogonal network under fixed remote stress conditions

In the following, we take the computed 3D stress field, apply the relation between LEFM and SCCG and calculate local propagation velocities of implemented micro cracks, to depict the development a saturated fracture network under fixed remote stress conditions, assuming steady state conditions and no transient pressure effects. For this modelling scenario, a remote effective tensile stress ratio of ($\frac{\sigma'_H}{\sigma'_h} = 0.7$) (i.e. $\sigma'_H = 3.5$ MPa, $\sigma'_h = 5.0$ MPa) and a Poisson ratio (ν) of 0.25 are applied to the boundaries and matrix of the model, respectively. The results depict a z-slice through the model, essentially cutting the model in half.

The initial fracture network (Figure 2.5) depicts two initially widely spaced parallel fractures placed perpendicular to the highest effective tensile stress. In between these fractures, 17 micro-fractures are placed perpendicular to one of the principal stress directions. These microfractures have an initial length of 0.025 m (2*element size) and have an initial spacing of $x = 0.1$ m for parallel fractures, and $y = 0.15$ m for orthogonal fractures, respectively. This geometry (Figure 2.5) is used as an initial fracture network for all modelling scenarios. Finally, for all simulations, the two outer fractures are not allowed to propagate throughout each timestep and we will only focus on the development of fractures within the area of interest (Figure 2.6).

The network geometry and the highest effective tensile stress field at the initial timestep are shown by Figure 2.6a. This figure depicts how the implemented mode I fractures open and perturb the local stress field following LEFM. Using Equations 2.1 and 2.2, the theoretical propagation velocity (m/s) of each micro fracture is calculated. As shown by the local stress field, local tensile stresses, and therefore, local fracture opening is highest at the centre of the model. This implies that the parallel fractures in these locations are most likely to grow. The resulting network derived from the initial timestep is depicted in Figure 2.6b and shows that the fractures in the centre of the model have indeed developed into a fully grown parallel fracture. Furthermore, some other micro fractures showed a few centimetres of growth (Figure 2.6b).

At intermediate stage [2], the local stress field is perturbed by the active fractures (orthogonal/parallel). The results show how the principal effective stresses perpendicular to the active parallel fractures ($\frac{\sigma'_x}{T_0}, \frac{\sigma'_y}{T_0}$) are becoming shadowed following LEFM. However, the local principal tensile stresses in the y-direction remain present (Figure 2.6b), resulting in a local stress flip ($\frac{\sigma'_x}{T_0} < \frac{\sigma'_y}{T_0}$). Despite the fact that a local stress flip occurs, the network geometry calculated during this stage is still a set off closely spaced parallel fractures (Figure 2.6c), which can be explained by the fracture growth implemented during the previous timestep.

At the third timestep, the effective stresses in the x-direction are now completely

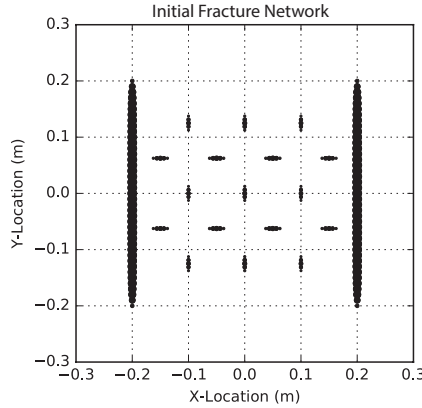


Figure 2.5: A z-slice through our model showing the initial fracture network geometry of two large bounding fractures (perpendicular to σ'_h), and 17 microfractures (perpendicular to σ'_h or σ'_H) having an initial length of 0.025 m. This network geometry is used in each modelling scenario

shadowed ($\frac{\sigma'_x}{T_0} \approx 0$), inhibiting further parallel fracturing. However, as was observed during the previous timestep, tensile stresses in the y-direction remain present (Figure 2.6c), causing the orthogonal microfractures to remain open. Given enough time (Myr) and prolonging tensile stresses, these fractures will develop into orthogonal fractures and this is also derived by our model (Figure 2.6d). The network geometry depicted at the final stage (Figure 2.6d) shows a fully developed orthogonal fracture network. Further, all initial tensile stresses are shadowed as a result of the developed fractures, ($\frac{\sigma'_x}{T_0}, \frac{\sigma'_y}{T_0} \approx 0$), and this implies that no new mode I fracture can grow in between the current active fractures. Therefore, the numerically derived fracture network depicted by Figure 2.6d shows a fully saturated orthogonal network, which is most probable to form given the applied boundary conditions, initial fracture network and material parameters.

2.4 Modelling results: saturated network geometries as a function of the remote stress state and Poisson's ratio

In the following, we use the same approach as described in the previous section, in order to investigate and depict how different boundary conditions lead to different saturated network geometries. The modelling scenarios are shown in Table 2.1.

The first three scenarios test the effect of Poisson ratio on the development of an orthogonal fracture network (Figure 2.7a–c), with the first, second and third scenario having high, intermediate and low implemented Poisson's ratios, respectively. The applied stresses are the same as shown in Section 2.3.2. The models show that a high Poisson's ratio results in a saturated geometry which is composed of a set of critically spaced parallel fractures (Figure 2.7a). In this scenario, the orthogonal micro fractures did not develop, and this effect can be explained by LEFM and linear elasticity. Here, the local compressive tangential stress response to the fracture opening is proportional to the implemented Poisson's ratio, with a higher Poisson's ratio resulting in a larger stress re-

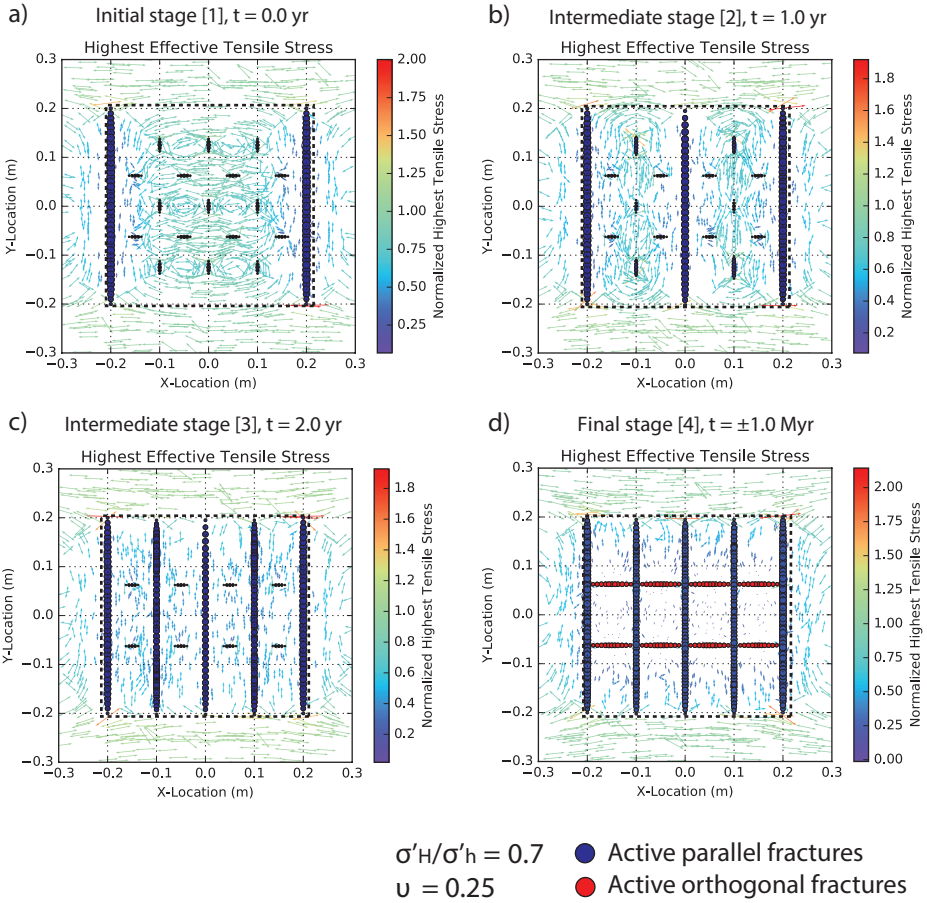


Figure 2.6: a) The highest effective tensile stress field for the initial development stage [1], in a x - y plane, within the centre layer of the model. The fractures are indicated by the connected circles. The size of the circle represents the opening of the fracture at that point. The colour of the circles (blue/red) indicates that the fracture has either developed into a parallel (blue) or an orthogonal fracture (red). b) Stress field and implemented fractures at the intermediate stage [2]. c) Stress field and implemented fractures at the intermediate stage [2]. d) Stress vector field of the final stage [4] and the resulting saturated ladder-like network.

Table 2.1: The different modelling scenarios depicted by figure 2.7

Scenario	Remote stress state ($\frac{\sigma'_H}{\sigma'_h}$)	Poisson's ratio (ν)
1	0.7	0.495
2	0.7	0.25
3	0.7	0.1
4	0.4	0.25
5	0.7	0.25
6	1.0	0.25

sponse [Pollard and Segall, 1987], resulting in a significant reduction of the local tensile stresses in the y-direction. For second modelling scenario, a more common Poisson's ratio of 0.25 is implemented and this lower ratio results in more favourable conditions regarding the presence of local tangential tensile stresses, and therefore, the development of the orthogonal microfractures. Hence, the saturated network geometry resembles a critically spaced set of systematic fractures (parallel) with orthogonal fractures in between (Figure 9c). Scenario 3 shows the end-member results of a model having low Poisson's ratio and as expected from LEFM, the final network geometry resembles a fully developed and saturated ladder-like fracture network pattern (Figure 2.7c).

Scenarios 4, 5 and 6 test the effect of the applied remote stress ratio on the development of a mode I fracture network (Figure 2.7d–f). Firstly, as expected from the low applied remote stress ratio in scenario 4 ($\frac{\sigma'_H}{\sigma'_h} = 0.4$), orthogonal failure becomes highly improbable. Therefore, the saturated network consists of a set of critically spaced parallel fractures (Figure 2.7d). In scenario 5 we increase the stress ratio to 0.7, making the development of orthogonal fractures possible. The results of this scenario therefore shows a ladder like orthogonal fracture network (Figures 2.7e). Finally, in scenario 6 (Figure 2.7f) we apply isotropic horizontal stress conditions ($\frac{\sigma'_H}{\sigma'_h} = 1.0$). Our results show that due to the magnitude of σ'_H , the first orthogonal fractures already develop after the initial stage, resulting in long orthogonal fractures in between the two initial fractures. These orthogonal fractures create a new stress shadow in the y-direction. However, local tensile stresses in x-direction are not completely shadowed, and this implies that the development of the smaller implemented parallel fractures is not halted. For this scenario, the fully saturated network geometry resembles a nested orthogonal fracture network (Figure 2.7f).

2.5 Discussion

2.5.1 Modelling effective tensile stresses: can boundary tensile stresses replace internal fluid pressure?

Applying effective tension on the model boundaries is a widely used method to simulate mode I fractures in the subsurface [Bai et al., 2002, Germanovich and Astakhov, 2004, Olson, 2007, Olson et al., 2009]. However, effective tensile stresses in the subsurface,

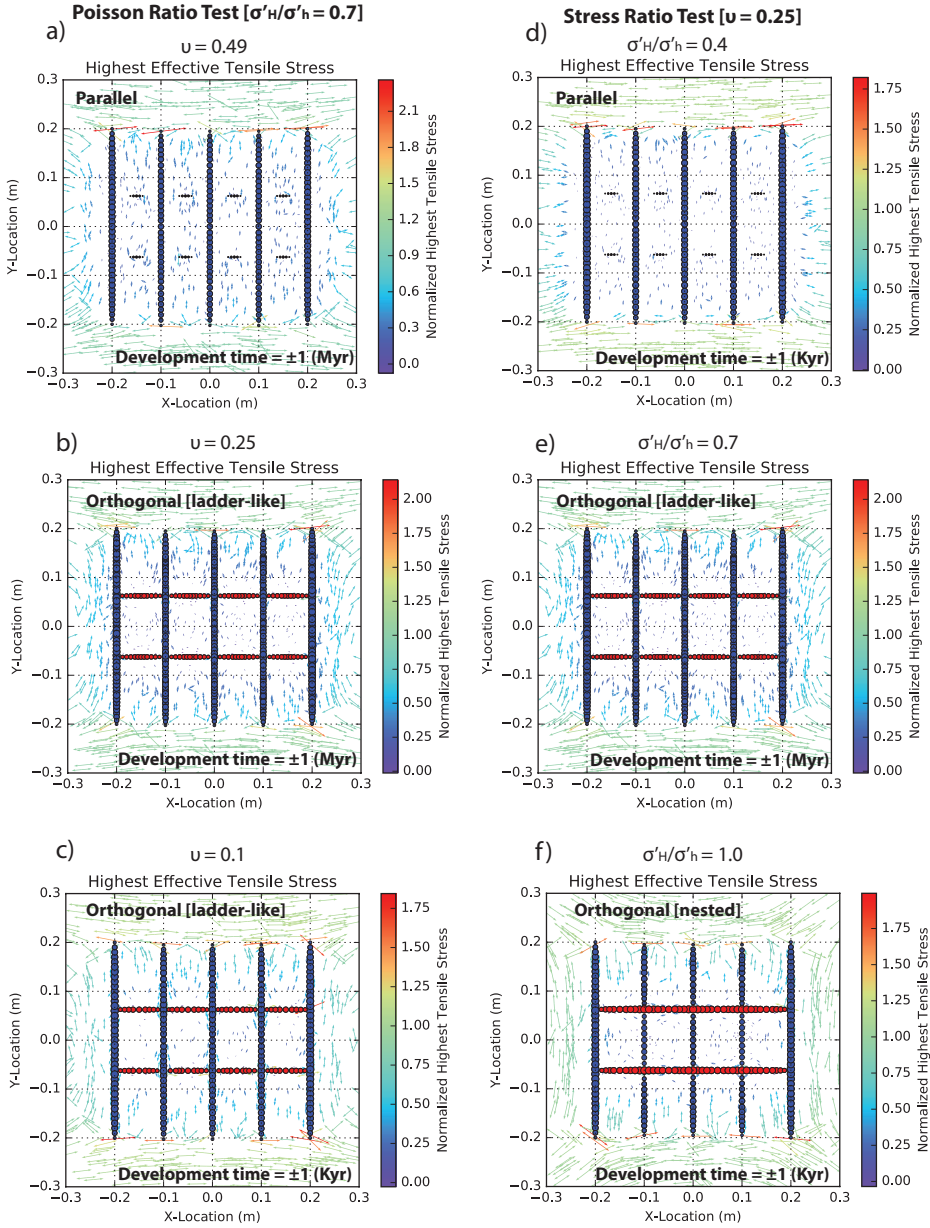


Figure 2.7: The end member results for different scenarios. a) Saturated network geometry for scenario 1 ($\sigma'_H/\sigma'_h = 0.7, \nu = 0.49$). b) Results for scenario 2 ($\sigma'_H/\sigma'_h = 0.7, \nu = 0.25$). c) Results for scenario 3 ($\sigma'_H/\sigma'_h = 0.7, \nu = 0.1$). d) Results for scenario 4 ($\sigma'_H/\sigma'_h = 0.4, \nu = 0.25$). e) Results from scenario 5 ($\sigma'_H/\sigma'_h = 0.7, \nu = 0.25$). f) Results for scenario 6 ($\sigma'_H/\sigma'_h = 1.0, \nu = 0.25$).

and therefore, mode I fracture development is often supported by pore fluid pressures [Olson, 1993]. Therefore, to test whether it is representative to replace this effective geological stress state with applied tensile stresses, we have created two 2D models. Both approaches are shown in Figure 2.8. Figure 2.8a shows our model design representing the effective stress state under the condition of a uniformly assigned fluid pressure within the matrix and compression to the boundaries. Figure 2.8b shows the alternative, commonly applied model design with effective tensile stresses assigned to the model boundaries. Both models tested assume steady state conditions and represent the crack tip as a singularity point. This required a structured meshing approach, which is different from the free meshing approach used for the 3D models. The results (Figure 2.8c–f) indicate that both approaches lead to an identical local stress distribution, which is expected from the superposition principle [Jaeger et al., 2007]. This confirms that the application of effective tension on the boundaries is a valid representation of modelling the effects of homogeneous distributed fluid overpressures within the matrix, assuming steady state static conditions.

However, our pore pressure models, and therefore the results presented in Figures 2.6, and 2.7, cannot account for any dynamic pressure behaviour, such as pore volume change, heterogeneous pressure fields or any fluid diffusion due to the opening of the cracks. All of these factors play an important role in the formation and development of natural hydraulic fractures [Mandl, 2005, Ouraga et al., 2018, Philipp et al., 2013]. Recent modelling work done by Ouraga et al. [2018] has shown that this dynamic pore pressure behaviour together with hydro-mechanical coupling results in transient fracture behaviour, at which fractures open and close as a result of local dynamic pressure changes. They showed that this dynamic fracture behaviour could have a significant impact on the resulting fracture network. Furthermore, their models showed more dynamic features such as small spacing/height ratios and non-elliptical fracture opening, which are also observed within natural fracture networks [Gudmundsson et al., 2010, Phillip, 2008]. However, these authors also showed that, given enough time, this transient behaviour ultimately resulted in similar network geometries and local effective stresses as depicted in this study and other mechanical modelling work [Bai et al., 2002, Olson et al., 2009, Ouraga et al., 2018].

2.5.2 Linking network geometries to remote stress, local perturbations and material conditions

Under steady state conditions and following the stress shadowing effect, the development of networks with closely spaced orthogonal fractures must occur under subcritical conditions [Bai et al., 2002, Olson, 2007]. Stresses in between two or more interacting fractures are greatly reduced and are, therefore, subcritical, with local conditions never reaching the theoretical tensile rock strength. This implies that without subcritical growth, no new fractures would grow in between two interacting opening mode fractures. However, when fracturing under sub critical stresses is acknowledged, the coeval development of orthogonal fractures in regions subjected to a local stress switch can occur, which can lead to the development of an intertwined nested network [Olson, 2007].

Our models used a relation between local stresses, fracture opening and propagation velocities to assess fracturing under subcritical conditions. The resulting models show

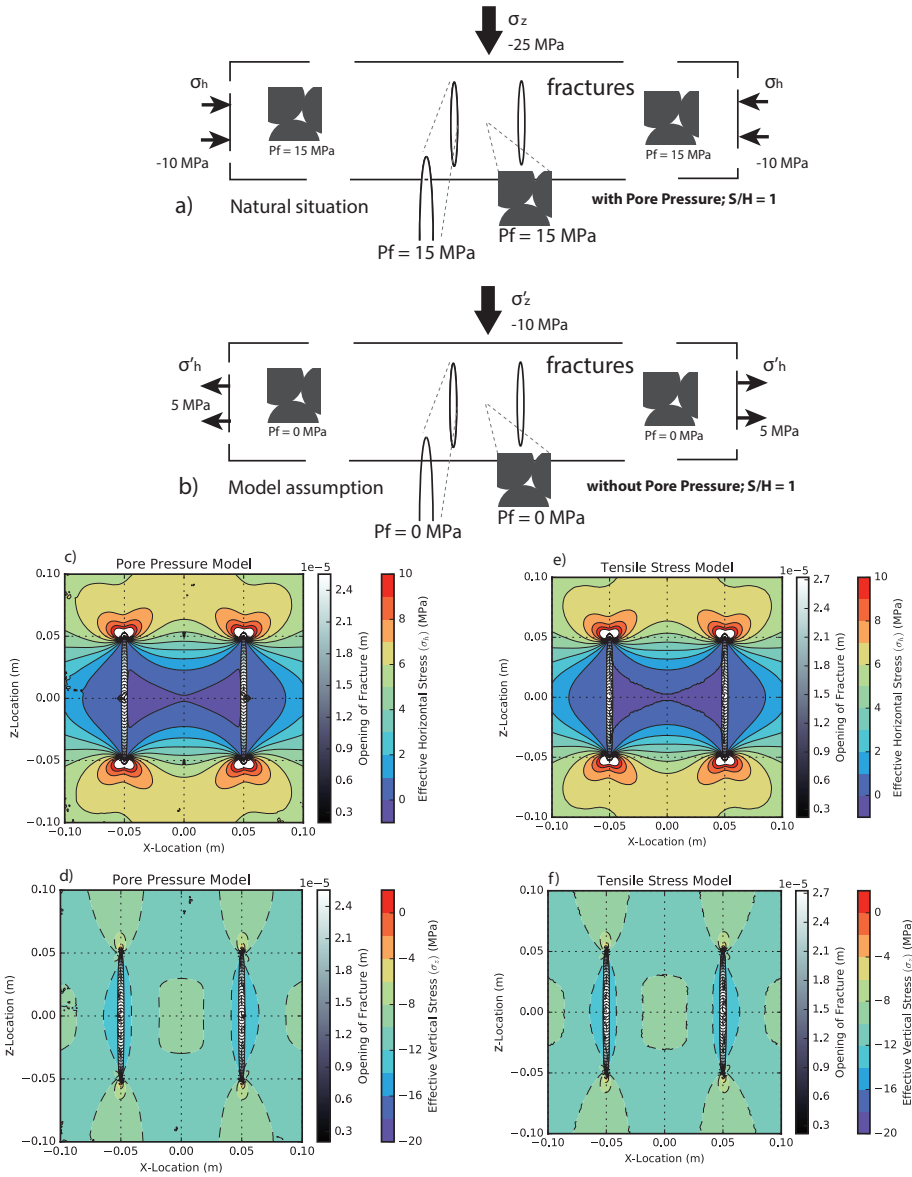


Figure 2.8: Conceptual outline of model conditions resulting in mode-I fracture opening a) Applying a uniformly distributed pore pressure of 15 MPa and a least compressional principal stress of $\sigma_h = -10$ MPa and an overburden stress of $\sigma_z = -25$ MPa. b) The alternative model at which we assign the effective stresses on the boundaries of the model and assign no internal pore pressure. c) Local horizontal stress distribution for our pore pressure model d) Local vertical stress distribution for our pore pressure model. e-f) The local stress distributions regarding our effective tensile stress models.

how the Mode I saturated network geometry (parallel, ladder-like or nested) is highly dependent on the applied stress conditions and material parameters (Figure 2.7). Our results showed that the successive development of an orthogonal fracture network requires sufficient remote tension in both horizontal directions and a favourable Poisson's ratio ($\frac{\sigma'_H}{\sigma'_h} \geq \pm 0.7, \nu \leq 0.25$). If these remote stress conditions are not satisfied, the saturated network geometry will probably be resembled out of a set of critically spaced parallel fractures. Our models also show that a small contrast between the applied horizontal stresses ($\frac{\sigma'_H}{\sigma'_h} \geq \pm 0.8$) will most likely result in the development of a nested network; a network pattern similar to hierarchies in orthogonal networks observed in outcrops [Engelder and Peacock, 2001, Mandl, 2005, Olson, 2008]. These model findings help distinguishing parameter space domains (remote stress state and Poisson's ratio) (Figure 2.9) at which the development of one of the saturated network geometries is most probable.

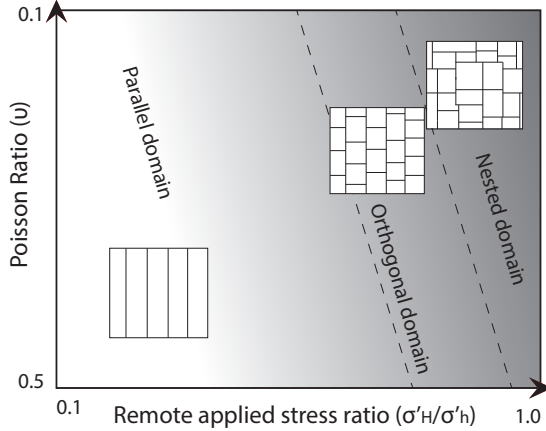


Figure 2.9: Parameter space plot depicting the remote conditions vs network geometry, based on the modelling done in Sect. 2.4 and 2.5. The borders between the different domains are indicated by the grey scale (White Parallel domain, Grey Nested). The oblique angle of these different domains is based on our models which tested the effect of the Poisson ratio (2.7)

2.5.3 Implications for field geology and subsurface reservoirs

The modelling results of this study show the conditions under which an orthogonal fracture network is most probable to form while experiencing one constant remote stress regime. The question is in how far these learnings can provide basic rules for predicting the presence of an orthogonal fracture network in the subsurface or on outcrops.

First of all, while our models depict relatively simple orthogonal network configurations with respect to observations made on outcrop analogues [Belayneh and Cosgrove, 2004, Houben et al., 2017, Olson, 2007], our findings do show how continued fracturing results in saturated network geometries at which further fracture infill is prohibited, and how this geometry is dependent on the applied boundary conditions. This could im-

ply that our findings can be utilized as a predictive tool for orthogonal fracture network geometries, assuming that the local stress conditions are known.

That being said, the development of orthogonal fracture networks observed on outcrops is generally assumed to be driven by uplift, erosion and the resulting extensional stresses in both horizontal directions [Fossen et al., 2007]. This could imply that these exhumation related features are unlikely to be present in the subsurface. Furthermore, because the exhumation of rocks occurs at geological time scales, horizontal tensile stresses can persist for millions of years, thereby allowing for fracture development under sub critical conditions as shown by our models.

Although the above stated argument is true, several case studies suggest that orthogonal fracture networks could form as a result of fluid overpressures and exist in low-permeable reservoir rock. For instance, recent studies on the Whitby Mudstone Formation and Cleveland Ironstone Formation (Cleveland basin, Yorkshire, UK) [Emery, 2016, Imber et al., 2014], argued that the observed orthogonal and nested fracture networks were created by pore fluid overpressures, which persisted over long timescales. Furthermore, micro seismicity and core studies from low permeability reservoirs in the Permian Basin (Texas, US) found evidence of open parallel and orthogonal fracture networks being present within the subsurface [Fisher et al., 2005, Gale et al., 2010, Warpinski, 2009]. Again, the observed fracture networks were believed to be created by fluid overpressures prolonging for a relatively long time, resulting in effective tensile stress and the development of closely spaced orthogonal fracture networks [Fisher et al., 2005, Warpinski, 2009, Warpinski et al., 2014]. These studies also argued that the stimulation, effective permeability and resulting production was significantly influenced by the presence and geometry of the natural fractures.

2.6 conclusions

This study shows how orthogonal and nested network arrangements can originate from stress shadowing and the resulting switching of the maximum tensile stress, caused by closely spaced Mode I fractures. First, the systematic development of an orthogonal and nested network requires that both principle horizontal stresses can act as a tensile driving stress and, therefore, are in sufficient tension. Second, due to the opening of systematic fractures and the resulting reduction in local effective stresses, the simultaneous development of an orthogonal network occurs under sub critical stress conditions.

Our modelling also depicts the underlying process on how the coeval development of mode I fractures (parallel and/or orthogonal) leads to a saturated fully developed network which can have a nested, orthogonal or parallel arrangement. As the network develops, local stresses and consequently local failure probabilities are greatly reduced by stress shadowing to the extent that eventually no new fracture can develop and a saturation of the network is reached.

Finally, this study confirms the mechanical feasibility of developing parallel, orthogonal or nested fracture network topologies under biaxial effective tensile stresses caused by, for example, pore fluid overpressures. The presented models illustrate that the geometry of the developed saturated network is highly dependent on the applied regional stress state and Poisson Ratio of the material. Here, a small contrast in magnitude of the horizontal effective tensile stresses ($\sigma'_H \approx \sigma'_h$) will result in the development of either

a nested or a ladder-like fracture network. Instead, a high stress contrast ($\sigma'_H \ll \sigma'_h$) or high Poisson ratios will inhibit the development of orthogonal fractures.

Data availability

The full dataset, modelling results and python scripts used for this chapter are freely available and can be downloaded via the following DOI: <https://doi.org/10.4121/uuid:4fc843b2-3cef-4637-9693-caf412c3b8df>

3

MECHANICAL CONTROLS ON THE DEVELOPMENT AND SATURATION OF CONJUGATE SHEAR FRACTURE NETWORKS

Conjugate-looking fracture networks are often observed on outcrops and generally show two fracture sets with systematic angles of 60° . Although these networks are widely observed, the factors controlling their development, characteristics and coeval abutment relationships are still poorly understood. In this study we address this issue using a similar workflow as introduced in chapter 2. To this end, we simulate the development of a conjugate fracture network from a set of initial micro cracks. We assume that fractures perturb the stress field following Linear Elastic Fracture Mechanics (LEFM) and that Sub Critical Crack Growth (SCCG) is a feasible model for fracture propagation. The results show that the conjugate micro fractures start to develop into a connected network arrangement once a critical differential stress is reached. These critical differential stresses are dependent on the implemented SCCG index and implemented rock strength. Further, our numerical simulations indicate that a higher applied differential stress, results in higher network intensities, more fracture opening and more critically stressed elements (i.e. elements which surpass the failure envelope). Finally, we show that fracturing continues within these critically stressed areas, which results in renewed stress localization and overall driving stress reduction, ultimately resulting in the development of a saturated nested conjugate fracture network.

3.1 Introduction

Conjugate-looking fracture networks are natural occurring arrangements of mode II fractures which generally consist of two sets having an approximate 60 degree difference in orientation [Bertotti et al., 2017, Fossen, 2010] (Figure 3.1a). These and other fracture networks generally form in response to distinct tectonic driving stresses and are widely observed on outcropping rocks and sub-surface reservoirs [Bertotti et al., 2017, Boersma et al., 2019b, Maerten et al., 2006, Toub Blanc et al., 2005] (Figure 3.1). However, while widely observed, the mechanical factors controlling the geometry, characteristics and saturation of these natural arrangements remain illusive and a topic of scientific debate [Laubach et al., 2019].

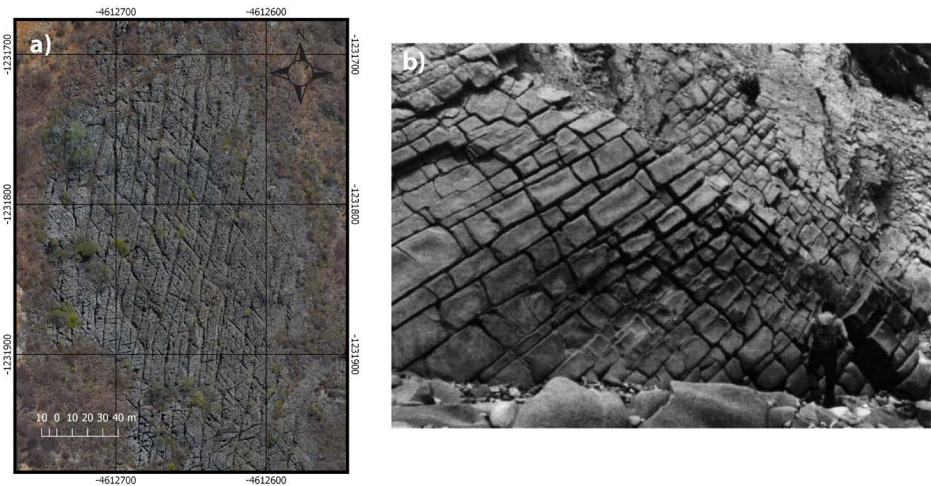


Figure 3.1: Drone image of a natural mode II conjugate fracture network (drone imagery first published by [Boersma et al., 2019b]). b) Picture of an inclined fractured pavement. The pavement highlights a mode I orthogonal fracture network. Figure modified after [Bai et al., 2002].

One way of investigating these controlling factors is by using numerical modelling. For instance, studies addressing the development of orthogonal fracture networks indicated that arrangements similar to those observed on outcrops can be obtained by applying tensile driving stresses [Bai et al., 2002, Bai and Pollard, 2000, Boersma et al., 2018a, Olson, 2007, Olson et al., 2009, Shen and Rinne, 2007] (Figure 3.1b). Furthermore, these studies showed that mode I fracture networks reach a saturated state due to local driving stress reduction, ultimately resulting in the development of predictable parallel -, ladder-like - or nested network arrangements (e.g. chapter 2).

On a first glance, conjugate fracture networks show a similar hierarchy and predictability with respect to orthogonal fracture networks (Figure 3.1). For example, on outcrops these networks commonly depict conjugate and hierarchical arrangements [Bertotti et al., 2017, Boersma et al., 2019b, Hardebol et al., 2015, Lamarche et al., 2012]. These geometries are also observed in small-scale numerical and laboratory experiments. For instance, studies addressing mode II rock failure under compressional conditions commonly show that conjugate fracture networks develop following a set of me-

chanical rules, thereby implying that there is a relation between the applied driving stresses, elastic parameters and the final network geometry [Barnhoorn et al., 2010, Douma et al., 2019, Guo et al., 2017, Shen and Rinne, 2007]. However, unlike mode I fracture networks, the exact mechanical factors controlling the development and saturation of conjugate shear fracture networks are still poorly understood.

In this chapter we expand on existing numerical techniques and model the gradual development of conjugate fracture networks whilst applying a compressive - and gradually increasing stress regime (e.g. increased tectonic compression). We also assess how the applied differential stress ($\sigma_H - \sigma_h$)_{applied} and implemented sub-critical crack growth parameter (n) control the network characteristics and saturation, by proposing six different modelling scenarios. For all simulations, we assume that the implemented fractures perturb the local stress field following Linear Elastic Fracture Mechanics (LEFM) and that fractures can propagate under sub critical stress conditions, which is a widely used approach in studies addressing natural fracture development (e.g. Boersma et al. [2018a], Ko and Kemeny [2011], Laubach et al. [2019], Olson [2007], Shen and Rinne [2007]). While this study shows promising results, it should be noted that the impact of the imposed boundary conditions and chosen workflow on the numerically-derived conjugate network arrangements might be significant and requires further investigation.

3.2 Modelling strategy

3.2.1 Initial model geometry and boundary conditions

For the presented mechanical simulations, we use the ABAQUS FEM modelling tool and simulate the development of a conjugate fracture network by applying a differential stress field (i.e. $\sigma_H > \sigma_h$) on the boundaries of the model. 55 initial fractures having a length of 1.0m were explicitly placed. The orientation of these features was set at an angle ranging between 20 and 70° with respect to the direction vector of the applied σ_H (Figure 3.2). The horizontal - and vertical spacing of the implemented fractures was set at 1.0 and 2.5 m, respectively (Figure 3.2).

The model domain (mesh) is compiled out of a linear elastic isotropic material which follows Hooke's law for 2D plane strain, with the behaviour of the material being defined by the Poisson ratio (ν) and the Young's modulus (E) (Table 3.1). The centre points (nodes) of the top and bottom boundary were fixed in the x-direction (figure 3.2). The left and right boundary were fixed in y-direction (figure 3.2). This way of 'fixing' the model boundaries provides in the most symmetric outcome regarding 2D modelling using the Abaqus finite element software. Finally, the key parameters which define the sub critical propagation of the fractures are shown in Table 3.1 and 3.2. These parameters are derived from previous laboratory and modelling studies, e.g. Bisdom [2016], Ko and Kemeny [2011], Olson [2007], Olson et al. [2009], Shen and Rinne [2007].

3.2.2 Calculating stress intensity and theoretical fracture propagation

A fundamental process in fracture network development is fracture interaction and local perturbations in the stress field caused by slip or opening of the initial flaws [Paluszny and Matthäi, 2009]. Our numerical models integrate these processes by combining Linear Elastic Fracture Mechanics (LEFM) with the assumption that fractures can propagate under sub critical stresses, using the theory of Sub Critical Crack Growth (SCCG).

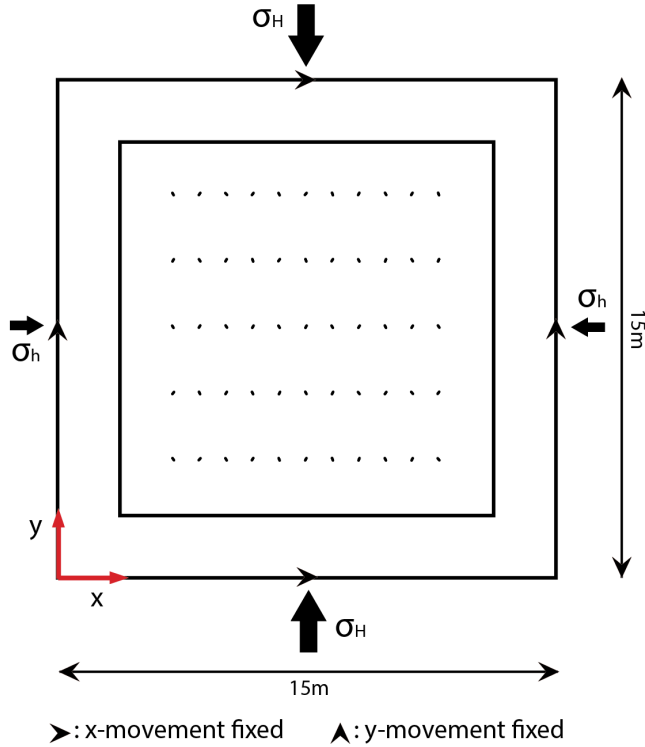


Figure 3.2: The initial model design. Compressive stresses are applied on the sides of the model and small micro fractures are implemented in the centre-part of the model. The ‘fixing’ of the model is indicated by the black triangles.

This theory has been used in numerous studies [Olson, 2007, Olson et al., 2009, Rijken, 2005, Shen and Rinne, 2007] and postulates that fracture growth rates are a function of the stress intensity (K_I, K_{II}) on each individual crack tip and the fracture toughness of the material (K_{IC}, K_{IIC}) [Atkinson, 1984]. Further, the theory of SCCG assumes that fracture propagation can occur at sub-critical conditions (i.e. $K_I < K_{IC}$ or $K_{II} < K_{IIC}$), at propagation rates ranging from the elastic wave speed to cm/Ma [Olson et al., 2009]. While SCCG is mostly used for describing mode I fracture propagation, several studies [Ko and Kemeny, 2011, Shen and Rinne, 2007] showed that this theory can also be used to describe sub critical crack propagation under mode II conditions. Below, we will shortly define the fundamental equations and key parameters describing SCCG 3.2.

The fracture toughness (K_{IC}, K_{IIC}) for mode I or II fracture behaviour, respectively is defined by the cohesion shear strength and tensile rock strength (Table 3.1 and 3.2) (assuming Mohr-Coulomb, Griffith failure and LEFM), and can be calculated using equations 3.1 and 3.2:

$$K_{IC} = Y T_0 \sqrt{\pi a_{\text{initial}}} \quad (3.1)$$

Parameters	Magnitude	Unit
Initial Fracture Length	0.1	m
Number of placed fractures	55	-
Young's Modulus (E)	30.0	GPa
Poisson's Ratio (ν)	0.25	-
Tensile Rock Strength (T_0)	7.5	MPa
Cohesion Shear Strength (S_0)	15.0	MPa
Friction on fracture plane (μ_p)	0.0	-
Friction parameter (rock) (μ_r)	0.6	-
Sub critical crack growth index (n)	50, 80	-
Maximum propagation rate (ν_{\max})	100.0	m/s

Table 3.1: Mechanical parameters and initial conditions used for all modelling scenarios. The sub critical crack growth parameters (n , ν_{\max}) are based on previous modelling and lab studies regarding both mode I and II failure [Ko and Kemeny, 2011, Olson, 2007, Olson et al., 2009, Rijken, 2005, Shen and Rinne, 2007].

Symbol	Definition	Unit
n	Sub critical crack growth index	-
ν_{\max}	Maximum propagation rate	m/s
K_{Ic} , K_{IIc}	Mode I/II fracture toughness	$\text{Pa}\sqrt{\text{m}}$
a_{initial}	Half the initial crack length	m
K_I , K_{II}	The stress intensity for mode I or mode II fracture propagation	$\text{Pa}\sqrt{\text{m}}$
a	Half the fracture length at a specific timestep	m
Y	Geometrical factor	-
C_{open} , C_{slip}	Modelled opening and slip on a fracture plane	m
ν_1 , ν_2	Mode I and II fracture propagation rates	m/s

Table 3.2: Overview of all the parameters used in the presented SCCG workflow

$$K_{IIc} = Y \tau_{\text{crit}} \sqrt{\pi a_{\text{initial}}} \quad (3.2)$$

where, Y is a geometrical factor and was set at 1.0, T_0 is the tensile rock strength ($T_0 = 7.5$ MPa), which was used for mode I failure, τ_{crit} is the critical shear stress, and is depended on the applied differential stress, cohesion shear strength and the rock friction parameter (i.e. $\tau_{\text{crit}} = S_0 + \mu_r \sigma_n$), and a_{initial} is half the initial fracture length. The stress intensity for each implemented fracture was calculated from the opening and/or slip on a crack plane, using equations 3.3 and 3.4 [Olson, 2007, Pollard and Segall, 1987]:

$$K_I = Y \frac{\sqrt{\pi} E}{4(1-\nu^2)\sqrt{a}} C_{\text{open}} \quad (3.3)$$

$$K_{II} = Y \frac{\sqrt{\pi} E}{4(1-\nu^2)\sqrt{a}} C_{\text{slip}} \quad (3.4)$$

Here, E is the Young's modulus of the matrix, ν the Poisson's ratio, a is the corresponding crack length and C_{open} and C_{slip} are the measured opening and slip on the crack plane, respectively.

Finally, equations 3.5 and 3.6 were used to relate the stress intensity to a local propagation rate, for mode I and II fracture growth. These power-law relations are used in multiple lab and modelling studies describing SCCG in geological materials [Atkinson, 1984, Charles, 1958, Ko and Kemeny, 2011, Nara et al., 2012, Olson, 2007, Shen and Rinne, 2007].

$$v_1 = v_{\max} \left(\frac{K_I}{K_{Ic}} \right)^n, \text{ if } K_I < K_{Ic} \quad (3.5)$$

$$v_2 = v_{\max} \left(\frac{K_{II}}{K_{IIc}} \right)^n, \text{ if } K_{II} < K_{IIc} \quad (3.6)$$

3.2.3 Sub critical crack growth in static finite element models

The Abaqus modelling tool can currently not assess multiple fracture propagation and interaction following SCCG. Therefore, we have chosen to use a ‘Quasi-Static’ modelling approach (similar to chapter 2), where each static modelling step is assumed to be a timestep in our modelling workflow (Figure 3.3).

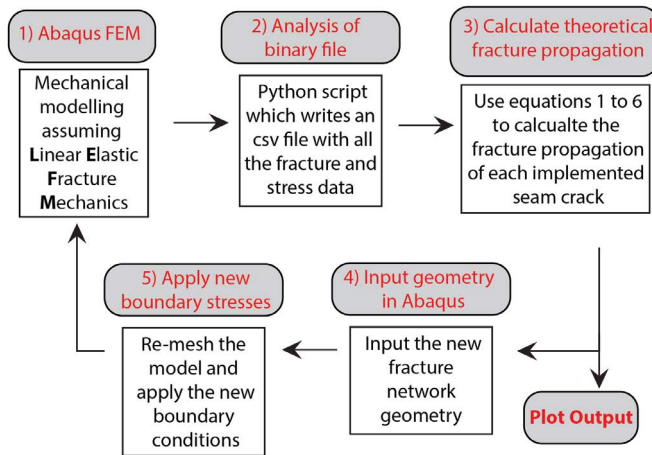


Figure 3.3: Flow chart which explains the processes of 1) mechanical modelling assuming LEFM, 2) data extracting and writing to a csv file, 3) calculation of the stress intensities and theoretical fracture propagation, 4) reimplementing of the new fracture network geometries in the Abaqus tool and 5) re-meshing of the model and reapplication of the new boundary conditions.

The first step is to extract the local stress and fracture data from the output binary file, acquired from Abaqus. This is done using a python script which loops through all the elements and nodes in the binary file, reading all the data, and writing it to a more manageable csv-file (Appendix B). Secondly, the local stress intensity for each individual crack seam is calculated using equations 3.1 to 3.4. Thirdly, the theoretical fracture propagation rate for each plane is calculated using equations 3.5 and 3.6. These rates are then converted to length and added as fracture segments to each respective crack tip.

Finally, the new network geometry is implemented into Abaqus model, which is then remeshed, and the new local stress field and stress intensities on the crack tips are then calculated (Figure 3.3). This process is repeated for each time step. Using this approach, we can slowly generate a conjugate fracture network from an initial set of micro-fractures, whilst assuming sub critical stress conditions.

3.2.4 Modelling scenarios and procedure

To address the controls on conjugate fracture network development and saturation, and to compare our results to previously conducted numerical studies, we apply a modelling procedure which is similar to Olson [2007], at which we gradually increase the applied driving stresses. To this end, all of the presented models have 25 time steps, with one time step representing 100.000 years. At each time step, the applied differential stress was slowly increased, with the rate of change being different for each stress scenario (Table 3.3 Figure 3.4a-b). To account for multiple and high velocity fracture propagation during one single time step, its respective duration is reduced to 1.0 second, so that simultaneous fracture propagation can be modelled correctly.

Further, we present six different modelling scenarios where we either change the applied stresses (rate and final magnitude) or the SCCG index (Table 3.3). First, the applied stress conditions differ between three different scenarios, with the scenario defining the maximum applied differential stress and stress increase per time step (Table 3.3 and Figure 3.4a-b). The conditions for the first - and second stress scenario remain sub-critical ($\tau_{\text{final}}/\tau_{\text{crit}} = 0.5$, $\tau_{\text{final}}/\tau_{\text{crit}} = 0.79$), which implies that the final stresses (at time step 25) never reach the theoretical failure envelope (Table 3.3 and Figure 3.4a-b). For the third scenario the final stress state reaches critical conditions, so that $\tau_{\text{final}}/\tau_{\text{crit}} = 1.0$ (Table 3.3 and Figure 3.4a-b). Second, the assigned SCCG index differs between 50 or 80, so that a total of six different modelling scenarios were generated (Table 3.3). These values were based on previously conducted laboratory work [Holder et al., 2001, Olson, 2007].

Model	Stress scenario	Max ential ($\sigma_H - \sigma_h$) _{applied} (MPa)	differ- stress factor ($\tau_{\text{final}}/\tau_{\text{crit}}$)	Sub critical stress	SCCG index (n)	K_{Ic} (Pa \sqrt{m})	K_{IIc} (Pa \sqrt{m})
1	1	25	0.5	50	2972495	7541360	
2	1	25	0.5	80	2972495	7541360	
3	2	45	0.79	50	2972495	9315798	
4	2	45	0.79	80	2972495	9315798	
5	3	65	1.0	50	2972495	11090235	
6	3	65	1.0	80	2972495	11090235	

Table 3.3: Differential stress, shear stress ratio, SCCG index and fracture toughness for each of the tested models.

The implemented K_{Ic} and K_{IIc} were calculated using equations 3.1 and 3.2, respectively. This implies that, since the mode II stress intensity is calculated from the critical shear stress (equation 3.2), each respective K_{IIc} is dependent on the applied stress scenario (Table 3.3). Here, scenario 1 has the lowest τ_{crit} and therefore lowest K_{IIc} , whereas stress scenario 3 has the highest τ_{crit} and K_{IIc} (Table 3.3 and Figure 3.4).

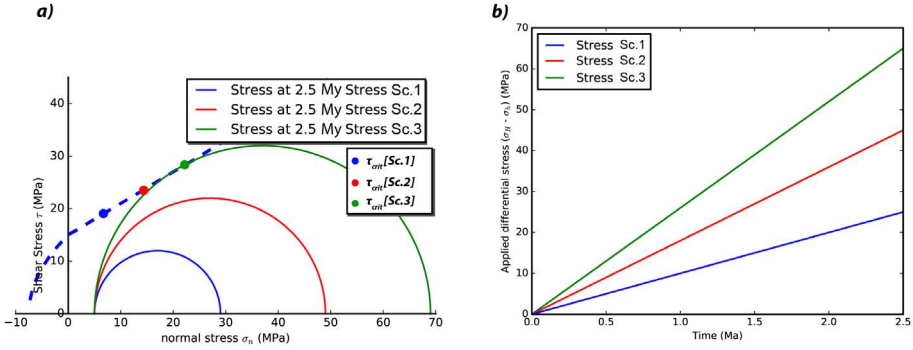


Figure 3.4: a) Final stress state and critical stress (τ_{crit}) for each stress scenario (i.e. $\tau_{final}/\tau_{crit} = 0.5$, $\tau_{final}/\tau_{crit} = 0.79$ and $\tau_{final}/\tau_{crit} = 1.0$). The utilized friction parameter of the failure envelope was set at 0.6 (table 3.1). b) Applied differential stresses $((\sigma_H - \sigma_h)_{applied})$ as a function of the modelled time for each stress scenario.

3.3 Results

3.3.1 Developing a connected conjugate network under sub-critical stress conditions

Using the presented modelling procedure, we develop a conjugate fracture network from the initial fracture network (Figure 3.2), whilst applying boundary conditions for modelling scenario three (stress scenario 2) (Table 3.3 and Figure 3.4a-b). For this modelling scenario, a differential stress increase of 1.8 (MPa/100Kyr) was applied, resulting in a maximum applied differential stress of 45 (MPa) and a sub-critical stress factor of 0.79 (Table 3.2 and Figure 3.4). Further, the SCCG index (n) of 50 was implemented for all crack tips (Table 3.2 and Figure 3.4). It should be noted that in this - and all other presented models, the mode of fracturing is defined by the modelled stress intensity on the crack tip (i.e. if $K_I/K_{IC} > K_{II}/K_{IIc}$, then mode I, else mode II). Further, the propagation angle with respect to the largest principal stresses is derived from classical fracture mechanics (i.e. mode I $\theta = 0$ deg and mode II $\theta = 30$ deg). Finally, it should be noted that fractures can not propagate through previously developed fractures.

For the presented modelling scenario, the onset of fracturing starts at time step 16 (i.e. 1.6 Myr and $(\sigma_H - \sigma_h)_{applied} = 28.8$ MPa), at fractures which show most slip, resulting in relatively high stress intensities and therefore a few centimetres of modelled crack growth (Figure 3.5a and b). This initial propagation results in a positive feedback loop, where the slightly longer fractures quickly develop into meter long conjugate features (Figure 3.5b). These fractures highly perturb the local stress field, resulting in immediate fracture propagation in areas showing significantly higher differential driving stresses (Figure 3.5b). This again result in a positive feedback loop of local stress increase and fracture growth, which results in the development of a fully connected conjugate fracture network in just a few time steps (Figure 3.5c). Because of the continued increase in applied differential stresses, fracturing continues in areas with localized driving stresses, resulting in continued fracture infill (Figure 3.5d). Fracture propagation stops in areas where the local differential stresses are significantly reduced or in areas where the principal stress orientation are either parallel or perpendicular to the respective fracture plane

(Figure 3.5d).

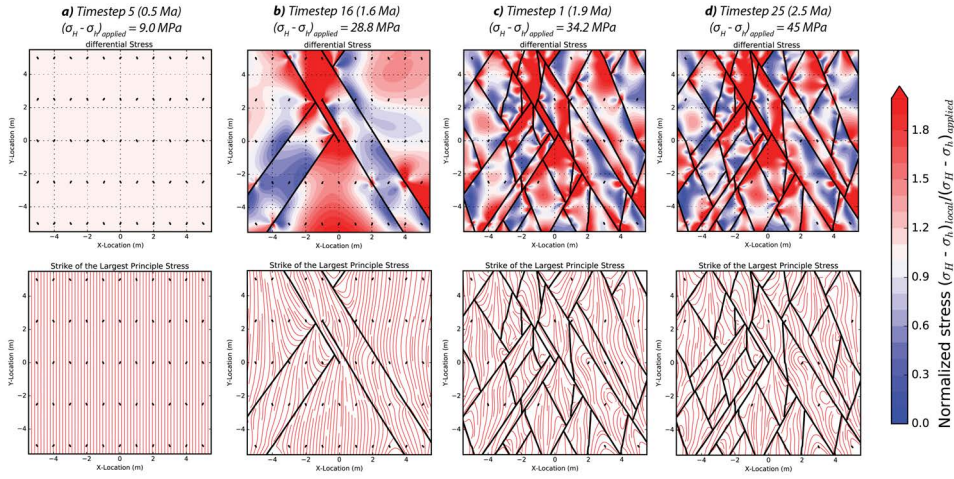


Figure 3.5: a-d) Local normalized stress field $(\sigma_H - \sigma_h)_{\text{local}} / (\sigma_H - \sigma_h)_{\text{applied}}$ and strike of the largest principal stress component, for timesteps 5 (0.5 Ma), 16 (1.6 Ma), 19 (1.9 v) and 25 (2.5 Ma) respectively. Applied differential stresses for each depicted time step are 9.0 (MPa), 28.8 (MPa), 34.2 (MPa) and 45.0 (MPa) respectively.

The final network geometry resembles a nested conjugate system (Figure 3.5d), with the final stress field being highly perturbed by the interacting fractures. For example, due to stress localization, significant tensile stresses are present within the modelling domain (Figure 3.5d and 3.6a). These tensile stresses cause local opening of fracture planes (Figure 3.6a and b). The modelled opening depends on the magnitude of the tensile stress and ranges from several millimetres to multiple centimetres (Figure 3.6a and b). The results also indicate that numerous elements show differential stresses which surpass the implemented failure envelope (i.e. reaching a critical state) (Figures 3.4a and 3.6c). Following Mohr-Coulomb theory, these critically stress areas theoretically fail. Therefore, these results indicate that under the proposed conditions, the acquired network geometry does not resemble a saturated state. This implies that as long as increasing boundary stresses are applied, fracture infill will most likely continue in areas showing critically stressed elements (Figure 3.6c).

3.3.2 Conjugate network geometries and characteristics as a function of the applied boundary conditions

In order to investigate and depict how the applied boundary conditions affect the resulting network geometry and characteristics, the modelling experiment shown by figures 3.5 and 3.6 is repeated for each of the presented scenarios (Table 3.3).

For modelling scenarios 1, 3 and 5, we test changing the sub critical stress factor from 0.5 to 1.0 (i.e. sub-critical - to critical conditions), whilst keeping the SCCG index (n) at 50 (Table 3.3). The results show that the network geometry is only slightly dependent on the applied sub critical stress factor ($\tau_{\text{final}} / \tau_{\text{crit}}$), with all models showing fully connected conjugate fracture networks (Figure 3.7a). While the acquired results look similar, the

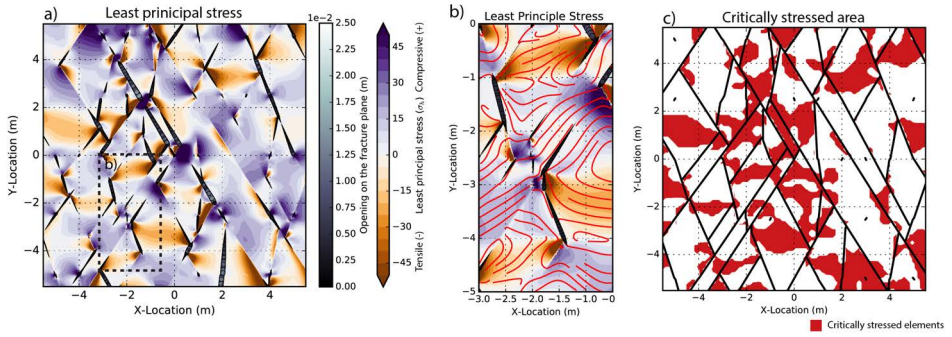


Figure 3.6: a) Contour plot of the least principal stress. The size and colour of the circles depicts the local fracture opening. b) Zoomed in area of the results depicted by Figure 6a. Depicted by the red stream lines are the local orientations of the least principal stress (σ_h). c) Critically stressed areas present within the final time step of the model. Red colours indicate areas where the local differential stress and/or tensile stress surpasses the implemented Mohr-Coulomb failure envelope (figure 4a).

degree fracture infill is being affected by changing the applied stresses, with higher stress resulting in more fracture infill (Figure 3.7a).

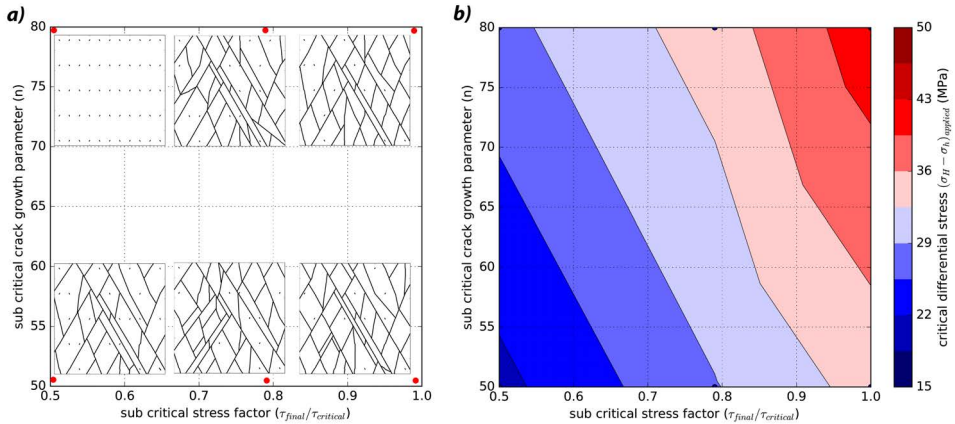


Figure 3.7: a) Final network geometries plotted with respect to the characteristics of each modelling scenario (sub critical stress factor (τ_{final}/τ_{crit}) and sub critical crack growth index (n)). b) Linearly interpolated map of the critical differential stress necessary for the initiation of the development of the conjugate fracture network, for each modelling scenario.

Scenarios 2, 4 and 6 show the impact of increasing the SCCG index ($n = 80$) (Table 3.3). The results show that for low stress factors ($\tau_{final}/\tau_{crit} = 0.5$), increasing the SCCG index has a high impact on the modelled fracture network development and final geometry (Figure 3.7a). In this scenario, the necessary stresses for the onset of fracture propagation are not reached, resulting in an undeveloped network geometry (Figure 3.7a). For the other two scenarios, these critical differential stress conditions are reached, thereby resulting in the development of a fully developed conjugate network (Figure 3.7a).

As was observed in figure 3.5 (scenario 3), these additional experiments highlight that once the critical differential stress is reached, the initial micro cracks quickly develop into a conjugate fracture network. Figure 3.7b shows an interpolated map of this critical differential stress. This figure highlights that the critical stress differs per modelling scenario, with a higher stress factor and SCCG index results in higher critical differential driving stress (Figure 3.7b). This observation can be explained by the SCCG crack growth laws (equation 1 to 6). These equations show that the critical differential driving stress needed for fracture network development is only dependent on three user defined variables namely, the rock strength (i.e. K_{IIc}), SCCG index (n) and initial crack length ($a_{initial}$). This implies that when assuming similar boundary conditions as presented in our models, equations 1 to 6 can be used to analytically derive the critical differential driving stresses necessary for fracture network development ($(\sigma_H - \sigma_h)_{applied}$), for a given SCCG index (n) and implemented critical shear stress (τ_{crit}) (i.e. stress scenario). The result of these calculations are shown by figure 3.8, and this figure highlights that the critical driving stress greatly depends on the assigned material properties.

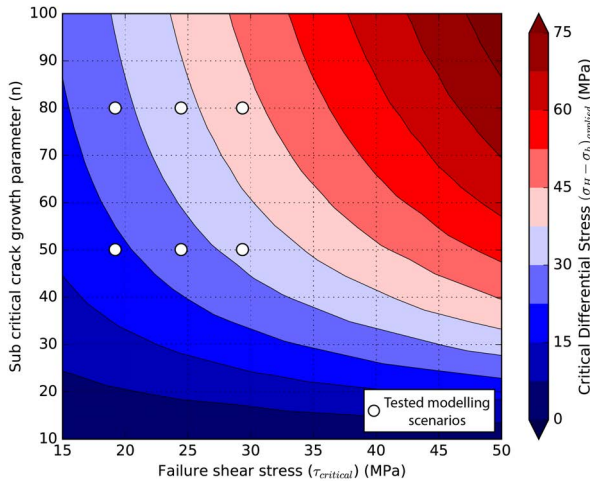


Figure 3.8: The critical differential driving stress need for fracture network development as a function of the failure shear stress and sub critical crack growth parameter. Highlighted by the white points are the conditions of the conducted modelling experiments.

The overall fracture opening of the final modelling time step (Figure 3.6a) is also greatly influenced by the assigned modelling scenario. The results indicate that models having a low maximum applied differential stress show a low fracture opening (Figure 3.9a), whereas models having a high applied differential stresses show the opposite effect (Figure 3.9a). This behaviour is expected from LEFM, because low applied stress will result in less stress localization and fewer tensile stress and less fracture opening. Changing the SCCG index has no significant impact on the overall fracture opening (Figure 3.9a).

Similarly to the fracture opening, the number of critically stresses elements are also

greatly influenced by the assigned modelling scenario (Figure 3.9b). Here, models having a low maximum stress will result in a smaller area of critically stressed elements, whereas models having a higher stress factor will result in a large quantity of the elements being critically stressed (up to 60 percent). These results indicate that apart from modelling scenario 2, the acquired network geometries are not saturated. In addition, these results highlight that the number of critically stressed elements is greatly dependent on the applied stress.

3

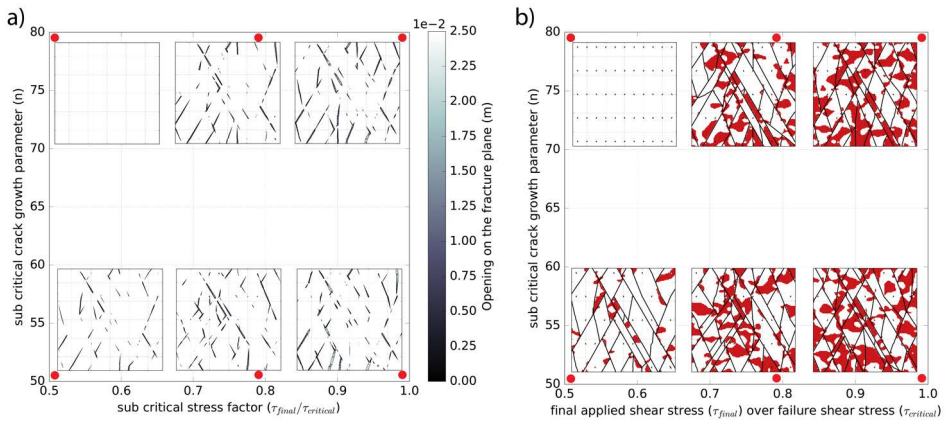


Figure 3.9: a) The local fracture opening plotted for each modelling scenario. The size and colour of the circles depicts the local fracture opening. b) Critically stress areas for the final time step plotted for each modelling scenario.

3.4 Discussion

3.4.1 Will continued fracture infill result in a saturated network geometry?

Our results indicated that as a result of stress localization the computed fracture networks are not saturated. This implies that given the applied boundary conditions, fracturing will most likely continue in critically stressed areas (Figures 3.6c and 3.9b). However, these results do not answer the question of whether a conjugate shear fracture network can ever reach a saturated state. To answer this question, we take the final network geometry shown in figure 3.5 (scenario 3), and run an additional experiment. To this end, we place 14 new fractures inside an area which shows critically stressed elements (Figure 3.10a), having an initial length of 0.05m and are a 30° angle with respect to the local largest principal stress orientation (Figure 3.10b).

The results show that the newly emplaced fractures quickly grow into large conjugate features (Figure 3.10c). These newly developed fractures significantly perturb, localize and reduce the modelled differential stress field. However, the modelled driving stresses still remain relatively high. Therefore, for the next time step, we place an additional 30 micro fractures (Figure 3.10c). Again, these features quickly develop into fractures, further localizing the modelled stress field (Figure 3.10d). At the final time step, the stress localization caused by the newly emplaced fractures has resulted in a significant reduc-

tion of the local driving stresses (Figure 3.10a, b and d). Therefore, these results suggest that when assuming the assigned boundary conditions, the process of stress localization, fracture infill and driving stress reduction will ultimately result in the development of a saturated conjugate fracture network, which shows a large variety in local fracture intensity.

3.4.2 Similarities and differences between numerically-derived conjugate - and orthogonal fracture networks

The mechanical controls on the development and characteristics of natural fracture networks have been widely studied using numerical modelling [Bai et al., 2002, Boersma et al., 2018a, Olson, 2007, Olson et al., 2009, Rijken, 2005]. For instance, studies addressing the development of orthogonal fracture networks showed that the observed hierarchy and organization is a product of the interplay between fractures and LEFM. Furthermore, these studies showed that as result of this interplay, the development of a mode I fracture network ultimately results in a so called saturated fracture network [Bai et al., 2002, Boersma et al., 2018a, Olson, 2007]. On outcrops, conjugate fracture networks show a similar form of hierarchy and organization (e.g. Boersma et al. [2019b]). This study addressed the question on how these networks develop and what controls their characteristics and saturation. This was done using a numerical modelling approach similar to studies addressing mode I fracture network development (e.g. chapter 2 or Olson [2007], Olson et al. [2009], Shen and Rinne [2007]).

The presented numerical experiments show that initially mode II conjugate develop fairly similar to numerically generated mode I fracture networks. Once a critical driving stress was reached, the implemented micro cracks quickly developed into a fully connected network. This was also observed in the numerical studies addressing mode I fracture networks [Olson, 2007]. However, this is where the similarities between the development of the two numerically derived arrangements stop. For example, unlike mode I fracture networks which reach a saturated state via significant driving stress reduction [Bai et al., 2002, Boersma et al., 2018a, Olson, 2007, Olson et al., 2009], conjugate fracture networks develop via stress localization, resulting in nested network geometries which show localized zones of intensive fracturing. The degree of fracture infill and local intensity of conjugate fractures are highly dependent on the applied driving stresses. This is not observed for numerically derived mode I fracture networks which reach a saturated state due to fracture infill, regardless of the applied tensile stresses (e.g. Bai et al. [2002], Boersma et al. [2018a], Olson [2007]).

3.4.3 Implications of the main modelling assumptions

The presented modelling results portray the mechanical controls on the development and characteristics conjugate shear networks. However, while showing promising results, our modelling workflow contained some significant assumptions, which may highly influence the numerically-derived conjugate fracture networks.

For instance, we assumed that SCCG is a feasible mechanism for mode II fracture propagation. Although SCCG has been observed for mode II fracturing in laboratory studies [Ko and Kemeny, 2011], the implemented governing equations (equations 3.5 and 3.6) are derived from laboratory studies modelling mode I fracture propagation

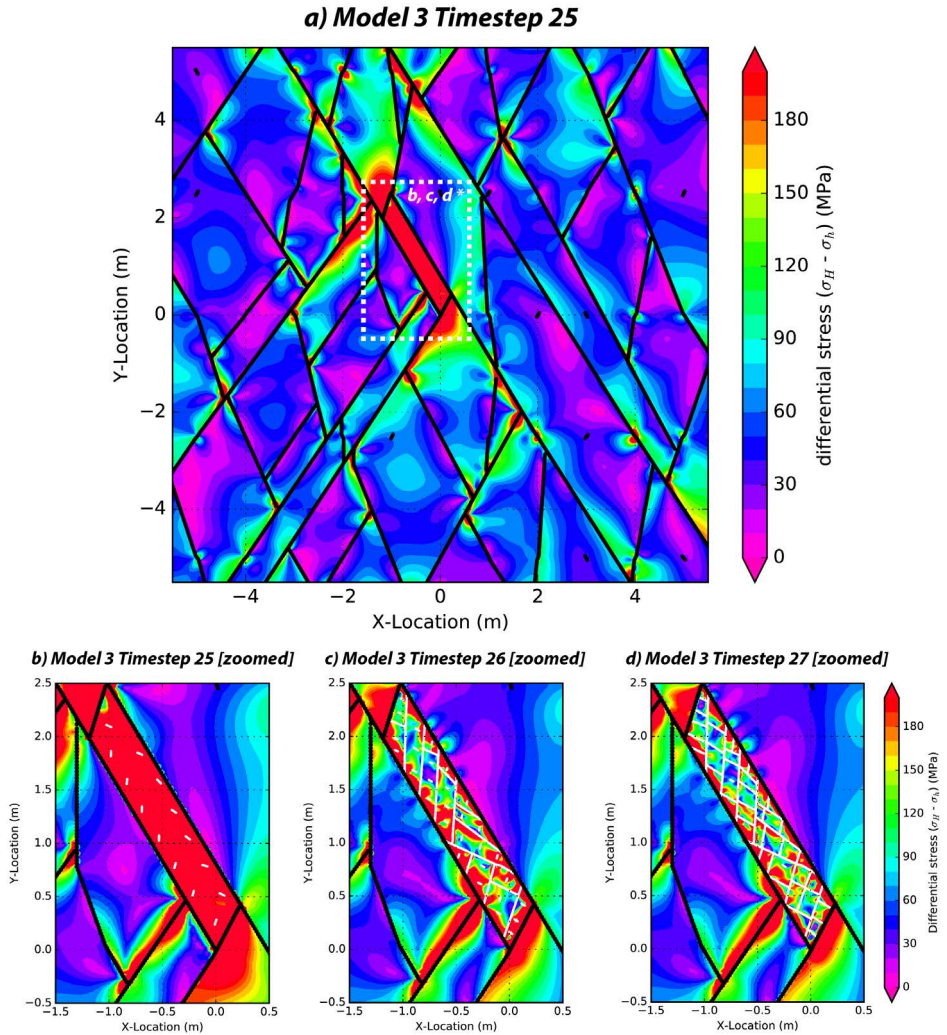


Figure 3.10: a) Differential stresses plotted for the final time-step of model 1. Highlighted by the white dashed rectangle is the location of figure 10b and c respectively. b) Initial implemented micro-perturbations. c) Developed and newly placed perturbations after one time-step. d) Developed perturbations after the second time step.

[Atkinson, 1984, Charles, 1958], which may result in inaccurate propagation estimations. Further, we used a modelling procedure similar to Olson [2007] at which we gradually increased the applied driving stresses even after the fractures started to develop. By doing so, local differential driving stresses surpassed the theoretical failure envelope, resulting in continued fracture infill. However, in most natural examples, applied driving stresses are generally assumed to be released once failure of a material occurs, and these examples generally show localized fracture zones rather than the connected fracture networks as observed by our models (e.g. Douma et al. [2019], Guo et al. [2017]). Another issue concerns crack tip stresses. In our models, the presence of crack tips considerably controls the development of conjugate networks (e.g. Figure 3.10). Although multiple natural examples of crack tip stresses and crack tip interaction exists [Fossen, 2010, Maerten et al., 2016], it is not known whether these crack tip stresses are present throughout the entire development of respective fracture networks.

Therefore, following from the above described assumptions and limitations, we argue that more work using different numerical approaches is necessary, so that the mechanical controls on the development and saturation of mode II conjugate fracture networks are better understood.

3.5 Conclusions

This study implements a numerical modelling workflow which combines LEFM and SCCG, to model and assess the mechanical factors controlling the development, characteristics and saturation for mode II conjugate fracture networks. For the presented scenarios, the applied stresses ranged from sub-critical to critical. The implemented SCCG indices were based on previously conducted laboratory work. The initial fracture network geometry was constant for all modelling scenarios.

Our numerical realizations highlight that once a critical differential driving stress is reached, the initial micro fractures quickly develop into a fully connected and nested conjugate fracture network. The magnitude of these necessary driving stresses are directly dependent on the applied stress conditions and SCCG index. Further, we show that these necessary driving stresses can directly be calculated from the equations governing SCCG.

Our models also show that the development of conjugate fracture networks results in significant stress localization, with local differential stresses overcoming the implemented failure envelope. In addition, our simulations indicate that due to stress localization, tensile stresses are present within the modelling domain, thereby causing local fracture opening. The amount of stress localization, number critically stressed elements and local fracture opening are directly dependent on the applied differential stress magnitude.

Lastly, by placing additional micro cracks in an area which has relatively high differential stresses, we show that fracturing continues in critically stress areas. This continued fracture infill results in an overall reduction of the local differential driving stresses. Therefore, we argue that conjugate fracture networks develop and reach a saturated state via stress localization, resulting in nested network geometries, which show localized zones of intensive fracturing.

Data availability

The full dataset, modelling results and python scripts used for this chapter are freely available and can be downloaded via the following DOI: <https://doi.org/10.4121/uuid:1b586b92-5e9d-4aeb-9d7b-76b289a1c791>.

4

MECHANICAL CONTROLS ON STRESS AND FRACTURE BEHAVIOUR IN LAYERED ROCKS

In layered materials, the deformation style, orientation, confinement, and 3D connectivity of natural fractures is generally impacted by changes in sedimentary facies and alternations in mechanical properties. In this study we address this effect and perform a numerical sensitivity analysis. Mechanical properties, confining pressure, and internal friction are varied for a three-layered model, to investigate and quantify the relation between contrasting material properties, the principal horizontal stresses and fracture behaviour (i.e. deformation style and orientation). Firstly, the results show that tensile stresses develop in the stiffer layers, due to the contrasting elastic parameters. The magnitude of these stresses is dependent on the ratio between the elastic parameters of stiffer and softer layers (i.e. $\frac{E_{\text{stiff}}}{E_{\text{soft}}}$ and $\frac{\nu_{\text{stiff}}}{\nu_{\text{soft}}}$). There are no horizontal tensile stresses, when applying a compressive horizontal confining pressure (approx. 1/5 of the applied vertical stress). Implementing an inter-facial friction lower than 0.2 will result in decoupling of the layers, resulting slip on the layer boundaries and no tensile stresses within the stiffer layers. Further, the acquired numerical results are in good agreement with previously conducted laboratory work. Finally, we discuss whether the presented results can be used for better relating contrasting mechanical properties to potential fracture deformation styles and orientations in layered outcrops or subsurface reservoirs.

4.1 Introduction

Rocks are generally deposited in alternating lithological units with significant variation in mechanical properties. These properties generally define the tensile and compressive rock strength [Ferrill et al., 2017b, Smart et al., 2014], indicating under which stress state a rock fails [Roche et al., 2013]. Field observations have also shown that geological layering can influence the mode, orientation, and abutment of natural fractures [Ferrill et al., 2014, Ferrill and Morris, 2003, Roche et al., 2013]. This implies that the natural fracture connectivity and geometry is at least partly dependent on geological layering and the coinciding alternating mechanical properties [Ferrill et al., 2017b].

In field geology, contrasting or changes in mechanical properties are generally referred to as the Mechanical Stratigraphy (MS) (i.e., mechanical properties, layer thickness, and the nature of the layer interface) [Laubach et al., 2009]. The effect of MS on fracture deformation style, orientation and confinement is widely observed in field examples. For instance, previous field studies on fractures in layered rocks have shown that the MS generally controls the fracture frequency and confinement in different layers [Cooke and Underwood, 2001, Hooker et al., 2013, Rijken and Cooke, 2001]. In addition, other field observations show that MS also affects the fracture deformation style and orientation [Brenner and Gudmundsson, 2004, Ferrill and Morris, 2003, Ferrill et al., 2017b, Larsen and Gudmundsson, 2010, Smart et al., 2014]. However, although the link between fracture behaviour and MS is clear, it should be noted that the MS can vary with diagenesis, implying that the observed fracture stratigraphy may not always be representative of the MS which was present at the onset of fracturing [Laubach et al., 2009]. This should be taken into account, else erroneous interpretations can ensue [Laubach et al., 2009].

The change in fracture behaviour as a result of a mechanical stratigraphy is also addressed by multiple laboratory and numerical studies [Bourne, 2003, Douma et al., 2019, Guo et al., 2017, Schöpfer et al., 2011, Teufel and Clark, 1984, Warpinski et al., 1981]. These studies showed that the change in fracture behaviour could be attributed to local horizontal principal stress changes which occur in response to alternating mechanical properties, since numerical models of the same experiments showed that horizontal tensile stresses are present in the stiffer layers (high E , low ν), whereas horizontal stresses are compressive in the softer layers (low E , high ν) [Bourne, 2003, Douma et al., 2019, Guo et al., 2017, Teufel and Clark, 1984].

Apart from contrasting mechanical parameters, laboratory and numerical studies also showed that the inter-facial friction and applied confining pressures have a high impact on the horizontal stress distribution and fracture behaviour. For instance, studies addressing the impact of the friction between the layers showed that a low inter-facial friction property resulted decoupling of the modelled layers, which minimized the effect of contrasting mechanical properties, resulting in no horizontal stress changes within the different layers [Bourne, 2003, Guo et al., 2017]. Studies addressing the impact of confining pressures showed that the application of horizontal confining pressures resulted in elimination of the observed tensile stress and fracture containment in the weaker layers [Chemenda et al., 2011, Douma et al., 2019, Kettermann and Urai, 2015, Nguyen et al., 2011, Ramsey and Chester, 2004].

The above stated field, laboratory, and numerical studies highlight that the relation between the mechanical stratigraphy, observed fracture behaviour and horizontal stress

changes is well documented. However, these studies have yet not addressed the range of conditions at which this different stress and fracture behaviour occurs.

Therefore, in this study, we perform a numerical sensitivity analysis, which assesses systematically the impact of changing the contrast in elastic properties (i.e. E and ν), inter-facial friction (μ) and confining pressures (P_{conf}) on the horizontal stress magnitude, for a wide range of material parameters and confining pressures. Our 3D three-layer modelling design and applied boundary conditions are based on a previously conducted laboratory study [Douma et al., 2019]. For the sensitivity analysis, we first test the impact of contrasting mechanical properties for the different layers, by changing the Young's modulus and Poisson's ratio of each layer. Secondly, we test the impact of the inter-facial friction by changing the friction parameter between the layer interfaces. Thirdly, the impact of the applied confining pressure is tested. Further, we discuss the numerical results and investigate the relation between the fracture behaviour and the implemented mechanical contrast. Finally, we discuss whether our results can be used for predicting fracture behaviour in the subsurface, or whether fracture observation made on outcrops can be used for assessing the contrast in elastic properties.

Throughout this study, we define stiff layers as having a high Young's modulus (E) and low Poisson's ratio (ν), and soft layers as having the opposite mechanical properties. Further, fracture deformation style, orientation and confinement will be referred to as fracture behaviour.

4.2 Model set-up and numerical procedure

4.2.1 Model design and material parameters

We used the Abaqus Finite Element Tool (SIMULIA Abaqus FEA®) for the 3D models. The modelling set-up and boundary conditions were largely based on the laboratory design presented by Douma et al. [2019] (Figure 4.1a). In our numerical experiments, we implemented three different layers, with an adjustable width and height (Figure 4.1a). We assumed linear elastic isotropic behaviour for each layer, so that the materials are defined by a constant and isotropic Young's modulus (E) and Poisson's ratio (ν), following Hooke's law for 3D stress. The elastic properties (E, ν) can be adjusted for each layer. Throughout this study, we used identical properties for the top and bottom layers. Further, we used the geological sign convention, making tensile stresses or extensional strains negative and compressive stresses or contractional strains positive.

The top and bottom layer were fixed in the lateral directions (x, y) to prevent any lateral rotation or translation (Figure 4.1a). Vertical translation and rotation were prevented by fixing the bottom layer in the z -direction (Figure 4.1a). The four corner lines of each layer were fixed in the x or y direction, to ensure that the deformation remains isotropic and no lateral rotation of the centre layer occurs (Figure 1a). Inter-facial friction between the different layers follows Coulomb friction, $\tau_s = \mu \sigma_n$, where: τ_s is static shear stress, μ the friction coefficient, and σ_n the stress acting normal to the interface, which in this case is the applied vertical stress (Abaqus 6.14, User Manual). Vertical and confining stresses ($\sigma_v, P_{\text{conf}}$) were applied to the top and side boundaries, respectively (Figure 4.1a). Figure 4.1b shows how the imposed boundary conditions prevent any lateral translation and rotation of the model and resulting in uniform lateral x -displacement (note: deformation is exaggerated 40 times).

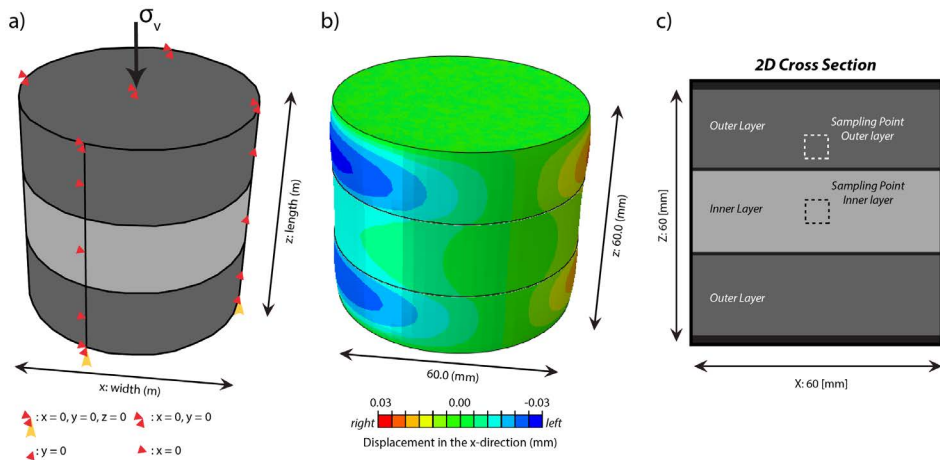


Figure 4.1: The finite element modelling set-up, using Abaqus. a) Numerical model set up and boundary conditions. The largest principal stress (σ_v) is applied to the top boundary. The displacement boundary conditions are depicted by the red and yellow triangles. For example, the boundary conditions indicating x , y and $z = 0$ prevent displacements in any of the free directions, whereas the $y = 0$ only prevents movement in the y -direction. b) Horizontal displacement in the x -direction. Imposed mechanical properties: $E_{\text{inner}} = 29.5$ GPa, $\nu_{\text{inner}} = 0.15$, $E_{\text{outer}} = 9.1$ GPa and $\nu_{\text{outer}} = 0.21$. Applied vertical stress is 50 MPa. c) Two-dimensional cross section through the model, which indicates the dimensions and stress sampling areas for the inner and outer layers respectively. The model set-up and boundary conditions are inspired by the laboratory set-up created Douma et al. [2019].

To compare the horizontal stresses for each layer, two sampling location were chosen. These locations were chosen so that they best account for the imposed boundary conditions and therefore best describe the horizontal stress behaviour of each layer (Figure 4.1c). For the inner layer, the sampling cube was taken at the centre of the layer. To account for the boundary conditions assigned at the top and bottom of the model (i.e. no lateral movement ($x, y = 0$)), the sampling cube for the outer layers was taken closer to the bounding interface (Figure 4.1a and c). For this study, the sampling cube covers multiple elements ($n = 144$) and the stresses calculated for each element within the cube are averaged to get one representative number for the respective layer.

4.2.2 Performed numerical experiments

In order to test the impact of contrasting mechanical properties, we changed the ratio in elastic parameters between the inner and outer layer, for 32 unconfined pressure tests (Table 4.1). The ratio between the elastic parameters (i.e., $\frac{E_{\text{inner}}}{E_{\text{outer}}}$ and $\frac{\nu_{\text{stiff}}}{\nu_{\text{soft}}}$) was changed by increasing or decreasing the Young's modulus and Poisson's ratio for the inner layer. The elastic parameters of the outer layers were kept constant (Table 4.1). Further, the different layers were assumed to be mechanically coupled (i.e. $\mu = 1.0$), which is a feasible assumption for layers experiencing high normal stresses. The impact of the inter-facial friction was tested by changing the friction coefficient (μ) whilst keeping the mechanical properties constant. In addition, the impact of the confining pressure was tested by repeating the elastic parameter tests whilst applying confining pressure (P_{conf}) of 10 MPa

(Table 4.1). For all models, the applied vertical stress was set at 50 MPa. To account for local stress deviations caused by the model aspect ratio (height/width), the width and height of the models were set equal for the numerical sensitivity analysis (Table 4.1). Additionally, it should be noted that the model validation uses different dimensions because it was based on a previously conducted laboratory experiment (Table 4.1 and Figure 4.2).

Name	Number of experiments	Inner Layer E, ν [GPa, -]	Outer Layer E, ν [GPa, -]	Friction and confining pressure [-, MPa]	Model dimensions
Elastic Parameter Test (Unconfined)	32	$5 \leq E \leq 150$ $0.1 \leq \nu \leq 0.4$	$E = 20 \nu = 0.2$	$\mu = 1.0$ $P_{\text{conf}} = 0.0$	Height Width = 2.0
Inter-facial Friction Test	7	$E = 50 \nu = 0.1$	$E = 20 \nu = 0.33$	$0.1 \leq \mu \leq 1.0$ $P_{\text{conf}} = 0.0$	Height Width = 1.0
Elastic Parameter Test (Confined)	32	$5 \leq E \leq 150$ $0.1 \leq \nu \leq 0.4$	$E = 20 \nu = 0.2$	$\mu = 1.0$ $P_{\text{conf}} = 10.0$	Height Width = 1.0
Model validation	1	$E = 9.1 \nu = 0.21$	$E = 29.5 \nu = 0.15$	$\mu = 1.0$ $P_{\text{conf}} = 10.0$	Height Width = 1.0

Table 4.1: List of performed numerical experiments.

The impact of internal pore fluid pressures will not be addressed in this sensitivity analysis. However, the impact potential impact of implementing a pore fluid pressure on the horizontal stress distribution and the coinciding fracture behaviour will be discussed in section 4.2.

4.3 Modelling results and sensitivity analysis

4.3.1 Model validation

We validated the model set up by making a numerical realization of an experiment performed in the laboratory by Douma et al. [2019], using identical boundary conditions and mechanical properties. For this experiment, the inner layer was relatively soft, whereas the outer layers were relatively stiff (i.e. $\frac{E_{\text{inner}}}{E_{\text{outer}}} < 1$, $\frac{\nu_{\text{stiff}}}{\nu_{\text{soft}}} > 1$) (Figure 4.2a). Further, no layer parallel shear was observed within the laboratory tests, which implies that the inner and outer layers were mechanically coupled. The results of the laboratory experiment indicate that mode II fracturing occurs in the inner layer, whereas the outer layers show mode I fracturing (Figure 4.2a). Our numerical realization of the laboratory experiment, highlights that the differences in fracture behaviour in each layer can be explained by the differences in the modelled stress field, which are compressive within the softer inner layer and tensile at the boundaries of the outer layers (Figure 4.2b and c).

The laboratory experiment (Figure 4.2a) also highlights that the mode I fractures in the outer layers stopped propagating in close proximity to the lower and upper bounds, respectively. This is consistent with our numerical results, which show compressive stresses at the upper and lower bound of the outer layers as a result of the implemented boundary conditions (x, y and $z = 0$ at the lower and upper bound) (Figures 4.1a and 4.2b-c).

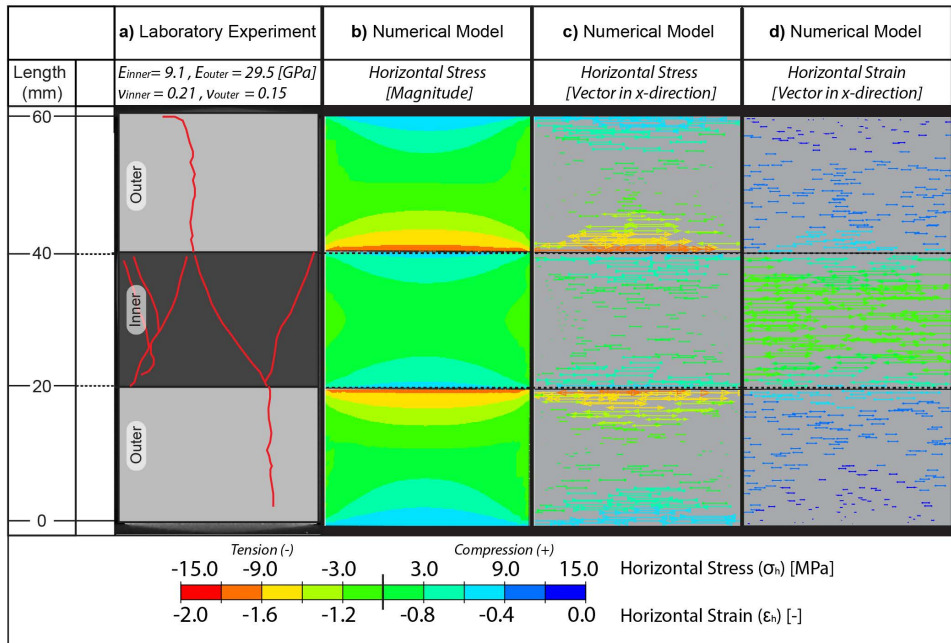


Figure 4.2: Validation of the numerical model, by comparing an interpreted micro-CT scan with our numerical results. Applied vertical stresses are set at 50 MPa and no confining pressures were applied a) Highlighted fractures on a x-z cross section through a micro-CT scan result taken from Douma et al. [2019]. The implemented Young's modulus and Poisson's ratio are listed above the interpreted micro-CT scan. b) Horizontal stress results of the numerical analysis. c) Horizontal stress in the x-direction depicted as a vector field. d) Horizontal strain field in the x-direction. It should be noted that the horizontal principal stress and strain vectors show a radial pattern (equal in all directions) as a result of shear stresses acting on the layer interfaces and the isotropic material properties. Therefore, we have chosen to depict the stress field in the x-direction on a x-z cross section. Due to the high vertical stress, rotation in the z-direction is minimal.

The horizontal stress differences between the three layers can be explained by the differences in horizontal deformation, which is depicted by the horizontal strain field (Figure 4.2d). Following from Hooke's law, the inner layer shows more horizontal strain with respect to the two outer layers (i.e. higher Poisson's ratio (ν_{inner}) and lower Young's modulus (E_{inner})). Since the inner and outer layers are numerically coupled ($\mu = 1.0$), the strain difference between the three layers results in an extensional pull on the outer layers, resulting in tensile stresses (Figure 4.2).

4.3.2 Local stresses as a function of contrasting elastic parameters

The modelling results (Figure 4.2) show that the horizontal stresses are dependent on the difference between the mechanical properties implemented within the inner and outer layers. This implies that changing these properties will result in different horizontal stress distributions. In this study, the mechanical contrast characterised by the ratio between the Young's modulus (YM) of the inner and outer, and the ratio between the Poisson's ratio (PR) of the inner and outer layers, respectively (i.e. $\frac{E_{inner}}{E_{outer}}$ and $\frac{\nu_{inner}}{\nu_{outer}}$). For

example, the results depicted by figure 4.2 had a low ratio in YM ratio and a PR ratio of approximately 1, and this implied that the inner layer is softer with respect to the outer layers.

The numerical experiments testing the relation between a contrasting YM and the horizontal stresses indicate that a high YM ratio between the inner and outer layer ($\frac{E_{\text{inner}}}{E_{\text{outer}}} > 1.0$), results in tensile stresses within the inner layer and compressive stresses within the outer layers (Figure 4.3a). A low ratio in YM ($\frac{E_{\text{inner}}}{E_{\text{outer}}} < 1.0$), results in tensile stresses in the outer layers and more compressive stresses in the inner layer (Figure 3a). Further, the results show that the magnitude of the difference in the implemented YM defines the difference in modelled horizontal stresses, with a higher YM difference resulting in highest stress difference (Figure 4.3a).

Changing the Poisson's Ratio (PR) of the inner and outer layers gives opposite results, with respect to changing the YM ratio (Figure 4.3a and b). A low ratio between the PR ($\frac{\nu_{\text{inner}}}{\nu_{\text{outer}}} < 1.0$) results in tensile stresses in the inner layer and compressive stresses in the outer layers (Figure 4.3b), whereas a high ratio ($\frac{\nu_{\text{inner}}}{\nu_{\text{outer}}} > 1.0$) gives compressive stress in the inner layer and tensile stress in the outer layer (Figure 4.3b). Similarly, to was observed with changing the YM ratio, the magnitude in the stress difference is defined by the difference in the PR of the inner and outer layers (Figure 4.3b).

By repeating this experiment for different ratios of the YM and PR (see Table 4.1), we can depict the relation between contrasting elastic properties and the horizontal stress field, for wide range of elastic properties (i.e., different rock layers). The horizontal stress field between the different experiments is linearly interpolated. Figures 4.3c and d show the resulting stress maps for the inner and outer layers, respectively, and highlight the elastic control on the modelled horizontal stress field in each layer. For example, these plots show that scenarios which have a low ratio in YM and high ratio in PR will results in compressive stresses in the inner layer (i.e. $\sigma_h = 0.2\sigma_v$) and tensile stresses in the outer layers (i.e. $\sigma_h = -0.2\sigma_v$) (Figure 3a and b). Alternatively, implementing opposite YM and PR ratios (high YM ratio and low PR ratio), results in the opposite horizontal stress effect (Figures 4.3 c and d). Finally, it should be noted that the stress deviations away from purely elastic behaviour (i.e. $\sigma_h = 0.0$ MPa at $\frac{E_{\text{inner}}}{E_{\text{outer}}} = 1.0$ and $\frac{\nu_{\text{inner}}}{\nu_{\text{outer}}} = 1.0$) are caused by the imposed boundary conditions and chosen sampling location for the outer layers (Figures 4.1 and 4.3)

4.3.3 Impact friction between layers

The numerical experiments testing the impact of changing the interfacial friction indicate that a low friction parameter ($\mu=0.1$) (Figure 4.4a), results in decoupling of the three layers, preventing horizontal stress transfer between the different layers. This implies that the stress difference between the modelled layers is low (Figure 4.4a). In addition, no tensile stresses are observed within the inner layer. As expected, increasing the implemented friction parameter results in a high stress difference between the inner and outer layers (Figure 4.4b), with the inner layer having significant tensile stresses ($\sigma_h = -0.2\sigma_v$).

Following from the Coulomb friction law, layer decoupling and the coinciding prevention of horizontal stress transfer is dependent on the interplay between the interfacial friction coefficient and the applied normal stress (in our models the applied vertical stress). For our modelling set-up, the effect of slip between the interfaces on the mod-

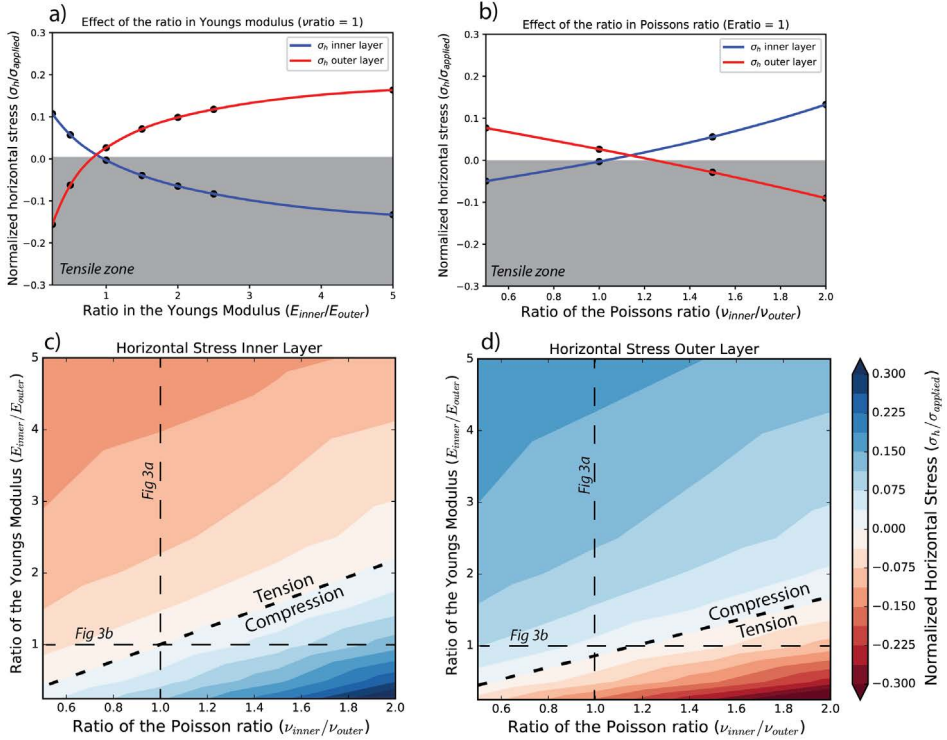


Figure 4.3: Results of the numerical sensitivity analysis assessing the effect of the ratio between the Young's moduli ($\frac{E_{inner}}{E_{outer}}$) and ratio of the Poisson's ratio ($\frac{\nu_{inner}}{\nu_{outer}}$), whilst applying no confining pressures and assuming that $\mu = 1.0$. Total number of models used for this analysis is 32. See Table 1 for the experimental boundary conditions. Normalization is done over the applied vertical stress. a) Normalized horizontal stress in the inner and outer layers as a function of the of the YM ratio. The ratio in PR is kept constant all models ($\frac{\nu_{inner}}{\nu_{outer}} = 1.0$). b) Normalized horizontal stress in the inner and outer layers as a function of the of the PR ratio ($\frac{E_{inner}}{E_{outer}} = 1.0$). c-d) Interpolated horizontal stresses as function of the ratios in YM and PR, for the inner layers (c) and outer layers (d).

elled horizontal stress field only becomes apparent for relatively low friction parameters ($\mu \leq 0.2$) (Figure 4.4c), which is lower than generally observed on rock interfaces ($0.2 \leq \mu \leq 0.85$) [Byerlee, 1978, Schöpfer et al., 2011]. This implies that for most of the layers will be coupled for relatively high layer-normal stresses (i.e. buried rocks).

4.3.4 Impact of the confining pressure

As expected by the superposition principle [Jaeger et al., 2007], changing the applied confining pressure has a significant effect on the modelled horizontal stresses distribution. Our modelling results indicate that high confining pressures result in a complete elimination of the horizontal tensile stresses caused by contrasting material parameters (Figure 4.5a and b). Additionally, the numerical results also indicate that the applied confining pressures also reduces the strain difference between stiffer and softer layers.

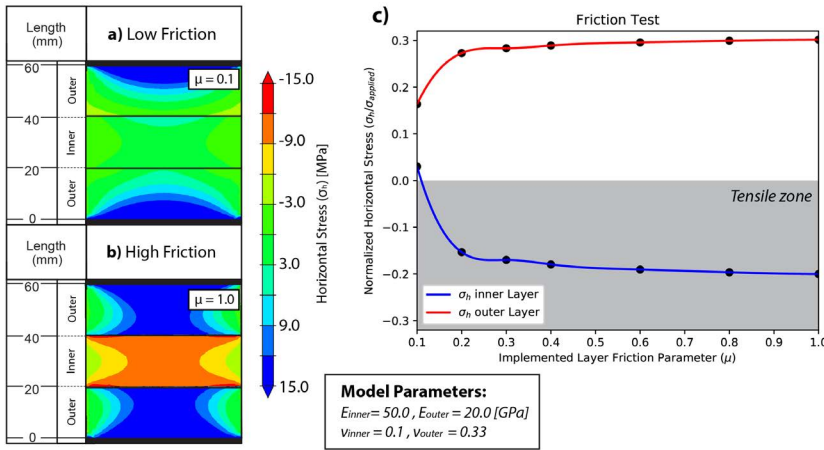


Figure 4.4: Impact of the inter-facial friction on the least principal horizontal stress. a) Horizontal stress field for a friction parameter (μ) of 0.1. b) Horizontal stress field for a rough interface ($\mu=1.0$). c) Normalized horizontal stress vs the implemented friction parameter for the inner and outer layers, respectively. Normalization is done over the applied vertical stress.

As was shown by figure 4.2, this difference in strain causes a tensile pull on the stiffer layer. Therefore, by mitigating this effect, confining pressures further prevent tensile stresses from forming within the stiffer layer (Figure 4.5).

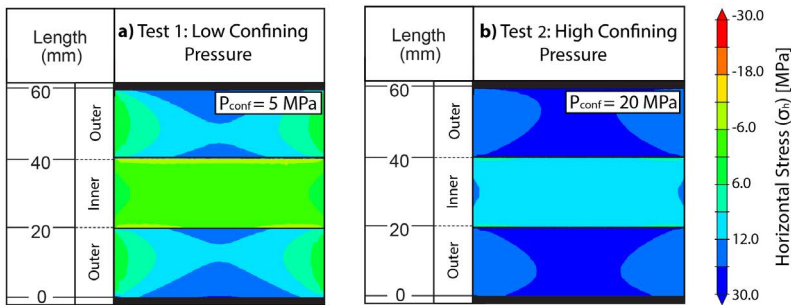


Figure 4.5: Impact of the applied confining pressure. a) Horizontal stress distribution for a low confining pressure ($P_{conf} = 0.1\sigma_v$ (5 MPa)). b) Horizontal stress distribution for a high confining pressure ($P_{conf} = 0.4\sigma_v$ (20 MPa)). For these two models the applied YM and PR ratios were 2.5 and 0.33, respectively.

By applying a confining pressure of 10 MPa (i.e. $P_{conf} = 0.2\sigma_v$) to the models previously shown in Figure 4.3, the effect of a horizontal confining pressure becomes especially apparent (Table 4.1) (Figure 4.6). For all tested modelling scenarios, the applied confining pressures result in a complete mitigation of the tensile stresses caused by contrasting elastic properties within the inner layer (Figure 4.6a). For the outer layers, tensile stresses are present when the contrasting elastic properties are extremely high (Figure

4.6b). Therefore, these results indicate that the presence of tensile stresses in layered rocks are very sensitive to the presence of confining pressures (Figures 4.5 and 4.6).

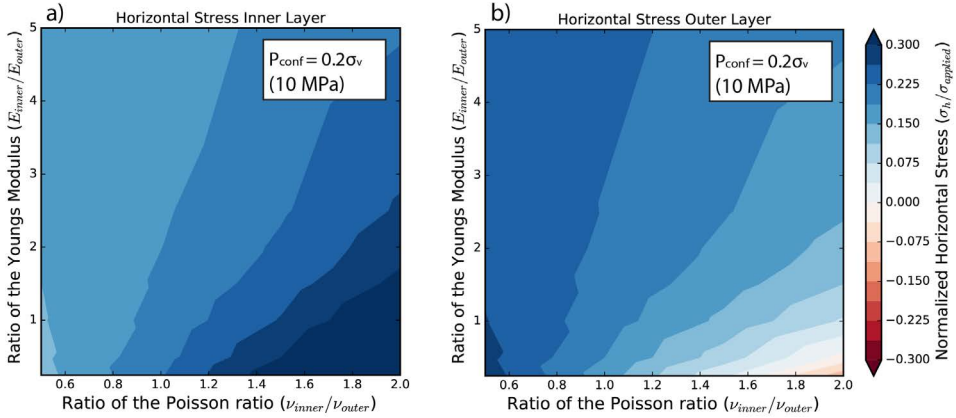


Figure 4.6: a-b) Sample testing ($\frac{\nu_{inner}}{\nu_{outer}}$ vs $\frac{E_{inner}}{E_{outer}}$) results whilst applying 10 MPa confining pressure (i.e. $P_{conf} = 0.2\sigma_v$). See figure 3 for additional information.

4.4 Discussion

4.4.1 Mechanical factors controlling fracture behaviour in layered materials

The effect that contrasting elastic properties, inter-facial friction and confining pressures have on the observed fracture behaviour and horizontal stress distribution has been well documented and is addressed by multiple field [Brenner and Gudmundsson, 2004, Larsen and Gudmundsson, 2010, McGinnis et al., 2017], laboratory [Douma et al., 2019, Ramsey and Chester, 2004, Teufel and Clark, 1984] and numerical studies [Bourne, 2003, Douma et al., 2019, Guo et al., 2017]. These studies showed that the change in fracture behaviour can be attributed to local stress changes, which are caused by differences in the horizontal deformation of the stiffer and softer layers [Bourne, 2003, Brenner and Gudmundsson, 2004, Douma et al., 2019, Ferrill et al., 2014, Guo et al., 2017, Teufel and Clark, 1984]. Further, these studies showed how low inter-facial friction and/or a high confining pressure resulted in layer decoupling and a complete removal of the effects caused by contrasting material properties [Bourne, 2003, Douma et al., 2019, Guo et al., 2017, Nguyen et al., 2011, Ramsey and Chester, 2004].

This study quantifies the effects caused by contrasting layer properties, interfacial friction and confining pressures on the horizontal stress distribution, for a wide range of elastic properties and applied boundary conditions. However, we did not relate these effects to a potential fracture behaviour. Therefore, for the purpose of relating our numerical results to potential fracture regimes, we propose that the stress results shown in Figure 4.3 can be converted to potential modes of fracturing (i.e. mode I, mode II and hybrid fracturing). For this conversion, we assume classical fracture mechanics and Mohr-Coulomb failure [Fossen, 2010], so that the mode I fracture domain start when tensile stresses surpass $-0.075\sigma_v$. This 0.075 value comes from the average ratio between the

Brittle Tensile Strength (BTS) and Uniaxial Compressive Strength (UCS), for most sedimentary rocks [Cai, 2010, Hoek and Brown, 1997]. For the hybrid and mode II domain, we assume $-0.075\sigma_v \leq \sigma_h \leq 0.075\sigma_v$ and $\sigma_h \geq 0.075\sigma_v$, respectively. The interpreted fracture regimes as function of contrasting elastic properties for inner and outer layer are shown by Figures 7a and b, respectively.

Using these converted plots, we can relate observations made in the laboratory to our numerical results (Figure 4.7) (laboratory results modified from Douma et al. [2019]). The first test (Sample A) shows a low elastic contrast between the inner and outer layers (i.e. $\frac{E_{inner}}{E_{outer}} = 1.044$ and $\frac{\nu_{inner}}{\nu_{outer}} = 1.200$), and shows hybrid/mode I fracturing for both layers (Figure 4.7c). Figures 4.7 a and b also highlight that under these elastic ratios, hybrid fracturing is the dominant regime for both the inner and outer layers. The second and third tests (Samples E and F) show a high contrast in mechanical properties (i.e. the inner layers are stiff and outer layers are soft). Both interpretations of the experiments show dominantly mode II fracturing in the outer layers and mode I fracturing in the inner layer (Figure 4.7a). Placing the two experiments into the converted fracture regime plots (figures 4.7a and b), indicates similar results. Here, the inner layers fall within the mode I regime and the outer layers fall in the mode II regime. Finally, the fourth test (Sample D) has a softer inner layer and stiffer outer layers, and the interpretation shows mode I fracturing in the inner, and mode II fracturing in the outer layers, respectively (Figure 4.7a). This is also highlighted by the fracture regime plots, with the outer layers plotting in mode I regime and the inner layer plotting in the mode II regime (Figures 4.7a and b).

These similarities imply that fractures can be used as clear indicators for estimating the ratios between contrasting material parameters. On the other hand, if the ratio between the elastic parameters are known, the modes of fracturing in the respective layers can be predicted. However, it should be noted that this predictability is only applicable for low effective confining pressures, since an applied confining pressure of $0.2\sigma_v$ already results in a complete removal of the observed tensile stresses (Figures 4.6a and b).

Apart from indicating how contrasting material properties can control the fracture behaviour, our results also indicate how the applied confining pressure and inter-facial friction can affect the modelled horizontal stresses (Figures 4.4, 4.5 and 4.6). As was shown here and by previous modelling and laboratory work [Douma et al., 2019, Guo et al., 2017, Kettermann and Urai, 2015, Nguyen et al., 2011, Ramsey and Chester, 2004], a high confining pressure and low inter-facial friction can result in a significant reduction or even a complete removal of the horizontal tensile stresses. Further, Douma et al. [2019] concluded that increasing the confining pressure resulted in a high probability of fracture confinement in the weaker layers. Therefore, by combining our results with these previous findings, we can derive expected fracture behaviour or abutment as a function of the contrasting layer properties, confining pressure and inter-facial friction. This behaviour is summarized in figure 4.8.

4.4.2 Are the modelled tensile stresses high enough to cause tensile failure?

Using the numerical results, we were able to relate fracture behaviour to contrasting material parameters and other implemented boundary conditions (Figure 4.7 and 4.8). However, equating the modelling stresses with measured BTS (Brittle Tensile Strength)

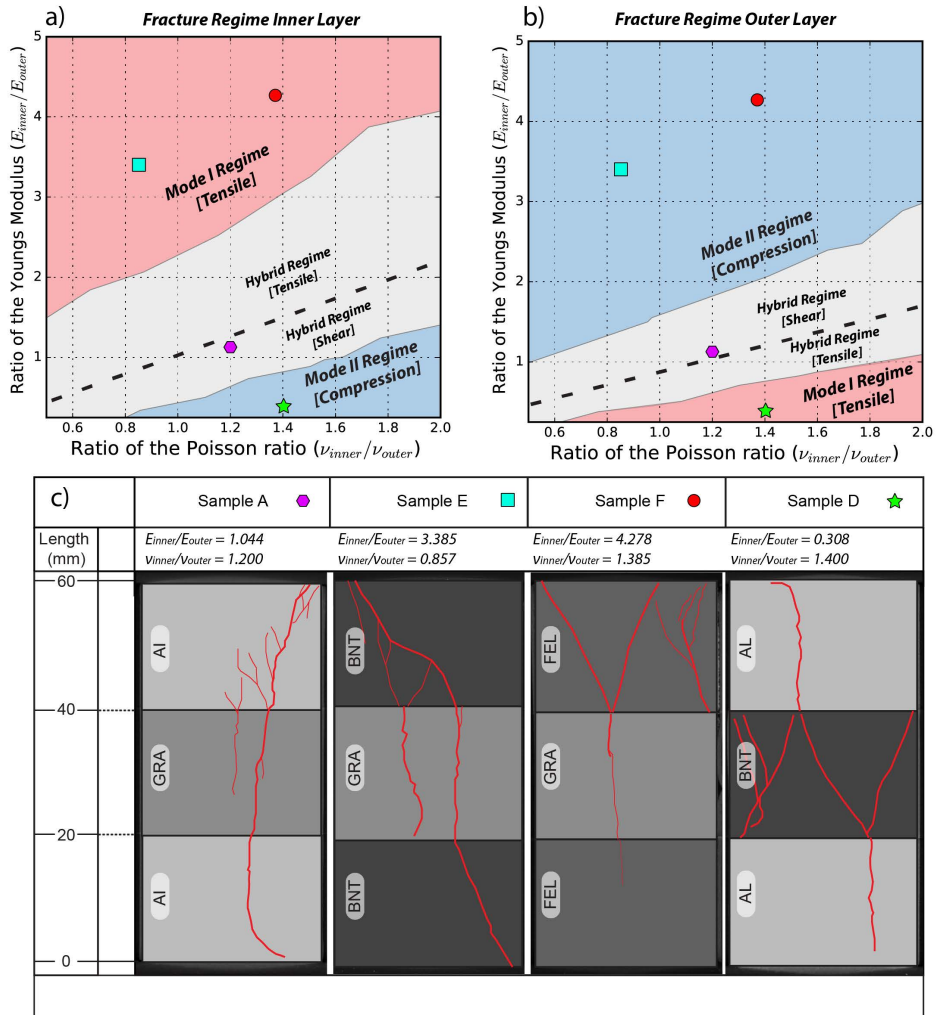


Figure 4.7: a-b) Fracture regime as a function of contrasting mechanical properties, for the inner (a) and outer layer (b). These plots are created using the stress results depicted by Figures 3b and c. For this figure, we assume $P_{conf} = 0.0$ and $\mu = 1.0$. See text for additional details. c) Fracture geometries in different layered experiments. Interpretations and are based on Micro-CT scan results from Douma et al. [2019]. Sample names were also taken from Douma et al. [2019]. The ratios between Young's modulus and Poisson's ratio are highlighted on the figure. It should be noted that these ratios are based on the static Young's modulus and Poisson's ratio. The rock names, tensile and compressive rock strengths (Brittle Tensile Strength (BTS) and Unconfined Compressive Strength (UCS)) can be found in table 2.

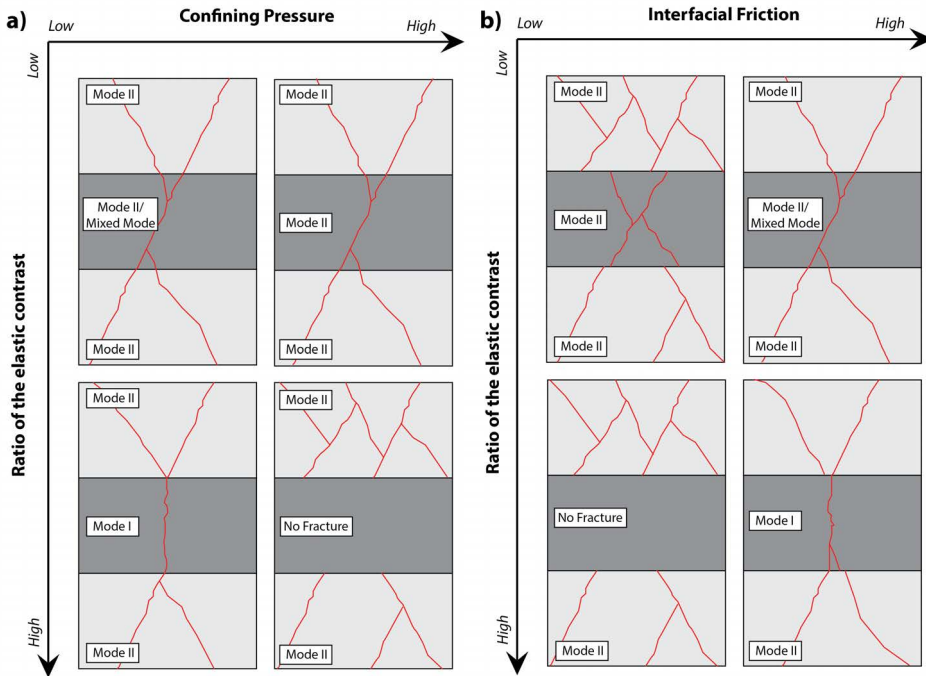


Figure 4.8: Impact of the tested parameters on the fracture behaviour and confinement. For this figure we assume that the inner layer is stiffer and stronger with respect to the outer layers. a) Impact of the assigned confining pressure. b) Impact of the implemented interfacial friction.

magnitudes, shows that the modelled tensile stresses are lower than the implemented rock strength (i.e. $\frac{\sigma_h}{BTS} < 1.0$) (Table 4.2). This essentially implies that the created tensile stresses are insufficient to explain the observed mode I fractures in the stiffer layers (Figure 4.7), and that additional processes are needed to describe the observed features.

Laboratory experiments performed by Douma et al. [2019] and numerical experiments performed by Guo et al. [2017] showed that in layered materials, fractures initiate within the weaker brittle layers, showing mode II behaviour. Further, these studies showed that these mode II fractures propagated into the stiffer brittle layers showing mode I behaviour. This observation can in part explain why mode I failure occurs under $\frac{\sigma_h}{BTS}$ ratios lower than 1.0, since following from Linear Elastic Fracture Mechanics (LEFM) [Irwin, 1957] tensile stresses are localized in close proximity to crack tips. These additional local tensile stresses may result in $\frac{\sigma_h}{BTS}$ greater than 1.0 near mode II crack tips, resulting in either hybrid or mode I fracturing in the stiffer layers (Figure 4.7 and 4.8). Under more natural conditions, the presence of pore fluids can also explain why mode I failure occurs for relatively low $\frac{\sigma_h}{BTS}$ ratios. For instance, the presence of fluid overpressures within certain layers may result in the development of sufficient tensile stress for mode I failure to occur [Roche and van der Baan, 2015]. Additionally, the presence of pore fluids within geological materials allows for sub critical crack growth to occur

Test	Rock type inner layer	Rock type outer layers	Fracture behaviour	USC, BTS inner layer (MPa)	USC, BTS outer layers (MPa)	Estimated tensile stress in stiff layer (MPa)	Stress over strength ratio ($\frac{\sigma_h}{BTS}$)
Sample A	Granite [GRA]	Ainsa Turbidite [AI]	Outer: Mixed, Inner: Mixed	221.1, 16.93	203.5, 14.96	3.663* *(compressive)	0.0
Sample E	Granite [GRA]	Bentheim Sandstone [BNT]	Outer: Mode II, Inner: Mode I	221.1, 16.93	42.7, 3.17	4.441	0.262
Sample F	Granite [GRA]	Red Felsler [FEL]	Outer: Mode II, Inner: Mode I	221.1, 16.93	31.4, 2.45	3.454	0.204
Sample D	Bentheim Sandstone [BNT]	Ainsa Turbidite [AI]	Outer: Mode I, Inner: Mode II	42.7, 3.17	203.5, 14.96	9.608	0.64

Table 4.2: Unconfined Compressive Strength (UCS) and Brittle Tensile Strength (BTS) test results from samples previously presented by Douma et al. [2019]

[Atkinson, 1984, Olson, 1993]. Under these conditions, fractures can propagate under significantly lower tensile stresses than the implemented rock strength [Boersma et al., 2018a, Ko and Kemeny, 2011, Nara and Kaneko, 2005, Nara et al., 2012, Olson, 2007].

4.4.3 Implications for subsurface reservoir studies

The impact that natural fractures can have on fluid flow and the effective permeability within tight reservoir rock is becoming increasingly recognized [Ferrill et al., 2017b, Gale et al., 2014, Smart et al., 2014], with the presence of fractures generally resulting in unpredictable or even unwanted fluid flow behaviour [Toublanc et al., 2005]. Numerous outcrop, laboratory and numerical studies have shown that the 3D geometry and 3D connectivity of these naturally fractured systems are in part controlled by layering and contrasting material parameters (i.e. Mechanical Stratigraphy) [Brenner and Gudmundsson, 2004, Cooke and Underwood, 2001, Douma et al., 2019, Ferrill et al., 2017b, Guo et al., 2017, Larsen and Gudmundsson, 2010, Rijken and Cooke, 2001, Smart et al., 2014, Teufel and Clark, 1984]. Therefore, understanding how these parameters relate to potential fracture behaviour is key for making accurate predictions in layered rocks present in the subsurface.

The modelling results shown in this study quantified the relation between contrasting material properties, inter-facial friction, confining pressures, the horizontal stress field and potential fracture regime, for layered materials. We argue that these results can help to better predict fracture behaviour in layered subsurface reservoirs, and could for instance help in creating mechanically constrained 3D discrete fracture network descriptions.

To illustrate these arguments, we have taken density and sonic velocity data of a lay-

ered reservoir rock from well K12-17, from the TNO geological survey well log database (NLOG) (data is freely available on: www.nlog.nl) (Figures 4.9a to c). This well is located within the North Sea Basin (offshore The Netherlands), and targeted the layered Upper Slochteren Sandstone Formation (Permian).

By combining the well data with figures 4.3 and 4.7, the local horizontal stress field and fracture regime is estimated for the different mechanical units within the well bore. For this small modelling exercise, we assume that $P_{\text{conf}} = 0.0$ and that $\mu = 1.0$. We acknowledge that applying no confining pressures is a big assumption. However, multiple studies have shown and observed that high pore fluid pressures in porous rock can reduce the effective confining pressures, even under relatively deep conditions [Emery, 2016, Fisher et al., 2005, Gale et al., 2010, Imber et al., 2014, Warpinski et al., 2014].

The dynamic elastic properties (Figures 4.9d-g) are derived using the elastic wave equation for isotropic media, the density (ρ_m), P-wave velocity (V_P) and S-wave velocity (V_S) [Mavko et al., 2009]. Here, the dynamic Young's modulus is calculated using equation 1:

$$E_{\text{dyn}} = (9K_{\text{dyn}}2u_{\text{dyn}})/(3K_{\text{dyn}} + u_{\text{dyn}}) \quad (4.1)$$

where the bulk and shear moduli (K_{dyn} and u_{dyn}) can be expressed as: $K_{\text{dyn}} = V_P^2 - \frac{4}{3}V_S^2$ and $u_{\text{dyn}} = V_S^2\rho_m$, respectively. The dynamic Poisson's ratio is calculated using equation 2:

$$\nu_{\text{dyn}} = 3(K_{\text{dyn}} - u_{\text{dyn}})/2(3K_{\text{dyn}} + u_{\text{dyn}}) \quad (4.2)$$

From these calculated elastic properties, 25 layers have been identified and for each of these 25 layers, an averaged YM and PR is calculated (Figures 4.9h and i) (See figure caption for additional details). Using these averaged elastic properties, the ratio between the YM and PR for each layer and the layer above is calculated (Figures 4.9j and k). Finally, the calculated ratios in elastic properties are placed in figures 4.3 and 4.7, to infer to horizontal stresses and potential fracture behaviour (Figure 4.9l).

The predicted horizontal stress and fracture behaviour highlights the impact of contrasting mechanical properties, with predicted fracture regimes mostly alternating between tensile hybrid fracturing (red) and compressive hybrid fracturing (blue) (Figure 4.9l). The transition between the Upper Slochteren sandstone and Ameland claystone shows a sharp contrast in elastic properties and this transition therefore indicates relatively high tensile stresses and mode I fracturing (Figure 4.9).

Although these results show a distinct impact of alternating layer properties (Figure 9l), increasing the applied confining pressure results in a different estimated stress distribution (i.e. no tensile stresses and no mode I fracturing). Further, under subsurface conditions, these horizontal confining pressures are generally present in the sub-surface (i.e. lithostatic and Poisson stresses), making the presence of tensile stresses in the sub-surface highly unlikely [Fossen, 2010, Zoback, 2007].

While the above statements are true, alternating mechanical properties can also play role under normal confined conditions. For instance, a hydraulic stimulation case study done by Roche and van der Baan [2015] highlighted that as a result of contrasting layer properties significant horizontal stress differences occurred within the different layers.

Input data and calculated elastic properties (K12-17 Well North Sea)

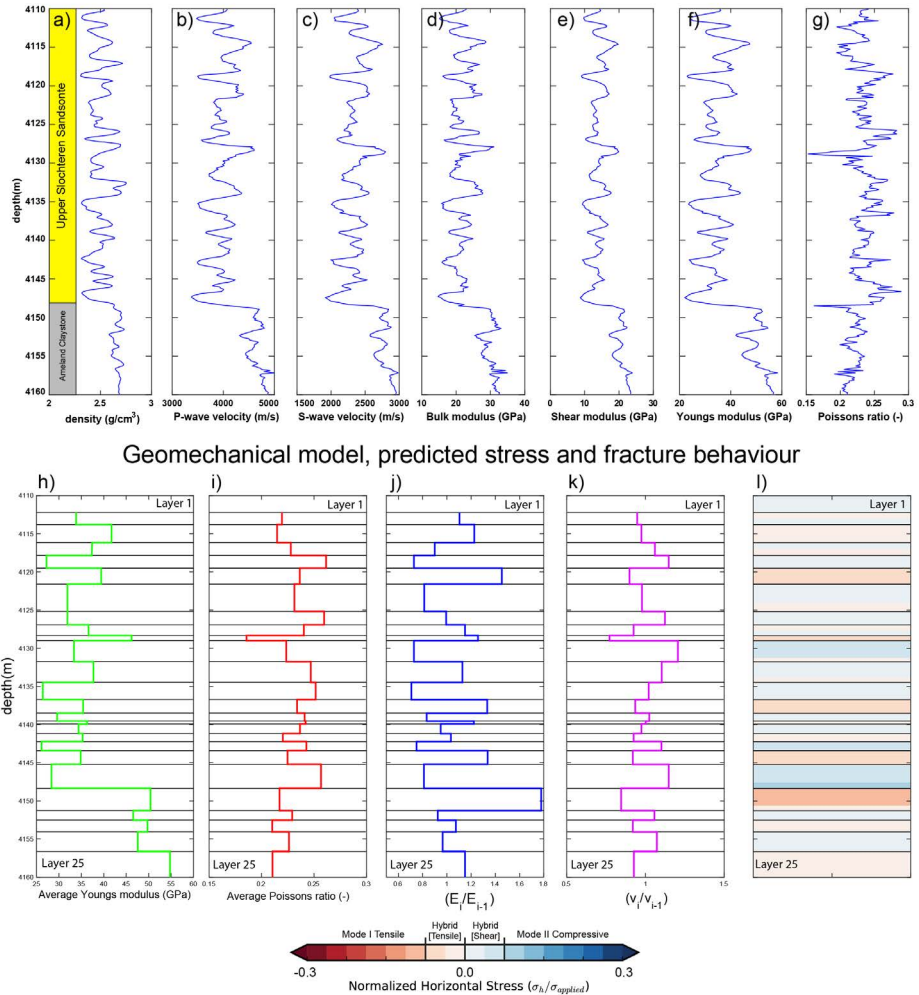


Figure 4.9: Input data, calculated dynamic elastic properties and the created geo-mechanical model (using figures 3 and 7) for the K12-17 well in the North Sea. For the modelling we assumed an effective confining pressure of 0.0 and an interfacial friction of 1.0. Data was taken from TNO geological survey well log database (NLOG) and is freely available on: www.nlog.nl. a) Density log (ρ_m). b-c) P-wave (V_p) (b) and S-wave (V_s) (c) velocities. d-g) calculated dynamic elastic properties: dynamic bulk modulus (K_{dyn}) (d), dynamic shear modulus (u_{dyn}) (e), dynamic Young's modulus (E_{dyn}) (f) and the dynamic Poisson's ratio (ν_{dyn}) (g). h-i) Averaged dynamic Young's modulus and Poisson's ratio for each interpreted layer, respectively. Layers are interpreted using the calculated elastic logs and could therefore represent a mechanical stratigraphy. j-k) Calculated ratio for the Young's modulus and Poisson's ratio (E_i/E_{i-1} and ν_i/ν_{i-1}). The ratios are calculated by dividing the elastic property of layer (i) over the elastic property of the layer above (i-1). l) The predicted horizontal stress and fracture behaviour for each layer within the geo-mechanical model. The prediction is done by placing the average ratios in elastic properties in figures 3 and 7. The colours are highlighted by the colour bar.

These authors showed that due to these stress differences, some layers were more prone to being hydraulically stimulated. Therefore, these and our results imply that properly accounting for changes in mechanical properties is key in identifying zones which either contain natural fractures or are prone to being fractured (Figure 4.9) [Roche and van der Baan, 2015].

4.4.4 Implications for field geology

While our results can be used for predicting fracture behaviour, outcrop descriptions generally provide fracture network geometries rather than the underlying physical mechanisms (Figure 4.10) [Brenner and Gudmundsson, 2004, Ferrill et al., 2014, Larsen and Gudmundsson, 2010]. Unfortunately, quantifying these mechanisms from a known fracture network geometry is difficult since, multiple conditions can result in similar fracture network geometries. Furthermore, because it can vary with time due to diagenesis and exhumation, the observed MS derived from outcrops may not be representative for the MS which was present at the moment fracturing [Laubach et al., 2009]. However, if these mechanisms are properly taken into account, we propose that the numerical results presented in this study, can be used to estimate and qualitatively define ratios in mechanical properties and applied boundaries from natural outcrop data. For instance, outcrops showing alternating layers of stronger and weaker intervals (Figure 4.10a and b), generally show mode II fracturing in the weaker layers and mode I/hybrid fracturing in the more competent layers [Brenner and Gudmundsson, 2004, Ferrill et al., 2014]. Following from figure 4.8, this behaviour requires relatively high ratios in mechanical parameters, low effective confining pressures and that the alternating layers are mechanically coupled. Alternatively, outcrops showing more homogenous layer alternations, generally depict mode II failure for all layers (Figure 4.10c) [Larsen and Gudmundsson, 2010], which following from our models implies low ratios in elastic properties. Furthermore, the interpretations highlighted by figure 4.10c, show that fracturing generally abuts against layer/stylolite interfaces, which could result from low inter-facial frictions and/or normal stresses (Figure 4.8). Finally, it should be noted that although our results can help in estimating mechanical properties and applied boundary conditions from fracture data, a full quantification of this correlation requires a different modelling workflow, at which fracture propagation in layered materials can directly be modelled.

4.5 Conclusions

This study investigates and quantifies the relation between different mechanical parameters, boundary conditions and different horizontal stress and fracturing regimes by performing numerical sensitivity analysis using FEM. The modelling design and implemented boundary conditions are based on previous deformation experiments on layered rocks conducted by Douma et al. [2019].

Firstly, the numerical results highlight the relation between elastic parameters and the modelled horizontal stresses, for the multi-layered experiments. The results show that a high ratio between the Young's modulus (i.e. $E_{\text{stiff}}/E_{\text{soft}} \geq 1$) and low ratio between the Poisson's ratio (i.e. $\nu_{\text{stiff}}/\nu_{\text{soft}} \leq 1$), results in tensile stresses in the respective stiffer layers. Furthermore, our results indicate that the magnitude of the modelled tensile stress is dependent on the difference between the implemented mechanical param-

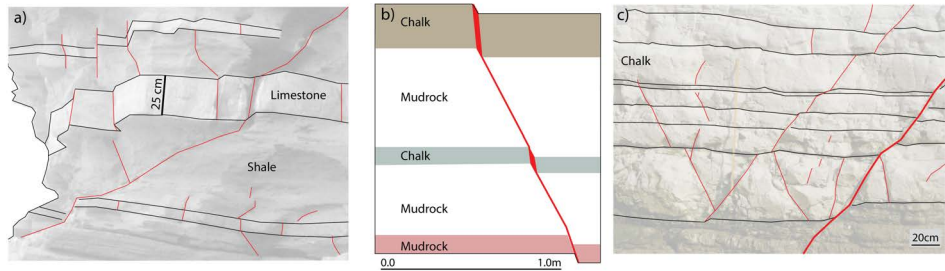


Figure 4.10: Interpreted fracture network geometries acquired from different layered outcrops. Figures are modified after: Brenner and Gudmundsson [2004], Ferrill et al. [2014], Larsen and Gudmundsson [2010], respectively. a) Outcrop and interpreted fracture network acquired from Kilve, UK. The outcrop shows alternating shale and limestone layers acquired from the Eagle Ford, Texas, US. b) Dilational normal fault and outcrop showing both chalk and mudrock layers. c) Interpreted shear fractures and layered chalk outcrop acquired from Flamborough Head, UK.

4

eters.

Secondly, the results show that the confining pressure and inter-facial friction have a significant impact on the horizontal stresses. Here, increasing the applied confining pressure results in a significant reduction in the observed tensile stresses, with tensile stresses being completely removed for confining pressures reaching approximately $0.2\sigma_v$. Our results also indicate that a low inter-facial friction (i.e. $\mu \leq 0.2$) will result in a complete decoupling of the modelled layers, resulting in no tensile stresses in the stiffer layers. Further, we show that the presented numerical results can be converted into plots that relate the elastic parameters to a certain fracture regime. These plots are in good agreement with previously conducted laboratory experiments [Douma et al., 2019].

Finally, we argue that the results can be used to predict fracture behaviour in layered rock, assuming that the elastic parameters are known. Alternatively, these results can help in estimating the elastic ratios between different layers from observations of different modes of fracturing.

Data availability

The full dataset, modelling results and python scripts used for this chapter are freely available and can be downloaded via the following DOI: <https://doi.org/10.4121/uuid:fabdd80b-02c8-4e83-81cb-4891459b3e9e>

5

LINKING NATURAL FRACTURES TO KARST CAVE DEVELOPMENT

In carbonate rocks, channelized fluid flow through fracture conduits can result in the development of large and connected karst networks. These cavity systems have been found in multiple hydrocarbon and geothermal reservoirs and are often associated with high permeable zones but also pose significant challenges in drilling and reservoir management. Here, we expand on the observed interplay between fractures, fluid flow and large cave systems, using outcrop analysis, drone imagery and fluid flow modelling. The studied carbonate rocks are heavily fractured and are part of the Salitre Formation (750-650 Ma), located in central Bahia (NE-Brazil). Firstly, the fracture, - and cave network data show a similar geometry and both systems depict three main orientations, namely; 1) NNE-SSW, 2) NW-SE and 3) ESE-WNW. Moreover, the two datasets are dominated by the longer NNE-SSW features. These observed similarities suggest that the fractures and caves are related. The presented numerical results further acknowledge this observed correlation. These results show that open fractures act as the main fluid flow conduits, with the aperture model defining the fracture-controlled flow contribution. Furthermore, the performed modelling highlights that geometrical features such as, length, orientation and connectivity play an important role in the preferred flow orientations.

5.1 Introduction

Natural fracture networks are commonly observed in outcropping carbonate rocks and sub-surface reservoirs. These features generally form in response to stresses which overcome the tensile or compressive rock strength. If open, fractures are an important factor for fluid flow in low permeability rocks and are believed to control multiple hydrogeology related processes [Bai and Pollard, 2001, Bisdorn et al., 2017a, Gale et al., 2010, Klimchouk, 2009, Philip et al., 2005]. One of these processes is the development of large cave systems. Here, fracture-controlled fluid flow is believed to at least partly control the geometry and spatial distribution of the observed cave system [Klimchouk et al., 2016].

These fracture-controlled cave systems are also believed to be present in limestone reservoirs, such as the sub-salt play offshore Brazil. Here, large karst tunnels control the effective permeability of the normally tight rock, significantly enhancing production [Bruhn et al., 2017, Cazarin et al., 2016]. Apart from aiding production, these high porosity zones also prove to be significant and unpredictable drilling hazards. For instance, a sudden increase in reservoir porosity can result in borehole collapse, potentially losing the entire well. This implies that an optimal field development plan of a carbonate reservoir for either petroleum or geothermal production, includes knowledge on the extent and geometry of the fracture- and cave systems, so that well planning and production is optimized. However, although the importance of fractures and karst cave systems is increasingly recognized, mapping these structures in sub-surface reservoirs is difficult because they generally fall below the seismic resolution.

Due to the lack of accurate sub-surface data, the presence of fractures and cave systems is often predicted from outcrop data. One way to make these predictions is by defining geometrical and quantitative relations between faults, fractures and cave network geometries. Several recent studies applying this approach have made clear advances in showing the link between the large scale tectonics, fractures, fluid flow circulation and possible karst conduit distributions [Billi et al., 2007, Cazarin et al., 2016, Klimchouk, 2009, Klimchouk et al., 2016]. Another way to quantify and understand this observed relation is by implementing acquired outcrop data into numerical models. Here, the impact of fractures on fluid flow orientations can be identified using numerical aperture and fluid flow modelling. Studies using this approach showed that the preferred flow directions and local effective permeability was largely dependent on the fracture network geometry and assigned aperture model [Bisdorn et al., 2017b, 2016b]. Although both approaches have resulted in significant advances in understanding the link between fractures and cave network geometries, case studies which integrate outcrop data with numerical modelling to describe this relation, have only sparsely been conducted.

In this study, we integrate the two approaches, and expand on the observed interplay between fractures and large cave conduits. Firstly, we present a new outcrop analogue (Brejoes, Bahia, Brazil) which highlights the correlation between a natural fracture network and an underlying cave system. Secondly, we discretise and implement the acquired field data into a numerical modelling workflow, to model how natural fractures act as conduits for fluid flow and affect the effective permeability. Finally, we discuss the modelling results and investigate the correlation between the fracture network geometry, modelled fluid flow and the observed cave tunnels.

5.2 Geological background and study area

The Brejoes outcrops and cave system are located in the Irece Basin, which includes Neoproterozoic carbonates of the Irece formation and underlying quartzites of the Chapada Diamantina group. This basin is positioned within the northern part of the São Francisco Craton (SFC) (Figure 5.1a) [Ennes-Silva et al., 2016, Klimchouk et al., 2016].

5.2.1 Tectonic setting

The Irece Basin developed due to extension related to the break-up of the Rodinia supercontinent (c. 900 - c. 600 Ma), and these extensional events occurred until the onset of the Gondwana assembly [Guimaraes et al., 2011] (Figure 5.1b). During this assembly (Brasiliano orogeny, 750-540 Ma), most of the contractional deformation was localized within the Riacho do Pontal Mobile Belt (RPMB) to north of the SFC (Figure 5.1a and b). However, far field stresses did affect the Neoproterozoic sedimentary cover within the craton interior. Here, outcropping rock formations exhibit E-W and N-S verging fold and thrust belts, indicating two main phases of deformation, namely: 1) N-S and 2) E-W [Cruz and Alkmim, 2006, Ennes-Silva et al., 2016, Guimaraes et al., 2011] (Figure 5.1a and b).

5.2.2 Stratigraphy

The Irece basin is mainly composed of Neoproterozoic carbonate platform deposits of the Salitre Fm. (750-650 Ma), which overlay the Mesoproterozoic to Neoproterozoic glacial deposits of the Bebedouro Fm. [Guimaraes et al., 2011, Misi et al., 2011]. These widespread carbonates have a thickness of up to 530 meters and are generally divided in to 5 main units, namely: red argillaceous dolostones (Unit C), laminated limestones (Unit B), dolomite (Unit B1), marls (Unit A) and black oolitic limestones (Unit A1) (Figure 5.1c) [Cazarin et al., 2019, Guimaraes et al., 2011, Misi et al., 2011, Neves et al., 2014]. Post Brazilian orogeny sediments are absent within the Irece basin, either due to non-deposition or erosion.

5.2.3 Study area

In the presented study area, the considered outcrops include a large fractured pavement and a large cave system (Figure 5.2a). The studied pavement ($8.1 \times 10^5 \text{m}^2$) consist of black oolitic limestones (Unit A1) and shows a gentle dip towards west (Figure 5.2b). Most of the structural features observed on the fractured pavement are weathered fractures, veins and tectonic stylolites (Figure 5.2b). The considered cave system ($31.2 \times 10^5 \text{m}^2$) underlies the fractured pavement, and is composed of laminated limestones (Unit B) (Figure 5.2c). The geometry of the cave system mainly shows long N-S verging tunnels and was fully mapped by an expedition in 2013 by Grupo Bambuí de Pesquisas Espeleológicas.

5.3 Methods: Outcrop Interpretation and Modelling Workflow

The presented workflow consists of three main parts namely: 1) drone image acquisition and outcrop interpretation (Figure 5.3a), 2) Meshing and mechanical aperture modelling (Figure 5.3b) and 3) Fluid flow modelling and effective permeability calculations (Figure 5.3c).

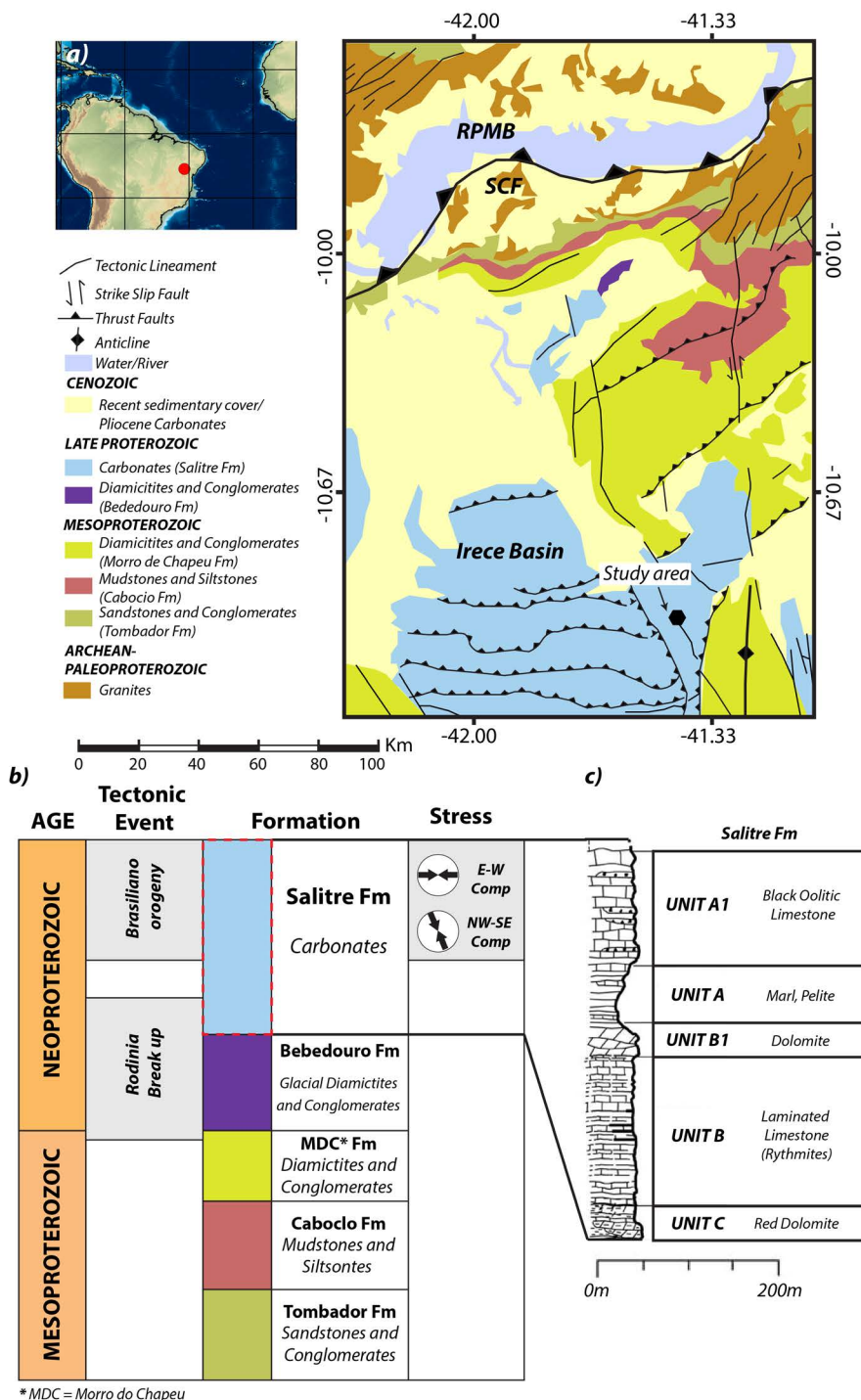


Figure 5.1: a) Regional geological map of the study area (SFC = Sao Francisco Craton, RPMB = Riacho do Pontal Mobile Belt) (Figure modified and simplified from [Bizzi et al. \[2003\]](#)). b) Simplified chart of the main tectonic events, depositions and stress regimes during the Meso- and Neo-Proterozoic. c) Simplified stratigraphic column of the Salitre formation. Figure modified from [Guimaraes et al. \[2011\]](#). Coordinate System: WGS 84.

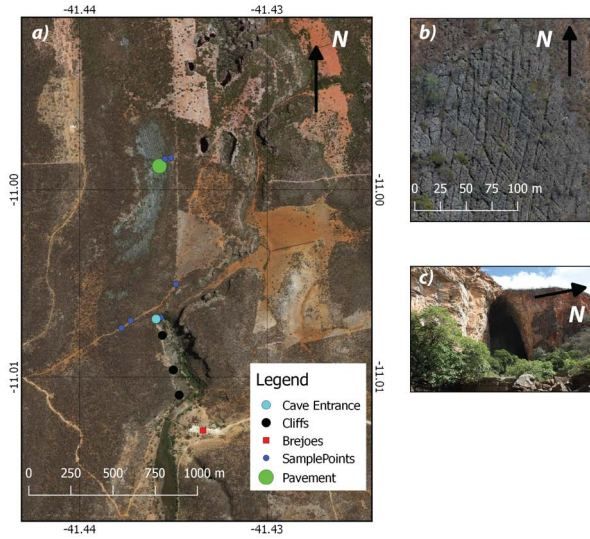


Figure 5.2: Study area highlighted on figure 1a. a) Satellite image of the Brejoes field area, including the locations of different sampling point, the entrance of the cave and the Brejoes fractured pavement. b) Drone image acquired from the pavement. c) Entrance to the Brejoes cave system. Coordinate System: WGS 84.

5.3.1 Digital outcrop acquisition and interpretation (steps 1.1 and 1.2)

Acquisition of the fracture network patterns was done using drone imagery (DJI Phantom 4®). To ensure that the acquired images had sufficient overlap, automated flight missions were used (PIX4DCapture®). The acquired images were processed using Agisoft Photoscan® and converted in to georeferenced digital outcrop models using photogrammetry (Figure 5.3a) [Bisdorn et al., 2017b].

Interpretation and digitization of the observed fractures was done using QGIS software, where fractures were traced and digitized using the polyline interpretation tool. For each polyline, structural information such as length and orientation were calculated (Figure 5.3a). The length of fracture was calculated by over summing each segmented part of the respective polyline. The orientation (strike) was calculated using the start and end coordinates of the polyline:

$$F_{\text{orient}} = \arctan\left(\frac{x_{\text{end}} - x_{\text{start}}}{y_{\text{end}} - y_{\text{start}}}\right) \left(\frac{180}{\pi}\right) \quad (5.1)$$

$$F_{\text{orient}} = F_{\text{orient}} + \begin{cases} 180, & \text{if: } F_{\text{orient}} < 0 \\ 0, & \text{if: } F_{\text{orient}} > 0 \end{cases} \quad (5.2)$$

where F_{orient} is the calculated strike of the fracture with respect to North and x_{start} , y_{start} , x_{end} and y_{end} are the start and end coordinates of the polyline respectively.

Due to the high quality of the acquired drone images, the digitized fractured pavement allowed for interpretation of millions of potential fractures. However, such an interpretation falls beyond the scope of this work. Therefore, we chose to interpret the

Brejoes Fracture network on three different scales namely: 1) Large scale (1:1000, resolution up to 10m), 2) Intermediate scale (1:250, resolution up to 1.0m) and 3) detailed scale (1:50, resolution up to 5cm (image quality)). Using these different scales, the digitized structural features cover a scale ranging from 10^{-2} m to 10^2 m.

5.3.2 Meshing and stress modelling using FEM (Steps 2.1 and 2.2)

The acquired 2D fracture network was simplified and meshed for mechanical and fluid flow modelling, using the unstructured Abaqus Meshing tool and triangulated elements (Figure 5.3b) (SIMULIA Abaqus FEA®). Simplification of the network was done by only taking the end coordinates in to account, resulting in straight fracture lines instead of segmented polylines. Further, to simplify the mesh element size relatively constant, fracture end-points in close proximity to other fracture planes, were snapped on to the respective plane.

In our models, fractures are meshed by duplicating the nodes, making slip and/or opening possible. However, since the meshed fracture network had multiple crossing and abutting fractures, additional node duplication and fracture segmentation was necessary. This was done using a set of 'in-house' python scripts which adjust the Abaqus input files (text files) by duplicating the nodes of crossing or abutting fractures [Bisdome et al., 2017b] (Figure 5.3 Step 2.1.1).

The local stress state, nodal fracture contact pressures and nodal fracture slip were calculated using the Abaqus Finite Element Solver. For the presented models, we assumed a 2D plane strain linear elastic isotropic matrix. 2D plane strain was used so that all modelled fracture planes were treated equally, in the z direction. Far field stresses were assigned to boundaries of the model. The centre node on each respective boundary was fixed in either the x or y direction so that translation and rotation is prevented (Figure 5.3 Step 2.2.2). The modelled local stresses, nodal contact pressures and slip were used to calculate the local stress induced aperture for each fracture.

5.3.3 Stress induced aperture calculations (Step 2.3)

Stress-induced aperture [Asadollahi and Tonon, 2010, Barton and Bandis, 1980, Olsson and Barton, 2001] is an empirical relation that describes the opening of rough fracture planes, whilst applying a compressive closure stress. Under these conditions, an intrinsic hydraulic fracture aperture can be present due to the roughness and shear displacement. This aperture is typically less than 0.5mm. The equations, general workflow and input parameters are based on previous work done by Asadollahi et al. [2010], Asadollahi and Tonon [2010]. All the used parameters and corresponding units are shown by table 5.1.

The initial fracture aperture [E_0] [mm] (table 1) describes the opening between two irregular/rough fracture walls which cannot fully close. This initial aperture is defined by the Joint Roughness Coefficient (JRC), Joint Compressive Strength (JCS) and the uniaxial compressive strength (σ_c) and is shown by equation 3:

$$E_0 = \frac{JRC}{50} \left(0.2 \frac{\sigma_c}{JCS} - 0.1 \right) \quad (5.3)$$

In the case un-weathered rocks $\sigma_c = JCS$, the initial fracture aperture [Bisdome et al.,

Table 5.1: Overview of the all the parameters used in the empirical Barton-Bandis Aperture model.

Symbol	Definition	Units
JRC	Joint Roughness Coefficient	-
JCS	Joint Compressive Strength	MPa
σ_c	Uniaxial Compressive Strength	MPa
σ_n	Contact Pressure (Normal stress)	MPa
E_0	Initial Fracture Aperture	mm
E_n	Mechanical Aperture	mm
v_m	Maximum closure	mm
K_{ni}	Initial stiffness	MPa/mm
μ_m	Modelled shear displacement	mm
L	Block length of the fracture (segmented)	m
μ_{peak}	peak shear displacement	mm
JRC_{MOB}	Mobilised Joint Roughness Coefficient	-
e	Hydraulic aperture	mm

2016a] is only a function of JRC , therefore:

$$E_0 = \frac{JRC}{50} \quad (5.4)$$

Throughout this study we used a $JRC = 15$ and $JCS = 25$ MPa, and following from equation 5.3, this resulted in an Initial fracture aperture, $E_0 = 0.3$ [mm]. The chosen values for JRC and JCS are typically used for describing irregular and rough fracture planes [Bisdorn et al., 2016b].

Following from the Barton-Bandis theory, the initial fracture aperture (E_0) can be closed by compressive normal stresses [Bisdorn et al., 2016b]. The amount of closure and remaining mechanical aperture are defined by a hyperbolic function (equation 5.5):

$$E_n = E_0 - \left(\frac{1}{v_m} + \frac{K_{ni}}{\sigma_n} \right)^{-1} \quad (5.5)$$

Here, the mechanical aperture (E_n) is depended on the initial aperture, maximum closure (v_m), stiffness (K_{ni}) and the applied normal stress (σ_n) [Barton et al., 1985, Barton and Bandis, 1980]. The maximum closure and stiffness are empirically measurable material parameters and depend on JRC , JCS as well as the number of deformation events [Asadollahi, 2009, Asadollahi et al., 2010]. For this study, we assumed that the modelled fractures are irregular and have a high roughness so that v_m and K_{ni} are equated as [Bisdorn, 2016]:

$$v_m = -0.1032 - 0.0074JRC + 1.135 \left(\frac{JCS}{E_0} \right)^{-0.251} \quad (5.6)$$

$$K_{ni} = 7.15 + 1.75JRC + 0.02 \left(\frac{JCS}{E_0} \right) \quad (5.7)$$

In stress induced aperture models, the conductive behaviour of fractures was quantified by calculating the hydraulic aperture (e), which is a function of the shear on a fracture plane (μ_s), the theoretical peak shear displacement (u_{peak}) and mobilized joint roughness coefficient (JRC_{MOB}). Firstly, the peak shear displacement (u_{peak}) was calculated using equation 5.8 [Asadollahi and Tonon, 2010]:

$$u_{peak} = 0.0077L^{0.45} \left(\frac{\sigma_n}{JCS} \right)^{0.34} \cos \left(\frac{JCS}{\sigma_n} \right) \quad (5.8)$$

This material parameter is dependent on the measured normal stress (σ_n), Joint Compressive strength (JCS) and the block length (L) (table 1). Secondly, the mobilized roughness coefficient (JRC_{MOB}) was calculated by implementing the calculated peak shear displacement into equation 5.9 [Asadollahi and Tonon, 2010]:

$$JRC_{MOB} = JRC \left(\frac{u_{peak}}{u_s} \right)^{0.381}, \text{ if: } \frac{u_s}{u_{peak}} \geq 1.0, \text{ else: } JRC_{MOB} = JRC \quad (5.9)$$

Finally, using the derived JRC_{MOB} , u_{peak} and mechanical aperture (E_n) for each fracture segment, the local hydraulic aperture was calculated using equation 5.10 [Bisdorn et al., 2016b, Olsson and Barton, 2001]:

$$e = \begin{cases} \frac{E_n^2}{JRC^{2.5}}, \text{ if: } \frac{u_s}{u_{peak}} \leq 0.75 \\ \sqrt{E_n} JRC_{MOB}, \text{ if: } \frac{u_s}{u_{peak}} \geq 1.0 \end{cases} \quad (5.10)$$

Concerning equation 5.10, the domain in between $0.75 \leq \frac{u_s}{u_{peak}} \leq 1.0$ is linearly interpolated. The derived hydraulic aperture (e) describes fracture segments which are conductive under a compressive stress field. This aperture description was used to describe fracture opening under regional compression.

5.3.4 Constant aperture in fluid flow models (Step 2.3)

Using constant aperture for all fractures is an alternative method for describing fracture aperture. Assuming a homogeneous aperture distribution allows for addressing the impact of the network geometry on fluid flow, instead of the assigned aperture model [Hardebol et al., 2015]. For this scenario, a constant aperture of 0.3 mm was assigned to all implemented fractures.

5.3.5 Power law aperture scaling derived from vein analysis (Step 2.3)

Numerous outcrop,- and core studies measuring the vein thickness along fracture planes have documented that the aperture vs frequency follows a negative power law frequency scaling [Hooker et al., 2014, Ukar et al., 2017, 2016], namely:

$$F = ae^{-b} \quad (5.11)$$

where F is the normalized fracture frequency, e is the fracture aperture [m], b is the power law exponent and a is the fracture density constant. In limestone rocks the power

law exponent (b) shows values varying from 0.2 to 2.0 (Hooker et al. [2014] and references therein). Here, we model the fracture aperture vs frequency using a power-law exponent of 0.8, a fracture density constant (a) of $\frac{1}{\text{AOI}}$ (AOI = area of interpretation), and an assigned frequency (F) which is derived from the normalized length-frequency distribution (section 4.2). Using these assigned parameters, the aperture attributed to each fracture plane is essentially dependent on the fracture length, with longer fractures having a larger calculated aperture. This aperture vs length relation is observed within natural examples [Olson, 2003, Vermilye and Scholz, 1995].

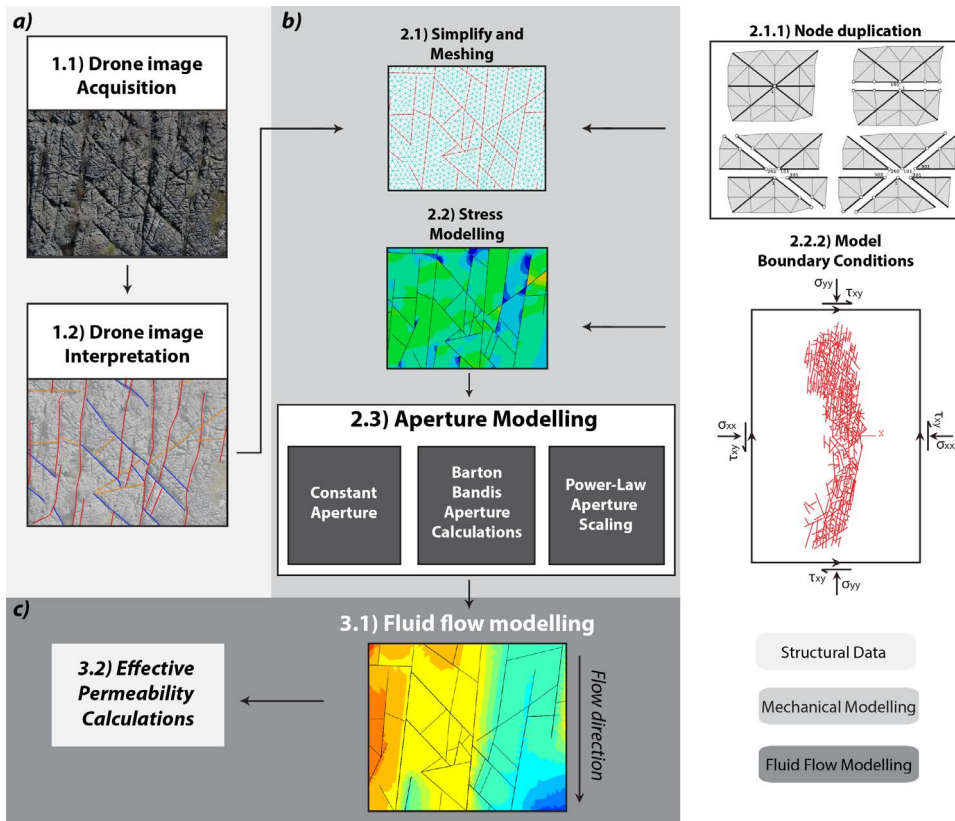


Figure 5.3: Data-driven workflow to obtain dynamic fluid flow model and structural data from acquired drone images. a) 1.1) Drone imagery, photogrammetry and 1.2) GIS based fracture interpretation (shown example has 1:1000 scale interpretation). b) 2.1) Simplification and meshing of the interpreted fracture network, 2.2) local stress modelling and 2.3) fracture aperture modelling using the simplified mesh. Node duplication and model boundary conditions workflow after [Bisdorn et al., 2017b]. c) 3.1) Fluid flow modelling and 3.2) effective permeability calculations using AD-GPRS (Stanford University's Automatic Differentiation based General Purpose Research Simulator) [Karimi-Fard et al., 2004, Karimi-Fard and Firoozabadi, 2001, Voskov et al., 2009].

5.3.6 Fluid flow modelling (Steps 3.1 and 3.2)

For the fluid flow simulations, the unstructured mesh from the ABAQUS FE-Tool was re-used (Figure 5.3b). The transmissibility field of the matrix and fracture network was calculated from the modelled fracture aperture and assigned matrix permeability. Fluid flow through the acquired transmissibility field was modelled using AD-GPRS [Karimi-Fard et al., 2004, Karimi-Fard and Firoozabadi, 2001, Voskov et al., 2009] by solving the incompressible single phase Darcy equation (5.12) for a differential pressure field:

$$q = -\frac{k}{\mu} \nabla p \quad (5.12)$$

where ∇p is the pressure gradient [Pa], μ is the viscosity [Pa × s] and k is the intrinsic local permeability m^2 . For our fluid flow models, we varied the matrix permeability between 1.0 mD and 250 mD assigned a constant viscosity of 5.0×10^{-5} Pa × s. The intrinsic permeability for each fracture segment was calculated using the parallel plate equation (5.13) assuming laminar flow:

$$k_f = \frac{e^2}{12} \quad (5.13)$$

here, k_f is the fracture permeability [m^2] and e is the modelled fracture aperture [m]. The initial pressure difference was created by placing both injector wells [BHP = 120 Bar] and production wells [BHP = 80 Bar] on each mesh element positioned on opposite boundaries of the model. Here, N-S flow was initiated by placing the injector wells at the northern boundary and the producer wells at the southern boundary. E-W flow was initiated by placing these wells on the eastern and western boundary respectively.

Finally, from the calculated fluid-pressure gradient and measured volume fluxes, the equivalent permeability in the two horizontal directions (E-W and N-S) was calculated, using equation 12. This equivalent permeability value is representative of the combined fracture and matrix flow within the modelling domain [Bisdorn et al., 2017b, Nick and Matthäi, 2011].

5.3.7 Cave map digitization and interpretation

The cave network geometry was acquired by digitizing and geo-referencing a manually created 2D map of the Brejoes cave system (courtesy of Grupo Bambuí de Pesquisas Espeleológicas) (Figure 5.4a and b). Structural information was acquired by drawing polylines through the centre of the tunnels of the digitized cave map, using QGIS software (Figure 5.4c). For our cave interpretation methodology, one tunnel segment is represented by one polyline.

5.4 Results: Structural data analysis

5.4.1 Field data analysis

On the ground investigation of the Brejoes outcrops show widespread brittle deformation features, with the dominant structures being low-strain barren-fractures and veins. These features generally show a sub-vertical dip. Beside fractures and veins, bedding-parallel and tectonic stylolites are observed.

The observed fractures and veins strike in three main fracture orientations, namely: set-1 (NNE-SSW), set-2 (NW-SE) and set-3 (WSW-ENE) (Figures 5.5a and b). The ob-

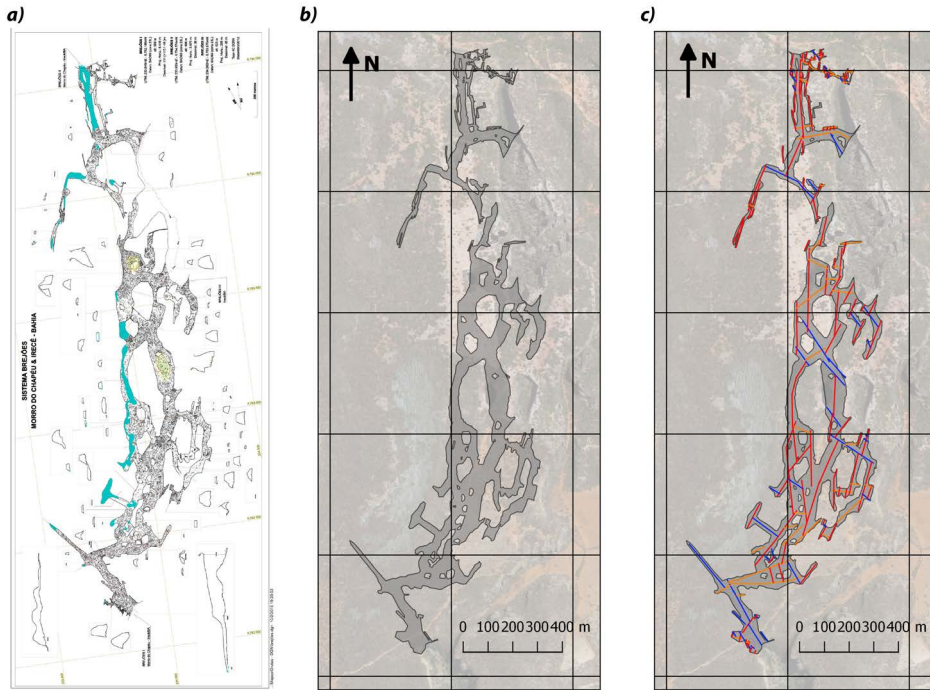


Figure 5.4: Cave map digitization and interpretation workflow. a) Original map of the Brejoes Cave System. The cave map is acquired by, and courtesy of Grupo Bambuí de Pesquisas Espeleológicas (<https://blogdobambui.wordpress.com/2013/04/07/expedicao-brejoes/>). b) GIS based geo-referencing and digitization of the cave map. c) GIS Based interpretation using the polyline tool.

served angles between the different fracture sets indicate that these features display conjugate relationships and form two conjugate pairs, namely: 1) set-1 and set-2 and 2) set-2 and set-3 (Figures 5a and b). Clear cross-cutting/abutment relationships between the smaller fractures and veins are hard to define (Figure 5b), but smaller features from set-1, 2 and 3 are generally confined by larger fractures from set-1 and 2 (Figure 5.5b). This observation is also visible on the acquired drone imagery. Because of the observed conjugate relationships and coeval cross cutting relationships, the fractures and veins are interpreted to be mode II/hybrid fractures [Fossen, 2010] (Figures 5.5a and b).

The measured sub-vertical stylolites show two main orientations (NNE-SSE and WSW-ENE), and strike perpendicular to the bisection planes of the observed conjugate pairs (set-1 and 2 and set-2 and 3) (Figures 5.5a to e). This implies that the observed conjugates pairs and tectonic stylolites are structurally related, with each conjugate pair being linked to one tectonic stylolite set. The bedding parallel stylolites are well developed, and tend to be several decimetres to several meters in length (Figure 5.5c). Fourier transform analysis on these stylolites have shown that these features formed at approximately 450m depth [Boersma et al., 2018b] (Appendix A). Fractures and veins generally abut against the observed bedding parallel stylolites, indicating that the horizontal fea-

tures are younger and overprint the observed fractures and veins (Figure 5.5c).

Using the right dihedron method (Win-Tensor®), the acquired structural data is used to estimate the responsible tectonic deformation events [Delvaux and Sperner, 2003]. The two stylolite sets are treated as compressional stress field indicators, which strike perpendicular to the maximum stress. The fracture sets are assumed to be mode II conjugate shear fractures. The results show two deformation phases, both falling in the strike slip regime, with σ_H striking NNW-SSE and WNW-ESE respectively (Figures 5.5f and g). The calculated stress orientations show a good correlation to the far field stress orientations observed for the Brazilian Orogeny [Cruz and Alkmim, 2006, Ennes-Silva et al., 2016].

Evidence that the fractures, veins and stylolites have been re-used as fluid flow conduits can be found at the cave entrance (Figure 5.6). Here, fractures from all three observed orientations enhance the fluid flow, resulting in conductive features striking parallel to main fracture orientations (Figure 5.6a). These conductive features are generally confined by bedding planes and horizontal stylolites (Figure 5.6a). Smaller fractures and veins in close proximity to the larger conductive fractures are not used as fluid flow conduits, implying that not all features are prone to enhance flow. Observations from the cave entrance also indicate that tectonic stylolites can at least partly act as conductive features (Figure 5.6b), which is also observed on other outcrops [Bruna et al., 2018].

5

5.4.2 Structural interpretation of the acquired drone images and cave system

The acquired drone imagery highlights a fractured pavement, with features striking parallel to observations made on the ground (Figures 5.5 and 5.7a). Furthermore, the interpretation clearly depicts the conjugate relationships between the observed structural features (Figure 5.7a). The results also show that for the large-scale interpretation (1:1000 scale, Figure 7a), the NNE-SSW fractures (set-1) are dominant. The detailed interpretation of the fractured pavement (1:250 and 1:50 scale) shows that set-2 and set-3 are more dominant on smaller length scales (length < 20 m) (Figure 5.7b). Therefore, these results indicate that set-1 dominates the overall geometry of the network on the larger scale, whereas the other two structural sets (set-2 and set-3) are more numerous on the smaller scale (Figure 5.7c). The interpreted cave data and acquired orientation distribution show features striking parallel to the main fracture orientations (Figures 5.7a and d). Therefore, these results suggest a geometrical correlation between the fractures and the caves.

The acquired length data also highlights this correlation (Figure 5.8a). These results indicate that on all scales, the NNE-SSW features (set-1) are longer with respect to the other observed orientations (Figure 5.8a). Moreover, the normalized length-frequency distribution indicates that all traced features follow a similar power-law distribution, for lengths ranging between 1.0 and 500 meters (Figure 5.8b). The normalization of the cumulative fracture and cave data is done over the area of interpretation, which is for example the size of the pavement, size of the interpretation box or area of the cave (Figures 5.7a and b). Using a least squares analysis, the general power-law fit for all scales was calculated ($R^2 = 0.91$), and is shown by equation 5.14:

$$F(l) = 0.93l^{-2} \quad (5.14)$$

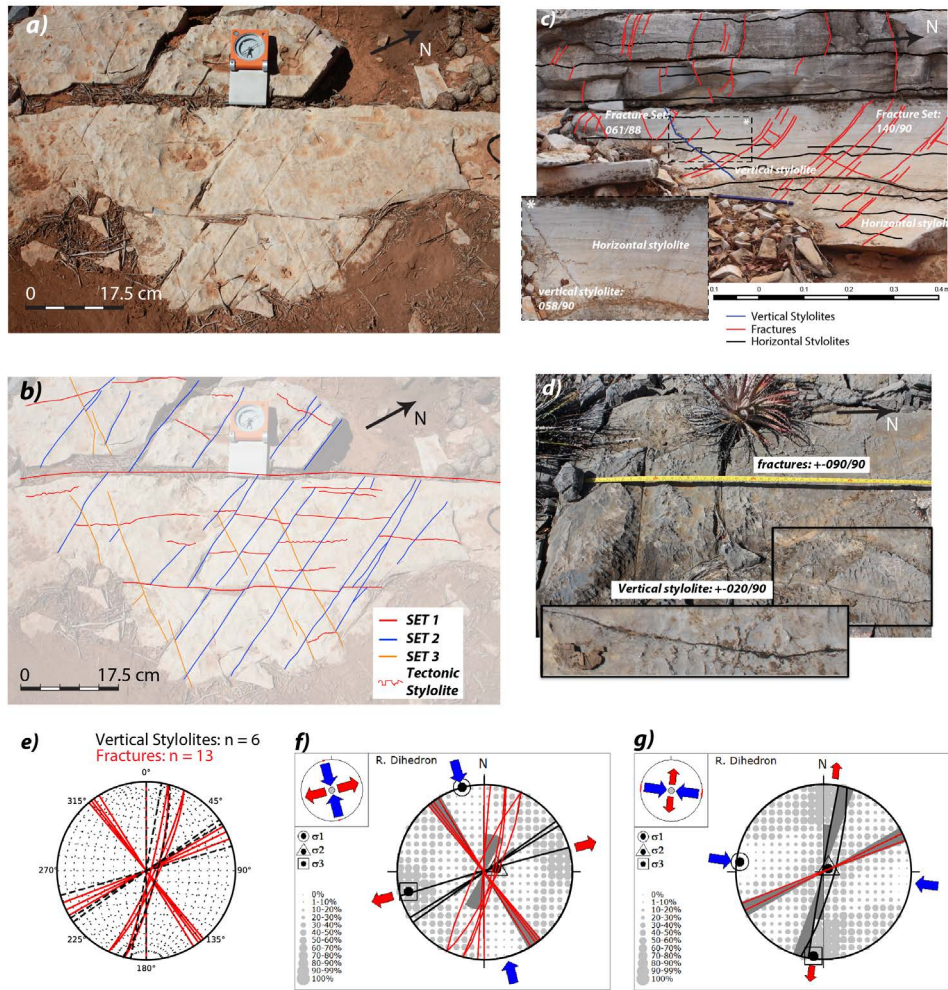


Figure 5.5: Detailed structural field data. a) Pavement outcrop depicting the structural features observed on the Brejoes fractured pavement. b) interpretation of the pavement outcrop. c) Vertical outcrop next to the Brejoes fractured pavement. d) Fractures and vertical stylolites on top of the Brejoes Pavement. e) Stereonet of the measured features (taken from different sampling points (figure 2)). f-g) Inversion analysis of the measured data using the Right Dihedron Methods. Results show two horizontal compression phases namely, 1) NNW-SSE compression and 2) ENE-WSW compression. Inversion calculations are done using Win-Tensor (Delvaux and Sperner, 2003). All data is shown in strike/dip.

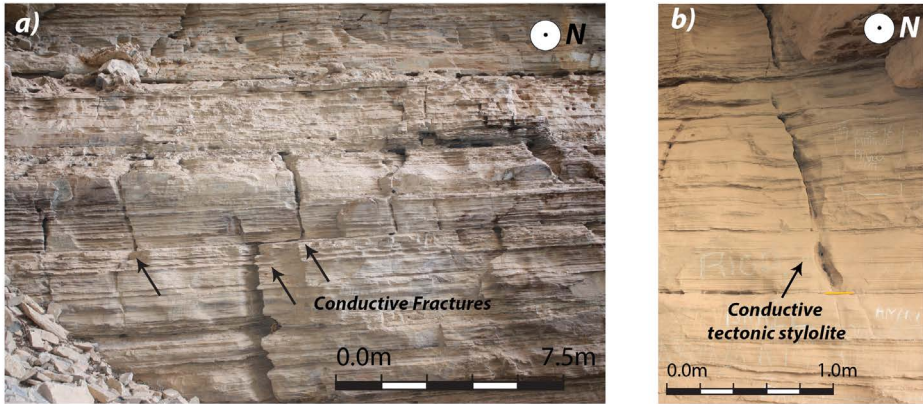


Figure 5.6: a) Cliff outcrop showing reactivated fractures acting as fluid flow conduits. b) Reactivated stylolite which acted as fluid flow conduit. Both images were taken at the Brejoes cave entrance.

5

As was observed in figure 5.7, these length results again highlight the geometrical correlation between the Brejoes fractured pavement and underlying cave system.

Although the resolution of the images allowed for interpretation up to cm scale, deviations from power-law fit still exist (Figure 5.8b). These deviations are most likely caused by truncation and resolution biases [Bonnet et al., 2001]. For instance, at the smaller scale, the resolution of the drone images only allowed for interpretation of the karstified barren fractures. However, interpretation of the smaller veins, fractures and stylolites (Figure 5.5a, b and c) was impossible, resulting in deviations away from the derived power-law. The same holds for the larger fractures, where the chosen interpretation scale (1:1000) results in a resolution bias, below which features are not interpreted. The cave data shows the largest deviations from the power-law. These results are significantly biased by the quality of the cave-map and chosen methodology. Nonetheless, these results indicate that the Brejoes fractured pavement and cave system have a similar length distribution. This implies that these multiscale features are most likely part of the same nested system, with smaller features being far more abundant.

5.5 Results: Fracture aperture and fluid flow modelling

The results acquired from the fractured pavement and underlying cave system indicate that there is a geometrical and statistical correlation between the two datasets. This implies that fluid flow through the fractures has most likely resulted in the development of the present-day cave geometry. To further understand how the fracture network geometry and aperture are linked to fluid flow patterns and the resulting cave network geometry, three aperture modelling scenarios are defined. For all scenarios, we do not discriminate between barren fractures, veins and stylolites and assume that all structural features can be treated as fractures which can act as fluid flow conduits.

The first scenario models the fracture opening and fluid flow, assuming stress induced aperture (Barton-Bandis). This approach is feasible for modelling fracture aperture under sub-surface conditions. For the second scenario we assume a constant frac-

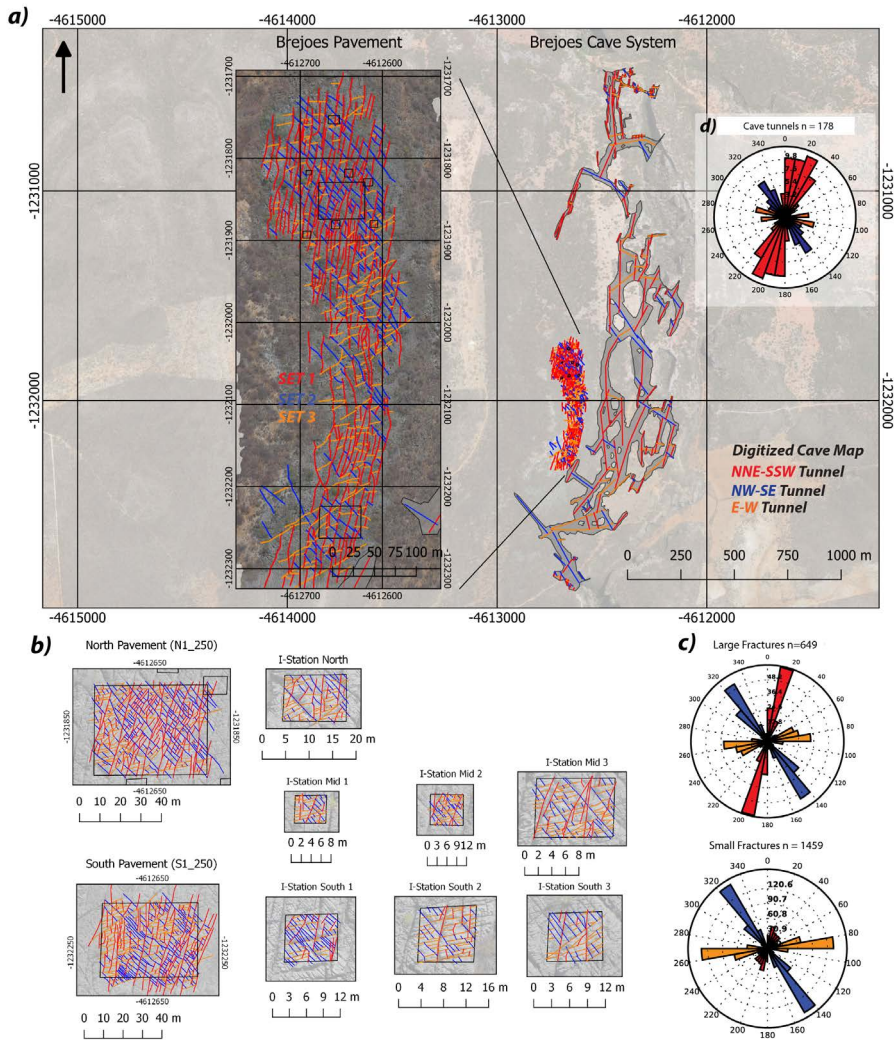


Figure 5.7: Structural interpretation of the Brejoes fractured pavement and cave system. a) Satellite image and drone image of the field area with the interpreted structural features (fractures and cave tunnels) highlighted as polylines. b). Drone images (stations) of the detailed fracture interpretations. Location of each station is highlighted on the fractured pavement (figure 8a). c) Rose diagrams acquired from the small- and large-scale fracture interpretations. d) Orientation distribution from the cave tunnel interpretation. Coordinate system WGS 84 Pseudo Mercator.

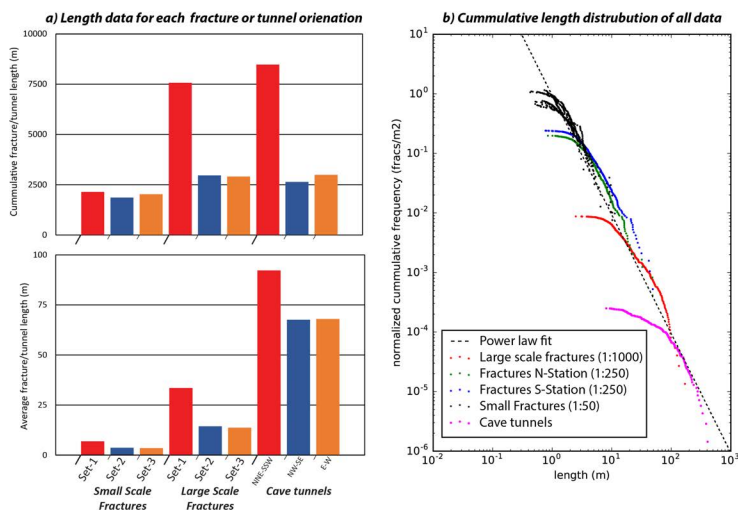


Figure 5.8: a) Length data from both caves and fractured pavement. The presented data has been discriminated for each fracture and cave orientations b) Normalized cumulative length distribution and power-law fit of the Brejoes fractured pavement and cave system.

ture aperture. This aperture model is mostly used for addressing the impact of the network geometry on fluid flow [Hardebol et al., 2015]. Finally, for the third scenario we model the aperture assuming a negative power-law aperture frequency relation based on literature data [Hooker et al., 2012, 2014].

5.5.1 Modelling scenario 1: Stress sensitive fracture aperture and fluid flow

For our stress induced aperture calculations, we assume that $\sigma_{H_{max}}$ strikes ENE-WSW ($\pm 70^\circ$) which is parallel to the current-day stress orientation, which is estimated from earthquake data [Heidbach et al., 2018, Riccomini and Assumpção, 1999]. The applied differential stresses is set at 20 MPa ($\sigma_H = 30\text{MPa}$, $\sigma_h = 10\text{MPa}$), which are feasible magnitudes for modelling compressive settings [Heidbach et al., 2018]. Further, we implement a Poisson's Ratio (ν) of 0.25 and a Young's Modulus (E) of 30 GPa. These values are feasible for carbonate rocks under sub-surface conditions [Goodman, 1989]. Finally, fracture planes are assumed to be frictionless so that all nodal shear stresses are converted in to nodal slip. It should be noted that the applied current-day stress orientation could be different from the paleo-stress field during the cave development. Further, we acknowledge that changing the applied stress directions and magnitudes will alter the modelled apertures and fluid flow responses. However, such a sensitivity analysis falls beyond the scope of this study.

The parameters calculated by our numerical stress simulations are the nodal contact pressures and nodal shear displacements on each implemented fracture (Figure 5.9a, b and c). The local Barton-Bandis aperture is calculated using these stress dependent nodal variables as well as other assigned mechanical parameters (see section 3.3). The resulting mechanical and hydraulic apertures show magnitudes up to 0.2 mm, for an ini-

tial intrinsic aperture of 0.3 mm (Figure 5.9e, f and g). These figures show that high nodal shear values results in fractures which are hydraulically conductive, with the calculated mechanical aperture slightly controlling the magnitude of the hydraulic aperture. Considering the stress field, features showing high hydraulic aperture mostly belong to set-1 and set-2.

Although the interpretation of the Brejoes fracture network showed an interconnected system (Figure 5.6), the stress induced aperture results indicate that the hydraulically 'open' fractures are disconnected, and that most implemented fractures are closed ($e \leq 5.0 \times 10^{-5}$ mm) (Figure 5.9e and f). Therefore, the average fracture aperture for this scenario is relatively low ($e_{\text{avg}} = 0.022$ mm). Furthermore, the hydraulically closed fractures may act as fluid flow barriers, preventing fluid flow from percolating the network (Figure 5.10e).

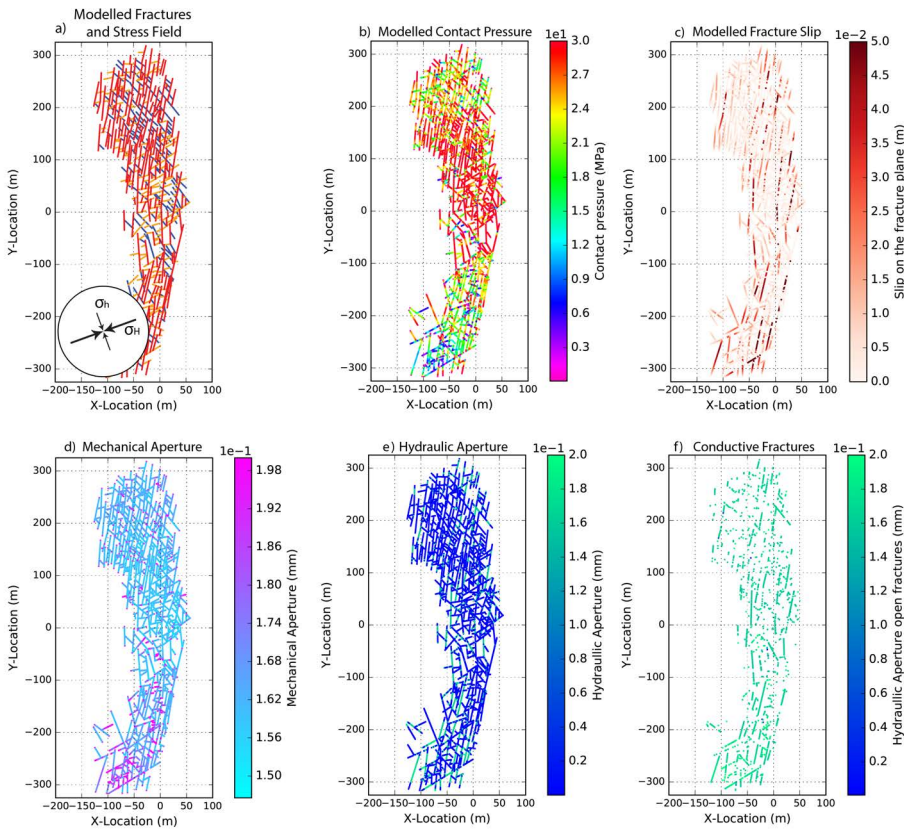


Figure 5.9: Stress and Aperture Modelling results. List of mechanical parameters and applied stresses: $E = 30$ GPa, $\nu = 0.25$, $\sigma_H = 30$ MPa, $\sigma_h = 10$ MPa and $\sigma_{H(\text{orient})} = 70^\circ$. a) The fracture network implemented in to the model. b) Nodal Fracture Contact Pressures [MPa]. c) Modelled Nodal Fracture Slip [m]. d) Calculated Mechanical Aperture [mm], using the Barton-Bandis equations (Appendix 2). e) Calculated hydraulic aperture [mm] (Appendix 2). f) Hydraulic conductive fractures (Fracture Aperture > 5.0×10^{-5} mm).

	Average/max fracture aperture (mm)	Matrix Permeability k_M (mD)	N-S Permeability k_{ns} (mD)	E-W Permeability k_{ew} (mD)	$\frac{k_{ns}}{k_{ew}}$	$\frac{k_{max}}{k_M}$
Barton-Bandis Aperture	$e_{avg} = 0.022, e_{max} = 0.2$	1	12.23	11.63	1.05	12.23
Constant Aperture	$e_{avg} = 0.3, e_{max} = 0.3$	1	37.35	15.08	2.48	37.35
Power-Law Aperture	$e_{avg} = 2.07, e_{max} = 10.0$	1	326.08	121.40	2.69	326.08

Table 5.2: Table 2: Aperture and equivalent permeability results for all three modelled scenarios.

The local pressures, flow velocities and equivalent permeabilities are calculated using the acquired hydraulic aperture and using a 1.0 mD matrix permeability (Figure 5.10a, b and c) (Table 5.2). Figures 5.10 b and c show the local pressure and velocity field after the injection, - and production wells reached steady state conditions (i.e. injection = production). Firstly, the derived pressure fields indicate that in close vicinity to the hydraulically conductive fractures, the local pressure field gets slightly perturbed, indicating that fluids are being channelled through the fractures (Figure 5.10b). This channelling is also shown by the velocity field (Figure 5.10c), with flow velocities being significantly higher in close proximity to the hydraulically conductive fractures. From the parallel plate law, the hydraulically closed fractures, have a lower permeability with respect to the surrounding matrix. Therefore, these closed features act as fluid flow barriers, forcing fluids to travel through the surrounding matrix and resulting in lower flow velocities (Figure 5.10c).

Although most of the implemented fractures are essentially closed, the calculated equivalent permeability (k_{eq}) is still influenced by the open and hydraulically conductive fractures. For the presented simulations, the calculated k_{eq} is 12.23 mD and 11.63 mD for the modelled N-S and E-W flow, respectively (Table 5.2), indicating flow is partly carried by the modelled fractures. Finally, the ratio between the equivalent permeability in both flow directions ($\frac{k_{ns}}{k_{ew}} = 1.05$), indicates that the fluid flow is equally channelled in the E-W and N-S directions (Table 5.2).

5.5.2 Modelling scenario 2: Fluid flow modelling assuming constant fracture aperture

For the second scenario we use a constant aperture of 0.3 mm, which is equal to the initial intrinsic aperture in simulations of scenario 1 (Figures 5.10d and e). Due to the relatively high aperture, and connectivity of the open fractures, the modelled pressure field is highly perturbed, resulting in fluid flow which is controlled by the implemented fractures. This is also depicted by the modelled velocity field, with flow velocities being significantly higher in all implemented fractures with respect to the surrounding rock matrix (Figure 5.10f). Furthermore, because all fractures are open and connected, fluid flow follows the overall network geometry (Figures 5.10e and f).

The equivalent permeability results also indicate that flow is dominated by the implemented fracture network. The calculated equivalent permeability values are higher than the results from scenario 1, with k_{ns} being 37.35 mD and k_{ew} being 15.08 mD (Table 5.2). Therefore, these results indicate fracture-controlled fluid flow [Bisdorn et al.,

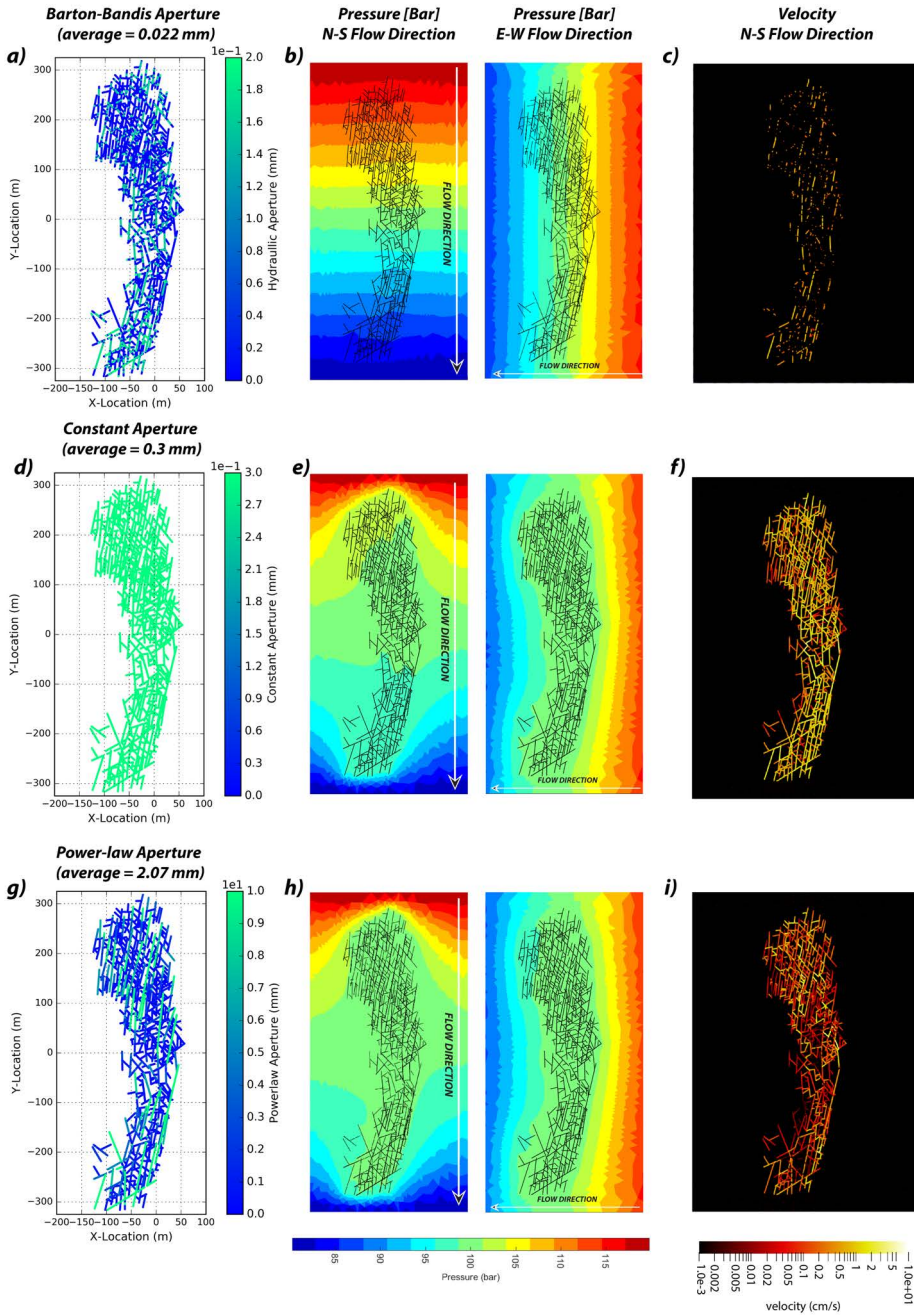


Figure 5.10: Fluid flow modelling results. a) Barton-Bandis aperture results. b) Fluid pressure field for both modelled flow directions. c) Modelled velocity field for both flow directions. d-f) The modelled Fracture apertures, fluid pressures and flow velocities for the constant aperture scenario. g-i) Modelled apertures, fluid pressures and flow velocities for the power-law aperture scenario. For these results, the modelled matrix permeability is 1.0 mD.

2017b]. Furthermore, these results indicate that flow is mainly enhanced in a N-S direction, again implying that flow mainly follows the overall fracture network geometry (Table 5.2).

5.5.3 Modelling scenario 3: Fluid flow modelling assuming power-law aperture scaling

The final scenario assumes power-law aperture frequency [Hooker et al., 2014]. The fracture opening is calculated using equations 5.11 and 5.14. Firstly, from the acquired length distribution and power-law fit (Figure 8b and equation 14), the fracture frequency is calculated. Secondly, the derived frequency is implemented into equation 9, so that the aperture for each fracture segment is calculated. For these calculations, we assume that the fracture density constant (a) can be defined by the area of interpretation ($a = \frac{1}{\text{AOI}}$, here $\text{AOI} = 8.1 \times 10^5 \text{m}^2$) and b is equal to 0.8 (Hooker et al., 2014). Finally, the maximum aperture is set at 10.0 mm, because higher aperture are rarely observed [Hooker et al., 2014]. The resulting model has an average fracture opening of 2.07 mm. Furthermore, due to the chosen aperture workflow, the longer NNE-SSW features show the largest opening (Figure 5.10g).

As it was observed with scenario 2, the modelled pressure field is highly perturbed by the implemented fractures (Figure 5.10h). This is also indicated by the modelled velocity field, where flow velocities in the fractures are significantly higher with respect to the surrounding matrix cells. Because of the high assigned fracture aperture, flow velocities inside the fractures are relatively low, especially when being compared to the results from scenario 2 (Figures 5.10f and i). However, these low velocities do not imply that the cumulative fluid flow fluxes are low, since the higher aperture allows for more transport. Therefore, these results indicate that flow is being completely controlled by the fracture network, with a large quantity of the injected fluid being channelled through the N-S orientated fractures. These observations are supported by the calculated equivalent permeabilities which show high values (Table 5.2). Furthermore, the ratio between the equivalent permeability in the two modelled flow directions ($\frac{k_{\text{ns}}}{k_{\text{ew}}} = 2.68$) indicates that preferred fluid flow direction is parallel to the larger NNE-SSW features.

5.5.4 Impact of the implemented matrix permeability

Previous studies showed that higher matrix permeabilities, result in a lower fracture contribution to the modelled fluid flow [Bisdom et al., 2017b, Matthäi and Belayneh, 2004]. For our fluid simulations, we tested this effect by running an additional batch of models with an implemented matrix permeability of 25 and 250 mD, respectively. The results are displayed in figure 5.11 and clearly show the influence of the higher matrix permeability. For all modelling scenarios, the ratio between the maximum equivalent and matrix permeability ($\frac{k_{\text{max}}}{k_{\text{M}}}$, i.e. $\frac{k_{\text{ns}}}{k_{\text{M}}}$ or $\frac{k_{\text{ew}}}{k_{\text{M}}}$) is lower for models having a higher matrix permeability (Figure 5.11a). Furthermore, the preferred flow orientations are less pronounced for models having a higher matrix permeability (Figure 5.11b). Therefore, these results indicate that a higher matrix permeability results in matrix dominated flow, where the effect of the implemented fractures is minimized (Figure 5.11).

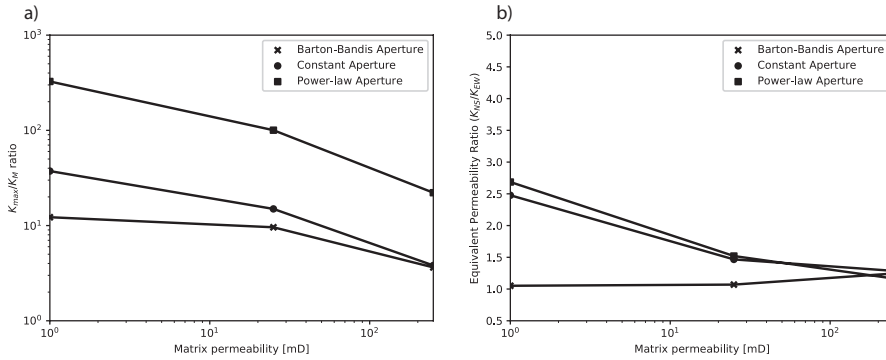


Figure 5.11: a) Maximum permeability over the matrix permeability for each modelling scenario ($\frac{k_{\text{max}}}{k_M}$). b) Ratio between the two modelled equivalent permeability directions ($\frac{k_{\text{ns}}}{k_{\text{ew}}}$).

5.6 Discussion

5.6.1 Lessons for reservoir modelling

Paleo-cave and brecciated zones are believed to highly impact the effective permeability and preferred flow orientations within normally tight carbonate reservoirs. These zones show relatively high porosities and permeabilities with respect to the surrounding host rock [Baomin and Jingjiang, 2009, Bruhn et al., 2017, Loucks, 1999, Loucks et al., 2004]. Furthermore, the geometry of these systems is believed to be largely controlled by structural interfaces such as fold -, fault - or fracture planes [Cazarin et al., 2019, Loucks, 1999, Loucks et al., 2004]. Therefore, understanding and quantifying the relation between fractures, fluid flow and localized karst conduits has become key in optimizing production from complex carbonate reservoirs.

In this study, we emphasised on this relation and the presented an additional case study which showed the correlation between a large fractured pavement and an underlying cave system. Our results showed that fractures acted as fluid conduits, and that the geometry of the fracture network controlled the geometry of the cave system. Furthermore, our results indicated that the studied fracture – and cave network followed a similar length frequency distribution. This implies that the two multiscale datasets are part of the same system, and that the frequency and length of the cave tunnels can be estimated from the fracture data. The numerical modelling results also highlighted that fluids were being channelled through open fractures, resulting in preferred fluid flow orientations following the overall fracture network geometry (Figure 5.10 and table 5.2). In addition, these numerical results indicated that the chosen aperture model has a high impact on the fracture-controlled flow and equivalent permeability. Therefore, the presented results could help in making better predictions on the lateral extend and geometry of fracture-controlled karst conduits, in the sub-surface. Moreover, the numerical results can help in making better estimations on the impact of fractures in normally tight carbonate reservoirs.

5.6.2 Link between the tectonics, fractures and the cave network geometry

The presented fracture network is composed of barren fractures, veins and stylolites, which strike in three main directions namely: 1) Set-1 (NNE-SSW), 2) Set-2 (NW-SE) and 3) Set-3 (ENE-WSW) (Figure 5.5). Structural analysis of the acquired data suggested that these features formed in response to two contractional deformation phases (NNW-SSE and WNW-ESE) (Figure 5.5), which are most likely related to the Brazilian orogeny [Cruz and Alkmim, 2006, Ennes-Silva et al., 2016]. Relative timing between the two deformation phases was hard to define due to insufficient cross cutting relationship between the observed structural features. Finally, field evidence showed that fractures and stylolites are being re-used as fluid flow conduits (Figure 5.6).

Although the observed correlation between the fractures and cave tunnels is clear, one question remains, namely: Why is there a distinct scale and size difference between the caves and the fracture network? One theory is that the caves tunnels initially represented larger fractures and fracture corridors, which contributed more the flow and the coinciding dissolution. Alternatively, this size difference may be a result from erosion processes itself, where erosive fluids preferred the more permeable fractured rock, which over time developed in to more permeable channels and larger cave tunnels.

We believe that the Brejoes cave system developed in response to both mechanisms, because we found clear evidence that fractures were being re-used as fluid flow conduits. Further, our models showed that larger fractures contributed more to the flow than smaller features. However, these observations can't completely explain the observed size difference, especially concerning the tunnel width and height. Therefore, we argue that the largest portion over the cave system developed at near surface conditions following the second theory. However, geochemical analysis is necessary to fully validate this point.

5.6.3 Implications of the chosen aperture model and matrix permeability

The numerical results indicate that the equivalent permeability ratio ($\frac{k_{eq}}{k_M}$) and anisotropy in the permeability field vary with the assigned aperture model and implemented matrix permeability (Figures 5.10 and 5.11). For all models, a higher matrix permeability lowers the relative contribution of the implemented fractures. Previous modelling studies showed that this effect was caused by the ratio between the fracture- and matrix permeability ($\frac{k_f}{k_M}$) [Bisdom et al., 2016b, Matthäi and Belayneh, 2004]. For instance, $\frac{k_f}{k_M}$ ratios which are smaller than 10^2 , result in a negligible contribution of the implemented fractures to the overall flow. On the other hand, having ratios higher than 10^3 to 10^4 , results in fractures partly controlling the fluid flow. Finally, fractures carry all the flow when these $\frac{k_f}{k_M}$ ratios exceed 10^5 to 10^6 [Bisdom et al., 2016b, Matthäi and Belayneh, 2004].

For our results, we find that the Barton-Bandis aperture realization show the lowest average aperture (0.022 [mm]), with most of the implemented fractures being closed. Here, the calculated $\frac{k_f}{k_M}$ range between 10^4 and 10^2 for matrix permeabilities ranging between 1 and 250 mD, respectively. This implies that for higher matrix permeabilities, the impact of the fractures becomes negligible. However, it should be noted that changing the applied stress orientations may result in different aperture descriptions, hence

changing the contribution of the implemented fractures [Bisdom et al., 2016b].

The constant – and power-law aperture descriptions show a relatively high average aperture (Table 5.2), resulting in high $\frac{k_f}{k_M}$ ratios. For the constant aperture approach the ratio ranges between 10^6 and 10^4 . This implies that for this aperture scenario, fractures have a strong impact on the fluid flow. The $\frac{k_f}{k_M}$ ratio is even higher for the models assuming power-law aperture descriptions. Here, the calculated ratios range between 10^8 and 10^6 , implying that the fractures completely control the modelled fluid flow.

5.6.4 Implications of the main assumptions

Because of erosion and karstification, discrimination between stylolites, joints and shear fractures was impossible. Therefore, for the presented numerical workflow, we assumed that all modelled features could be treated as reactivated fractures, and that the fracture aperture could be modelled.

Although widely used in reservoir modelling, this assumption is inaccurate when modelling complex features such as stylolites or partly cemented fractures. For instance, depending on their geometry and mineralogy, tectonic stylolites can either enhance or inhibit fluid flow [Bruna et al., 2018]. Furthermore, fluid flow could be significantly inhibited by cemented fractures. Here cementation often lowers the effective aperture of a fracture plane [Gale et al., 2010, Olson et al., 2009]. Another issue is that the length and dominance of certain fracture sets could be enhanced as result of uplift, erosion and the coinciding stress relaxation. This implies that certain features could be over interpreted, resulting in different network geometries with respect to their sub-surface counterparts. Therefore, more accurate subsurface flow models could be realized by implementing these known geological - and modelling processes in to the presented numerical workflow.

Apart from better descriptions of the implemented structural features, having better knowledge on the stress conditions and elastic parameters, could also help in better aperture descriptions for reservoir models. For instance, a recent sensitivity study which tested the impact of these parameters on the modelled stress induced aperture, showed that the modelled stress orientation and magnitude of the differential stress had a high impact on the resulting aperture description [Bisdom et al., 2016c]. Furthermore, this study showed that a higher Young's Modulus results in higher modelled apertures, and therefore, a higher flow contribution of the modelled fractures.

5.7 Conclusions

This study implements a multiscale approach of structural field data analysis and numerical modelling, to define the correlation between fractures, fluid flow and large karst conduits. The presented workflow is exemplified on a fractured pavement and an underlying cave network (Bahia, NE Brazil).

Firstly, the structural field data highlights a fracture network composed of fractures, veins and tectonic stylolites, striking in three main orientations namely: set-1) NNE-SSW, set-2) NW-SE and set-3) ESE-WNW. The observed fractures and veins form two conjugate pairs. Each pair has a tectonic stylolite set striking perpendicular to its respective bisection plane. Inversion analysis of the interpreted fractures, veins and stylolites highlight that these features developed in response to two contractional deformation

events, namely: 1) NNW-SSE – and 2) WNW-ESE compression.

Secondly, interpretation of the acquired drone imagery and underlying cave system highlights the same three orientations being present. Furthermore, the results indicate that the two multiscale datasets have a similar orientation- and length distribution, with the NNE-SSW features being most dominant. These similarities suggest that the Brejoes fractured pavement and cave system are structurally related.

Thirdly, the observed correlation is further exemplified by our numerical models. The results clearly depict the impact that open fractures have on the modelled fluid flow, especially concerning low permeable matrix permeabilities. For all considered scenarios, open fractures act as fluid flow conduits, resulting in significantly higher flow velocities with respect to the surrounding matrix. In addition, the results indicate that the impact that the fractures have on flow decreases significantly, for models having a higher matrix permeability.

Finally, the presented results indicate that the geometry of the cave system is controlled by the geometry of the fracture network, where open fractures most likely acted as fluid flow conduits, which ultimately developed in to the observed cave system. Furthermore, due to the extent of the cave network and size of the tunnels, we argue that the Brejoes cave system developed after exhumation at near-surface conditions.

Data availability

The full dataset, interpretations and modelling results presented in this chapter are freely available and can be downloaded via the following DOI: <https://doi.org/10.4121/uuid:7dede8dd-538a-4b70-a110-3f899e37e8ca>

6

FRACSIM2D: A NEW METHODOLOGY FOR GENERATING GEOLOGICAL CONSTRAINED 2D DISCRETE FRACTURE NETWORKS

Natural fracture networks often show hierarchal patterns and a substantial degree of organization. These characteristics are believed to greatly control the overall geometry and connectivity of a fracture network. In this chapter, we present FracSim2D an open source python code which is able to simulate 2D Discrete Fracture Networks (DFN) based on the fracture characteristics commonly observed on outcrops, including hierarchy, topology, spacing along with different length - and orientation distributions. The code is exemplified using natural fracture data acquired from four different pavement outcrops, which show distinctly different fracture network geometries. The results show that by implementing controls such as: 1) different fracture levels, 2) hierarchical behaviour, 3) topological rules, and 4) a strict fracture spacing relationship, this algorithm is able to simulate the network geometries which show a close resemblance to their outcrop counterparts, especially with respect to simulations which only account for the statistical observations. Further, we show that, geologically constrained DFN's generated using FracSim2D are better able to capture the fluid flow behaviour and effective permeability estimations with respect to non-constrained DFN's. Finally, we argue that the output of FracSim2D could be used as input Training Images for Multiple Point Statistics algorithms, thereby potentially helping in creating better constraint 2D fracture network descriptions on a large scale.

This chapter presents a python-based fracture simulator which has been developed together with Nico Hardebol

6.1 Introduction

Outcrop, laboratory and subsurface studies commonly show that natural fracture networks have relationships with regional tectonics, large scale features such as faults or folds, the local lithology and contrasting mechanical parameters (i.e. mechanical stratigraphy) [Boersma et al., 2019b, 2020, Bourne, 2003, Hanke et al., 2018, Maerten et al., 2016, McGinnis et al., 2015, Roche and van der Baan, 2015]. In addition, outcrop studies have shown that natural fracture networks have hierarchal patterns, distinct topologies with and a substantial degree of organization, all of which are regarded to be an important measure for estimating the percolation potential and the impact on fluid flow of natural fracture network geometries [Nyberg et al., 2018].

Due to the seismic resolution gap and limited hard data points, the presence, extent and geometry of natural fractures are often predicted and modelled. This is often done using commercial Discrete Fracture Network (DFN) simulators which use an iterative and statistical approach in combination with additional information acquired from numerical models, outcrop analogues and/or seismic data (if applicable) [Jaglan and Qayyum, 2015, Maerten et al., 2019, Williams et al., 2017]. Apart from new versions of FracMan®, fracture network characteristics such as hierarchy or topology are generally implemented in these statistically driven simulators.

Another method for modelling DFN's is by using growth algorithms. These algorithms use probabilistic and mechanically derived rules defined by the user to systematically 'grow' geologically and mechanically feasible network geometries [Josnin et al., 2002, Libby et al., 2019]. The resulting fracture networks show a close resemblance to geometries observed on outcrops, especially with respect to statistically controlled simulations [Libby et al., 2019].

A relatively new approach in fracture network modelling is using Multiple Point Statistics (MPS), e.g. Bruna et al. [2019]. This approach does not use any statistically- or mechanically-derived relations, but uses training images and elemental zones defined by the user, in order to populate reservoir scale DFN's. Therefore MPS grants the user a great deal of freedom to generate DFN's similar to those observed on outcrops [Bruna et al., 2019]. However, because the training images and elemental zones are defined and 'drawn' by the user, this method could be sensitive to interpretation biases.

Although modelling tools which can generate geologically feasible DFN's have already been developed and presented (e.g. Bruna et al. [2019], Josnin et al. [2002], Libby et al. [2019]), open source tools which incorporate distinct geological observations such as fracture hierarchy, levels, topology and spacing are generally not fully available to the public and scientific community. Therefore, in this chapter we present FracSim2D, a python-based algorithm which is able to incorporate these distinct geological controls into 2D DFN simulations. It should be noted that throughout this chapter, fracture hierarchy, levels, topology and spacing are referred to as being geological controls. The output of the algorithm are georeferenced shapefiles, which can easily be analysed in GIS software packages or incorporated in fluid flow simulators. The code, user documentation and several examples are freely available as supplementary material.

This chapter is organized as follows. First, we provide an explanation of the organization of the algorithm and user-defined input files (i.e. files which describe the statistical and geological controls and different fracture levels). Second, we demonstrate how the

algorithm develops a 2D DFN based on a distinct input file. Third, we exemplify the tool using data extracted from naturally fractured pavement outcrops. Fourth, the importance of implementing geological controls in to a DFN is illustrated by incorporating interpreted and simulated DFN's into a fluid flow modelling workflow. Finally, the potential value and pitfalls of the algorithm are discussed.

6.2 Design of the algorithm

FracSim2D is a python-based algorithm which uses defined statistical and geological controls in order to stochastically populate 2D DFN's (Figure 6.1). The tool has been developed on top of Quantum GIS 2.4 (QGIS 2.4) (<https://qgis.org>) and uses multiple functions taken from the QGIS 2.4 library. Therefore, this algorithm requires QGIS 2.4 Chugiak to be installed and properly referred to in order to work (See supplementary materials). Further, the algorithm only runs on a windows operating system. FracSim2D is organized as follows: 1) Input python files, 2) the main algorithm, 3) background functions and 4) model output folders.

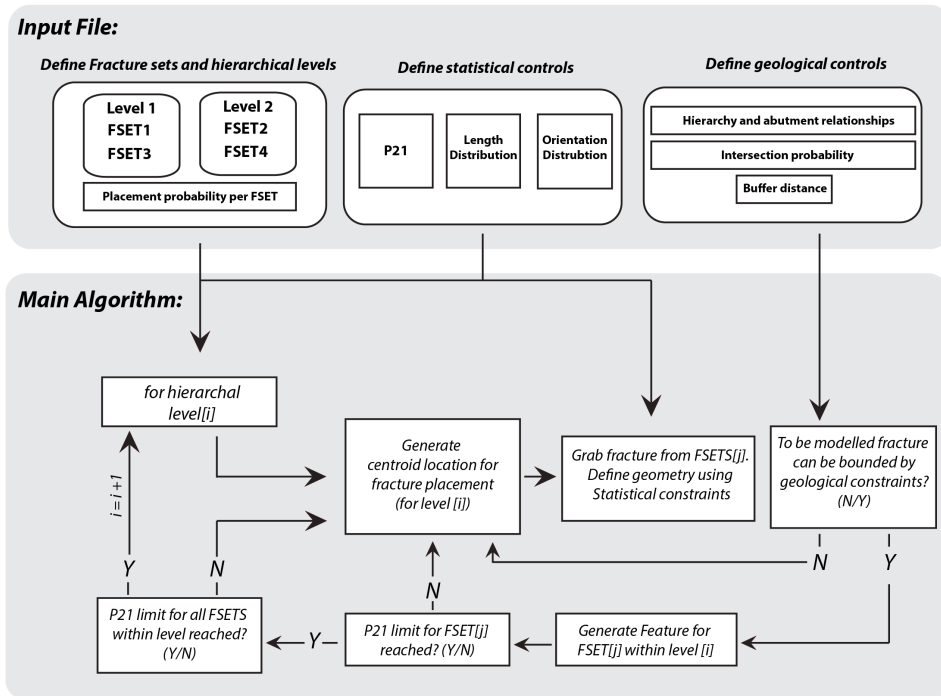


Figure 6.1: The workflow of the algorithm. This algorithm simulates a fracture network geometry for a number for fracture sets and levels, based on the assigned statistical (P21, Length distribution and the orientation distribution) and geological (Hierarchy, intersection probability and buffer distance) controls. This algorithm continues to place fractures until the P21 limit for each fracture set is reached.

6.2.1 The workflow of the algorithm

To illustrate how the algorithm stochastically generates a 2D DFN (Figure 6.1), we show a simulation with distinct geological and statistical controls. For this simulation we assume that three fracture sets orientated N-S or E-W are present. Further, we assume that the different fracture sets can be sub-divided into three levels and that a distinct hierarchy is present. To do this we explicitly tell the algorithm that fractures of a lower order cannot intersect fractures belonging to a higher order, by assigning the placement control: No Higher Order Fracture Intersect (NHOFI) (see section 6.2.2.) (Table 6.1, Figure 6.2). Additionally, a fixed fracture spacing was assigned for all fracture sets (Table 6.1). More information on the different statistical and geological controls used in this simulation will be explained in section 6.2.2.

FSET	Fracture Level	P21 Limit	Length distribution	Buffer distance (m)	Orientation distribution	Placement constraint
FSET1	1	0.75	Fixed: 30.0m	0.75	VM: $\mu = 0$, $\kappa = 250$	NHOFI
FSET2	2	0.75	Fixed: 5.0m	0.75	VM: $\mu = 90$, $\kappa = 250$	NHOFI
FSET3	3	0.25	Fixed: 5.0m	0.25	VM: $\mu = 0$, $\kappa = 250$	NHOFI

Table 6.1: Input parameters for the step by step modelling simulation (Figure 2). See section 2.3 for more information regarding the input parameters. Note that VM = Von Mises and NHOFI = Non Higher Order Fracture Intersection. Additional information on the different settings can be found in section 6.2.2.

The first loop within FracSim2D is over the hierarchical levels (Figure 6.1). Therefore, in this example, the algorithm first places N-S fractures (FSET1) at a roughly equal spacing within the modelling domain (Table 6.1, Figure 6.2a). Once the P21 limit for FSET1 is reached, the simulator starts placing E-W striking fractures belonging to FSET2 (Table 6.1 and Figure 6.2b to e). Because of the assigned geological controls, these fractures cannot intersect the previously generated N-S fractures (Table 6.1). Therefore, these fractures are clipped (shortened in length) so that they fit in between the features belonging to FSET1 (Figure 6.2 and Table 6.1). Clipping fractures in order to honour the assigned geological controls is one of the key characteristics of FracSim2D. However, this does imply that the assigned statistical input is generally not completely respected by the resulting DFN (Table 6.1 and Figure 6.2). Finally, in between the E-W fractures, new N-S features (FSET3) are placed (Figure 6.2e and f). Again, the modelled lengths are clipped due to the no higher order intersection control.

6.2.2 The input file

In order to generate different DFN's, the user defines a model input file. In this file the user can detail the characteristics of the DFN such as, 1) the modelling domain, 2) the different fracture sets and levels, and 3) different characteristics including length - and orientation distributions, hierarchy, intersection probability and spacing (Figure 6.1). FracSim2D reads the input file, and together with multiple function libraries, generates a DFN (Figure 6.1 and 6.2). The main algorithm and background functions do not need to be changed by the user. However, the file paths of the input file and output folder need to be properly defined. Additional information on how to define different constraints in the input file can be found in the supplementary materials.

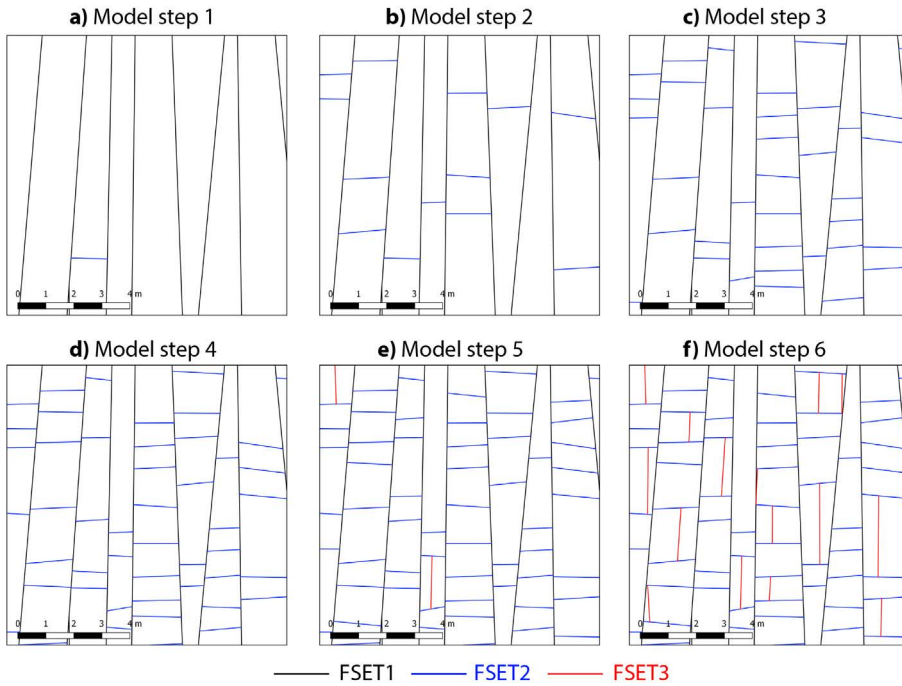


Figure 6.2: a-f) Step by step modelling workflow for generating a nested orthogonal network (see table 1 for modelling parameters).

Fracture sets and levels

Within FracSim2D, fracture sets describe a group of fractures which have a shared orientation. Fracture levels describe the hierarchy of the network, and within this tool multiple fracture sets can belong to one level. For each set within a level, a placement probability needs to be defined (Figure 6.1). An example of a simulation which had distinct fracture levels and sets was shown in section 6.2.1 (Figure 6.2 and Table 6.1).

Statistical controls and distributions

To determine how the fractures within a level and set are populated, different statistical input controls such as, a fracture intensity limit, a length distribution and an orientation distribution need to be defined by the user (Figure 6.1). The fracture intensity (P21) limit describes the maximum cumulative trace length of fractures within a set over the modelling area [Dershowitz and Herda, 1992, Sanderson and Nixon, 2015]. Within FracSim2D, this limit is a single scalar value defined by the user. A P21 distribution or map cannot be implemented in the current version of the algorithm.

The second statistical control is the chosen length distribution. Within this tool, the user can choose from five different length distributions, namely: 1) fixed, 2) uniform, 3) Log-Normal, 4) negative power-law and 5) negative exponential. For the fixed length, the algorithm aims to generate fractures having the assigned length (for example 10m). For

the second length distribution (Uniform), the algorithm populates fractures uniformly in between a user defined minimum and maximum length (Figure 6.3a). Thirdly, the log-normal distribution uses the log-normal function taken from the scipy (python) library (Figure 6.3b), so that the length distribution can be defined as follows:

$$P(\ln(l); \mu, \sigma) = \frac{1}{\sigma\sqrt{2\pi}} \exp\left(-\frac{(\ln(l) - \mu)^2}{2\sigma^2}\right), l > 0 \quad (6.1)$$

Where, l is the fracture length (m), σ is the shape parameter (standard deviation of the logarithm of the variable) and μ is the scale parameter (i.e. $Median = \exp(\mu)$) of the function, respectively (Figure 6.3b). For the negative power-law distribution we use a python package called power-law [Alstott et al., 2014], so that the length population is defined by equation 2:

$$P(l; a) = al^{-a} \quad (6.2)$$

Where, l is the fracture length (m) and a is the power-law exponent and scaling parameter (Figure 6.3c). Finally, for the exponential distribution (Figure 6.3d), we use the exponential function within the python scipy library so that the length distribution can be defined by equation 3:

$$P(l; \lambda) = \lambda e^{-\lambda l} \quad (6.3)$$

Where l is the fracture length (m) and λ is the shape parameter (in the scipy function, shape = scale = $1/\lambda$). Further, a loc parameter is added in the function, which can be used to additionally shift the exponential function.

Two different orientation distributions can be chosen, namely: 1) uniform and 2) Von-Mises. For the uniform distribution, the user assigns a minimum and maximum value, and the algorithm populates fractures which have an angle ranging in between the two defined values. For the Von-Mises distribution we also use a scipy package so that fractures are normally (i.e. Gaussian distribution) populated around a user defined mean angle (equation 4):

$$P(\theta; \mu, \kappa) = \frac{e^{\kappa \cos(\theta - \mu)}}{2\pi I_0(\kappa)} \quad (6.4)$$

Where, θ is the fracture orientation (radians) (in this algorithm strike), μ is the user defined mean orientation and $1/\kappa$ is analogues to the variance of the orientation distribution (i.e. σ^2). $I_0(\kappa)$ is the modified Bessel function of the zeroed order.

Geological controls: Placement constraints, hierarchy and buffer distance

In order to generate fracture network geometries which show organization and hierarchy, two geological controls can be assigned, namely: 1) placement constraints and 2) the buffer distance (parameter used for modelling fracture spacing) (Figure 6.1).

Within FracSim2D four different placement constraints can be assigned, namely: 1) Random (no geological controls), 2) No Self Intersect (NSI) (fractures belonging to the same set cannot intersect), 3) No Equal Level Fracture Intersect (NELFI) (Fractures belonging to the same level cannot intersect each other), 4) No Higher Order Fracture Intersect (NHOFI) (fractures belonging to this level cannot intersect fractures of a higher

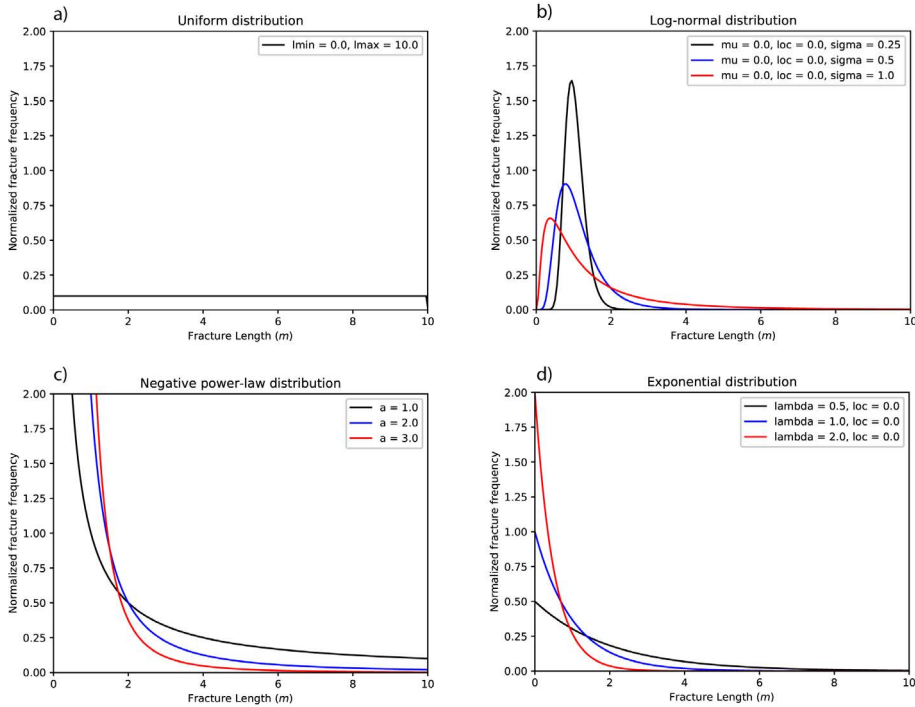


Figure 6.3: Different length distributions used within the algorithm. a) Uniform length distribution. b) Different log-normal length distributions. c) Different negative power-law length distributions. d) Different exponential distributions.

level) and 5) Place at Higher Order Fracture (PHOF) (explicitly place fractures to fractures belonging to a higher order). These different placement constraints are exemplified by Figure 6.4. See the caption for more information on the simulation settings 6.4.

The fracture spacing is implemented by assigning a specific buffer distance to a fracture set. If activated, the algorithm tries to place fractures belonging to the same set at a spacing which is bigger than the defined buffer distance. For example, figure 6.5a shows a simulation with an assigned buffer distance of 0.1m whereas the simulation shown by figure 6.5, has a buffer distance of 0.5m. While showing promising results, it should be noted that some minor deviation from the assigned buffer distance can occur. This problem occurs because FracSim2D uses the central node of a to be placed fracture to calculate the relative spacing between the different fractures. In addition it should be noted that assigning strict spacing relationships between fractures results in simulations which may take a long time to compute.

By combining different fracture levels and sets with specific placement constraints and buffer distances, FracSim2D can essentially capture different fracture network geometries commonly observed on outcrop analogues. This was for instance demonstrated in section 6.2.1, where an nested orthogonal network was generated using different fracture levels, the NHOFI placement constraint and explicit buffer distances (Figure

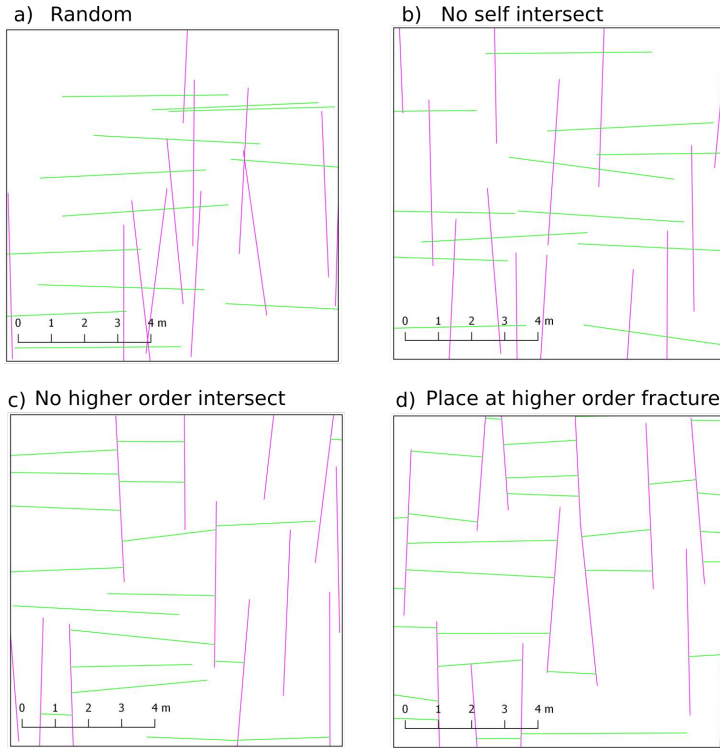


Figure 6.4: Different placement constraints. All network realizations had a fixed length distribution ($l = 5.0\text{m}$) and two fracture sets (FSET1 (N-S) (Pink) and FSET2 (E-W) (Green)). Both fracture sets have a von-mises orientation distribution (FSET1: $\mu = 0.0$, $\kappa = 250$, FSET2: $\mu = 90.0$, $\kappa = 250$) and have a P21 limit of $0.5 (1/\text{m})$. The buffer distance was set at 0.5m (see figure 6.5). a) Random fracture placement. b) No self-intersect constraint. c) No higher order fracture intersect constraint. d) Place at higher order fracture.

6.2).

Finally, it should be noted that within FracSim2D, the assigned geological controls are regarded to be more important than the statistical distributions. This implies that, the modelled fracture population can deviate away from the assigned statistical distributions in order for the geological constraints to be honoured. For instance, modelling a fracture network which has one fracture set with a fixed length distribution and a non-self-intersecting placement constraint, will result in a DFN containing fractures with different lengths, because the algorithm clips the length of individual fractures in order to honour the implemented geological controls. This way of clipping the lengths was for example demonstrated in section 6.2.1. (Figure 6.2)

6.3 Results

6.3.1 Case study: Brejoes fractured pavement

To exemplify how FracSim2D can be used to capture network geometries observed on outcrop analogues, data taken from a fractured pavement is used to simulate two differ-

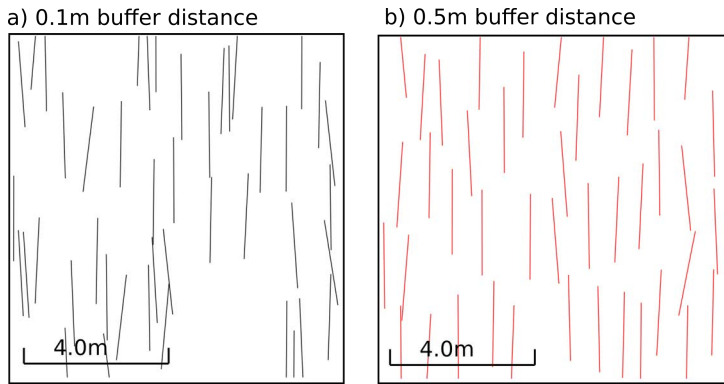


Figure 6.5: Changing the assigned buffer distance. Both network realizations had a fixed length distribution ($l = 2.5\text{m}$) and one fracture set (FSET1 (N-S) which has a von-mises orientation distribution ($\mu = 0.0$, $\kappa = 350$)). The P21 limit was set at 1.0 (1/m). Finally, the fracture placement constraint was set at no self intersect a) Buffer distance = 0.1m. b) Buffer distance = 0.5m.

ent 2D DFN's. The first simulation uses conventional random population together with statistical distributions. For the second simulation, we use geological input to constrain the generated DFN. The simulations are then compared to the original interpretation of the outcrop (Figure 6.6a).

The Brejoes fractured pavement is located in Bahia, Brazil (long: -41.44W , lat: -11.00S). The pavement outcrop is composed of Neoproterozoic carbonates from the Salitre formation deposited within the Irece Basin. The carbonates of the Salitre formation are believed to be influenced by two subsequent contractional deformation events related to the Brazilian Orogeny (750–540 Ma) [Boersma et al., 2019b, Ennes-Silva et al., 2016, Guimaraes et al., 2011], and outcropping rocks show E-W and N-S verging folds and thrust belts [Bizzi et al., 2003].

Drone Imagery of the Brejoes outcrops highlight a large and connected fracture network which has three main fracture sets (FSET1, FSET2 and FSET3) (Table 6.2, Figure 6.6a). On-site analysis of the different fracture sets, indicates that these features most likely formed in response to N-S and E-W contractional deformation events [Boersma et al., 2019b]. The orientation distribution of each FSET is best represented by a characteristic von-Mises distribution, which has a distinct mean and standard deviation (Table 6.2, Figure 6.6a). Using a linear regression, each individual FSET can be described by a characteristic exponential function (Table 6.2) (Figures 6.6b-d). Fracture intensity analysis shows that longer fractures mostly belong to FSET1. Smaller features generally belong to FSET2 and FSET3 (Figure 6.6a, Table 6.2). Finally, the extracted network shows a clear hierarchy between the longer and shorter fractures (Figure 6.6a). The interpretation and acquired statistical information are used as a reference to bench mark the quality of the simulation (figure 6.7a and b)

The first simulation is based on the extracted statistical distributions and data (Tables 6.2 and 6.3). Fractures are placed using the random fracture placement function, thereby assigning no geological controls (Table 6.3). The length and orientation of each fracture set is populated using its respective exponential function, and a Von Mises dis-

Fracture set	Fracture strike (degrees)	P21 ($\frac{m}{m^2}$)	Length distribution	Hierarchical order
FSET1	14.98 ± 13.08	0.320	Exponential: $\kappa = 0.103$, loc = -10.00	Equal level
FSET2	134.69 ± 7.77	0.249	Exponential: $\kappa = 0.272$, loc = -5.00	Equal level
FSET3	77.84 ± 10.32	0.246	Exponential: $\kappa = 0.300$, loc = -4.25	Equal level

Table 6.2: Statistical and geological data extracted from the interpreted fracture network from the Salitre formation pavement near Brejoes (Brazil).

tribution based on the extracted orientation data, respectively (Figure 6.6, Table 6.3). Using these settings, we simulate a statistically controlled and randomly populated DFN and the resulting network geometry honours the observed length and orientation distribution (Figure 6.7 a to d). However, the observed hierarchy, abutment and spacing relationships have not been captured by this simulation (Figure 6.7a to d).

For the second simulation, the geological observations made on the outcrop, such as the fracture hierarchy, spacing relationships and equal level abutment relationships are incorporated into the simulation workflow. To include the observed hierarchy, the modelled fractures are separated in to two levels (i.e. FSET(i) (HO) and FSET(i) (LO) (Table 6.3). For the higher order fractures (i.e. level 1), we simulate the larger fractures in all orientations and the assigned P21 limit for each FSET is calculated by only using fractures longer than 10m (Table 6.3). The orientation distribution for each higher order FSET is also calculated using fractures longer than 10m (Table 6.3). Buffer distances of 3.0 m and 4.0 m were set for FSET1 and FSETS 2 and 3, respectively (Table 6.3). To ensure that an interconnected fracture network is generated, the length distribution for each FSET is set at fixed value (i.e. $l \gg$ buffer distance). Finally, fractures belonging to level 1 were not allowed to intersect each other. For the lower order FSETS we used a similar approach as discussed above, and the settings for each FSET are summarized in table 6.3, respectively. Note that the Non Higher Order Fracture Intersection (NHOFI) placement constraint is activated for the lower order fractures so that smaller fractures are confined by the larger features.

The results show that by incorporating hierarchy and spacing in to the simulation, the modelled DFN shows a much closer resemblance to the observations made on the outcrop (Figure 6.7). Further, even though a fixed length was assigned for all FSETS (Table 6.3), the assigned geological constraints clipped the fractures in such a way that the resulting length distribution shows distinct similarities with the length distribution observed on the outcrop (Figure 6.7b and f). By performing a topology and connectivity analysis (done using Network GT [Nyberg et al., 2018]), the impact of implementing geological controls becomes more apparent. For instance, the results of the analysis show that the topology of the interpreted fracture network is dominated by abutting fractures (Y-connections). Because of rules assigned, this topology is captured by the geologically constrained DFN (Figure 6.7g). In contrasts, by assigning no geological rules, the randomly populated DFN shows a topology which is different with respect to the interpretation (Figure 6.7g). The connectivity analysis shows similar results. The results indicate

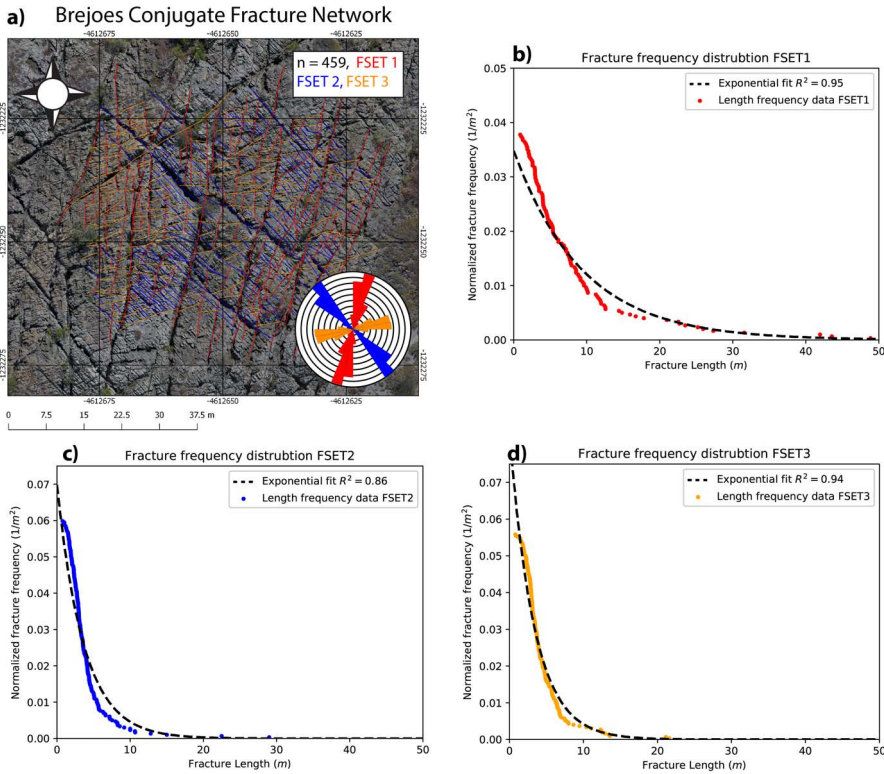


Figure 6.6: The Brejoes limestone fracture network interpretation and analysis. a) Brejoes fracture network interpretation and on fractured pavement. The three fracture sets are highlighted by their colour (Figure modified after [Boersma et al. \[2019b\]](#)). b-d) Fracture length distributions and the exponential fit for FSET1, FSET1 and FSET3, respectively. Normalization of the length data is done over the area of interpretation.

that the interpretation and geologically controlled simulation both show connected fracture networks which are dominated by fully connected branches. The randomly populated simulation shows more isolated and partly connected branches and therefore does not represent the connectivity of the interpreted network geometry (Figure 6.7h).

6.3.2 Simulations of other natural examples

To further exemplify FracSim2D, we have simulated three additional DFN's which are controlled by geological input data taken from three different pavement outcrops. The analysed networks show distinct differences in geometry, hierarchy and topology (Figures 6.8a to c). The first outcrop shows a nested orthogonal fracture network and is located Port Mulgrave (Whitby, UK) (Figure 6.8a). The fracture interpretation of this outcrop was taken from [Houben et al. \[2017\]](#). The second outcrop highlights isolated and roughly parallel fractures observed on a large carbonate platform outcrop (Parmelan, France) (Figure 6.8b). The network interpretation was taken from [Prabhakaran et al. \[2019\]](#). The third pavement outcrop is located in the Bristol Channel Basin (UK), and the

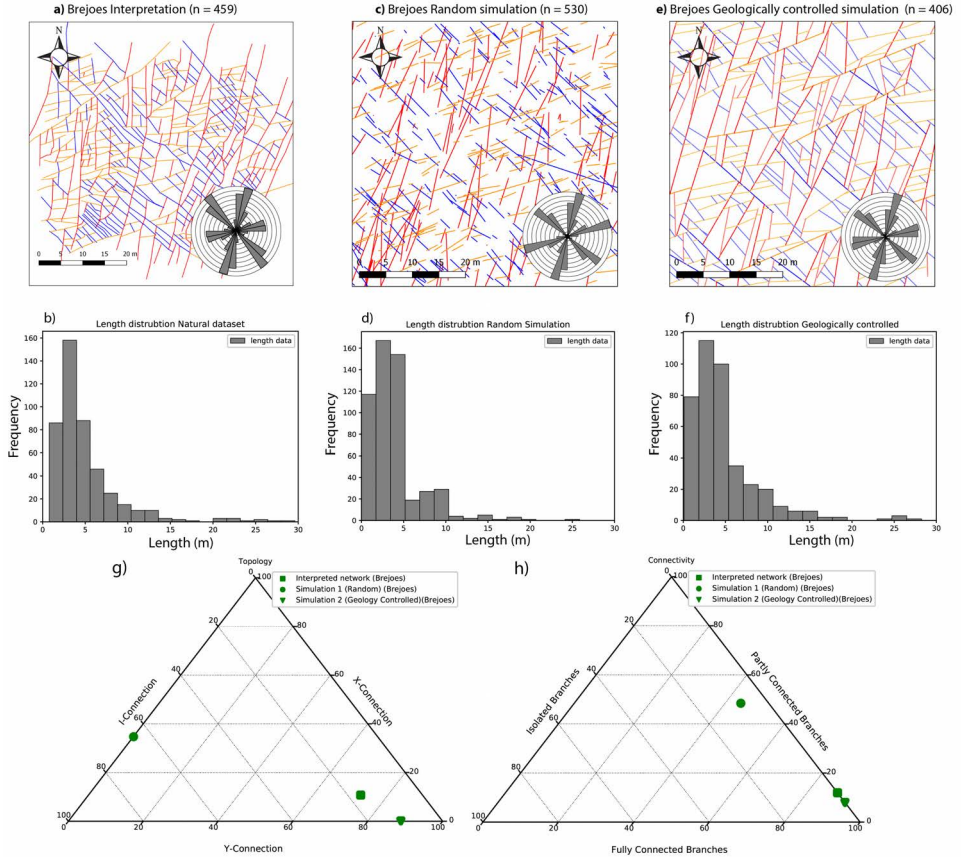


Figure 6.7: Interpreted and simulated network geometries based on the data acquired from the Brejoes fracture network. a-b) Interpreted fracture network and acquired length distribution. c) Statistically controlled and randomly populated simulation. No geological controls have been assigned. Settings are shown in table 3. d) Length distribution for statistically populated network geometry. e) Network simulation which is controlled by the observed hierarchy and coeval abutment relationships. Settings can be found in table 3. f) Length distribution for the second simulation. g-h) Network topology and connectivity for the Brejoes fracture network interpretation, statistically based simulation and geologically controlled simulation, respectively. Network topology analysis is done using Network GT [Nyberg et al., 2018].

Simulation	FSET	Fracture level	P21 Limit ($\frac{m}{m^2}$)	Length distribution	Buffer distance (m)	Orientation distribution	Placement constraint
Sim 1	FSET1	1	0.320	Exponential: $\kappa = 0.103$, loc = -10.00	none	VM*: $\mu = 14.98$, $\kappa = 40$	RFP*
	FSET2	2	0.249	Exponential: $\kappa = 0.272$, loc = -5.00	none	VM: $\mu = 134.69$, $\kappa = 80$	RFP
	FSET3	3	0.247	Exponential: $\kappa = 0.300$, loc = -4.25	none	VM: $\mu = 77.84$, $\kappa = 60$	RFP
Sim 2	FSET1 (HO)	1	0.180	Fixed: 50m	3.0	VM: $\mu = 14.98$, $\kappa = 40$	Equal level*
	FSET2 (HO)	1	0.040	Fixed: 25m	4.0	VM: $\mu = 134.69$, $\kappa = 80$	Equal level
	FSET3 (HO)	1	0.047	Fixed: 25m	4.0	VM: $\mu = 77.84$, $\kappa = 60$	Equal level
	FSET1 (LO)	2	0.140	Fixed: 15m	0.75	VM: $\mu = 14.74$, $\kappa = 70$	NHOFI*, Equal level
	FSET2 (LO)	2	0.200	Fixed: 15m	0.75	VM: $\mu = 135.0$, $\kappa = 80$	NHOFI, Equal level
	FSET3 (LO)	2	0.210	Fixed: 15m	0.75	VM: $\mu = 79.77$, $\kappa = 50$	NHOFI, Equal level

Table 6.3: Statistical and geological controls for the Brejoes simulations. Note that VM = Von Mises, RFP = Random Fracture Placement, NHOFI = Non higher order fracture intersection and Equal level = Cannot intersect fracture of a higher or the same order

interpretation of this outcrop highlights a complex multi-tier fracture network (Ladder-like geometry cross-cutted by conjugate fractures) (Figure 6.8c) [Belayneh and Cosgrove, 2004].

The three simulations of the fracture networks are shown by Figures 6.8d to f. These DFN's use the statistical and geological data taken from the interpretations as input for the simulation (input settings can be found in Appendix B). The results show that Frac-Sim2D is able to generate feasible DFN's which show a close resemblance to their outcrop counterparts. While showing distinct similarities, it should be noted that characteristics such as curving features, en-echelon fracturing, fracture clustering or changes in P21 cannot be simulated using this algorithm. The effects of these limitations can be seen with simulation of the Parmelan outcrops (Figure 6.8b).

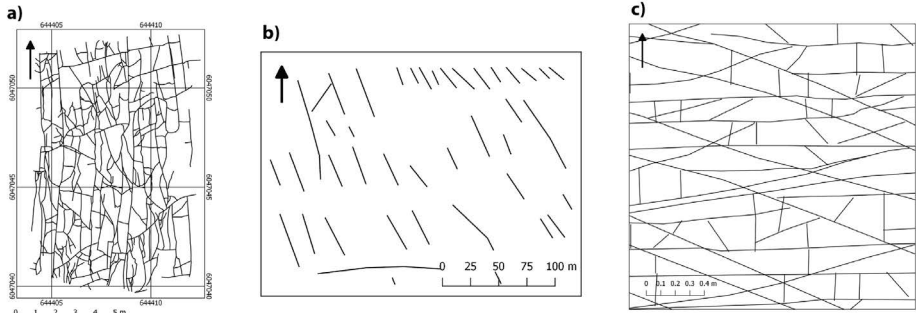
6.3.3 The importance of geological constraints: Implications for fluid flow

To illustrate the importance of implementing geological controls into DFN simulations, the interpreted and simulated DFN's from the Brejoes case study were implemented into a fluid flow simulation workflow. The 2D fracture network geometries were clipped by a bounding box, and meshed using the algorithm available within Abaqus 6.14 (using triangular elements and a seed size of 0.25 m on each fracture). For all simulations, we assumed a constant matrix permeability (k_{mat}) of 5.0 (mD), a constant fracture aperture (e) of 0.1 (mm) and fluid viscosity of $5.0 \cdot 10^{-5}$ ($Pa \cdot s^{-1}$). Using a constant aperture is best for checking the impact of the fracture network geometry on fluid flow and effective permeability. The assigned fracture aperture was translated to a fracture permeability using equation 6.5 (parallel plate law):

$$k_{frac} = \frac{e^2}{12} \quad (6.5)$$

Where, k_{frac} is the fracture permeability [m^2], and e is the fracture aperture [m]. The transmissibility field was calculated using the k_{frac} on each fracture node and the k_{mat}

Interpreted Fracture Networks



Simulated Fracture Networks

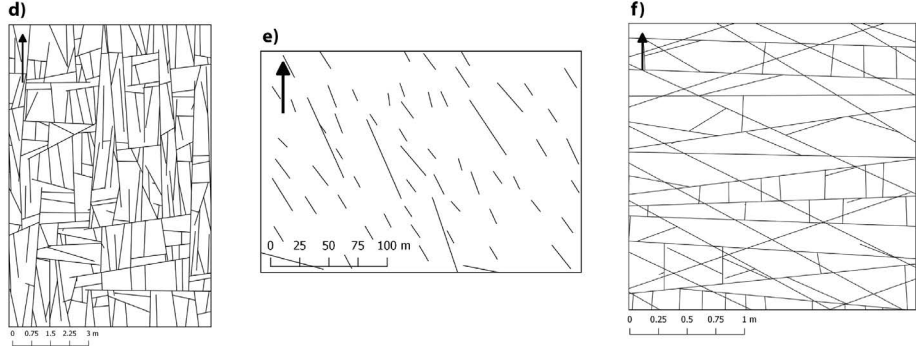


Figure 6.8: Interpreted fracture networks and their simulated counter-parts. a) Orthogonal fracture network interpretation (Whitby Mudstone, UK). Interpretation taken from [Houben et al. \[2017\]](#). b) Interpretation of a fractured carbonate platform (Parmelan, France) taken from [Prabhakaran et al. \[2019\]](#). c) Fracture network geometry observed in the Bristol Channel Basin (UK) (interpretation modified after [Belayneh and Cosgrove \[2004\]](#)). d-f) Geologically constrained simulations of the three fracture network interpretations. See appendix B for the input settings of the simulations, and see the original articles for additional information on the three different outcrops.

in each mesh element (see [\[Karimi-Fard et al., 2004\]](#) for additional details). Fluid flow through the transmissibility field was modelled in ADGPRS (Stanford University’s Automatic Differentiation-based General Purpose Research Simulator) ([\[Karimi-Fard et al., 2004\]](#)), by solving the incompressible single-phase Darcy equation for a differential pressure field (equation 6.6):

$$q = -\frac{k}{\mu} \nabla p \tag{6.6}$$

Where, q is the modelled flux (m^2/s), μ is viscosity ($Pa \cdot s^{-1}$) and k is the local permeability (m^2) (i.e. k_{frac} or k_{mat}), and ∇p is the pressure gradient (Pa).

For the presented simulations, an initial N-S pressure difference of 10.0 (Bar) (1.0e6 (Pa)) was generated by placing injector wells (BHP = 10 (Bar)) and production wells (BHP = 0 (Bar)) on each mesh element positioned on the Southern and Northern boundary of

model, respectively. Further, the initial pressure in each matrix cell was set at 5.0 (Bar). Each simulation was run for 100 days to ensure that steady state conditions were reached (i.e. injection is production).

To assess the impact that fractures have on fluid flow, an effective permeability was calculated for each simulation. This was done by implementing the simulated volume fluxes in each production well in to equation 6, and the calculated value is representative for both fracture and matrix flow within the modelling domain [Bisdorn et al., 2017b, Hardebol et al., 2015, Nick and Matthäi, 2011].

The results show that for all simulations, the fractures have a high impact on the modelled fluid flow and effective permeability calculations (Figure 6.9, Table 6.4). Further, the results clearly portray the impact of fracture connectivity. For example, both the interpreted - and geologically-constrained DFN's show a high connectivity (Figure 6.7), and due to this high connectivity, the pressure front flow velocities through the fractures are relatively homogenous. Additionally, the effective permeability calculations indicate that the effective contribution of the fractures is similar (Table 6.4). The randomly populated DFN showed less fracture connectivity, thereby resulting in different fluid flow behaviour with respect to the interpreted - and geologically-constrained simulations (Figure 6.9). For this simulation, flow is mainly controlled by the connected fracture clusters, resulting in a more serrated pressure field and low flow velocities in isolated fractures (i.e. all flow goes through the fracture clusters) (Figure 6.9e and f). In addition, the lower fracture connectivity also results in a lower effective permeability for the modelling domain (Table 6.4). Therefore, the presented models indicate that incorporating geological observations in DFN simulations, results in better estimations of the effective permeability and fluid flow patterns of (Figure 6.9, Table 6.4).

Simulation	Matrix permeability (k_{mat}) (mD)	Fracture aperture (e) (mm)	Effective permeability (k_{eff}) (mD)	$\frac{k_{eff}}{k_{mat}}$
Interpretation (reference)	5.00	0.10	2956.35	591.27
Geologically controlled simulation	5.00	0.10	3216.71	643.34
Randomly populated simulation	5.00	0.10	1954.84	390.97

Table 6.4: Effective permeability and production results for all three fluid flow simulation models (see figure 8).

6.4 Discussion

6.4.1 An open source code for creating statistically or geologically constraint 2D DFN's

Fracture network geometries often show a clear hierarchical patterns, topology and fracture spacing relationships. On outcrops, fracture networks exhibit a wide variety of hierarchical and topological patterns such as two tier orthogonal networks [Bai et al., 2002, Belayneh and Cosgrove, 2004, Gross, 1993, Hanke et al., 2018, Odling et al., 1999], fractures showing a nested or coeval hierarchy [Boersma et al., 2019b, Houben et al., 2017, Olson, 2007] and multiscale networks [Hardebol et al., 2015, Odling et al., 1999, Strijker et al., 2012]. Furthermore, fluid flow simulations and sub-surface case studies have shown that the geometry and connectivity of fracture networks is of great importance

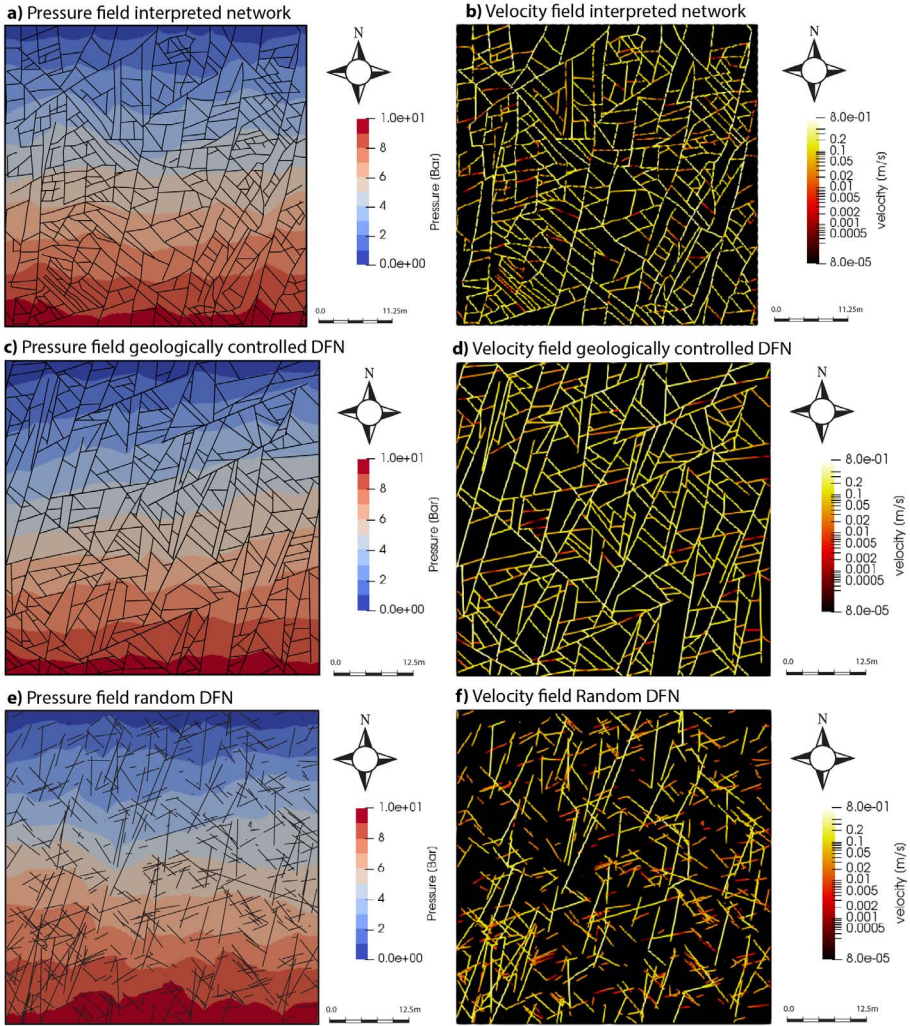


Figure 6.9: Fluid flow simulation results. a-b) Acquired pressure and velocity field for the interpreted fracture network, respectively. c-d) Acquired pressure and velocity field for the geologically controlled fracture network. e-f) Acquired pressure and velocity field for the randomly populated fracture network. Note that the flow velocity is on a log scale.

to fluid flow behaviour and effective permeability calculations, especially when considering tight matrix rocks [Bisdorn et al., 2017b, Healy et al., 2017, Houben et al., 2017, Toublanc et al., 2005].

In this study we have presented FracSim2D, a DFN simulator which can incorporate these geological fracture network characteristics. In general, the tool works similar with respect to conventional methodologies, e.g. 2D fracture networks are generated using statistical relationships and random fracture placement. However, FracSim2D also accounts for characteristics such as, hierarchy and spacing. The DFN simulations accounting for these geological controls show a much closer resemblance to their outcrop counterparts. Further, the output of FracSim2D are shapefiles which can easily be analysed using tools such as FracPaq [Healy et al., 2017] and NetworkGT [Nyberg et al., 2018]. The shapefiles can also be meshed and implemented in to fluid flow simulators such as ADGPRS [Karimi-Fard et al., 2004], CSMP [Matthäi et al., 2007] or DARTS (Delft Advanced Research Terra Simulator) [Khait and Voskov, 2018], so that the impact of different network geometries and hierarchies on fluid flow behaviour can be assessed.

6.4.2 Main limitations of the current version of the code

Although showing promising results, FracSim2D has some limitations. For instance, due to crude methodology used (i.e. trial and error), simulating large fracture networks with 1) high fracture intensities, 2) multiple hierarchical levels and 3) and strict spacing relationships, will take a relatively long time to complete, especially with respect to randomly populated DFN's. Further, in extreme cases with high fracture intensity and strict geological constraints (i.e. intersection and spacing rules), the algorithm has difficulties in finding suitable locations for fracture placement. This process repeats itself for each to be placed fracture, resulting in simulations which essentially don't converge. For the current version of the code, this issue can only be resolved by placing less strict geological rules to the model or by changing the fracture intensity limit.

Further, the current version of the code does not allow for the implementation of fracture intersection probabilities (i.e. the likelihood that two fractures will intersect or abut). This implies that fracture network geometries showing mixed topologies (e.g. 50 % crossing fractures and 50 % abutting fractures) are difficult to model using FracSim2D. We are planning to incorporate intersection probabilities in future versions of the code.

Another limitation is with changing fracture characteristics over the modelling domain. FracSim2D uses fixed behaviour for each fracture characteristic such as: 1) fracture intensity, 2) fracture length and orientation behaviour, or 3) topology and hierarchy. On outcrops, these characteristics can change. For example, based on its proximity to large scale features such as faults or fold hinges, the fracture intensity, dominant orientation and/or intersection probability of each fracture set can change drastically [Bisdorn et al., 2017a, Hanke et al., 2018]. These local deviations cannot be modelled by the current version of FracSim2D. In future versions of the code we are planning to account for varying fracture characteristics within the modelling domain. This will be done by implementing an additional loop to the main workflow (Figure 6.1), so that laterally varying fracture characteristics (intensity, orientation, abutment and spacing) can be incorporated.

6.4.3 Potential applications for field and reservoir studies

While having some limitations, we argue that the algorithm has some potential applications for field and reservoir studies. For instance, the simulated DFN's can be used to test the impact of that different hierarchies, connectivities of topologies could have on fluid flow and the effective permeability. An example of such a study was done by [Hardebol et al., 2015]. This study used an earlier version of FracSim2D in order to address the impact of the fracture connectivity and topology on the effective permeability. Their results showed that the connection intensity greatly impacted the calculated effective permeability.

Apart from sensitivity studies, we think that FracSim2D can also be used for generating DFN's on a reservoir/field scale, by combining this algorithm with other workflows such as Multiple Point Statistics [Bruna et al., 2019]. Here, we argue that the different training images for each specific elementary zone can be generated using FracSim2D. These training images are then implemented in the MPS workflow developed by Bruna et al. [2019] in order to generate a geologically constrained DFN's for structurally complex outcrops or reservoirs. However, it should be noted that both modelling tools work in the 2D domain and this implies that this methodology cannot be used for modelling large scale 3D DFN's.

6.5 Conclusions

In this chapter we present FracSim2D, a new tool for simulating geologically constrained 2D DFN's. This algorithm uses a new workflow of iterative and statistically controlled random fracture placement and user-defined geological rules, in order to generate a wide variety of geologically feasible fracture network geometries. The user defined geological rules include fracture hierarchy, topology and buffer distance (parameter used for modelling spacing). The resulting simulated fracture networks are georeferenced shapefiles which can easily be analysed using statistical packages or implemented in to fluid flow simulations. The different python scripts and corresponding user documentation have been made publicly available via the 4TU data service.

To exemplify the methodology, we have used the algorithm to generate multiple simulations using data from four different outcrop analogues. The results show that by implementing geological controls in to the modelling workflow, the observed hierarchy and topology of the interpreted fracture networks were captured by the simulated DFN's. Furthermore, fluid flow modelling results of both interpreted and simulated DFN's indicated that geologically constraint simulations, better captured the effective permeability and fluid flow behaviour of original interpretation. Finally, we believe that by combining this algorithm with other workflows such as MPS, the development of reservoir scale and geologically constrained 2D fracture networks can be realized.

Data availability

The FracSim2D code, guide and examples used in this chapter are freely available and can be found via the following DOI: <https://doi.org/10.4121/12987584.v1>.

Input settings for the Whitby, Parmelan and Bristol channel simulations

Simulation	FSET	Fracture level	P21 Limit ($\frac{m}{m^2}$)	Length distribution	Buffer distance (m)	Orientation distribution	Placement constraint
Sim: Whitby	FSET1 (HO)	1	0.962	Fixed: 1.0m	0.5	VM*: $\mu = -1.493, \kappa = 100$	NHFI, Coeval
	FSET2 (HO)	1	0.352	Fixed: 5.0m	0.5	VM: $\mu = 78.02, \kappa = 25$	NHOFI, Coeval
	FSET1 (LO)	2	1.715	Fixed: 2.5m	0.15	VM: $\mu = 1.62, \kappa = 35$	NHOFI, Coeval
	FSET2 (LO)	2	0.644	Fixed: 2.5m	0.15	VM: $\mu = 88.90, \kappa = 25$	NHOFI, Coeval
Sim: Parmelan	FSET1	1	0.0216	Power-law: $a = 3.0, \min L = 10m \text{ Max } L = 60m$	10.0	VM*: $\mu = 151, \kappa = 60$	NELFI
	FSET2	1	0.001	Uniform: $\min L = 30m, \text{ Max } L = 70m$	50.0	VM: $\mu = 90, \kappa = 10$	NELFI
Sim: Bristol Channel	FSET1	1	4.234	Fixed: 10.0m	0.15	VM: $\mu = 90, \kappa = 250$	NHOFI
	FSET2	2	1.117	Fixed: 7.5m	0.15	VM: $\mu = 0, \kappa = 250$	NHOFI
	FSET3	3	2.530	Fixed: 5.0m	0.25	VM: $\mu = 113, \kappa = 100$	NSI
	FSET4	4	1.000	Fixed: 5.0m	0.25	VM: $\mu = 71.6, \kappa = 100$	NSI
	FSET5	5	0.500	Fixed: 1.0m	0.1	VM: $\mu = 113, \kappa = 100$	NHOFI
	FSET6	5	0.500	Fixed: 1.0m	0.1	VM: $\mu = 71.6, \kappa = 100$	NHOFI

Table 6.5: Input settings for the Whitby, Parmelan and Bristol channel simulations (see figure 7 for the results). Note that, VM = Von Mises, NHOFI = Non higher order fracture intersection, NELFI = Non equal level fracture intersect, NSI= No self intersect, Coeval = Can't intersect fracture of a higher or the same order

7

THE IMPACT OF FRACTURES ON HEAT EXTRACTION FROM TIGHT TRIASSIC RESERVOIRS IN THE WEST NETHERLANDS BASIN

The positive impact that natural fractures can have on geothermal heat production from low permeability reservoirs has become increasingly recognized and proven by subsurface case studies. In this study, we assess the potential impact of natural fractures on heat extraction from the tight Lower Buntsandstein Subgroup targeted by the recently drilled NLW-GT-01 well (West Netherlands Basin (WNB)). We integrate: 1) reservoir property characterisation using petrophysical-analysis and geostatistical-inversion, 2) image log- and core interpretation, 3) large-scale seismic fault extraction and characterisation, 4) Discrete Fracture Network (DFN) modelling and permeability upscaling, and 5) fluid-flow and temperature modelling. First, the results of the petrophysical analysis and geostatistical inversion indicate that the Volpriehausen has almost no intrinsic porosity or permeability in the rock volume surrounding the NLW-GT-01 well. The Detfurth and Hardegsen sandstones show better reservoir properties. Second, the image-log interpretation shows predominately NW-SE orientated fractures, which are hydraulically conductive and show log-normal and negative-power-law behaviour for their length and aperture, respectively. Third, the faults extracted from the seismic data have four different orientations: NW-SE, N-S, NE-SW and E-W, with faults in proximity to the NLW-GT-01 having a similar strike to the observed fractures. Fourth, inspection of the reservoir scale 2D DFN's, upscaled permeability models and fluid-flow/temperature simulations, indicate that these potentially open natural fractures significantly enhance the effective permeability and heat production of the normally tight reservoir volume. However, our modelling results also show that when the natural fractures are closed, production values are neglectable. Finally, because active well tests were not performed prior to the

abandonment Triassic formations targeted by the NLW-GT-01, no conclusive data exists on whether the observed natural fractures are connected and hydraulically conductive under sub-surface conditions. Therefore, based on the presented findings and remaining uncertainties, we propose that measures which can test the potential of fracture enhanced permeability under sub-surface conditions should become standard procedure in projects targeting deep and potentially fractured geothermal reservoirs.

7.1 Introduction

In the Netherlands, geothermal energy is regarded to be a viable contribution to the required sustainable energy mix, and it is estimated that the total recoverable heat from sedimentary aquifers is 55 times larger than the Dutch annual heat consumption [Kramers et al., 2012, Willems, 2017]. Because of this potential, the Dutch government wants to increase geothermal production to 50 peta joules per year in 2030, which is equivalent to the annual heat consumption of 1 million Dutch households.

A good location for geothermal energy development is the West Netherlands Basin (WNB) (Figure 7.1), which is densely populated, thereby having a high energy demand. Furthermore, large amounts of energy are believed to be stored in the deep aquifer layers [Kramers et al., 2012, Willems, 2017]. The WNB has also been heavily explored with regard to hydrocarbon production, making the regional geology and depth of the different aquifers well established [Duin et al., 2006, Kombrink et al., 2012, Pluymaekers et al., 2012, Van Balen et al., 2000, Wong et al., 2007]. Another reason why the WNB is attractive for geothermal energy development is that large quantities of geological and geophysical data (e.g. seismic data, well data and geological models) are freely available online (www.nlog.nl) [Duin et al., 2006, Kombrink et al., 2012, Willems and Nick, 2019].

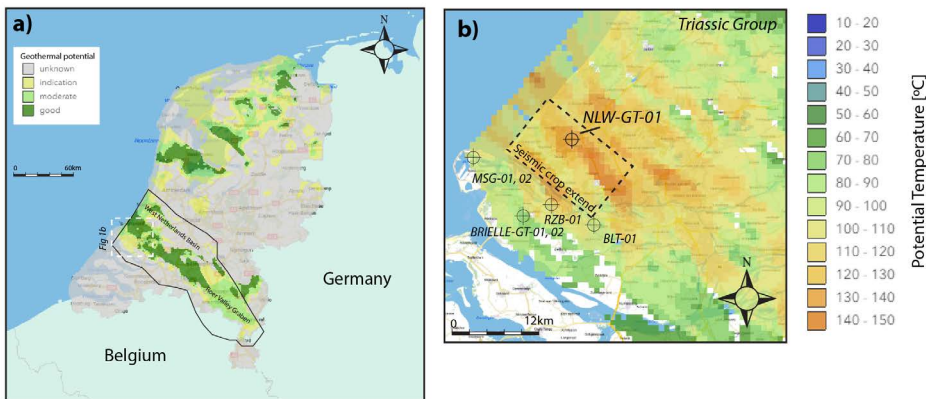


Figure 7.1: a) map of the Geothermal potential of the Netherlands. Black line highlights the extent of the Roer Valley Graben and West Netherlands Basin. b) Expected temperature for the Triassic aquifers in the West Netherlands Basin (study area). Also note the location of different wells which have drilled the Lower-Triassic formation and the extend of the 3D seismic volume used in this study. The maps have been generated using ThermoGIS (www.thermogis.nl), see Bonté et al. [2012], Kramers et al. [2012], Pluymaekers et al. [2012], Van Wees et al. [2012], Vrijlandt et al. [2019] for additional details. Location of the NLW-GT-01 and other wells targeting the Lower-Triassic formation have also been highlighted.

The WNB contains two aquifers which are generally considered as good candidates for heat extraction, namely: 1) the Nieuwekerk Formation (Schieland group, Upper-Jurassic to Lower-Cretaceous) and 2) the Main Buntsandstein Group (Lower-Triassic) [Kramers et al., 2012]. Up to 2018, thirteen doublet systems have been realised in the WNB, with most wells targeting the Nieuwekerk Formation, which generally shows good reservoir properties and doublet capacities [Willems and Nick, 2019].

While most geothermal wells in the WNB target the low risk Nieuwekerk forma-

tion, the deeper positioned Main Buntsandstein Subgroup (Volpriehausen, Detfurth and Hadsegsen) (Lower Triassic) is increasingly being recognized as a high potential hot sedimentary aquifer, with expected temperatures ranging between 80 °C and 140 °C (Figure 7.1b) [Kramers et al., 2012]. However, as a result of its relatively complex geological and diagenetic history, the Triassic is also regarded as a high-risk target. This is for example observed by multiple hydrocarbon exploration - and geothermal wells (e.g. BRIELLE-GT-01 and -02, RZB-01, BTL-01, MSG-01 and -02 (Figure 7.1b)). The data from these wells show a wide variety in measured porosities and permeabilities (www.nlog.nl), with wells positioned at the basin fringe generally having better reservoir properties with respect to wells located more towards the basin centre.

The complexity of the Lower-Triassic was further exemplified by a recent geothermal exploration well (NLW-GT-01), which targeted the Triassic sandstones within the basin centre, expecting temperatures surpassing 120 °C (Figure 7.1b). Although the test results showed temperatures of 120 °C, the reservoir quality was much poorer than anticipated (i.e. porosity \leq 5.0 %, permeability \leq 0.1 mD). Because of these poor reservoir properties, the NLW-GT-01 well was plugged and abandoned above the Triassic and the well is now activity producing from the more permeable Lower-Cretaceous Schieland group.

While showing poor reservoir quality, image logs and core samples taken from the NLW-GT-01 well did show that the targeted reservoir layers are heavily fractured, and multiple studies have shown that these natural features can significantly enhance the effective permeability of a normally tight rock, even under sub-surface conditions [Holdsworth et al., 2019, Nelson, 2001, Toubanc et al., 2005]. For this reason, the characterizing and modelling of natural fracture networks has become an integral component in predicting fluid flow patterns and the optimizing of hydrocarbon production from structurally complex/tight reservoirs [Laubach et al., 2019].

Natural fracture and fault systems are also known to influence/enhance geothermal heat production. For example, in the Upper Rhine Graben most geothermal projects exploit heat which is stored in fluids positioned in large and connected fault and fracture networks [Vidal and Genter, 2018]. Here, data from multiple geothermal wells targeting fractured intervals have shown that natural fractures/faults significantly enhance the effective permeability of normally impermeable basement rocks, making the production of heat possible [Schill et al., 2017, Vidal et al., 2017, Vidal and Genter, 2018].

The aim of this study is to investigate and model the potential impact of natural fractures on geothermal heat extraction from the Main Buntsandstein Subgroup (Volpriehausen, Detfurth, and Hadsegsen) targeted by the recently drilled NLW-GT-01 well (Figure 7.1b). This is done by expanding upon seismic reservoir characterisation - and Discrete Fracture Network (DFN) modelling methodologies commonly used in the petroleum industry. This study is structured as follows: First, the geological and structural setting of the study area are presented. Second, a reservoir scale property model is generated using petrophysical data analysis and geostatistical seismic inversion. Third, the faults and fractures are characterized using image log - and core interpretation and seismic discontinuity analysis. Fourth, three reservoir-scale 2D DFN's are generated, using the acquired fracture/fault data and three different aperture models (power-law -, length-based - and stress-based aperture). Fifth, the modelled DFN's, are upscaled to three fracture permeability models. Sixth, the acquired results are integrated into cou-

pled fluid-flow and temperature simulations, such that the impact of natural fractures on geothermal heat extraction can be investigated. Finally, the implications of the results, modelling workflow and assumptions are discussed.

7.2 Geological setting and geothermal energy within study area

7.2.1 Present-day geometry of the West Netherlands Basin (WNB)

The WNB is located in the Western part of the Netherlands and together with the Roer Valley Graben (RVG) and Broad Fourteens Basin (BFB), forms a large failed rift system (Figure 7.2a). From the Late-Carboniferous onward, the WNB experienced several rifting (e.g. (Triassic and Late-Jurassic) and compression events (e.g. Alpine (Late-Cretaceous to Early-Tertiary)) [de Jager, 2007, Van Balen et al., 2000]. The present-day geometry of the WNB is characterized by up to 5000m of Permian to Tertiary deposits and a connected fault network of WNW-ESE to NNW-SSE striking features [de Jager, 2007, Kombrink et al., 2012, Worum et al., 2005]. (Figure 7.2a-b). In the Jurassic to Triassic levels, secondary faults striking N-S and E-W are also observed [de Jager, 2007]. Due to the NNE-SSW Late-Cretaceous to Early-Tertiary compression events, most of the faults within the WNB have been inverted via dextral and sinistral transpression forming large inversion highs and positive flower structures at the base of the Cretaceous (e.g. Figure 7.2b) [de Jager, 2007]. Significant oil and gas accumulations, sourced by the Jurassic Posidonia Shale and Carboniferous coal layers, can be found within these inverted structures [de Jager et al., 1996, Van Balen et al., 2000]. Additionally, these compression events resulted in significant uplift and erosion (down to the Jurassic near the inversion axis) (Figure 7.2b) [de Jager, 2007].

7.2.2 Stratigraphy and diagenesis of the Main Buntsandstein Subgroup (Early-Triassic) in the WNB

The Main Buntsandstein Subgroup is composed of the Volpriehausen, Detfurth and Hadsegsen formations. These formations were deposited under fluvial and aeolian conditions (Paleolatitude 20 to 25 °N) and have a combined thickness ranging between 100-150m [Geluk, 2005]. The Volpriehausen is generally subdivided into a lower and an upper part. The lower part is comprised of fluvial sandstones which were sourced from the London-Brabant Massif. Thicker and coarser grained sandstones concentrate in the southern basin fringes (i.e. close to the London-Brabant Massif), with more distal parts being dominated by fine grained sandstones and playa lake deposits [Geluk, 2005]. The Upper-Volpriehausen formation is comprised of a succession of lacustrine siltstones and claystones, with subordinate sandstone layers [Geluk, 2005]. The overlying Detfurth formation is relatively thin and is generally composed of sandstone layers followed by a succession dominated by claystones [Geluk, 2005]. The Hardegsen formation is an alternation of sandstone and siltstone strata [Geluk, 2005].

The Main Buntsandstein Subgroup is characterized by two diagenetic events, the earliest of which occurred during or right after deposition [Purvis and Okkerman, 1996]. This diagenetic event mainly resulted in halite and anhydrite cementation, illite and clayey grain coating, and ferroan dolomitisation, and is believed to be related to the infiltration of meteoric waters [Purvis and Okkerman, 1996]. This event was predominant in the Volpriehausen formation and generally resulted in a significant reduction of

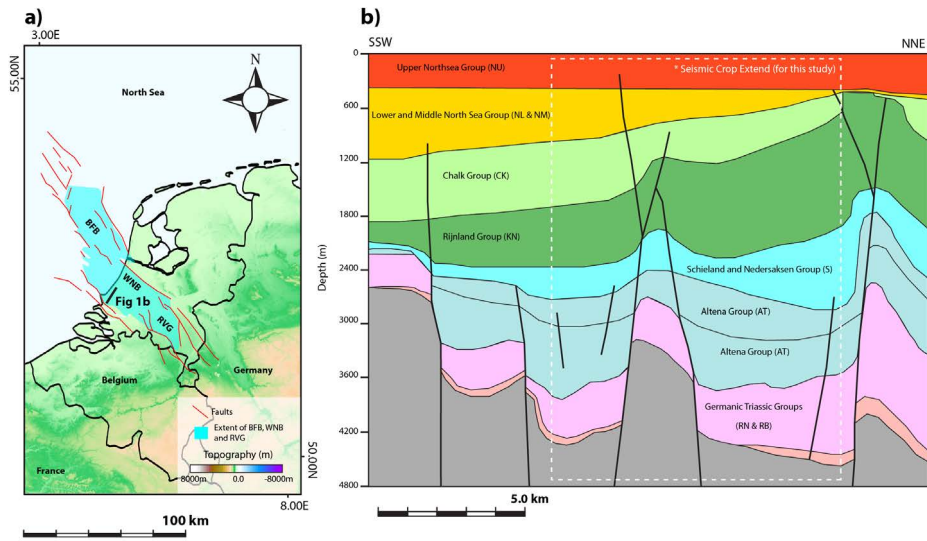


Figure 7.2: a) Map of the extend of the BFB, WNB and RVG within the Netherlands. Coordinates are in WGS 84. Basin geometry and faults after de Jager [2007]. Note that the cross section (Figure 2b) is depicted by the black line. b) SSW-NNE Cross section through the study area (WNB). Faults locations and geometry after Van Balen et al. [2000]. Cross-section has been created using the DGM-deep model [Kombbrink et al., 2012]. See Duin et al. [2006], Van Balen et al. [2000] for details on the nomenclature and age of the different formations.

the initial porosity and permeability (i.e. depositional pore space became cemented) [Purvis and Okkerman, 1996]. The second phase of diagenesis occurred during the main alpine inversion events (Late-Cretaceous to Early Paleogene), where areas which recorded strong exhumation experienced renewed surface conditions, causing the dissolution of the anhydrite and halite cements, and a general increase in the effective porosity and permeability of the Triassic formations [Matev, 2011].

7.2.3 Previous reporting on the data extracted by NLW-GT-01

The data extracted by the NLW-GT-01 well has been extensively studied as part of the DE-STRESS program and most of the reporting is freely available (www.nlog.nl). Core analysis showed that primary porosities and permeabilities of the cored interval of the Main Buntsandstein Subgroup are very poor, with measurements ranging between 1.4 % to 3.9 % and 0.00 mD to 0.02 mD, respectively. These poor properties are mainly attributed to the primary depositional texture (very fine sands), compaction and excessive cementation of dolomite, quartz and anhydrite. The measured porosities and permeabilities are similar to other wells targeting the Main Buntsandstein Subgroup in the Northern of the WNB (e.g. VAL-01, MKP-10, Q13-04-S1 and Q13-07-S2), which also showed significant reduction of primary properties due to cementation. The presence of natural fractures is also reported. However, no definitive conclusions were reached on the conductivity of the observed structural features. Finally, due to gas infiltration and the poor reservoir properties the decision was made to plug and abandon the NLW-GT-01 above the

Triassic without performing a conventional well test.

7.2.4 Other mentions of natural fractures within the Lower-Triassic formations of the WNB

Apart from the NLW-GT-01 well, other wells have also encountered fractured intervals within the Lower-Triassic formations of the WNB. For instance, image log and core data taken from the VAL-01 well showed significantly fractured intervals in proximity to a larger normal fault. In total, 288 closed – and 22 partially open fractures were observed and the interpreted features showed an overall NW-SE strike and dips ranging between 50° and 90°. Additionally, core photos taken from the PKP-01 well showed evidence of partially-open and non-cemented fractures being present within the Lower-Triassic formations. Moreover, data from the P18-A-06 and Q13-07 wells indicated that reported mud losses could be attributed to fractured and faulted areas, which is a good indicator that these natural features locally enhance permeability [Matev, 2011]. However, while mentions of open fractures exists, most reported fractures are cemented or closed.

7.3 Data and methods

7.3.1 The dataset, velocity model and 2D modelling domain

This study focuses on the Triassic formations in the area surrounding the recently drilled NLW-GT-01 well (Figures 1 and 3). The main input data consists of reprocessed 3D seismic amplitude data, the VELOMOD-2 layer-cake velocity model, petrophysical wireline logs, a conductivity image log, and 30 m of core data (Figures 3a-b).

The 3D seismic data is a reprocessed version of the 3D seismic volume L3NAM1990C and is available for research purposes upon request (courtesy of TNO) (Figure 3). The reprocessing of the seismic data has been done by the Nederlandse Aardolie Maatschappij (NAM) in 2011. To speed up the geophysical computations, we have cropped the seismic to the extent shown in figure 3a.

For the velocity model we use input data from VELOMOD-2, which is a statistical layer-cake model using all available well data and the main horizons within The Netherlands [van Dalfsen et al., 2006]. In this study, the different interval velocities ($v_{\text{int}(i)}(x, y, z)$) for the main horizons within the WNB (see figure 2b) were calculated using equation 7.1:

$$v_{\text{int}(i)}(x, y, z) = v_{0(i)}(x, y) + k_{(i)} \left(Z(x, y)_{(i-1)} + \frac{Z(x, y)_{(i)} - Z(x, y)_{(i-1)}}{2} \right) \quad (7.1)$$

where, $v_{\text{int}(i)}(x, y, z)$ (m/s) is the interval velocity for layer i , $v_{0(i)}(x, y)$ (m/s) is the initial velocity for layer i , $k_{(i)}$ (1/s) is the slope in the in the velocity increase with depth and $Z(x, y)_{(i-1)}$ and $Z(x, y)_{(i)}$ are the depth surfaces for layer i and the layer above. More information on the velocity model and the data used can be found in the see supplementary materials or at <https://www.nlog.nl/en/seismic-velocities>.

Two wells which targeted the Main Buntsandstein Subgroup were used, namely: 1) NLW-GT-01 and 2) DE-LIER-45 (Figure 7.3). From the NLW-GT-01 well, wireline logs, the conductivity image log (FMI-8 Fullbore-formation-micro-imager (Schlumberger)), and core data were used for the petrophysical analysis, fracture interpretation and reservoir modelling. The depth of the different formations in the NLW-GT-01 well was based on

the interpretation done by TNO in 2018 (Figure 7.3b) (see supplementary materials or www.nlog.nl). The DE-LIER-45 well was used for wavelet extraction and synthetic seismic generation (see supplementary materials).

In this study, the reservoir property, DFN and temperature modelling domain is the area surrounding the NLW-GT-01 well (Figure 7.3a). This 2D domain has grid dimensions of ($dx = 1469$ m, $dy = 1371$ m and $z = 3940$ m) and cell dimensions of 10 by 10 m. All modelling results (i.e. reservoir properties, DFN's, and temperature/energy data) presented in this study will be constrained to this area.

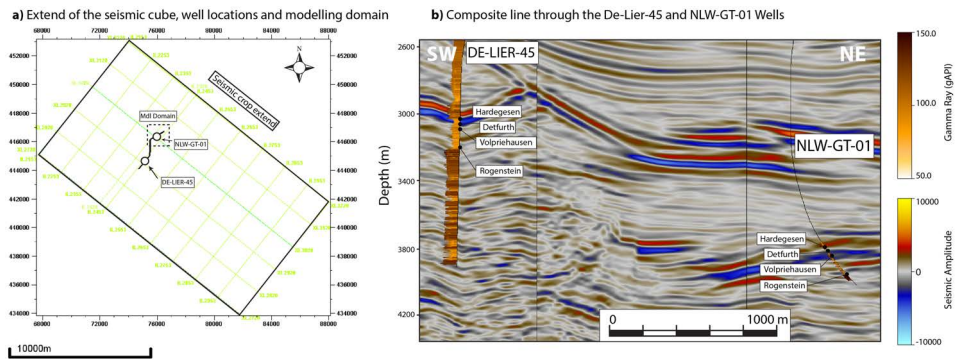


Figure 7.3: a) Extent of the seismic crop, location of the NLW-GT-01 and the DE-LIER-45 wells and location of the modelling domain. b) Composite line through the two wells. Here and in all other figures, the coordinate system used is RD-Amersfoort (EPSG: 28992).

7.3.2 General workflow

The workflow and results presented in this study consists of three main parts, namely:

1. Reservoir property (porosity and permeability) characterisation using i) petrophysical wireline analysis, ii) geostatistical inversion for acoustic properties, and iii) porosity and permeability computations for the modelling domain (Figure 7.4);
2. Fracture/fault characterisation using i) image log and core interpretation, ii) seismic attribute analysis (Figure 7.4);
3. Assessment of the impact of natural fractures on geothermal heat extraction from the Lower-Triassic successions, using: i) DFN modelling, ii) fracture aperture modelling using three different scenarios, iii) permeability upscaling, and iv) fluid flow and temperature modelling (Figure 7.4).

7.3.3 Petrophysical analysis

Petrophysical logs (bulk/grain density, S- and P-sonic-velocities, gamma ray and effective porosity (HILT)) from the two wells (NLW-GT-01 and DE-LIER-45) were taken from the Dutch repository for subsurface data (www.nlog.nl). From these different wireline logs, the P- and S-Impedance, P- and S-Velocity and the total and effective porosity

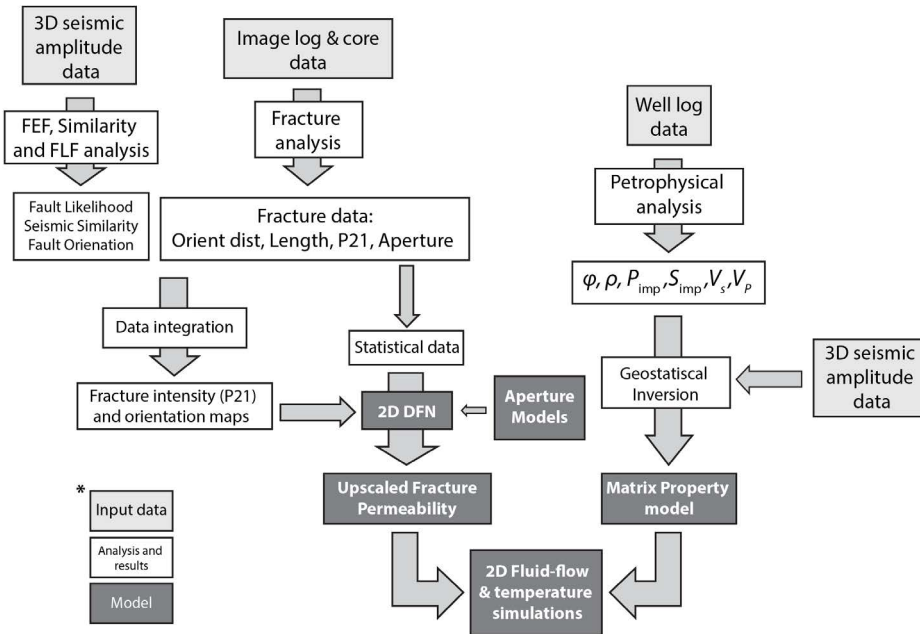


Figure 7.4: Overall workflow used in this study. The main steps involve 1) Petrophysical analysis, 2) Geostatistical inversion, 3) Matrix property calculations, 4) Fracture interpretation, 5) Seismic discontinuity analysis, 6) DFN modelling and permeability upscaling, and 7) Fluid flow - and temperature modelling. See text for additional details on the input data and each analysis/modelling step.

were computed. These different datasets were then used for i) finding correlations between the different elastic and reservoir properties, ii) creating a representative wavelet and synthetic seismics, iii) well-to-seismic correlations, and iv) geostatistical inversion (Figure 7.4). More information on the computations and results can be found in the supplementary materials.

7.3.4 Geostatistical inversion and property modelling

The seismic and well data were integrated using geostatistical inversion, which allows for the generation of high-frequency property models [Delbecq and Moyen, 2010, McCranks et al., 2009] (Figure 7.4). The tool used in this study was the StatMod package in Jason (developed by CGG). This tool uses 1) statistical functions (Probability Density Functions and Variograms) describing the petrophysical properties observed within wells, 2) a tailored seismic wavelet, 3) seismic amplitude data (in TWT), 4) wavelet deconvolution, 5) Bayesian interference and 6) a Markov-Chain-Monte-Carlo sampling algorithm (e.g. Sams et al. [2011]), in order to statistically invert seismic amplitude data to different acoustic and/or petrophysical properties (e.g. acoustic impedance or rock density) (Figure 7.4). The StatMod algorithm also aims at honouring the well and seismic data by minimizing the residual between the modelled synthetic and the original seismic data.

In this study, we inverted for the acoustic impedance using the time-converted post-

stacked seismic-amplitude data, extracted wavelet and computed P-Impedance wireline log (see supplementary materials for more information). The model had lateral grid dimensions equal to the seismic voxel spacing (i.e. 20 by 20 m). The vertical spacing was set at 0.5 milliseconds, so that detailed petrophysical changes could be incorporated in the geostatistical inversion workflow. The NLW-GT-01 input well was assumed to be 'blind', so that the petrophysical well data were only used as statistical input and not as hard constraining data. For the presented results, the input settings and statistical functions were tailored, so that the match between the inverted results, blind well data and original seismic data had a qualitative fit and no large discrepancies. See appendix A for more information on the used settings.

From the inverted impedance data, the porosity (effective and total) and density were computed using the relations determined from the petrophysical analysis (Figure 7.4). The effective- and total porosities were then used to calculate the matrix permeability within the modelling domain using measurements from a core hot shot analysis done on the NLW-GT-01 core (measurements done by Panterra, report is available on nlog) (equation 7.2):

$$\ln(K_{\text{mat}}) = C + D\phi \quad (7.2)$$

Where C and D are constants and are set at -2.512 and 0.233, respectively. K_{mat} is the computed matrix permeability in mD. ϕ is the porosity (effective or total) in percentage.

7.3.5 Borehole image log and core interpretation and fracture characterisation

The aforementioned conductivity image log of the NLW-GT-01 well was interpreted using Schlumberger's wellbore software program Techlog (Techlog®). The image log has a total length of 170m (MD: 4205 m to MD: 4375 m), covering the full Volpriehausen formation and parts of the Detfurth and Rogenstein formations (Rogenstein is underlying the Volpriehausen). Apart from the image log, 30 m of core (MD: 4250 m to MD: 4280 m) was analysed and interpreted using PanTerra's core interpretation tool (Electronic Core Goniometry®) (see supplementary materials for the interpretation).

On the image log, fracture planes were interpreted as features showing a distinct sinusoid shape and an increase in conductivity with respect to the surrounding rock matrix. Furthermore, the interpretation was guided by the resistivity log and the available core interpretation. One distinct characteristic of the NLW-GT-01 well data is that the conductivity image log shows much more interpretable discontinuities than core data (for the same interval). These additional discontinuities observed within the FMI data have been interpreted as being hydraulically- or drilling-induced fractures. For this reason, we have interpreted the image log using a very conservative methodology. This implies that only features which were visible in the core or show a full sinusoid were interpreted.

From the interpreted data, the fracture intensity (P21) along the NLW-GT-01 well was calculated using two different sampling windows of 2.5m and 10m, respectively. The larger sampling window was chosen to compare the interpreted fracture intensity to discontinuities observed in the seismic signal.

Characteristics such as height, length, and aperture were calculated for all the interpreted fractures. The fracture height was assumed to be equal to the measured dip-height (m). The fracture length was calculated from the computed heights, assuming a constant aspect ratio (length/height) of 4.0, which is commonly observed in outcrop analogues (e.g. [Schultz and Fossen \[2002\]](#)). However, it should be noted that assigning a constant aspect ratio is a significant assumption which may introduce non representative results. Fracture aperture computation requires image logs to be calibrated, which for this study was done using the mud-resistivity and by manually fitting a calibration curve (see supplementary materials and the Techlog user documentation for additional information). From the calibrated data, the fracture aperture was calculated using the aperture equation proposed by [Luthi and Souhaite \[1990\]](#) (equation 7.3):

$$W = cAR_m^b R_{x0}^{1-b} \quad (7.3)$$

where, W is the fracture width (mm) at each location along the fracture, A is excess current which can be injected into the formation divided by the voltage, R_{x0} is the formation resistivity, R_m is the mud resistivity, and c and b are tool-specific and numerically derived values (for FMI-8: $c = 0.004801\mu\text{m}$, $b = 0.863$) [[Luthi and Souhaite, 1990](#)]. From the fracture width (W) the mean and hydraulic aperture were calculated using the standard settings in Techlog (see Techlog user documentation for additional information).

7.3.6 Seismic discontinuity analysis

Discontinuities detectable on the reprocessed seismic (Figure 7.5a) were automatically extracted using three volume attributes available in OpendTect (OpendTect[®]). The extracted seismic discontinuities were subsequently used as input for our DFN models (Figure 7.4).

The first step was to ‘enhance’ the input seismic data for discontinuity analysis using a collection of subsequent volume attributes collectively called, the Fault Enhancement Filter (FEF) [[Jaglan and Qayyum, 2015](#)]. This filter smooths seismic data which have a ‘clean’ signal and sharpens seismic data with a distorted signal, essentially enhancing faulted areas (e.g. [Jaglan and Qayyum \[2015\]](#)).

From the FEF seismic cube, the similarity attribute was computed (Figure 7.5b). This attribute has values ranging between 0-1, with clean seismic data having values close to 1, and distorted seismic data having lower values (Figure 7.5b). This attribute is commonly used for characterizing seismic discontinuities [[Jaglan and Qayyum, 2015](#)]. In this study, the similarity attribute cube (Figure 7.5b) was used as input for populating the fracture intensity in the modelling domain.

The FEF seismic cube was also used as input for the Thinned-Fault-Likelihood (TFL) attribute, which has been developed by [Hale \[2013\]](#) and implemented in OpendTect [[Jaglan and Qayyum, 2015](#)]. The TFL attribute highlights areas which show a distorted seismic amplitude signal (i.e. $\text{TFL} = (1 - \text{semblance})^B$ [[Hale, 2013](#)]), with semblance being representative for the continuity in the seismic signal. We used this attribute to thin and enhance areas which show sharp changes in the seismic-data, along user-defined dip- and dip-azimuth ranges (dip-range of 45-85 and azimuth-range of 0-360) (Figure 7.5c). The resulting TFL attribute forms the fault cube which is further utilized in the DFN modelling workflow (Figure 7.4).

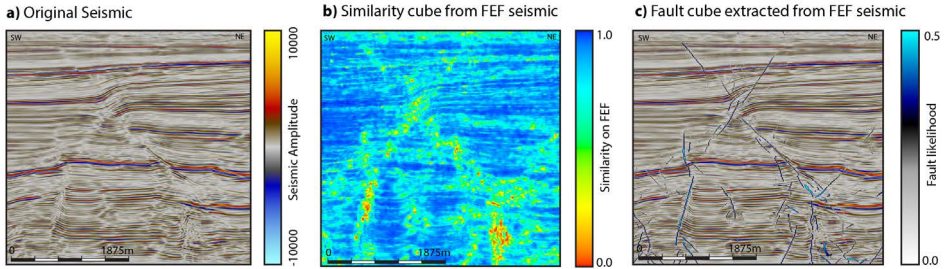


Figure 7.5: Fault cube extraction workflow using OpendTect 6.0.0. a) Original seismic data. b) Similarity cube extracted from the Fault Enhancement Filtered (FEF) seismic. c) Fault Likelihood (FLH) cube extracted from the FEF seismic data. See text and Jaglan and Qayyum [2015] and Hale [2013] for additional information. For all figures, there is no vertical exaggeration.

7.3.7 Discrete Fracture Network (DFN), aperture and permeability modelling

The 2D DFN in the modelling domain was populated by implementing the interpreted fracture data from the image log and results of the seismic discontinuity results (Figures 7.4 and 7.5b), into the Petrel (Petrel[®]) Fracture Network modelling workflow. The fracture intensity map was based on the inverse similarity map (1- seismic similarity) and the correlation between fracture intensity and similarity. Further, we assumed that faults and fractures are related, so that the local fracture orientation is parallel to the seismic faults within the modelling domain. To this end, the orientation of each fault was manually measured and the extracted data was linearly interpolated in to an orientation map (Figure 4 and Table 1). Lastly, the spread in local fracture orientation was modelled using a constant Fisher coefficient ([Fisher, 1953]), which was derived from the observed standard deviation in fracture orientation.

To model the aperture on each fracture within the DFN, we have created three different scenarios, namely: 1) measured aperture, 2) length-based aperture and 3) mechanical aperture. These three aperture models were chosen so that potential differences in fracture characteristics are captured and depicted. However, we do acknowledge that the full range of potential uncertainties involved in modelling fracture aperture cannot be described by only using three different models.

In the first scenario, aperture was based on observations from the image log data. The observed aperture data was used to create a probability density function which was in turn used to populate the aperture on each fracture in the DFN.

For the second scenario, we assume that fracture length and aperture are related via the often observed sub-linear scaling law (e.g. Olson [2003], Vermilye and Scholz [1995]), so that the fracture aperture can be calculated using equation 7.4:

$$e_L = CL^a \tag{7.4}$$

where e_L is the modelled length-based fracture aperture in m, C is the pre-exponential constant, which was set at 5.0×10^{-5} , L is the total fracture length in m, and a is the power-law scaling exponent which was set at 0.5.

For the third scenario, we use the mechanical aperture model first defined by Barton and Bandis [1980]. This model uses empirical relationships to describe mechanical closure of initially open fractures due to an applied normal stress (e.g. Asadollahi et al. [2010], Bisdorn et al. [2017b, 2016b], Boersma et al. [2019b]). This closure can be described by a hyperbolic function so that the mechanical aperture follows equation 7.5:

$$e_n = e_0 - \left(\frac{1}{v_m} + \frac{K_{ni}}{\sigma_n} \right)^{-1} \quad (7.5)$$

where e_n is the resulting mechanical aperture (mm), e_0 is the initial fracture aperture (mm), v_m is the maximum closure (mm), K_{ni} is the fracture stiffness, and σ_n is the normal stress on the fracture plane ([Barton and Bandis, 1980]). The maximum closure (v_m) and stiffness (K_{ni}) are empirically measurable material parameters, which depend on the Joint Roughness Coefficient (JRC) and the Joint Compressive Strength (JCS) of each fracture plane [Asadollahi, 2009]). In this study, we assumed that the modelled fractures are irregular and have a JRC of 7.5 and JCS of 17.5 (MPa), so that v_m and K_{ni} are equated as [Asadollahi, 2009, Bisdorn et al., 2016b]:

$$v_m = -0.1032 - 0.0074JRC + 1.135 \left(\frac{JCS}{E_0} \right)^{-0.251} \quad (7.6)$$

$$K_{ni} = 7.15 + 1.75JRC + 0.02 \left(\frac{JCS}{E_0} \right) \quad (7.7)$$

For all scenarios, the modelled aperture is translated to a permeability on each fracture plane, using the Parallel plate law (equation 7.8):

$$K_{frac} = \frac{e^2}{12} \quad (7.8)$$

where e is the respective fracture aperture in m and K_{frac} is the fracture permeability in m^2 .

Finally, the K_{frac} on each fracture in the DFN was upscaled to an effective fracture permeability for respective grid cell using the Oda method [Oda, 1985]. This method assumes that individual fractures within a grid cell can be upscaled to an effective crack (permeability) tensor using geometrical statistics (i.e. fracture orientation, fracture crack length and fracture permeability). In total three upscaled fracture permeability models based on the different aperture models were created (i.e. Power-law (measured), length-based aperture and stress-based aperture).

7.3.8 Fluid-flow/temperature modelling

Fluid and temperature simulations were done using the Delft Advanced Research Terra Simulator (DARTS), which is a python/C++ based simulator capable of simulating high-enthalpy (water and steam) systems using operator-based linearisation [Khait, 2019, Wang et al., 2020]. Here, we assume that the two-phase thermal system can be described by mass and energy conservation equations (7.9 and 7.10) [Wang et al., 2020]:

$$\frac{\partial}{\partial t} \left(\phi \sum_{p=1}^{n_p} \rho_p s_p \right) - \text{div} \sum_{p=1}^{n_p} \rho_p u_p + \sum_{p=1}^{n_p} \rho_p q_p = 0 \quad (7.9)$$

$$\frac{\partial}{\partial t} \left(\sum_{p=1}^{n_p} \rho_p s_p U_p + (1 - \phi) U_r \right) - \text{div} \sum_{p=1}^{n_p} h_p \rho_p u_p + \text{div}(\kappa \nabla T) + \sum_{p=1}^{n_p} h_p \rho_p q_p = 0 \quad (7.10)$$

where p is the phase ($p = 1$ (water) and $p = 2$ (vapor)), ϕ is the porosity, s_p is the phase saturation ($s_1 + s_2 = 1.0$), ρ_p is the phase density (kg/m^3), U_p is the phase internal energy (kJ), U_r is the rock internal energy (kJ), h_p is the phase enthalpy (kJ/kg), κ is the thermal conduction (kJ/m/day/K), T is the temperature (K), u_p is the phase velocity (m/s), and q_p is the phase mass-flow rate (m^3/s).

Fluid flow is described using Darcy's law (equation 7.11):

$$q_p = K \frac{k_{rp}}{\mu_p} (\nabla P_p - \gamma_p D) \quad (7.11)$$

where, q_p is the mass flow rate for phase p (m^3/s), K is the permeability matrix (mD), k_{rp} is the relative permeability for phase p (mD), μ_p is the phase viscosity, P_p is the pressure for phase p , γ_p is the phase specific weight (N/m^3), and D is the depth (m).

To assess the impact that fractures could have on geothermal heat production, the computed matrix properties and upscaled fracture permeability models (one for each aperture scenario) were used to create four different simulation scenarios. These scenarios will be explained in more detail in the results section.

For each scenario, one injector - and one producer well were placed vertically in two cells showing a relatively high fracture intensity. Fluid flow was initiated by creating a bottom-hole pressure difference between injector and producer (Injector BHP = 375 Bar, Producer BHP = 425 Bar). The injection temperature was set at 30.0 °C. The initial reservoir temperature and pressure were set at 120 °C and 400 Bar, respectively (Table 7.1). Simulation run time was set at 30 years. Finally, the model was assumed to be a closed system, implying that no flow in/out of the model boundaries was possible. See table 7.1 for the rest of the initial conditions.

Parameters	Value
Simulation time (years)	30
Depth (m)	3940
Initial Temperature (°C)	120
Volumetric heat capacity (C) (kJ/m ³ /K)	2450
Thermal conductivity (κ) (kJ/m/day/K)	0.25
Initial reservoir pressure (Bar)	400
BHP injector (Bar)	425
BHP producer (Bar)	375
Grid dimensions (i,j)	147x138x1
Grid cell size	10x10x1
Injector location (i,j)	i = 71 and j = 33
Producer location (i,j)	i = 82 and j = 100

Table 7.1: Constant parameters used for each simulation

7.4 Results: Petrophysical analysis, geostatistical inversion, and property computations in the modelling domain

7.4.1 Petrophysical analysis of the NLW-GT-01 well

The available wireline logs cover the Main Buntsandstein formations (Figure 7.6a). The Hardegsen and Detfurth formations show a relatively low density ($\rho = 2.58 \pm 0.056$ g/cm³), P- and S-velocity ($V_P = 4782.32 \pm 241.12$ m/s and $V_S = 3035.63 \pm 14.851$ m/s) and low P- and S-Impedance ($I_P = 12376.10 \pm 839.59$ (g/cm³)(m/s) and $I_S = 7853.33 \pm 498.586$ (g/cm³)(m/s)) (Figure 7.6a). The effective and total porosities are relatively high ($\phi_{\text{eff}} = 0.028 \pm 0.013$, $\phi_{\text{tot}} = 0.057 \pm 0.02$) (Figure 7.6a). The Volpriehausen formation shows higher density, P- and S-velocity and low P- and S-Impedance values, with respect to the Detfurth and Hardegsen formations (Figure 7.6a). Additionally, the petrophysical analysis indicates that the Volpriehausen formation has almost no intrinsic porosity (i.e. $\phi_{\text{eff}} = 0.010 \pm 0.006$ and $\phi_{\text{tot}} = 0.022 \pm 0.012$) (Figure 7.6a). These lower porosities were also observed in core plug measurements, and are believed to be caused by diagenetic events (i.e. dolomite and anhydrite cementation) (www.nlog.nl).

Linear regression analysis indicates that the different petrophysical properties can be related (Figures 7.6b-d). The results show that rock density vs. effective and total porosity follows a negative-exponential and negative-linear relation, respectively (Figure 7.6b). The effective and total porosity vs. acoustic impedance (I_P) also shows a negative-exponential and negative-linear relationship (Figure 7.6c). The density and acoustic impedance follow a negative-linear relationship (Figure 7.6d).

7.4.2 Geostatistical inversion and property modelling

The geostatistical inversion results show that relatively low acoustic impedance values occur in areas where there is a distinct change from positive to negative amplitude (Figures 7.7a-b). Our results also indicate that areas showing low acoustic impedance correlate very well with the more porous portions of the Hardegsen and Detfurth formations (Figure 7.7a-c). This is for example seen in the NLW-GT-01 well which goes through a succession with relatively low acoustic impedance values that coincide with the Hardegsen and Detfurth formations (Figures 7.7a-c).

Using the relations extracted from the petrophysical analysis (Figure 7.6), the inverted acoustic impedance is converted to a total and effective porosity. The resulting properties show a good correlation with the porosity data observed in the NLW-GT-01 well (Figures 7.6 and 7.7c). However, some discrepancies between the well and seismic data exist. For instance, the peaks in porosity observed from the wireline data do not completely overlap with peaks detected within the properties calculated from seismic inversion (Figure 7.7c). These differences could be explained by the uncertainties in the velocity model which has been used in the seismic inversion workflow [van Dalfsen et al., 2006], or uncertainties in the reprocessing of the seismic data.

Within the 2D modelling domain, changes in seismic amplitude coincide with changes in the acoustic impedance and computed porosities (Figures 7.8a-d). Because the data is depicted on a z-slice ($z = 3940$ m), the stark changes in the seismic properties correspond to changes in the rock properties (i.e. Hardegsen/Detfurth = low I_P and (relatively) high ϕ and Volpriehausen = high I_P and low ϕ) (Figures 7.8a-d). Using equation 7.2, the total and effective porosities (Figures 7.8c-d) are converted to a total and effec-

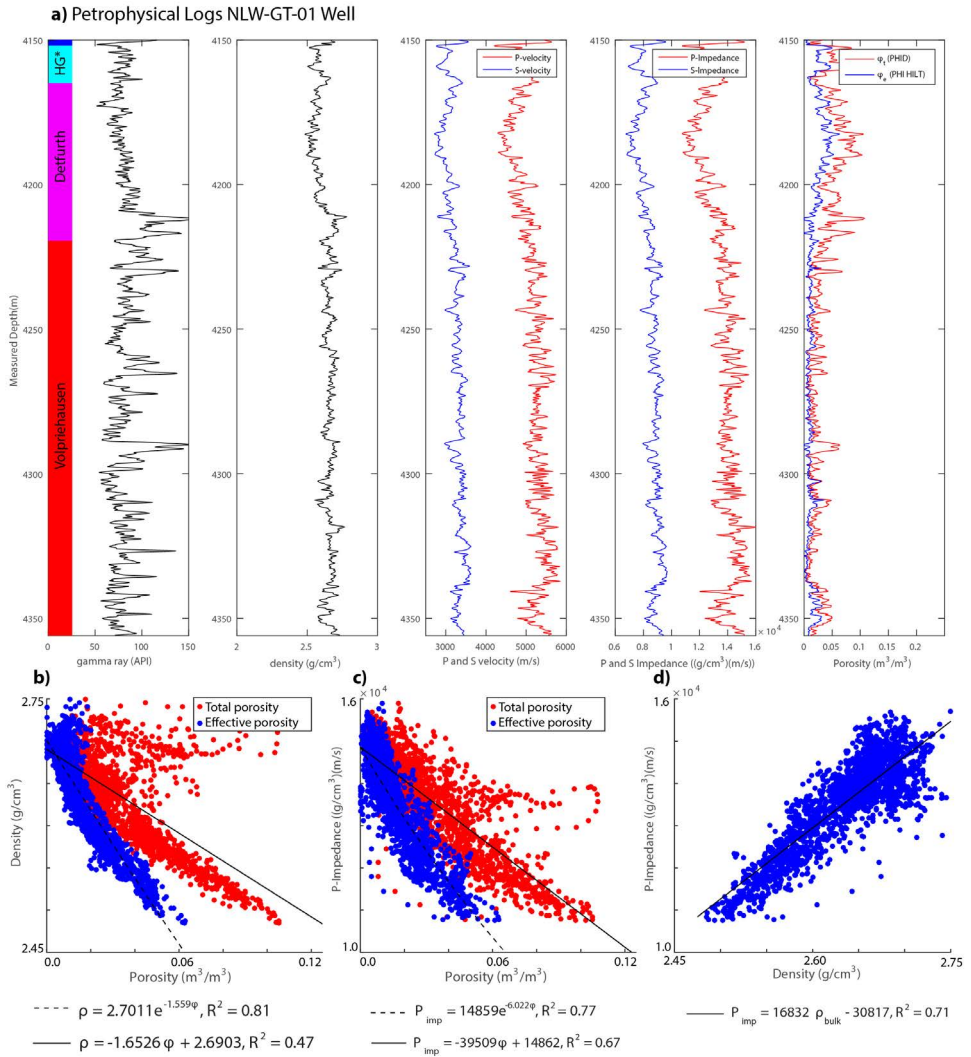


Figure 7.6: Petrophysical analysis of the NLW-GT-01 well. a) From left to right: Gamma ray, Density, P- and S-Velocity, P- and S-Impedance and total and effective porosity logs, respectively. b) Effective and total porosity (Blue and red dots) vs the measured density. c) Effective and total porosity (Blue and red dots) vs the P-Impedance. d) Rock density vs the P-Impedance. Note that the different relations are depicted at the bottom of figures b, c and d, respectively.

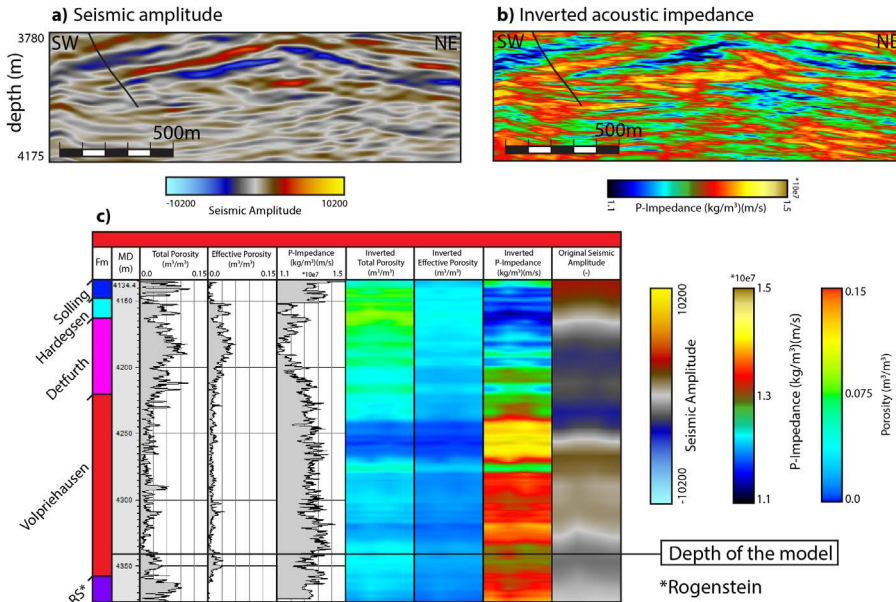


Figure 7.7: a-b) Inline through the seismic amplitude data and inverted acoustic impedance data at the NLW-GT-01 location. c) Porosity and P-impedance well logs, inverted seismic properties and the depth-converted seismic data extracted along the NLW-GT-01 well. Note that small discrepancies between the inverted data and well logs likely exist due to uncertainties in the velocity model.

tive permeability (Figures 7.8e-f). For the total permeability field, the computed values range between 0.072 mD, for the areas showing low porosities and 1.92 mD for areas showing high porosities (Figure 7.8e). The effective permeability values range between 0.077 and 0.46 mD (Figure 7.8f).

7.5 Results: Fracture and fault network characterisation

7.5.1 FMI and core interpretation and fracture analysis

Using the conservative interpretation method explained in section 3.6, a total of 58 fractures have been interpreted, which is 6.7 % of the observed conductive features in the image log data. The resulting interpretation shows that fractures and faults mainly occur in clustered intervals within the Volpriehausen formation (Figure 7.9a), with an average intensity (P10) of 0.53 (1/m) (Figure 7.9a). Fractures and faults show a relative increase in the conductivity image log, implying that they are conductive and have a measurable aperture (Figure 7.9b). All interpreted features strike NW-SE and have dips ranging between 60 and 90 degrees (faults = ± 60° and fractures = ± 85°) (Figure 7.9c). This general NW-SE strike is parallel to the main faults in the WNB. The image log and core interpretations also highlight that the faults which show minor displacement (mm - to cm scale) of the bedding planes have been sampled by the NLW-GT-01 well (Figure 7.9b and d). The fractures/faults observed in the cored interval show a similar NW-SE strike with measured dips ranging between 45° and 90° (Figure 7.9e).

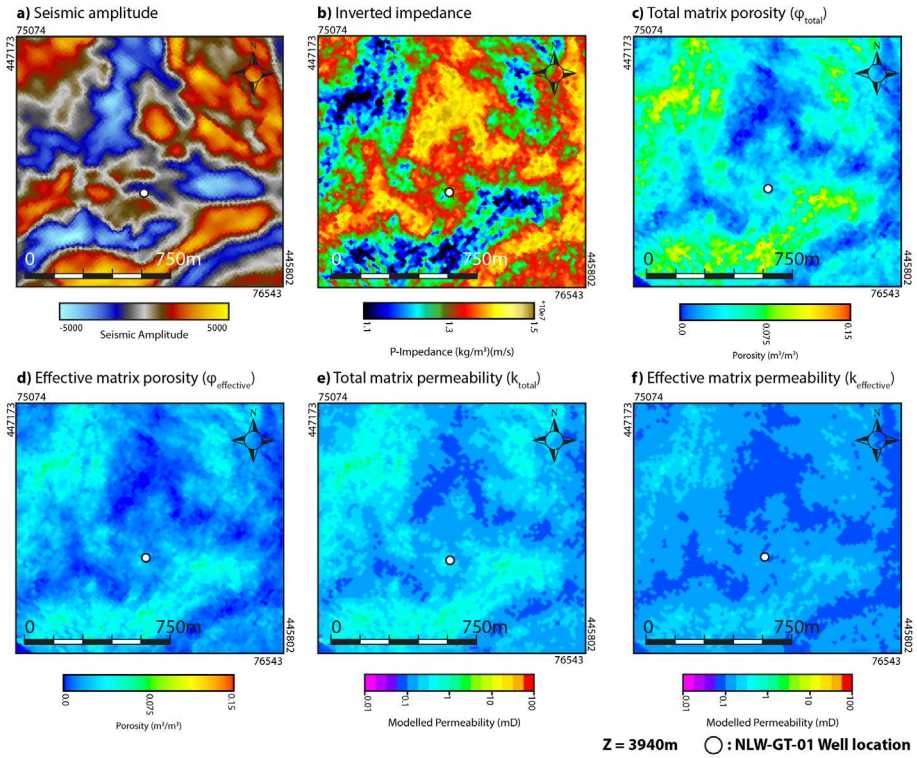


Figure 7.8: a-b) Seismic amplitude and inverted impedance within the modelling domain. c-d) Modelled total and effective porosity within the modelling domain. f) Permeability map calculated from the total porosity. g) Permeability field calculated from the effective porosity (HILT Porosity). The relation between porosity and permeability was taken from [Pluymaekers et al. \[2012\]](#).

By calibrating the conductivity image log (Figure 7.9), the mean and hydraulic aperture of the interpreted fractures can be calculated. The results show that all fractures are more conductive than the surrounding rock matrix, with some large fractures in the lower part of the Volpriehausen formation showing a distinct reduction in the calibrated resistivity log (Figure 7.10). This is also indicated by the computed fracture apertures, which show that most fractures have a hydraulic and mean aperture ranging between 0.01 and 0.1 mm (Figure 7.10). Highly conductive features have an aperture ranging between 0.1 and 0.5 mm (Figure 7.10). These results imply that all fractures are at least partly open and most likely enhance the effective permeability of the normally tight Volpriehausen sandstones.

The measured fracture apertures range between 0.01 and 0.5 mm, with the aperture distribution showing negative power-law behaviour (Figure 7.11a). The probability density function of the fracture aperture can be best described by equation 7.12:

$$P(e; a, b) = be^{-a} \quad (7.12)$$

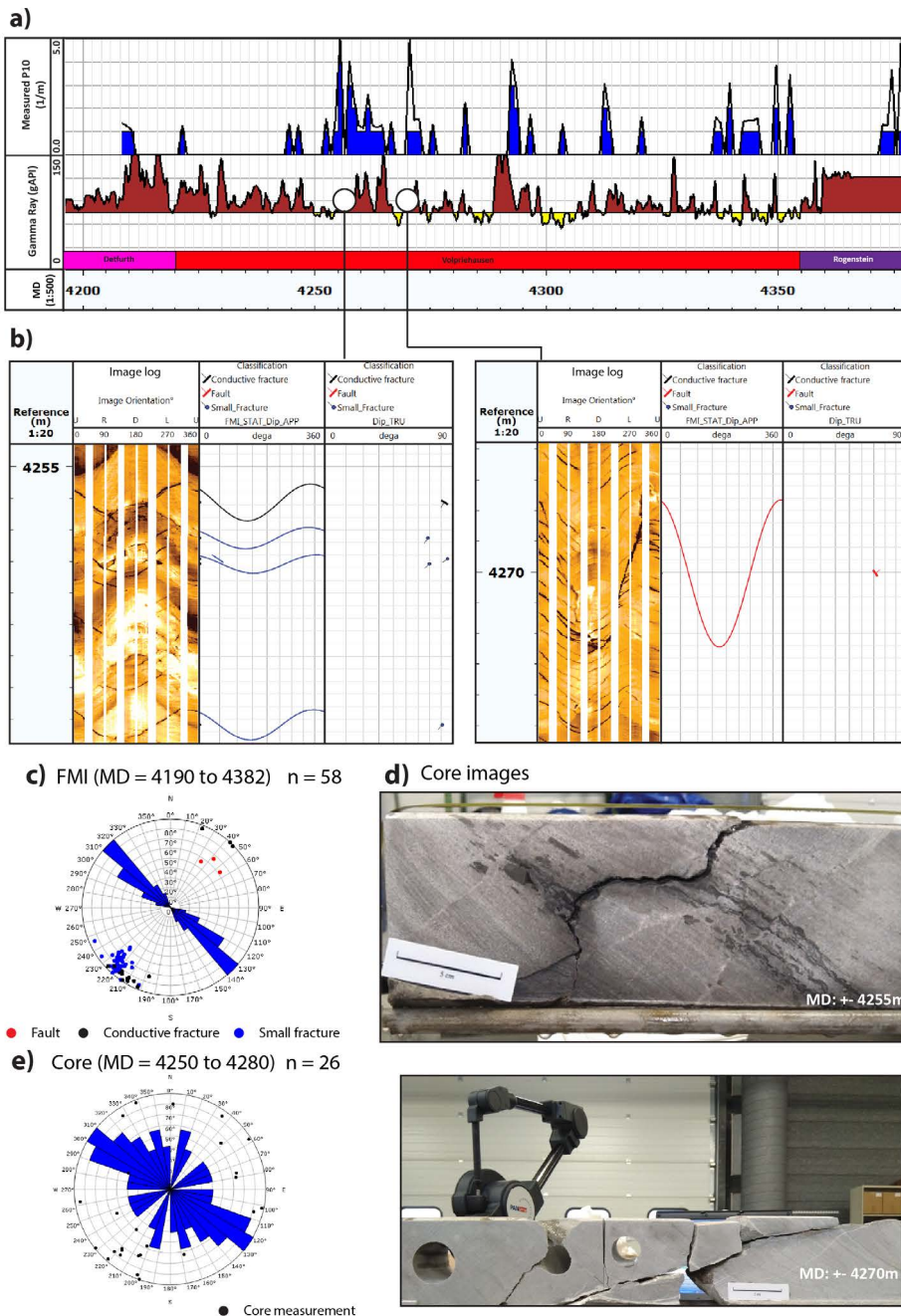


Figure 7.9: Structural fracture data extracted from the FMI and core data. a) Fault and fracture intensity (P10) and gamma ray log for the entire NLW-GT-01 well. b) Two examples of large fractures interpreted from the FMI data. c) Rose diagram depicting the orientation distribution and poles for all interpreted fractures and faults. d) Example of faults and fractures observed within the cored interval of NLW-GT-01 well. Note that Figure 8b (left) represents the same interval.

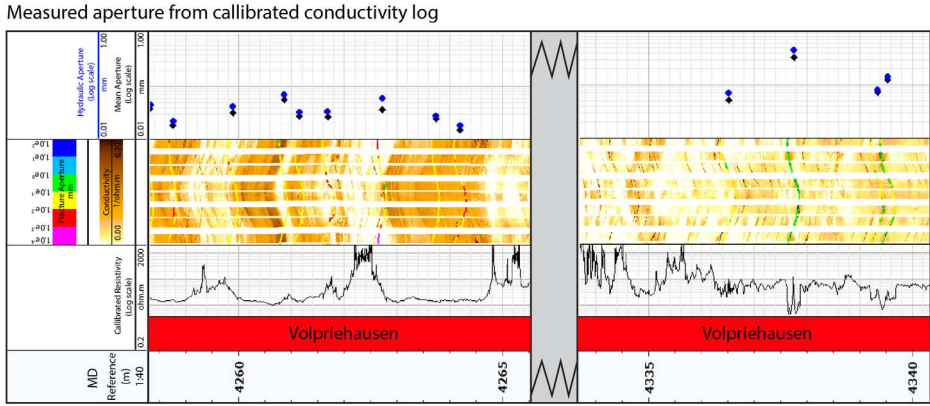


Figure 7.10: Calibrated FMI log and fracture aperture results for the Upper and Lower Volpriehausen, respectively. Note that fractures are more conductive than the surrounding reservoir rock.

where, e is the fracture aperture in mm, a is the power-law exponent which is set at 1.543 and b is a scaling factor which is set at 0.191 (Figure 7.11a).

The computed fracture lengths range between 0 and 12 m (Figure 7.11b). The frequency distribution highlights that the fracture lengths can best be described by a log-normal function (equation 7.13):

$$P(\ln(l); \mu, \sigma) = \frac{1}{\sigma\sqrt{2\pi}} \exp\left(-\frac{(\ln(l) - \mu)^2}{2\sigma^2}\right), l > 0 \quad (7.13)$$

where, l is the fracture length (m), μ is proportional to the median (set at 0.2) and σ is proportional to the variance in the data and is set at 0.6 (Figure 7.11b). The extracted probability density function (equations 7.12 and 7.13) will be used as input parameters for the DFN modelling workflow (aperture scenario 1 and fracture length).

7.5.2 Automated fault extraction and characterisation

At 3940 m depth, the TFL cube shows that faults have a dominant orientation striking NW-SE to N-S and are mainly aligned along the inverted horst structures (Figure 7.12a). The extracted faults largely consistent with previous fault interpretations within the WNB (e.g. de Jager [2007], Van Balen et al. [2000]).

At the Triassic/Jurassic intervals (± 2800 -3800m), the extracted faults show both normal - and reverse displacement. The larger faults follow the dominant NW-SE to N-S strikes and are part of large uplifted horst structures which show significant offset (750m) with respect to lower-lying graben (Figures 7.12a-b). At the Cretaceous intervals (± 1000 -2500m), faults have a dominant NW-SE orientation. Above the horst structures, these faults generally show inversion and coincide with erosion of the Cretaceous intervals (Figures 7.12a-b). Away from the uplifted regions, these NW-SE striking- faults show normal offset (Figure 7.12b). Within the Tertiary succession (± 0 -1000m) faults strike NW-SE and show normal displacement (Figure 7.12b).

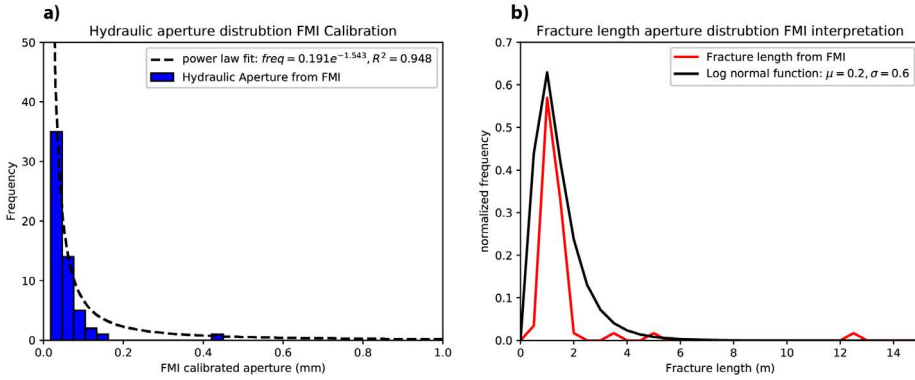


Figure 7.11: a) Histogram and power-law fit through of the hydraulic apertures. b) Normalized frequency of the fracture length taken from the FMI and log normal function fitting the data. The fracture length is calculated from the measured fracture height.

Within the modelling domain ($z = 3940\text{m}$) (Figure 7.12c), longer faults generally have an orientation ranging from E-W to N-S (Figure 7.12). Smaller faults striking NE-SW are also observed (Figure 7.12c). Near the NLW-GT-01 well, faults strike NW-SE and NE-SW, and this NW-SE strike is similar to the dominant fault and fracture orientation observed in the FMI interpretation (Figures 7.9b-c and 7.12c).

7.6 Results: DFN modelling, aperture computations, permeability up-scaling and fluid flow and temperature simulations

7.6.1 A Reservoir scale DFN

Using the fracture and fault data as observed and interpreted from the available FMI -, core -seismic data, a reservoir scale DFN is generated within the 2D modelling domain (Figure 7.4).

In the presented workflow, the inverse similarity cube (1-similarity) is used as a proxy for modelling the fracture intensity (P21) (Figure 7.5b). By extracting the inverse similarity data along the NLW-GT-01 well, we can quantitatively compare the measured P21 with the changes in the seismic signal (Figure 7.13a). The results indicate that the peaks observed in the P21 log roughly correlate with peaks observed in the inverse similarity signal. For simplicity, we have decided to describe the rough correlation using a simple linear model ($P21 = 1.119(1 - \text{similarity})$) (Figures 7.13a-b).

However, while showing a correlation, detailed changes in the image log interpretation (i.e. peaks and throughs in the P21 data) have not been observed in the seismic data (Figures 7.13a-b). For example, the large peak observed MD = 4260 has not been detected by the inverse similarity cube (Figure 7.13a-b). This observation can imply two things, namely: 1) the detailed changes in the image-log data fall below the seismic resolution and therefore cannot be detected by the inverse similarity data, or 2) that the observed data cannot be described by a simple linear correlation because of the complexity in the two datasets. That being sad and taking these discrepancies and simplifications into account, we are confident that the seismic similarity can be used as a measure for

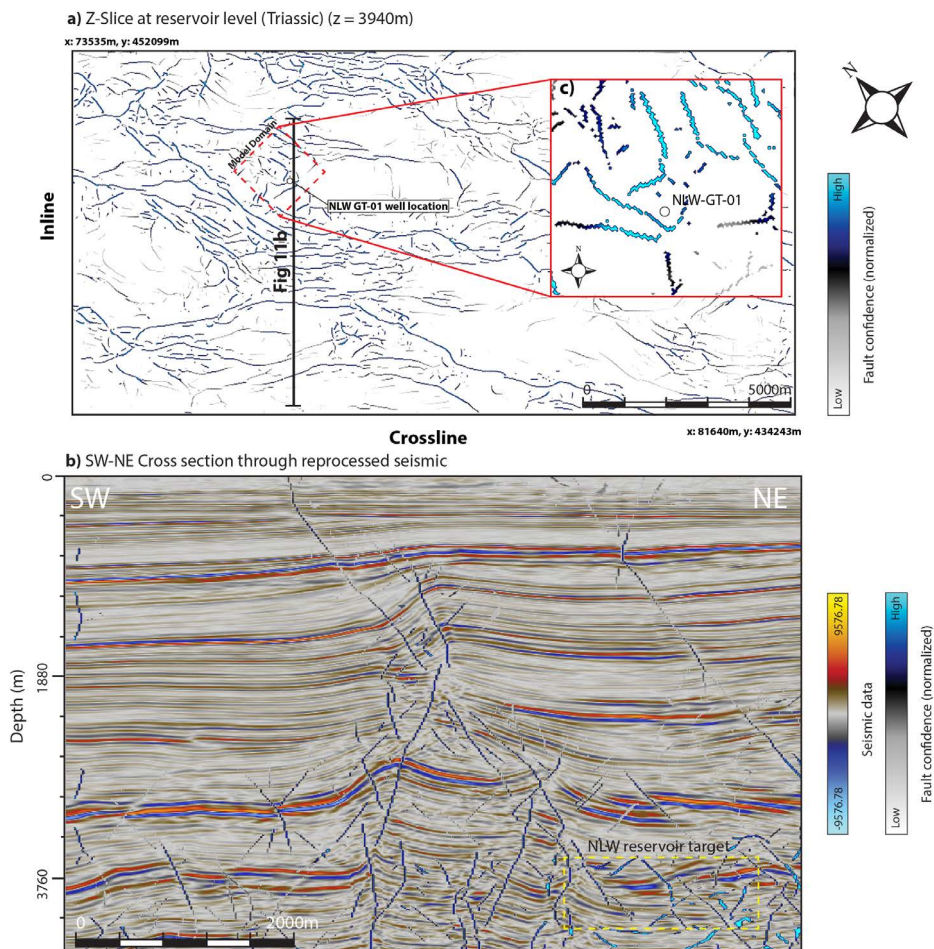


Figure 7.12: Extracted fault cube data. a) Z-slice at 3904m depth (at Triassic interval near reservoir target) showing the extracted Triassic faults, modelling domain, well location and the location of the cross section. Note that the z-slice has been rotated 38.59° with respect to the North. b) NE-SW cross section through the 3D seismic and fault cube. c) Faults extracted within the modelling domain.

modelling fracture intensity (Figure 7.13a-b).

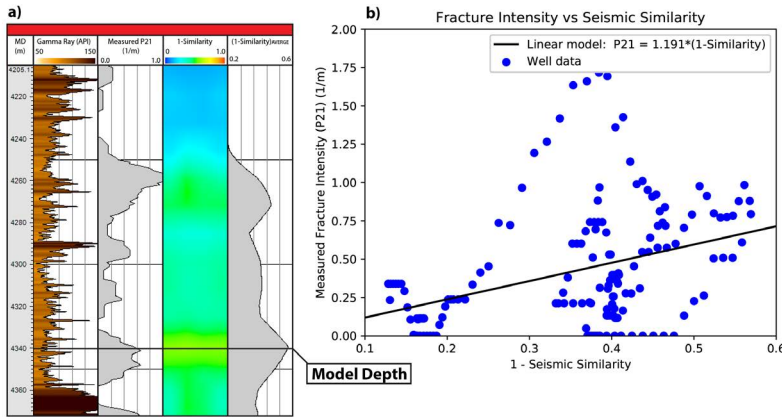


Figure 7.13: a) Extracted fracture intensity (10m sampling) vs the seismic 1 – similarity cube. a) Measured P21 and seismic dissimilarity extracted along the NLW-GT-01 well. Note that the model depth (z-slices shown in figure 7.14) is highlighted. b) Cross plot of the fracture intensity vs 1-Similarity and the linear model which will be used for fracture intensity modelling.

Utilizing the correlation depicted by figure 7.13b, the fracture intensity is calculated for the 2D modelling domain (Figures 7.4 and 7.14a-b). The results show that, the NLW-GT-01 well corresponds to a relatively high peak in the inverse similarity data, resulting in a modelled fracture intensity of ± 0.6 (1/m) (Figures 7.14a-b). Overall, the modelled fracture intensity has values ranging between 0 and 1.20 (1/m), with high fracture intensities mostly occurring along the interpreted faults (Figure 7.14b).

The local average fracture strike is based on the fault orientation map (Figure 7.14c). The fracture average dip is set at 90° . For the spread in strike and dip, we used a constant Fisher K coefficient [Fisher, 1953] throughout the modelling domain. This coefficient was derived from the standard deviation in the FMI measurements and is set at 20.0 (Figure 7.9c). Lastly, the fracture length is modelled using the log-normal function (equation 7.13) derived from the FMI interpretation (Figure 7.11b). The parameters in the log-normal functions are kept constant over the 2D modelling domain.

The resulting DFN has a total of 1.3e6 fractures which are, on average, parallel to the interpreted fault orientations. The modelled lengths follow the observed log-normal distribution (equation 7.13) and range between 0.5 and 10.0 m with a peak at 1.5 m (Figures 7.11b and 7.14d). Finally, it should be noted that for modelling purposes, fractures shorter than 0.5m have been modelled implicitly and have a constant aperture of 0.01 mm.

7.6.2 Aperture and upscaled permeability results

The aperture of each fracture in the DFN is dependent on the assigned aperture model (i.e. Power-law - (Figure 7.11a), length-based - and stress-based aperture). For first model, the computed aperture was based on FMI interpretation and extracted probability density function (Figure 7.11a and equation 7.12). The resulting fracture apertures

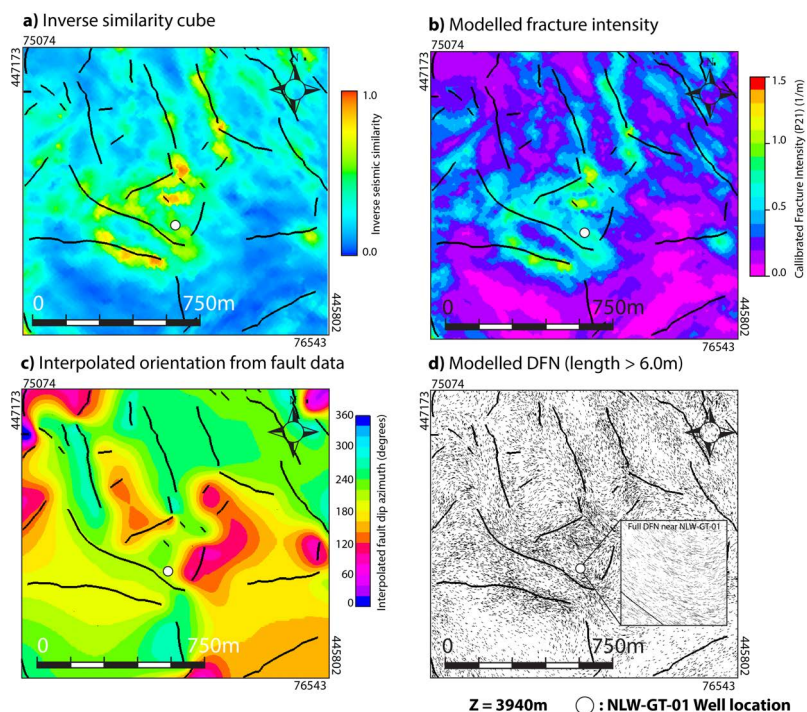


Figure 7.14: 2D DFN modelling results. Note that the model depth is set at 3940 m. a) Inverse similarity map extracted from the seismic similarity cube. b) Fracture Intensity map. The fracture intensity is calculated from the inverse similarity cube and calibrated using NLW-GT-01 well data. c) interpolated dip azimuth map extracted from the interpreted fault data. d) DFN model created from the input maps. Note that on the 'large' scale, only fractures longer than 6.0m have been depicted. The full DFN is shown by the zoomed in box near the NLW-GT-01 well. For all figures, the faults observed on the seismic are highlighted by the black polylines.

follow the assigned power-law relation with values ranging between 0.01 and 1.0 mm (Figures 7.11a and 7.15a). For the second model, the aperture was based on the fracture length (assuming equation 7.4), and the results show that the apertures follow a log-normal distribution with a peak at 0.04 mm (Figure 7.15b). For the third model, we assumed that the fracture aperture is influenced by an assigned stress field, assuming the stress induced aperture model first proposed by Barton and Bandis [1980]. To this end, we assumed a regional stress field parallel to the present-day stress in the WNB, so that σ_H strikes WSW-ENE (130°) [Heidbach et al., 2016, Worum et al., 2005]. The magnitude of the differential stress between the horizontal components (i.e. $\sigma_H - \sigma_h$) was assumed to be 5.0 MPa, which is feasible for the tectonic setting in WNB (i.e. normal faulting regime in a tectonically quiet area). The results show fractures which are at an angle larger than 40° to the assigned regional stress show almost no aperture (i.e. $e_n \leq 0.03$ mm), whereas fractures which have a small intersection angle (angle $\leq 10^\circ$) show apertures closer to the assigned initial aperture ($e_0 = 0.15$ mm). The resulting frequency distribution shows that modelled apertures have peaks at $e_n \leq 0.03$ mm and $e_n = 0.15$ mm (Figure 7.15c). In between the two peaks, fracture apertures are approximately uniformly distributed (Figure 7.15c).

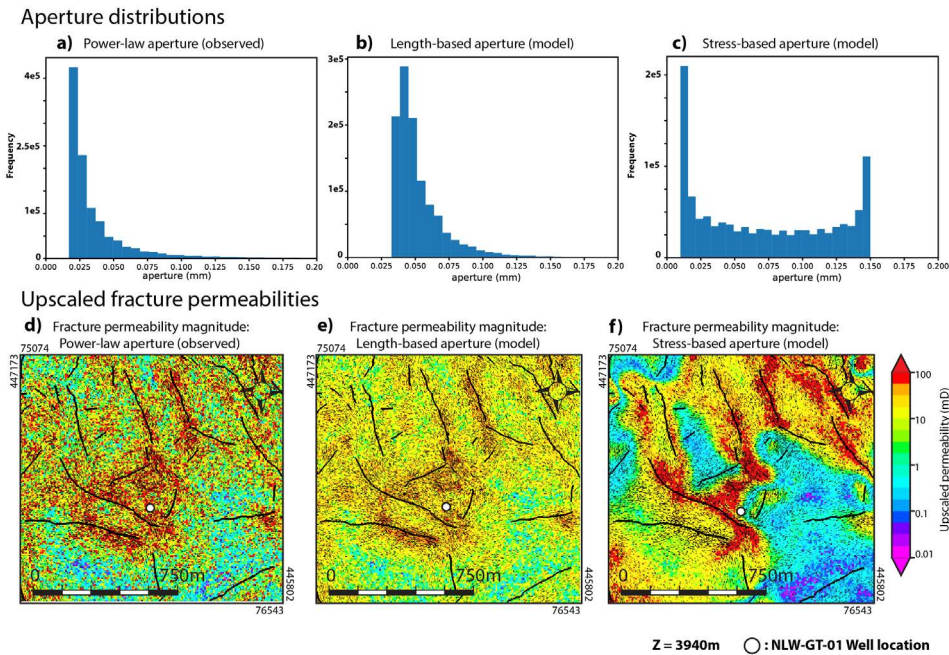


Figure 7.15: Aperture and upscaled permeability results within the modelling domain. a) Aperture distribution for the power-law aperture model (model 1) (equation 12). b) Aperture distribution for the length-based aperture model (model 2) (equation 4). c) Aperture distribution for the stress-based aperture model (model 3) (equations 5-7). d-f) Upscaled permeability magnitudes for the power-law, length-based and stress-based aperture models, respectively (i.e. $K_{mag(x,y)} = \sqrt{K_{upscaled(i)(x,y)}^2 + K_{upscaled(j)(x,y)}^2}$). For figures d to f, the faults and modelled DFN are highlighted by the black lines.

For each aperture model, the DFN's was upscaled to an effective fracture permeability for each grid cell ($K_{\text{Upscaled}(ij)(x,y)}$) (Figure 7.15d-f). The results show that for the models having a power-law aperture distribution, the upscaled permeabilities range between 0.01 and 5.0 mD, for grid cells having a low fracture intensity (Figures 7.14b and 7.15d). Grid cells having a high fracture intensity have upscaled permeability values ranging between 5.0 and 100 mD (Figures 7.14b and 7.15d). The upscaled permeabilities for the length-based aperture model show a similar pattern, with permeabilities ranging between 0.5 and 100 mD (Figure 7.15e). For the third model, the upscaled permeabilities are highly dependent on the modelled fracture orientation. For example, in areas where the modelled fractures strike sub-parallel to the assigned σ_H , upscaled permeabilities generally surpass 100 mD (Figure 7.15f). In areas where fractures are at angle to assigned stress orientation, upscaled permeabilities are dependent on the fracture strike and range between 0.01 to 100 mD (Figure 7.15f).

7.6.3 Fluid flow and temperature modelling

From the computed reservoir properties and the three upscaled fracture permeability models, four different fluid flow/temperature modelling scenarios have been realised, namely:

1. Matrix permeability model (Table 7.2). In this scenario, we assume that modelled fractures have no aperture, so that the upscaled fracture permeability is set at 0 and only the effective matrix permeability is taken into account (Figure 7.8f).
2. Fractured reservoir simulation (Power-law aperture) (Table 7.2). In this scenario, we assume fractures to be open and follow the measured power-law description (equation 7.12), so that the effective permeability in each grid cell is given by the summation of the respective upscaled fracture permeability (Figure 7.15d) and effective matrix permeability (Figure 7.8f).
3. Fractured reservoir simulation (Length-based aperture) (Table 7.2). In this scenario, we assume fractures to be open, following our length-based aperture description (equation 7.4), so that the effective permeability in each grid cell is given by the summation of the respective upscaled fracture permeability (Figure 7.15e) and effective matrix permeability (Figure 7.8f).
4. Fractured reservoir simulation (Stress-based aperture) (Table 7.2). In this scenario, we assume fractures to be open, following the presented stress-based aperture description (equation 7.5), so that the effective permeability in each grid cell is given by the summation of the respective upscaled fracture permeability (Figure 7.15f) and effective matrix permeability (Figure 7.8f).

Using these different modelling scenarios, the impact of fractures and different aperture models on fluid-flow and heat extraction was assessed. For all scenarios, the reservoir porosity was based on the computed effective porosity (Figure 7.7d) (Table 7.2). Furthermore, fluid flow was driven by a differential pressure between the injector - (BHP = 425 Bar) and producer well (BHP = 375 Bar) (Figure 15 and Table 7.1) More information on the different simulation settings can be found in Table 7.1.

Scenario	Permeability Model (mD)	Porosity Model	Average injection rate (m ³ /day)	Average production rate (m ³ /day)	Average energy production of the model (MWth)	Cumulative energy production (GJ)
(1) Matrix permeability model	$K_{(ij)(x,y)}$ = $K_{mat(eff)(x,y)}$ (Fig 7.8f)	$\phi_{(x,y)}$ = $\phi_{eff(x,y)}$ (Fig 7.7d)	0.46	0.50	0.11	33.44
(2) Fractured reservoir model (Power-law aperture)	$K_{(ij)(x,y)}$ = $K_{Upscaled(ij)(x,y)}$ + $K_{mat(eff)(x,y)}$ $K_{Upscaled(ij)(x,y)}$ = Fig 7.15d	$\phi_{(x,y)}$ = $\phi_{eff(x,y)}$ (Fig 7.8d)	56.51	59.12	13.19	554.56
(3) Fractured reservoir model (Length-based aperture)	$K_{(ij)(x,y)}$ = $K_{Upscaled(ij)(x,y)}$ + $K_{mat(eff)(x,y)}$ $K_{Upscaled(ij)(x,y)}$ = Fig 7.15d	$\phi_{(x,y)}$ = $\phi_{eff(x,y)}$ (Fig 7.8e)	45.42	49.45	11.23	451.47
(4) Fractured reservoir model (Stress-based aperture)	$K_{(ij)(x,y)}$ = $K_{Upscaled(ij)(x,y)}$ + $K_{mat(eff)(x,y)}$ $K_{Upscaled(ij)(x,y)}$ = Fig 7.15d	$\phi_{(x,y)}$ = $\phi_{eff(x,y)}$ (Fig 7.8f)	65.08	69.84	15.69	638.75

Table 7.2: Permeability and porosity models and production results for each scenario.

The results show that for the matrix permeability model (i.e. fractures are closed) (Figure 7.8f), the injection and production rates are low (Table 7.2), resulting in only slight changes of the reservoir temperature throughout the modelled timesteps (Figure 7.16a). However, when assuming that the modelled fractures are open (scenarios 2-4), the upscaled fracture permeability models are added to each grid cell (Table 7.2). This extra permeability, makes fluid flow possible, resulting in higher injection rates, production rates and therefore significant changes in the reservoir temperature over time (Table 7.2 and Figures 7.16b-d). Furthermore, for all fractured reservoir models, fluids are channelled along high permeability zones, resulting in anisotropic temperature changes and for scenario 4, communication between the injector- and production well (Figure 7.16b-d).

The extracted production profiles show a similar image (Figures 7.17a-b and Table 7.2). Here, the capacity and cumulative energy production of the matrix permeability model (fractures are closed) shows low values (0.11 MWth and 4.59 GJ). As expected, the output of the open fractured reservoir models (scenarios 2-4) are much higher and range between 11.23 to 15.69 MWth and 451.47 to 638.75 GJ (depending on the assigned aperture model) (Figure 7.17d-e and Table 7.2). The results also indicate that for scenarios 2 to 4, the capacity of the doublet system decreases over time (Figure 7.17).

In summary, our results clearly show that open natural fractures can significantly enhance geothermal production from the tight Lower-Triassic sandstones near the NLW-GT-01 well (Figures 7.16 and 7.17 and Table 7.2), thereby further exemplifying the importance of accounting for open natural fractures when assessing heat extraction from naturally fractured and/or tight reservoirs.

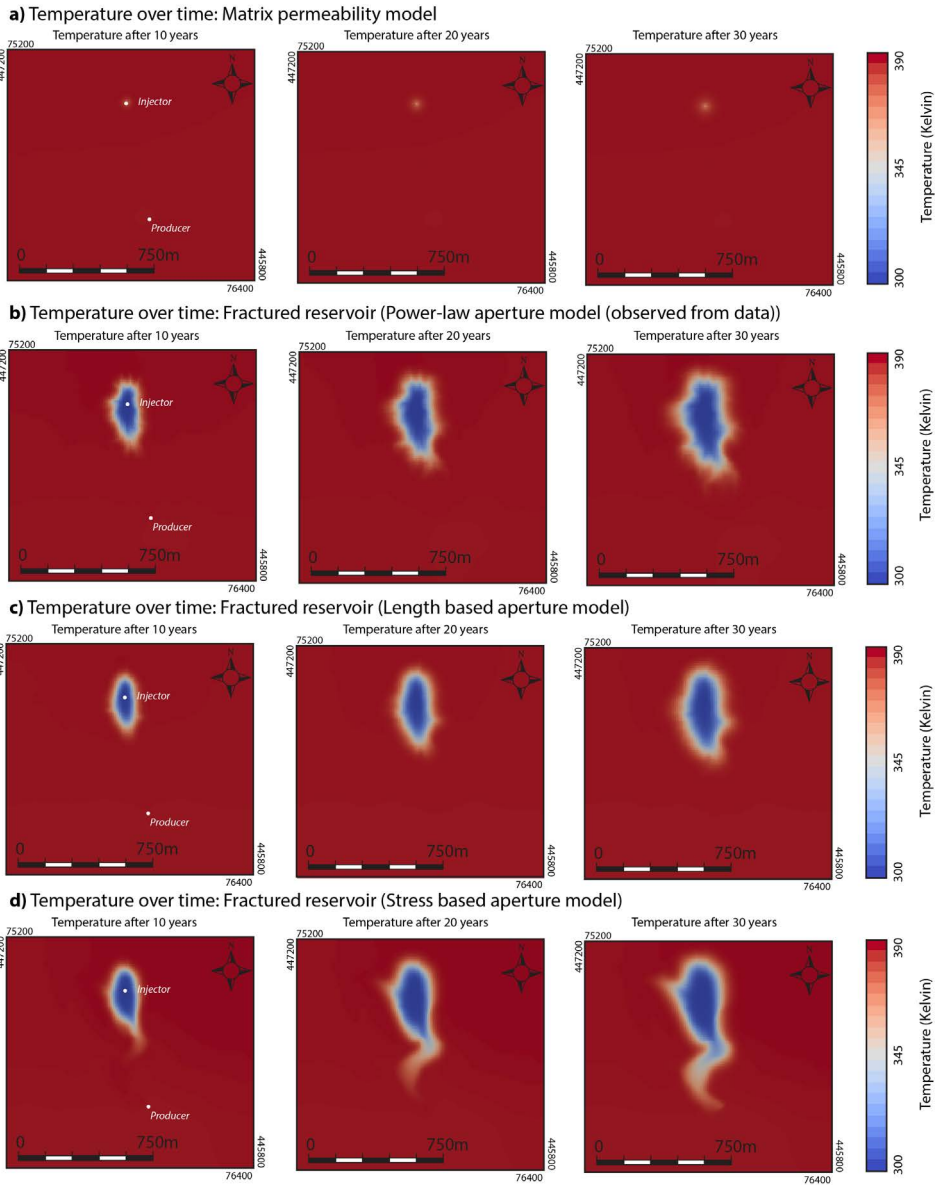


Figure 7.16: Fluid and temperature modelling results. a-d) Modelled temperature fields at time steps 10, 20 and 30 years for the four different scenarios, respectively. See text and table 7.2 for more information on the different scenarios.

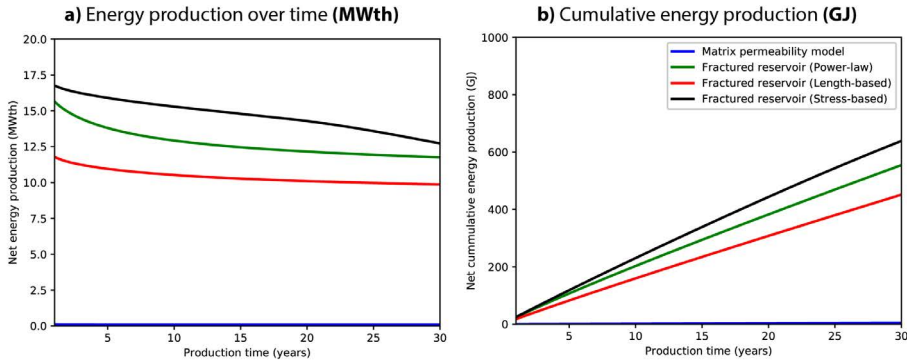


Figure 7.17: a-b) Net energy production (MWth) (Energy Producer – Energy Injector) and cumulative energy production (GJ) for the four modelling scenarios. Note that one GJ = 0.28 MWth.

7.7 Discussion

7.7.1 Impact of natural fractures and faults on heat production from the Main Buntsandstein Subgroup near the NLW-GT-01 well

The impact that natural fractures can have on the extraction of hydrocarbons or geothermal energy from tight or structurally complex reservoirs has been addressed by numerous studies (e.g. Holdsworth et al. [2019], Laubach et al. [2019], Toublanc et al. [2005], Vidal and Genter [2018]). These studies generally show that, if open, natural fractures and/or faults can significantly enhance the effective permeability of the low-permeable rocks, thereby making production possible. For example, Vidal and Genter [2018] showed that within the Upper Rhine Graben substantial amounts of heat are being produced from an open and connected natural fracture/fault network. Without the presence of these structural features, heat production would have been impossible. Holdsworth et al. [2019], shows similar results for hydrocarbon extraction out of a fractured/faulted basement reservoir.

In this case study, we assessed the impact of natural fractures and faults on geothermal heat extraction from Lower-Triassic sandstone reservoirs within the WNB. The presented results indicate that the Lower-Triassic sandstone formations near the NLW-GT-01 well are significantly faulted and fractured and that the observed structural features are hydraulically conductive (Figures 7.9-7.12). The obtained modelling results indicate that, when these fractures are closed, the modelled matrix permeabilities are too low to support any heat production (Figures 7.8, 7.16a and 7.17). However, when open, these fractures significantly enhance the reservoir permeability, thereby aiding geothermal production from the normally tight sandstones (Figures 7.15, 7.16 and 7.17). Moreover, for these fractured reservoir simulations, the modelled doublet capacities reached relatively high doublet capacities whilst injection and production rates were relatively low (Figure 7.17 and Table 7.2) (e.g. Willems and Nick [2019]). Therefore, these results imply that when the observed natural fractures have an intrinsic aperture and are hydraulically conductive, the Triassic formations surrounding the NLW-GT-01 hold significant potential and may be suitable for geothermal energy development.

While the main conclusions of this study suggest that the observed natural fractures can positively impact flow and geothermal heat extraction, it should be noted that as a result of the seismic resolutions gap, the prediction and characterisation of natural fractures remains a relatively uncertain process [Laubach et al., 2019, Maerten et al., 2006]. Furthermore, because no active flow tests were performed prior to the abandonment of the Lower-Triassic formations targeted by NLW-GT-01 well, no conclusive data exists on whether the natural fractures are connected and hydraulically conductive under subsurface conditions. Because of these uncertainties and limited hard data points, no definitive remarks can be made on the feasibility of the presented results and chosen modelling workflow. Therefore, in order to better address these significant uncertainties in future projects, we propose that the implementation of measures which can investigate the potential of fracture enhanced permeabilities (e.g. active well tests) should become a standard procedure.

Another process which could be investigated is how the presence of natural fractures affects different development strategies such as enhanced geothermal systems (EGS) or water injection under relatively high overpressures, both of which are commonly applied in projects extracting heat from tight reservoirs [Genter et al., 2016, Vidal and Genter, 2018]. To this end, a numerical modelling study could be conducted which assesses how natural fractures re-open under fluid-overpressures or affect hydraulically-induced fractures (e.g. [Zou et al., 2016]). However, it should be noted that injecting fluids at overpressures is known to trigger induced seismicity, which is something that needs to be avoided, especially in naturally fractured/faulted reservoirs (e.g. Buijze et al. [2020]).

7.7.2 Potential implications of the dataset and workflow for future geothermal energy development in the WNB

We believe that the reprocessed seismic dataset and presented workflow could have large implications for geothermal energy development in the WNB. For example, using geostatistical inversion, seismic discontinuity analysis and DFN modelling, the new seismic dataset was integrated with available wells in order to map rock properties and natural fractures on a reservoir scale. By doing so, we could for instance map the rock permeability and fracture intensity in the area surrounding the NLW-GT-01 well. Furthermore, the presenting modelling output can easily be incorporated in fluid flow/temperature modelling tools such as DARTS. All these presented methodologies and results could be utilized for a better prediction of reservoir properties away from the available well data, thereby helping in finding adequate locations for geothermal energy development.

7.7.3 Potential improvements to the modelling workflow

Although the main results of this study are positive (e.g. Figures 7.15, 7.16 and 7.17), it should be noted that the workflow contained some major uncertainties and modelling assumptions (Figure 7.4). For example, the DFN- and property models were based on data from only one well (NLW-GT-01), which may imply that the extracted fracture - and property data (e.g. porosity, permeability, fracture aperture, fracture length and fracture orientation) could well be biased due to the limited lateral sampling [Bisdorn et al., 2017a, Hanke et al., 2018, Maerten et al., 2016]. Further, the presented reservoir property models were mostly computed using statistical relations which cannot account for

the observed spread in the data. Additionally, in the presented DFN, we assumed the measured fracture height and length were related via a fixed aspect ratio, which is generally not observed in natural examples. In the presented workflow, we also assumed that the fracture intensity and orientation were proportional to discontinuities in the seismic signal, which may not be the case everywhere. Furthermore, to simplify the models, we upscaled the DFN's to an effective media, and this implies that our models cannot properly replicate effects caused by strong permeability contrasts between the fracture and surrounding rock matrix (e.g. only production from the connected fracture network or early water breakthrough) [Lepillier et al., 2019, Wang et al., 2020]. The presented workflow also does account for elastic rock properties and local stress perturbations, both of which are known to be important when predicting fracture network characteristics in the sub-surface (e.g. [Bourne, 2003, Maerten et al., 2006, Roche and van der Baan, 2015]). Finally, for the presented modelling results (Figures 7.15, 7.16 and 7.17), we used a 2D modelling domain with a closed boundary and thermal properties which were laterally constant. By imposing these assumptions, we have introduced significant simplifications with respect to the actual 3D geometry and conditions of the subsurface, thereby making the results less comparable to real world projects.

Therefore, in order to better address and quantify the uncertainties introduced by the main modelling assumptions, we propose that the presented workflow could be improved and that additional modelling studies should be conducted. These improvements and studies could for example investigate the impact of 1) using probability density functions and variograms for property modelling, 2) different fracture length descriptions and distributions (e.g. Bonnet et al. [2001], Odling et al. [1999]), 3) different aperture distributions (e.g. [Hooker et al., 2014]) 4) using explicitly modelled faults and fractures (DFM) in fluid-flow/temperature simulations (e.g. [Boersma et al., 2019b, Lepillier et al., 2019, Wang et al., 2020]), 5) different fracture population methodologies (e.g. stress based fracture intensity drivers [Maerten et al., 2006, 2019, 2016]), 6) creating 3D rather than 2D reservoir models and DFN's, and 7) optimising the location of the injector and production wells whilst accounting for geological uncertainties (e.g. [Kahrobaei et al., 2019]). By doing so, we believe that a wider range of geologically realistic modelling results and well placement designs could be realized, which can potentially better account for the uncertainties introduced by limited data and subsurface knowledge.

7.8 Conclusions

This study implements a multiscale workflow of petrophysical analysis, geostatistical inversion, image-log interpretation, seismic discontinuity analysis and DFN- and geothermal modelling, in order to assess the potential impact of fractures on heat extraction from tight Lower-Triassic sandstones in the WNB. This study focusses on the Volpriehausen, Detfurth and Hardegsen formations surrounding the recently drilled NLW-GT-01 well.

First, the results of the petrophysical analysis and geostatistical inversion show that overall, the Lower-Triassic formation have poor reservoir properties. This was also observed by previous core analysis. Our results also indicate that the Volpriehausen formation has relatively low -, and the Detfurth and Hardegsen formations have relatively high porosities and permeabilities in the area surrounding the NLW-GT-01 well. Further-

more, our results show that relatively low acoustic impedance and high-porosity values coincide with positive to negative seismic amplitude changes, implying that the seismic data can be used to accurately indicate the relatively porous Hardegsen and Detfurth formations.

Second, the results of the image-log interpretation indicate that the Volpriehausen formation is significantly fractured and faulted, with the interpreted features mainly striking NW-SE and being hydraulically conductive. The extracted dips range between $\pm 60^\circ$ for the faults and $\pm 85^\circ$ for the fractures, respectively. The measured length and apertures range between 0.1 m to 12.0 m and 0.01 mm to 0.42 mm, respectively. The results also show that the fracture length and aperture follow a log-normal distribution and a negative power-law distribution, respectively. The seismic discontinuity analysis indicates that the extracted faults mainly show a NW-SE to N-S strike and generally align with the inverted horst structures. Near the NLW-GT-01 well, the extracted faults show orientations similar to those of the fractures observed in the image-log data (i.e. NW-SE).

Third, by integrating the results of the image log interpretation, the seismic discontinuity analysis with different aperture models (power-law, length-based, stress based), three different reservoir scale DFN's and upscaled fracture permeability models were generated. The resulting permeability models are dependent on the assigned aperture model and have effective permeabilities ranging from 0.01 mD for lowly-fractured areas to over 100 mD for highly fractured areas. These upscaled permeabilities are significantly higher than the observed matrix permeabilities. The geothermal modelling results indicate that, if open, the modelled natural fractures significantly aid the geothermal heat production from the normally tight sandstones, with modelled capacities ranging between 11.23 to 15.69 MWth for relatively low production rates. However, our models also suggest that when the natural fractures are closed, the Triassic formations are not suitable for geothermal production.

Finally, based on our findings, we suggest that measures which can investigate the potential of fracture aperture and connectivity under sub-surface conditions (e.g. active well tests) should become standard procedure for future geothermal wells targeting complex reservoirs in the WNB. In addition, we propose that the seismic inversion and discontinuity workflows could be utilized for mapping reservoir properties and highly fractured/faulted areas on a basin-wide scale, thereby helping the identification of potential sweet spots or hazardous areas

Supplementary materials and data availability

The presented data and supplementary materials (velocity modelling, image log calibration, wavelet generation and seismic well tie, and variograms and PDFs) can be found at via the following DOI: <https://doi.org/10.4121/uuid:646c3c27-71e9-4fcb-98d7-4d658f0c5859>

8

CONCLUSIONS AND RECOMMENDATIONS

The aim of this thesis was to characterize natural fracture networks using 1) numerical modelling, 2) outcrop analogue interpretation and characterization and 3) a subsurface case study. The findings of this work give insights in how natural fracture network development and saturation is affected by the regional stress conditions and material parameters. In addition, the presented results can help in assessing the impact on fracture characteristics such as aperture, hierarchy or connectivity on the fluid-flow, effective permeability or geothermal heat extraction. In the following, the main findings of this thesis are summarized. Further, the potential relevance and implications for future work are discussed.

8.1 Synopsis

8.1.1 Mechanical and tectonic controls on natural fracture network development and characteristics

Natural fracture networks form when the applied stresses overcome the rock strength. Following from linear elasticity and Linear Elastic Fracture Mechanics, the mode of fracturing (i.e. Mode I or II) and resulting network geometry are dependent on the type of stress applied (i.e. tensile or compressive) and mechanical parameters of the host rock. For example, we showed that orthogonal fracture networks (chapter 2 of this thesis) can form in response to bi-axial tensile stresses and reach a saturated state due to driving stress reduction caused by continued fracture infill. Our modelling also indicated that the numerically-derived networks are largely dependent on the applied tensile stress ratio with geometries ranging from critically-spaced parallel fractures to orthogonal networks where fractures have coeval abutment relationships.

In chapter 3, we showed that conjugate fracture networks can form in response to compressive stresses. Our modelling results indicated that these Mode II fracture networks develop via stress localization caused by Linear Elastic Fracture Mechanics, resulting in nested network geometries which show localized zones of intensive fracturing coinciding with areas having a low fracture intensity. Additionally, our findings showed that the fracture-intensity and fracture-porosity were largely dependent on the applied differential driving stresses, with larger stress magnitudes resulting in higher intensities and porosities.

Alternating layer properties also play a role in the development of natural fracture networks. For instance, our and previously presented studies indicated that within layered materials differences in elastic properties can cause significant local stress changes (i.e. Tensile or Compressive). These local stress changes generally cause differences in fracture behaviour (i.e. Mode I or II). By performing a sensitivity study (chapter 4), we mapped these local changes in stress and fracture behaviour. The results showed that large ratios in elastic properties resulted in tensile stresses and mode I fracturing in stiff layers, whereas soft layers showed an opposite effect. In addition, our results highlighted that low inter-facial frictions and high confining pressures negate the effect caused by alternating layer properties.

8.1.2 Characterization of natural fracture network patterns using outcrop analogues

By investigating natural fractures on outcrop analogues, potential links between different network geometries, characteristics, large scale features and imposed tectonic stresses can be investigated. Additionally, the impact of natural fractures on fluid flow and upscaled permeabilities can be quantified. The investigated sub-horizontal outcropping carbonate pavements of the Salitre fm are heavily fractured, with the interpreted network showing a hierarchical conjugate pattern (chapter 5). On site investigation showed that the natural fractures most likely formed in response to two subsequent compressive events striking NNW-SSE and WNW-ESE and were not affected by large scale faults or folds. Furthermore, the presented results point towards clear correlations between the natural fractures and a large underlying cave system. Therefore, these findings provide evidence that within the Brejoes study area, open natural fractures act as conduits for fluid flow, thereby controlling the geometry of large dissolution features such as karst tunnels. Finally, in addition to controlling the geometry of the Brejoes cave system, the presented numerical results indicate that the natural fractures greatly enhance the effective permeability of the studied carbonates.

Outcrop examples generally indicate that natural fracture arrangements have distinct hierarchical, spacing and/or topological relationships (e.g. chapters 2, 3 or 5). However, while these relationships control the overall geometry of natural fracture networks, they are generally not incorporated in Discrete Fracture Network (DFN) simulators. Therefore, in chapter 6, we presented a new DFN simulator (FracSim2D) which is able to account for observed fracture network characteristics by incorporating user defined placement rules in to the iterative workflow. The acquired results showed that by accounting for these geological rules, observations made on outcrop analogues were captured by the simulated DFN's. Furthermore, the impact on fluid flow and upscaled permeabilities were better captured by geologically controlled simulations.

8.1.3 The impact of natural fractures on heat extraction from low-permeability reservoirs

To assess the potential impact of open natural fractures on geothermal energy extraction from hot sedimentary aquifers, we presented a new case study which integrates well data analysis, seismic reservoir characterization and DFN - and temperature modelling (chapter 7). In this case study, the targeted reservoir were low-permeability Triassic sandstones located in the West Netherlands Basin. The available image logs indicated that the targeted reservoir is heavily fractured, with fracture apertures ranging between 0.01-0.5 mm. Further, the presented results indicated that when using the observed aperture distribution, the modelled natural fractures greatly enhance the effective permeability of the normally tight reservoir rock, thereby making geothermal heat production possible. However, when closed the results indicated that Triassic sandstones are not suitable geothermal energy development. Finally, while the presented results show that fractures can positively impact heat extraction from low-permeable reservoirs, it should be noted that the prediction and characterisation of natural fractures in the subsurface remains a relatively uncertain process.

8.2 Outlook and recommendations for future work

8.2.1 Placing the key findings in a broader conceptual understanding

The results presented in this Thesis further illustrate the mechanical and tectonic controls on fracture network development and saturation. When combined with other modelling techniques, we believe that our findings can help with establishing better constrained fracture network descriptions on a variety of scales.

For example, large scale numerical models of faulted - and/or folded outcrops/reservoirs provide detailed descriptions of local stress and strain matrices [Bisdom, 2016, Maerten et al., 2006, 2019, 2016, Watkins et al., 2015, 2018]. These detailed descriptions can be compared or used as input for fracture network development workflows as presented here or in other studies (e.g. chapters 2 and 3 or Guo et al. [2017], Ko and Kemeny [2011], Olson [2007], Shen and Rinne [2007]), such that mechanically constrained network descriptions for different locations within the respective models could be generated. Further, using tools such as Multiple Point Statistics (MPS) (e.g. Bruna et al. [2019]) these locally constrained networks could be extrapolated over the outcrop/reservoir modelling domain.

In chapters 2, 3 and 5 we modelled the fracture aperture for specific mechanical conditions (e.g. tensile stress, compressive stress, or stress induced aperture). The presented results and models provide mechanically constrained aperture descriptions for geologically realistic fracture network geometries. We believe that these aperture models could be utilized as input for small-scale thermodynamic models (e.g. Gale et al. [2010], Lander and Laubach [2014], Lander et al. [2008], Olson et al. [2009] or DARTS), so that fracture cementation and/or dissolution could be modelled whilst applying in-situ stress conditions. If done correctly, this allows for realistic descriptions of the natural fracture characteristics on outcrops and under subsurface conditions.

Therefore, if sufficient knowledge on the geological - and mechanical parameters is available, the aforementioned approaches can help in creating realistic natural fracture network descriptions on a wide variety of scales. However, if not available, utilizing these approaches may introduce significant uncertainties due to the lack of hard data points, thereby resulting in DFN's which may not be representative. In those situations, we believe it is more effective to use conceptually-, data- and/or statistically-driven methodologies (e.g. chapter 7).

Apart from numerical modelling, outcrop analogues studies (e.g. chapter 5) can also help in increasing our conceptual understanding natural fracture networks. For instance, if correctly interpreted and placed in a geological/tectonic context, outcrop descriptions can provide valuable lessons for linking tectonic and geological settings to potential end-member fracture network geometries. For example, interpretations done on drone imagery acquired from the Portuguar and Irece Basins (Brazil) showed that sub-horizontal tectonic stresses generally result in fracture networks comprised of connected conjugate and/or mixed-mode fractures and stress perpendicular tectonic stylolites [Bertotti et al., 2017, Bisdom et al., 2017a, Boersma et al., 2019b]. Alternately, orthogonal fracture networks are commonly believed to be created under a biaxial tensile stress field caused by pore-fluid over pressures, exhumation or alternating layer properties (e.g. Bai et al. [2002], Fossen [2010], Houben et al. [2017], Olson [2007]). These examples provide two possible end-members and their responsible driving stresses. We

believe that by combining these findings with other geological examples, an atlas of potential fracture network geometries and their responsible tectonic or geological drivers can be established, thereby widening our conceptual understanding of natural fractures within rocks.

8.2.2 Numerical techniques for modelling the development of a natural fracture networks

While our findings presented in chapters 2, 3 can help in providing a better understanding of the mechanical controls on fracture network development and saturation, the utilized methodology is numerically expensive and requires user input for each modelled time-step. This implies that the method used in thesis is time-consuming and could be susceptible to biases introduced by the user. Further, due to limitations in the Abaqus code, meshing intersecting or abutting fractures was difficult (e.g. [Bisdorn \[2016\]](#)), thereby introducing potential errors in to the modelling of connected fracture networks (see section 3.4.2).

Due to these limitations, we propose that for future studies which model the development of natural fracture networks, other numerical techniques should be considered. For example, different dedicated Boundary Element Method (BEM) - and Displacement Discontinuity Method (DDM) tools (e.g. [Olson \[2007\]](#) or FRACOD [Shen and Rinne \[2007\]](#)) have been developed to model natural fracture network development. These tools have shown promising results and are numerically less expensive than the quasi-static FEM method presented in this Thesis. Another numerical technique which could be investigated is the Discrete Element Modelling (DEM). For instance, a DEM code developed by the University of Manchester has shown promising results in modelling the development of 3D fault networks in layered materials (e.g. [Deng et al. \[2018\]](#), [Finch et al. \[2004\]](#), [Pichel et al. \[2019\]](#)). Finally, we propose that the combined finite-discrete element method (FEMDEM) could be investigated [[Munjiza, 2004](#)]. This tool has successfully been applied to model natural fracture network development in layered materials by [Guo \[2014\]](#) and [Guo et al. \[2017\]](#).

8.2.3 Future of drone imagery in outcrop analogue studies

With drones becoming cheaper in the last decade, their usage has become fully embedded within outcrop analogue - and/or fracture characterization studies. This has led to a wealth of high quality outcrop data now being publicly available (e.g. appendix C). These datasets can for example help in 1) providing detailed descriptions of naturally occurring fracture networks and 2) with establishing links between small - and large-scale structural features. Additionally, newer drones can also be used for characterizing natural fractures on cliff outcrops, thereby allowing for detailed interpretation of the vertical plane (e.g. DJI Phantom 4 (chapter 5 and appendix C)). We also propose that when combined with data from fractured pavements, cliff outcrop data can be used for establishing better statistical links between the vertical - and horizontal component of natural fractures (i.e. length, height and aspect ratio). Finally, new and high quality drone imagery can be utilized as input for image processing - and automated fracture interpretation algorithms (e.g. [Prabhakaran et al. \[2019\]](#)). By doing so, natural fracture networks can be characterized in great detail and without any biases introduced by the interpreter.

8.2.4 Using FracSim2D as input for MPS models

Using FracSim2D (chapter 6), we were able to include fracture characteristics such as spacing, hierarchy and topology in to 2D DFN simulations. By doing so, the presented results provided accurate descriptions of network geometries observed on outcrop analogues (e.g. Figures 6.7 or 6.8). We believe that FracSim2D could be used in combination with MPS (e.g. Bruna et al. [2019]). To this end FracSim2D can be utilized for generating geologically - and statistically constrained Training Images, which can be used as input for MPS algorithms in order to create large scale and geologically feasible fracture network descriptions.

8.2.5 Basin scale seismic reservoir characterization for the purpose of geothermal energy exploration

In chapter 7 of this dissertation, we introduced a newly reprocessed seismic dataset and a multidisciplinary seismic reservoir characterization workflow. This chapter showed promising results for the studied Triassic reservoir. We believe that the presented workflow could be upscaled for the extent of the seismic dataset (xmin: 59542, ymin: 422783 and xmax: 97553, ymax: 459549 (CRS: RD-Amersfoort)). For example, the large number of freely available wells within the West Netherlands Basin could be integrated with the reprocessed seismics using geostatistical - or deterministic inversion, so that the properties of the different aquifers (e.g. the Nieuwekerk Formation or Main Buntsanstein Sub-Group) are mapped on a basin scale. In addition, we propose that the seismic discontinuity workflow may be utilized for identifying highly fractured or faulted areas. The resulting property maps and seismic discontinuity maps could then be used to identify potential sweet spots or hazardous areas for geothermal energy development. Finally, we believe that if the quality of the seismic data is sufficient, the workflow presented in this dissertation could also be applied to other areas in the Netherlands (e.g. Parts of the Roer Valley Graben or other areas of the West Netherlands Basin).

A

**INTERACTIVE PYTHON SCRIPT FOR
ESTIMATING STYLOLITE DEPTH OF
FORMATION**

Introduction

Stylolites form serrated and rough paired surfaces and are commonly observed in carbonate rocks. These features develop due to stress induced dissolution with the applied stresses acting perpendicular to the stylolite plane [Ebner et al., 2009]. Studies have shown that depending on their geometry and mineralogy, stylolites can either enhance or inhibit fluid flow [Bruna et al., 2018]. Therefore, when concerning geothermal or petroleum production from tight carbonate reservoirs, the presence of stylolites will have a significant effect on the effective permeability and preferred flow directions of injected or produced fluids [Bruna et al., 2018, Teufel and Farrell, 1990, Toublanc et al., 2005]. This implies that an optimal field development plan of a carbonate reservoir for either petroleum or geothermal production, includes knowledge on the extend and geometry of these features, so that well planning and production is optimized.

Although the impact that stylolites have on fluid flow and production is increasingly recognized, mapping these structures in sub-surface reservoirs is difficult because they generally fall below the seismic resolution. Due to the lack of hard data, the presence of stylolites in the subsurface is often predicted, with the help of outcropping rocks. In general, these predictions are made using quantitative relations between the feature's geometry and the underlying physical mechanisms. A significant breakthrough in quantifying these mechanisms was achieved using numerical modelling [Ebner et al., 2009, Koehn et al., 2007, Schmittbuhl et al., 2004]. These authors showed that the characteristic geometry of a stylolite features can be used as a proxy for estimating the depth and pressure of formation, using a Fourier Spectrum Analysis (FSA). Therefore, this approach could be utilized to better quantify the relation between stylolite geometry and the responsible stresses, thereby helping in making better predictions for the presence and geometry of stylolites in the subsurface.

While this approach is widely established, tools which can calculate the depth and pressure of formation from natural stylolite geometries are generally not freely available. Therefore, in this appendix, we present an interactive python script, which uses FSA to estimate pressure and depth of stylolite formation [Ebner et al., 2009]. For validation, the proposed workflow is tested on multiple stylolite samples which were acquired from the same outcrop.

Methods and theoretical background

Before the FSA can be applied, samples taken from outcrop analogues need to be prepared and interpreted. Preparation is ideally done by cutting the sample perpendicular to the stylolite plane, so that the geometry of the stylolite feature is clearly revealed (Fig A.1). As of now, the script requires manual interpretation and digitization of the stylolite sample. For this study, the interpretation of the stylolite sample was done using QGIS. The interpreted stylolite features were converted to x-y point-sets so that they could be implemented into our python tool.

In order to apply an FSA, we assume that the stylolite samples are self-similar/fractal surfaces. These surfaces are characterized by negative power law behaviour and a specific Hurst component, which describes the slope [Ebner et al., 2009, Toussaint et al., 2018] (equation A.1):

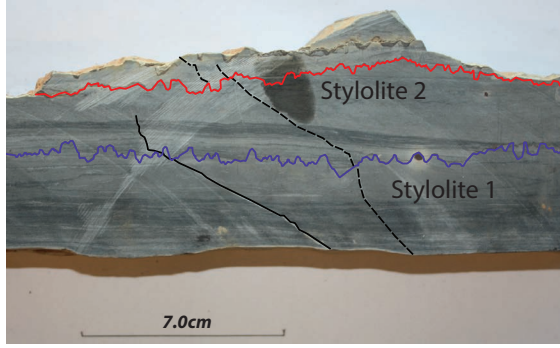


Figure A.1: Showing a stylolite sample from Brejoes (Bahia, Brazil) which has been analysed using this script.

$$P_{(k)} \approx ak^{-1-2H} \quad (\text{A.1})$$

where, k is the wavenumber, H is the Hurst component, a is the constant dependent on the stylolite sample and $P_{(k)}$ is the Fourier power spectrum. Stylolites are generally characterized by two of these self-similar regimes (equation A.1), working on the small and large scale, respectively. Each regime is characterised by a specific Hurst component, with measurements usually showing a higher roughness values for the small scale wavelengths ($l < 1\text{mm}$) lower values for the large scale wavelengths ($l > 1\text{mm}$). The characteristic wavelength (cross-over length (L_c)), by which the two characteristic regimes are separated is dependent on the stylolite geometry.

In our workflow the characteristic Hurst components and cross-over lengths for a given stylolite sample are extracted using a Fourier power spectrum analysis. The first step in this workflow is to interpolate the initial stylolite data, and apply the Fourier power spectrum analysis (Figs A.2a and b). The resulting power spectrum is then smoothed using a dynamic average approach, so that the two regimes are better defined (Fig A.2b). From the binned dataset, two different power law descriptions are defined (fig A.2c). However, it should be noted that the specific bin parameters differ for each stylolite sample (i.e. defining which points belong to the long and short wavelengths, and defining which points should be excluded). The cross-over point between the two power laws then defines the characteristic cross-over length (L_c) of the initial stylolite sample [Ebner et al., 2009] (fig A.2c). A possible link between this cross-over length and the underlying thermodynamic and elastic processes was first defined by [Schmittbuhl et al., 2004]. These authors proposed that the relation between L_c and the state of stress can be described by equation A.2:

$$L_c = \frac{\gamma E}{\beta \sigma_m \sigma_d} \quad (\text{A.2})$$

where E is the Young's modulus [GPa], γ is the solid-fluid interfacial energy [J/m²], $\beta = \frac{\nu(1-2\nu)}{\pi}$, ν is the Poisson's ratio and σ_m and σ_d are the mean and differential stress respectively. For this appendix we assume that both horizontal stresses are equal so that

the horizontal principal stresses can be expressed in terms of Poisson's ratio (ν) and the vertical stress (σ_{zz}) [Ebner et al., 2009]:

$$\sigma_m \sigma_d = \left(\frac{1}{3} \left(\frac{1+\nu}{1-\nu} \right) \left(\frac{1-2\nu}{1-\nu} \right) \right) \sigma_{zz} \quad (\text{A.3})$$

From σ_{zz} the depth of stylolite formation can be estimated assuming: $\sigma_{zz} = \rho g z$, where ρ is the rock density (kg/m^3) and g is the gravitational acceleration (m/s^2) and z is the depth (m). Finally, these equations and the extracted L_c (Fig A.2a-c), we can estimate the pressure and depth of stylolite formation (assuming that the other variables are known) (Fig A.2d).

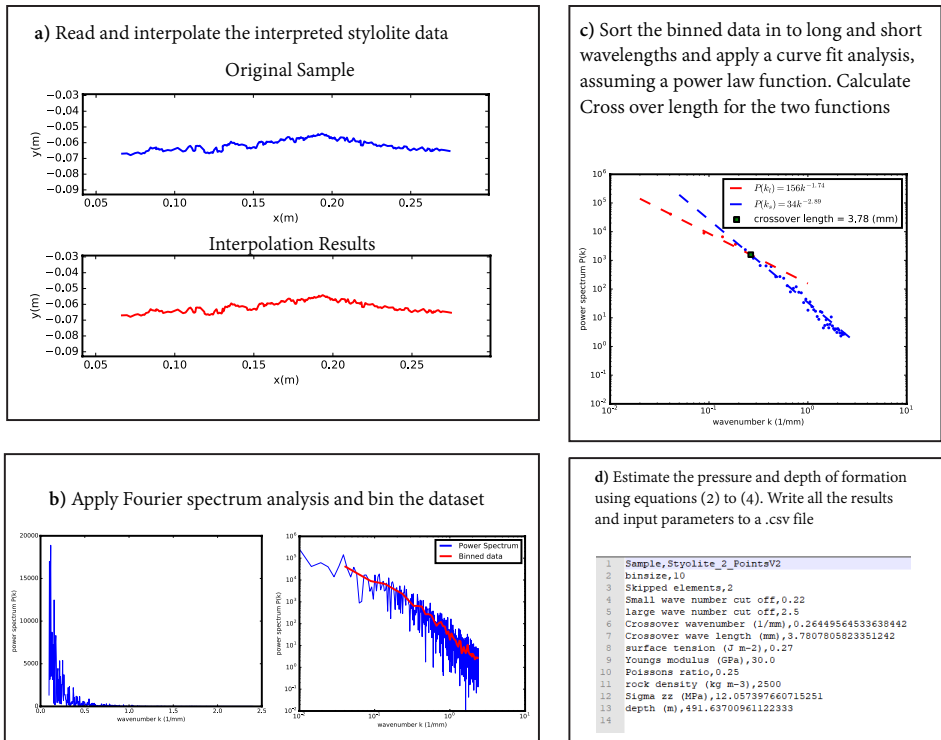


Figure A.2: Workflow for estimating the stylolite depth of formation from a natural stylolite sample, using Fourier spectrum analysis.

Results

The FSA workflow is applied on four different stylolite geometries (sample 1A, 1B, 2A and 2B respectively) which were taken from the same rock sample (Fig A.1). Here, sample 1A and 1B and 2A and 2B are essentially different depictions of two stylolites. The resulting power-spectra show that each stylolite geometry has a cross over length (L_c) at which the two power-law regimes are separated (i.e. a shallow slope for the long wavelengths

and a steep slope for short wavelengths). Although there are differences between each extracted power spectrum, there are also distinct similarities. For instance, samples 1A and 1B show almost identical power spectra, Hurst components and cross-over lengths (Figs A.3a and b). Samples 2A and 2B show less similarities and these samples were also more difficult to interpret, especially regarding sample 2A (Figs A.3c and d). For this sample, the difference between the two power-law regimes was not apparent, making a correct estimation of the cross-over length difficult. For the other samples, this problem did not occur and from the Fourier Power Spectrum, we were able to clearly derive two different power-law regimes and a cross-over lengths. The results from the Fourier Spectrum Analysis are summarized in table A.1.

Using the presented equations and the extracted cross-over length, we could estimate the depth and pressure of formation. The results from all analysed samples are displayed in table A.1. For the calculations, we assumed a Young's Modulus (E), Poisson's Ratio (ν), surface tension (γ) and rock density (ρ) of 30 (GPa), 0.25, 0.27 (J/m^2) and 2500 (kg/m^3) respectively. Furthermore, we assumed that no additional tectonic stresses were active during stylolite development. The results show that all stylolites developed at similar depths (420 to 491 m) and overburden stresses (10.35 to 12.06 MPa).

Table A.1: Results from the FSA and depth estimations for four analysed stylolite samples.

Sample	(a_s, a_l) and (H_s, H_l)	L_c (mm)	ν, E, γ, ρ (-, GPa, $\text{J/m}^2, \text{kg/m}^3$)	σ_{zz}, z (MPa, m)
1a	$a_s = 16, a_l = 1140,$ $H_s = 1.42, H_l = 0.06$	$L_c = 4.69$	$\nu = 0.25, E = 30, \gamma =$ $0.27, \rho = 2500$	$\sigma_{zz} = 10.50,$ $z = 428.04$
1b	$a_s = 37, a_l = 997,$ $H_s = 1.20, H_l = 0.18$	$L_c = 4.99$	$\nu = 0.25, E = 30, \gamma =$ $0.27, \rho = 2500$	$\sigma_{zz} = 10.50,$ $z = 428.04$
2a	$a_s = 54, a_l = 138,$ $H_s = 0.7, H_l = 0.42$	$L_c = 5.13$	$\nu = 0.25, E = 30, \gamma =$ $0.27, \rho = 2500$	$\sigma_{zz} = 10.35,$ $z = 421.92$
2b	$a_s = 34, a_l = 156,$ $H_s = 0.945, H_l =$ 0.37	$L_c = 3.78$	$\nu = 0.25, E = 30, \gamma =$ $0.27, \rho = 2500$	$\sigma_{zz} = 12.06,$ $z = 491.70$

Discussion and conclusions

An interactive python script for estimating the depth of stylolite formation

We have presented an interactive python script which uses an existing methodology of Fourier Spectrum Analysis, curve fit analysis and key relations derived from numerical modelling [Ebner et al., 2009, Schmittbuhl et al., 2004], in order to estimate the depth and pressure of stylolite formation for a given stylolite geometry. The presented results show similar depths and pressures for all analysed stylolites, indicating that the applied workflow delivers consistent results (Fig A.3 and Table A.1). However, it should be noted that the magnitude of these calculated depths and pressures is strongly dependent on the implemented material parameters and assumed tectonic stresses [Bertotti et al., 2017]. Therefore, having accurate knowledge of the rock characteristics and tectonic setting is key in making accurate depth and pressure estimations. Another important observation, is that stylolite samples need to have two clearly distinct power law regimes in order for this workflow to calculate a distinct cross-over length. For example, as was shown with

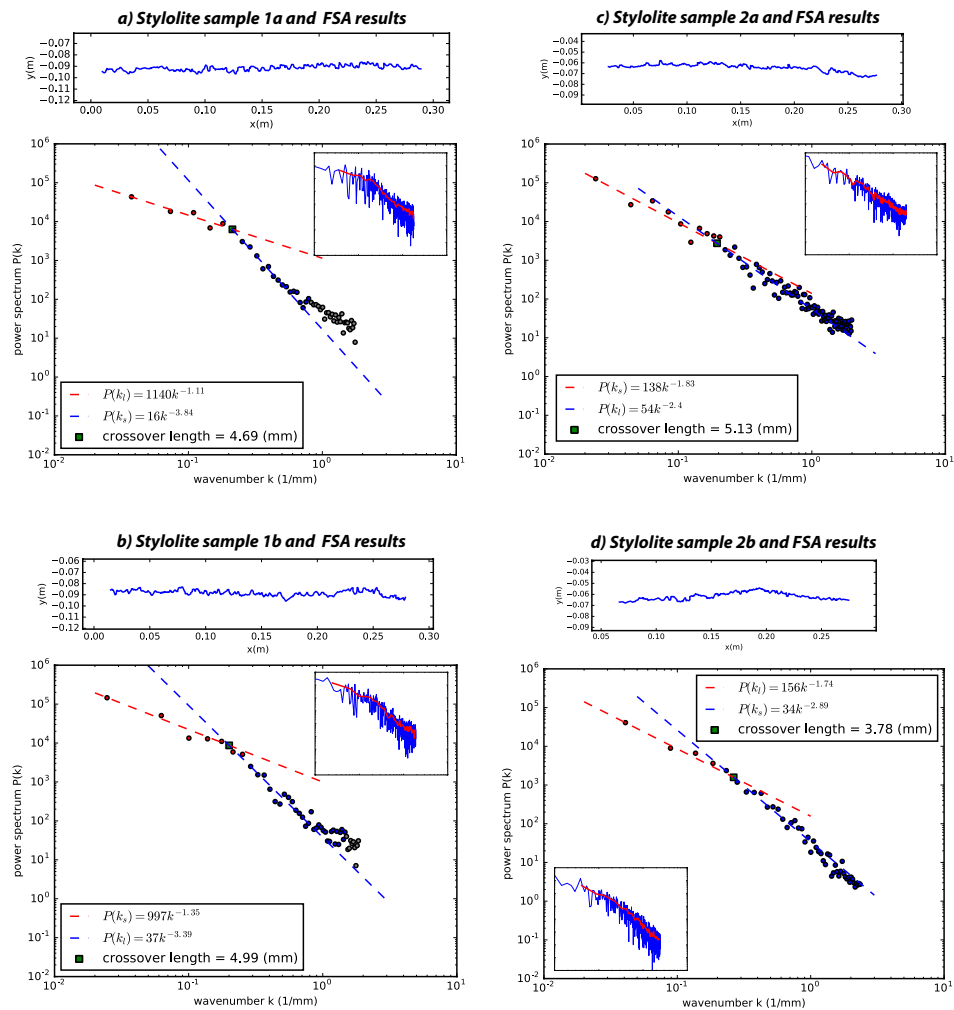


Figure A.3: a-d) Interpolation and FSA results for each stylolite 1A, 1B, 2A and 2B respectively. The grey dots represent sub-sampled points which are excluded from the power law fitting.

sample 2A, defining a clear cross-over length was difficult because the two power-law regimes shared similar Hurst components (Fig A.3c and table A.1). Therefore, analysing multiple stylolites from one rock sample is advised in order to fully validate the extracted cross-over length.

Implications and future work

Being able to relate and quantify a stylolite geometry to the depth of formation is important for both reservoir - and field case studies. For instance, the question of whether stylolites will act as fluid flow conduits is dependent on their mineralogy, geometry and roughness [Bruna et al., 2018]. The presented script can help in relating these key features to a depth of formation, and can therefore help in making better predictions for subsurface reservoirs. Furthermore, using the presented workflow, stylolite geometries can be used as paleo-stress indicators which can help in making better descriptions of rock diagenesis and tectonic settings [Bertotti et al., 2017, Ebner et al., 2009]. Finally, although the presented results show a clear consistency, this workflow needs to be further validated using for instance stylolite samples from different outcrops, so that the relation between the observed stylolite geometry and depth of formation is better defined.

Data availability

The python code and examples presented in this appendix are freely available and can be downloaded via the following DOI: <https://doi.org/10.4121/uuid:8b76aff7-4a55-463a-acb5-86af1c519a11>

B

SCRIPTS FOR EXTRACTING 2D AND 3D DATA FROM ABAQUS DATABASE FILES

The presented scripts were created in collaboration with Nico Hardebol

Introduction

Throughout this thesis we use the ABAQUS FEM code to model stress, strain and Linear Elastic Fracture Mechanics. The modelled results are saved as .odb files, which can be opened and displayed the user interface (ABAQUS CAE). However, displaying these .odb files outside of ABAQUS user interface is impossible. Furthermore, extracting the 2D or 3D data using the provided tools is cumbersome. To overcome this limitation, we have created a set of python scripts which can read these .odb files and extract the stress and strain results for each meshed element. The presented scripts (Figure B.1) are written in Python and need to be run inside the ABAQUS user interface. Moreover, as of now the scripts require quadratic triangular or tetrahedral elements (for 2D and 3D, respectively), in order to work.

General workflow of the scripts

The general purpose of the presented python tool is to automatically extract stress and strain results for an array of odb database files. These results are then written to CSV files, which can be analysed and plotted in software programs such as excel, python and matlab. It should be noted that the provided scripts are fitted to models presented throughout this thesis, and therefore, these scripts need to be adjusted accordingly in order to work for different models.

The first step in the workflow is to define the different filepaths and input parameters (i.e: 1) database location, 2) output folder, 3) database name, 4) stepname, 5) setname 6) frame index (number of iteration steps) and 7) element type). Here, the stepname, setname, frame index and element type are parameters dependent on the model design and output file and need to accordingly (Figure B.1). Secondly, the script loops through the array of defined odb files and extracts the stress and strain data. The variables to be extracted can be changed by the user. Thirdly, for each subset (i.e. different instances in the model), two CSV files are generated, one which stores the stress and strain matrix and one which stores the principal stresses. Fourthly, the script enumerates through the element list and extracts all connecting nodes numbers for each respective element. Fifthly, the stress data and coordinates are extracted from the respective elements and connecting nodes, respectively. Finally, the stresses, strains and corresponding coordinates are stored in the created CSV files (Figure B.1).

It should be noted that because of the difference in dimensions and different element shapes (triangular and tetrahedral), the scripts for the 2D and 3D modelling data are slightly different. The two scripts are depicted by figure B.1 a and b, for 2D and 3D modelling data, respectively.

Apart from using this workflow for extracting stress and strain data from 2D or 3D models, the presented workflow can also be used to extract slip, shear, opening and contact pressures from 2D and 3D fracture planes. Here, the scripts extract the modelled variables for each fracture nodes again storing the data in a respective CSV file.

Data availability

The presented python scripts for chapter 2 can be downloaded via the following DOI: <https://doi.org/10.4121/uuid:4fc843b2-3cef-4637-9693-caf412c3b8df>.

The python scripts presented in chapter 3 can be downloaded using <https://doi.org/10.4121/uuid:1b586b92-5e9d-4aeb-9d7b-76b289a1c791>. The

scripts used in chapter 4 can be found using <https://doi.org/10.4121/uuid:fabdd80b-02c8-4e83-81cb-4891459b3e9e>.

C

ACQUIRED DRONE DATA AND NATURAL FRACTURE INTERPRETATIONS

For this thesis we acquired and interpreted drone imagery from both pavement and cliff outcrops (see chapter 5). The data is publicly available via the 4TU database and can be downloaded via the following DOI: <https://doi.org/10.4121/uuid:7dede8dd-538a-4b70-a110-3f899e37e8ca>

The cliff interpretations have been done by Cindy Dubbeld

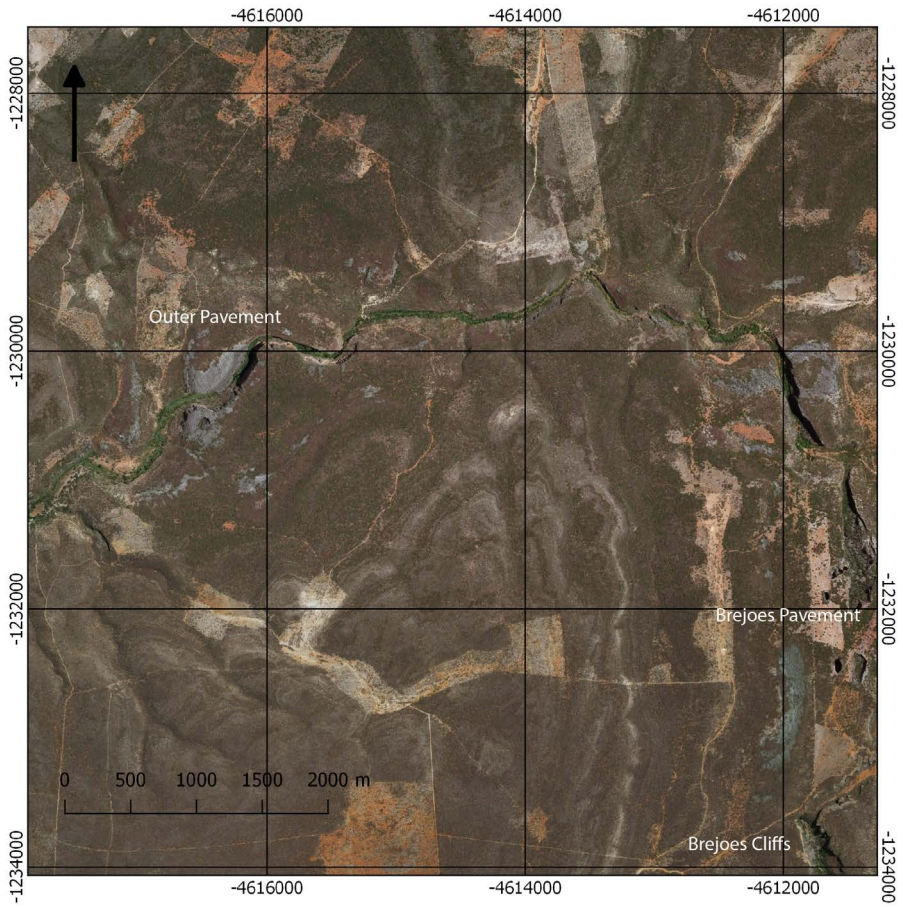


Figure C.1: Satellite image and outcrop locations of Brejoes study area

Brejoes Large Scale Pavement Interpretation

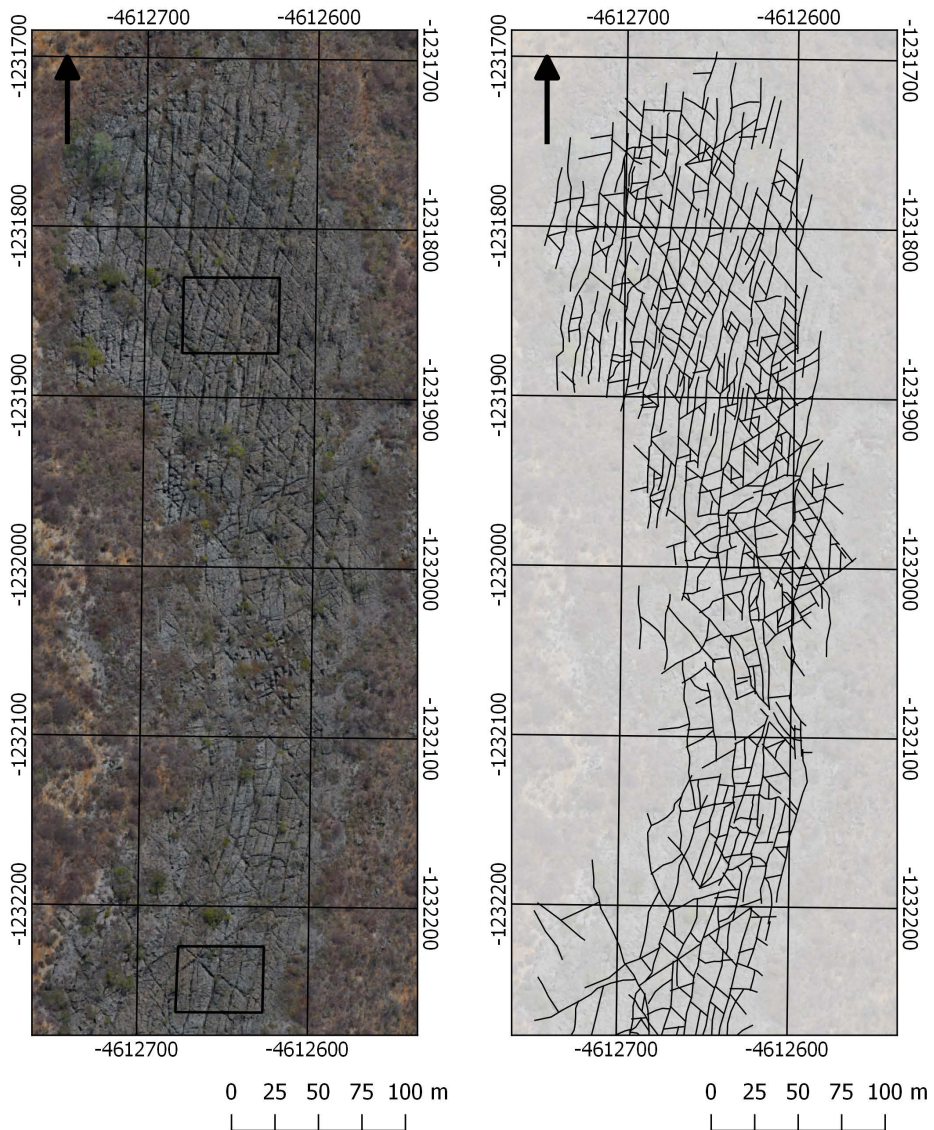
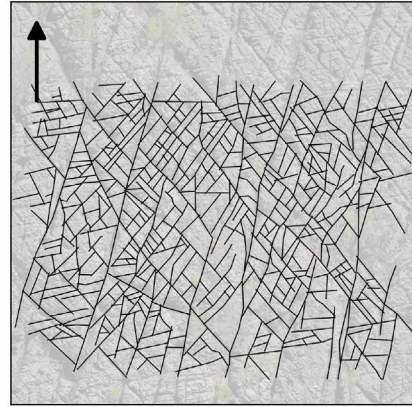


Figure C.2: Orthomosaic and interpretation of the Brejoes fractured pavement. The location of the interpretations shown in figure C.3 are highlighted by the black boxes

Brejoes North Station



0 5 10 15 20 m

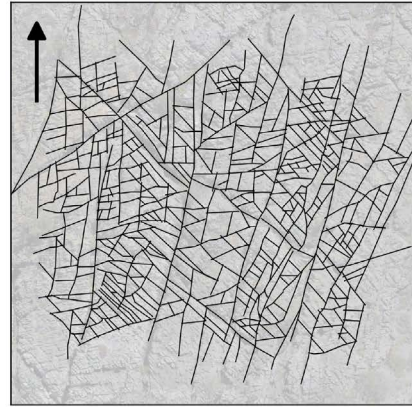


0 5 10 15 20 m

Brejoes South Station



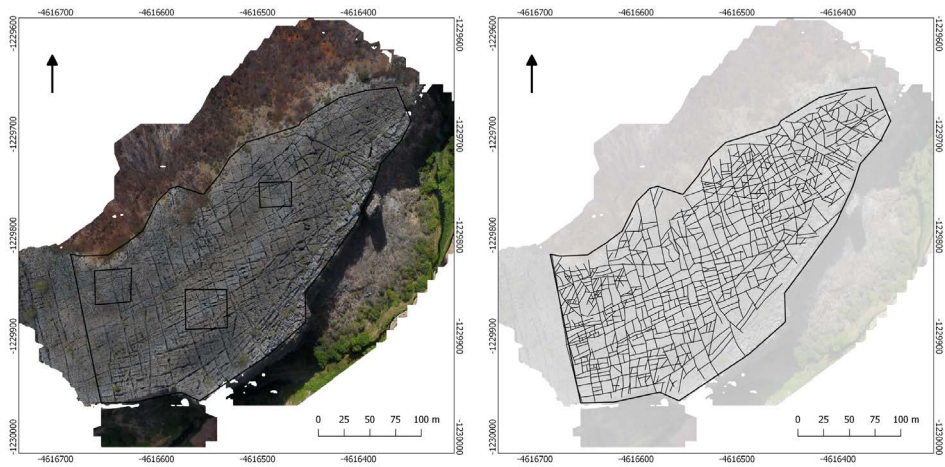
0 5 10 15 20 m



0 5 10 15 20 m

Figure C.3: Detailed interpretations of the Brejoes pavement.

Outer Pavement Large Scale Interpretation



West Station



Mid Station



East Station

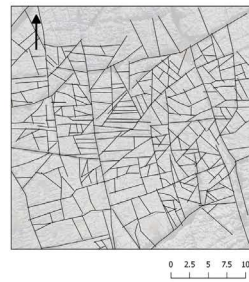
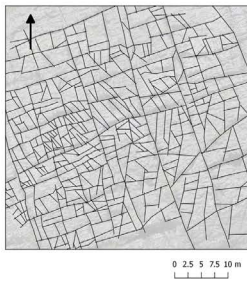
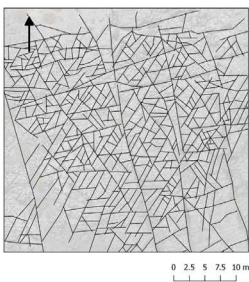


Figure C.4: Outer pavement orthomosaics and interpretations on the large and small scales, respectively.

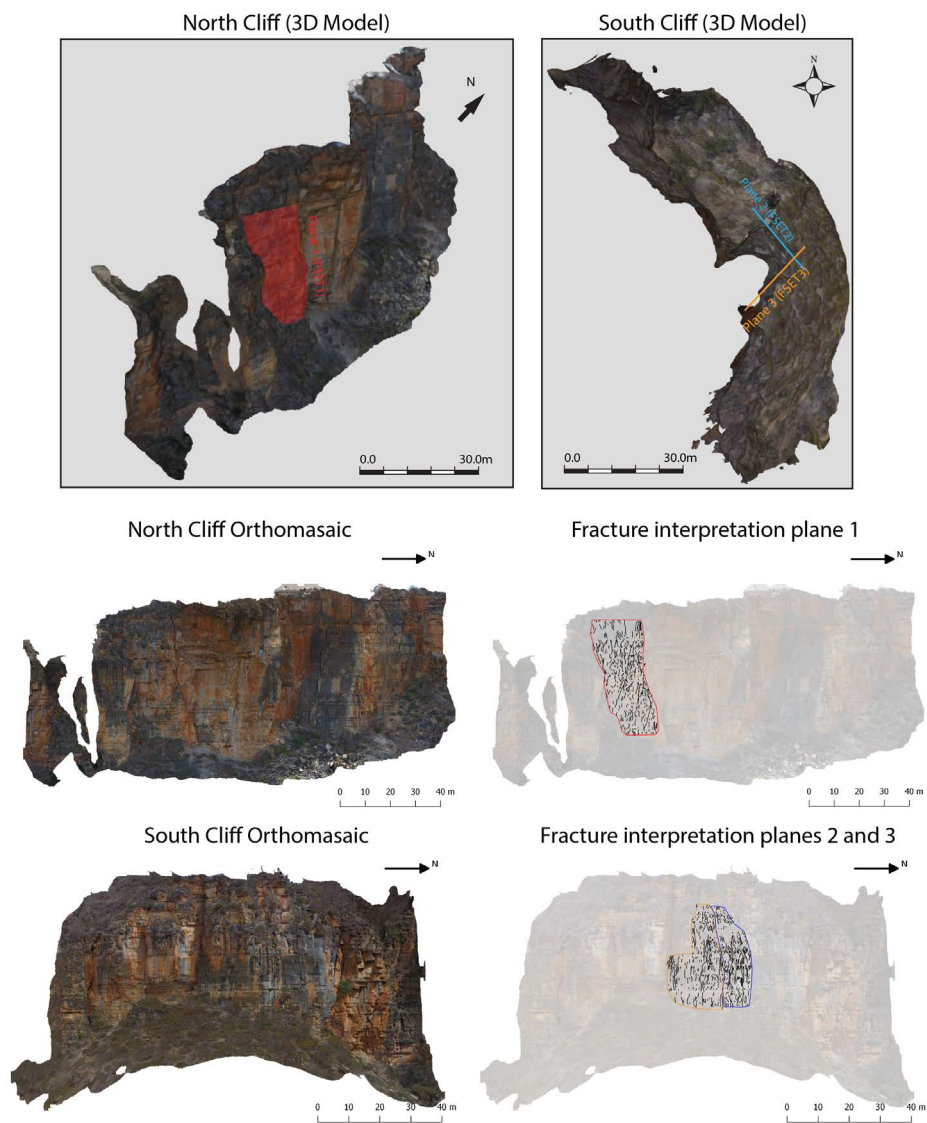


Figure C.5: 3D models, orthomosaics and fracture interpretations done of the Brejoes cliff outcrops. It should be noted that fractures have been interpreted on different planes, which run parallel to one of the interpreted fracture sets (see chapter 5).

BIBLIOGRAPHY

References

- Alstott, Jeff, Ed Bullmore, and Dietmar Plenz (2014), "Powerlaw: A python package for analysis of heavy-tailed distributions." *PLoS ONE*, 9.
- Asadollahi, Pooyan (2009), *Stability analysis of a single three dimensional rock block- Effect of dilatancy and high-velocity water jet impact*. The University of Texas at Austin, URL <https://repositories.lib.utexas.edu/handle/2152/7526>.
- Asadollahi, Pooyan, Marco C.A. Invernizzi, Simone Addotto, and Fulvio Tonon (2010), "Experimental validation of modified Barton's model for rock fractures." *Rock Mechanics and Rock Engineering*, 43, 597–613.
- Asadollahi, Pooyan and Fulvio Tonon (2010), "Constitutive model for rock fractures: Revisiting Barton's empirical model." *Engineering Geology*, 113, 11–32.
- Atkinson, Barry Kean (1984), "Subcritical Crack Growth in Geological Materials." *Journal of Geophysical Research*, 89, 4077–4114.
- Bai, Taixu, Laurent Maerten, Michael R. Gross, and Atilla Aydin (2002), "Orthogonal cross joints: Do they imply a regional stress rotation?" *Journal of Structural Geology*, 24, 77–88.
- Bai, Taixu and David D. Pollard (2000), "Fracture spacing in layered rocks: A new explanation based on the stress transition." *Journal of Structural Geology*, 22, 43–57.
- Bai, Taixu and David D Pollard (2001), "Getting more for less: The unusual efficiency of fluid flow in fractures." *Geophysical Research Letters*, 28, 65–68.
- Baomin, Zhang and Liu Jingjiang (2009), "Classification and characteristics of karst reservoirs in China and related theories." *Petroleum Exploration and Development*, 36, 12–29, URL [http://dx.doi.org/10.1016/S1876-3804\(09\)60107-5](http://dx.doi.org/10.1016/S1876-3804(09)60107-5).
- Barnhoorn, Auke, Stephen F. Cox, David J. Robinson, and Tim Senden (2010), "Stress- and fluid-driven failure during fracture array growth: Implications for coupled deformation and fluid flow in the crust." *Geology*, 38, 779–782.
- Barton, N., S. Bandis, and K. Bakhtar (1985), "Strength, deformation and conductivity coupling of rock joints." *International Journal of Rock Mechanics and Mining Sciences and*, 22, 121–140.
- Barton, Nick and Stavros Bandis (1980), "Some Effects of Scale on the Shear Strength of Joints." *International Journal of Rock Mechanics and Mining Sciences*, 17, 69–73.
- Belayneh, Mandefro and John W. Cosgrove (2004), "Fracture-pattern variations around a major fold and their implications regarding fracture prediction using limited data: an example from the Bristol Channel Basin." *The Initiation, Propagation, and Arrest of Joints and Other Fractures*. Geological Society, London, *Special Publications*, 231, 89–102.

- Bertotti, Giovanni, Stefan de Graaf, Kevin Bisdom, Brigit Oskam, Hubert B. Vonhof, Francisco H. R. Bezerra, John J. G. Reijmer, and Caroline L. Cazarin (2017), "Fracturing and fluid-flow during post-rift subsidence in carbonates of the Jandaíra Formation, Potiguar Basin, NE Brazil." *Basin Research*.
- Billi, Andrea, Andrea Valle, Mauro Brilli, Claudio Faccenna, and Renato Funicello (2007), "Fracture-controlled fluid circulation and dissolutional weathering in sinkhole-prone carbonate rocks from central Italy." *Journal of Structural Geology*, 29, 385–395.
- Bisdom, K., G. Bertotti, and F. H. Bezerra (2017a), "Inter-well scale natural fracture geometry and permeability variations in low-deformation carbonate rocks." *Journal of Structural Geology*, 97, 23–36, URL <http://dx.doi.org/10.1016/j.jsg.2017.02.011>.
- Bisdom, K, H M Nick, and G Bertotti (2017b), "Computers & Geosciences An integrated work flow for stress and flow modelling using outcrop-derived discrete fracture networks." *Computers and Geosciences*, 103, 21–35, URL <http://dx.doi.org/10.1016/j.cageo.2017.02.019>.
- Bisdom, Kevin (2016), *Burial-related fracturing in sub-horizontal and folded reservoirs: Geometry, geomechanics and impact on permeability*.
- Bisdom, Kevin, Giovanni Bertotti, and Hamidreza M. Nick (2016a), "A geometrically based method for predicting stress-induced fracture aperture and flow in discrete fracture networks." *AAPG Bulletin*, 100, 1075–1097.
- Bisdom, Kevin, Giovanni Bertotti, and Hamidreza M Nick (2016b), "The impact of different aperture distribution models and critical stress criteria on equivalent permeability in fractured rocks." *Journal of Geophysical Research: Solid Earth*, 121, 4045–4063.
- Bisdom, Kevin, Giovanni Bertotti, and Hamidreza M. Nick (2016c), "The impact of in-situ stress and outcrop-based fracture geometry on hydraulic aperture and upscaled permeability in fractured reservoirs." *Tectonophysics*, 690, 63–75, URL <http://dx.doi.org/10.1016/j.tecto.2016.04.006>.
- Bizzi, L.A., C. Schobbenhaus, R.M. Vidotti, and J.H. Gonçalves (2003), *Geology, Tectonics and Mineral Resources of Brazil. Text, Maps and GIS*. 1.
- Boe, Trond Hellem (2012), "Enhancement of large faults with a windowed 3D Radon transform filter." In *SEG Technical Program Expanded Abstracts 2012*, 1–5, URL <http://library.seg.org/doi/abs/10.1190/segam2012-1008.1>.
- Boersma, Q, W Athmer, M Etchebes, J Haukås, and G. Bertotti (2019a), "Natural fracture prediction: A multiscale integration of seismic data, image logs and numerical forward modelling." In *81st EAGE Conference & Exhibition*, June, 3–6.
- Boersma, Q., R. Prabhakaran, F.H. Bezerra, and G. Bertotti (2019b), "Linking natural fractures to karst cave development: A case study combining drone imagery, a natural cave network and numerical aperture modelling." *Petroleum Geoscience*.
- Boersma, Quinten, Nico Hardebol, Auke Barnhoorn, and Giovanni Bertotti (2018a), "Mechanical Factors Controlling the Development of Orthogonal and Nested Fracture Network Geometries." *Rock Mechanics and Rock Engineering*, 51, 3455–3469, URL <http://dx.doi.org/10.1007/s00603-018-1552-8>.

- Boersma, Quinten D, Lisanne A N R Douma, Giovanni Bertotti, and Auke Barnhoorn (2020), “Mechanical Controls on Horizontal Stresses and Fracture Behaviour in Layered Rocks : A Numerical Sensitivity Analysis.” *Journal of Structural Geology*, URL <https://doi.org/10.1016/j.jsg.2019.103907>.
- Boersma, Quinten D, Hilario Bezerra, and Giovanni Bertotti (2018b), “Structural Modelling of a Fractured Carbonate Reservoir Analogue.” *AAPG ACE 2018 Conference, Salt Lake City*.
- Bonnet, E, O Bour, N E Odling, P Davy, I Main, P Cowie, and B Berkowitz (2001), “Scaling of fracture systems in geological media.” *Reviews of Geophysics*, 347–383.
- Bonté, D., J. D. Van Wees, and J. M. Verweij (2012), “Subsurface temperature of the onshore Netherlands: New temperature dataset and modelling.” *Geologie en Mijnbouw/Netherlands Journal of Geosciences*, 91, 491–515.
- Bounaim, Aicha, Marie Etchebes, Jarle Haukås, Hilde Borgos, Bjørn Harald Fotland, and Lars Sonneland (2019), “Vector attributes - A family of advanced seismic attributes to assist in geological interpretation.” In *SEG International Exposition and Annual Meeting 2019*, 1813–1817.
- Bourne, Stephen J. (2003), “Contrast of elastic properties between rock layers as a mechanism for the initiation and orientation of tensile failure under uniform remote compression.” *Journal of Geophysical Research*, 108, 2395.
- Brenner, Sonja L. and Agust Gudmundsson (2004), “Arrest and aperture variation of hydrofractures in layered reservoirs.” *Geological Society, London, Special Publications*, 231, 117–128, URL <http://sp.lyellcollection.org/lookup/doi/10.1144/GSL.SP.2004.231.01.08>.
- Bruhn, Carlos H. L., Antonio C. C. Pinto, Paulo R. S. Johann, Celso C. M. Branco, Marcelo C. Sa-lomão, and Ednilson B. Freire (2017), “Campos and Santos Basins: 40 Years of Reservoir Characterization and Management of Shallow- to Ultra-Deep Water, Post- and Pre-Salt Reservoirs - Historical Overview and Future Challenges.” In *OTC Brasil*, 1–24, URL <http://www.onepetro.org/doi/10.4043/28159-MS>.
- Bruna, Pierre Olivier, Arthur P.C. Lavenu, Christophe Matonti, and Giovanni Bertotti (2018), “Are stylolites fluid-flow efficient features?” *Journal of Structural Geology*, 1–8, URL <https://doi.org/10.1016/j.jsg.2018.05.018>.
- Bruna, Pierre Olivier, Julien Straubhaar, Rahul Prabhakaran, Giovanni Bertotti, Kevin Bisdom, Gre-goire Mariethoz, and Marco Meda (2019), “A new methodology to train fracture network simulation using multiple-point statistics.” *Solid Earth*, 10, 537–559.
- Buijze, Loes, Lonneke Van Bijsterveldt, Holger Cremer, Bob Paap, Hans Veldkamp, Brecht B.T. Wassing, Jan Diederik Van Wees, Guido C.N. Van Yperen, and Jan H. Ter Heege (2020), “Review of induced seismicity in geothermal systems worldwide and implications for geothermal systems in the Netherlands.” *Geologie en Mijnbouw/Netherlands Journal of Geosciences*, 2019.
- Byerlee, J. (1978), “Friction of rocks.” *Pure and Applied Geophysics*, 116, 615–626.
- Cai, M. (2010), “Practical estimates of tensile strength and Hoek-Brown strength parameter m_i of brittle rocks.” *Rock Mechanics and Rock Engineering*, 43, 167–184.

- Cazarin, Caroline L, Francisco H Bezerra, Renata De A Ennes-silva, Fabrizio Balsamo, and Augusto S Auler (2016), "Using Analogue Hypogene Karst Systems to Understand the Pre-Salt Carbonate Reservoirs Offshore Brazil *." In *AAPG 2016 International Conference and Exhibition, Cancun, Mexico, September 6-9*, URL http://www.searchanddiscovery.com/pdfz/documents/2016/41792cazarin/ndx{}_cazarin.pdf.html.
- Cazarin, Caroline L, Francisco H R Bezerra, Leonardo Borghi, Roberto V Santos, Julia Favoreto, José A Brod, Augusto S Auler, and Narendra K Srivastava (2019), "The conduit-seal system of hypogene karst in Neoproterozoic carbonates in northeastern Brazil." *Marine and Petroleum Geology*, 101, 90–107, URL <https://doi.org/10.1016/j.marpetgeo.2018.11.046>.
- Charles, R. J. (1958), "Static fatigue of glass. II." *Journal of Applied Physics*, 29, 1554–1560.
- Chemenda, Alexandre I., Si Hung Nguyen, Jean Pierre Petit, and Julien Ambre (2011), "Mise en évidence expérimentale d'une transition entre fissuration en mode I et formation de bandes de dilatation." *Comptes Rendus - Mécanique*, 339, 219–225, URL <http://dx.doi.org/10.1016/j.crme.2011.01.002>.
- Cooke, Michele L. and Chad A. Underwood (2001), "Fracture termination and step-over at bedding interfaces due to frictional slip and interface opening." *Journal of Structural Geology*, 23, 223–238.
- Cruz, Simone C.P. and Fernando F. Alkmim (2006), "The tectonic interaction between the Paramirim aulacogen and the Araçuaí belt, São Francisco craton region, Eastern Brazil." *Anais da Academia Brasileira de Ciências*, 78, 151–173.
- de Jager, J, M A Doyle, P J Grantham, and J E Mabillard (1996), "Hydrocarbon habitat of the West Netherlands Basin." In *Geology of Gas and Oil under the Netherlands: Selection of papers presented at the 1983 International Conference of the American Association of Petroleum Geologists, held in The Hague* (H E Rondeel, D A J Batjes, and W H Nieuwenhuijs, eds.), 191–209, Springer Netherlands, Dordrecht, URL https://doi.org/10.1007/978-94-009-0121-6{}_17.
- de Jager, Jan (2007), "Geological development." In *Geology of the Netherlands*, December, 5–26.
- Delbecq, F and Remi Moyen (2010), "SAGD Well Planning using Stochastic Seismic Inversion.pdf." *CSEG Recorder*, 43–47.
- Delvaux, D. and B. Sperner (2003), "New aspects of tectonic stress inversion with reference to the TENSOR program." *Geological Society, London, Special Publications*, 212, 75–100, URL <https://pubs.geoscienceworld.org/books/book/1591/chapter/107360955/>.
- Deng, Chao, Robert L. Gawthorpe, Haakon Fossen, and Emma Finch (2018), "How Does the Orientation of a Preexisting Basement Weakness Influence Fault Development During Renewed Rifting? Insights From Three-Dimensional Discrete Element Modeling." *Tectonics*, 37, 2221–2242.
- Dershowitz, William S. and Hans H. Herda (1992), "Interpretation of fracture spacing and intensity." In *The 33th U.S. Symposium on Rock Mechanics (USRMS), 3-5 June, Santa Fe, New Mexico*.
- Douma, L.A.N.R., J.A. Regelink, G. Bertotti, Q. D. Boersma, and A. Barnhoorn (2019), "The mechanical contrast between layers controls fracture containment in layered rocks." *Journal of Structural Geology*.

- Duin, E. J. T., J. C. Doornenbal, Richard H. B. Rijkers, J. W. Verbeek, and Th. E. Wong (2006), "Subsurface structure of the Netherlands - Results of recent onshore and offshore mapping." *Geologie en Mijnbouw/Netherlands Journal of Geosciences*, 85, 245–276.
- Ebner, Marcus, Daniel Koehn, Renaud Toussaint, François Renard, and Jean Schmittbuhl (2009), "Stress sensitivity of stylolite morphology." *Earth and Planetary Science Letters*, 277, 394–398.
- Emery, Andy (2016), "Palaeopressure reconstruction to explain observed natural hydraulic fractures in the Cleveland Basin." *Marine and Petroleum Geology*, 77, 535–552, URL <http://dx.doi.org/10.1016/j.marpetgeo.2016.06.007>.
- Engelder, Terry and David C. P. Peacock (2001), "Joint development normal to regional compression during flexural-flow folding: The Lilstock buttress anticline, Somerset, England." *Journal of Structural Geology*, 23, 259–277.
- Ennes-Silva, Renata A., Francisco H. R. Bezerra, Francisco C. C. Nogueira, Fabrizio Balsamo, Alexander Klimchouk, Caroline L. Cazarin, and Augusto S. Auler (2016), "Superposed folding and associated fracturing influence hypogene karst development in Neoproterozoic carbonates, São Francisco Craton, Brazil." *Tectonophysics*, 666, 244–259, URL <http://dx.doi.org/10.1016/j.tecto.2015.11.006>.
- Ferrill, David A., Mark A. Evans, Ronald N. McGinnis, Alan P. Morris, Kevin J. Smart, Sarah S. Wigginton, Kirk D. H. Gulliver, Daniel Lehrmann, Erich de Zoeten, and Zach Sickmann (2017a), "Fault zone processes in mechanically layered mudrock and chalk." *Journal of Structural Geology*, 97, 118–143, URL <http://dx.doi.org/10.1016/j.jsg.2017.02.013>.
- Ferrill, David A., Ronald N. McGinnis, Alan P. Morris, Kevin J. Smart, Zachary T. Sickmann, Michael Bentz, Daniel Lehrmann, and Mark A. Evans (2014), "Control of mechanical stratigraphy on bed-restricted jointing and normal faulting: Eagle Ford Formation, south-central Texas." *AAPG Bulletin*, 98, 2477–2506.
- Ferrill, David A. and Alan P. Morris (2003), "Erratum to: "Dilational normal faults"." *Journal of Structural Geology*, 25, 827, URL <http://linkinghub.elsevier.com/retrieve/pii/S0191814102001967>.
- Ferrill, David A., Alan P. Morris, Ronald N. McGinnis, Kevin J. Smart, Sarah S. Wigginton, and Nicola J. Hill (2017b), "Mechanical stratigraphy and normal faulting." *Journal of Structural Geology*, 94, 275–302, URL <http://dx.doi.org/10.1016/j.jsg.2016.11.010>.
- Finch, Emma, Stuart Hardy, and Rob Gawthorpe (2004), "Discrete-element modelling of extensional fault-propagation folding above rigid basement fault blocks." *Basin Research*, 16, 467–488, URL <http://doi.wiley.com/10.1111/j.1365-2117.2004.00241.x>.
- Fisher, Marc Kevin, Christopher A. Wright, Brian Michael Davidson, Nicholas P. Steinsberger, William Stanley Buckler, Alan Goodwin, and Eugene O. Fielder (2005), "Integrating Fracture Mapping Technologies To Improve Stimulations in the Barnett Shale." *SPE Production & Facilities*, 20, 85–93, URL <http://www.onepetro.org/doi/10.2118/77441-PA>.
- Fisher, R. (1953), "Dispersion on a Sphere." *Proceedings of the Royal Society A: Mathematical, Physical and Engineering Sciences*, 217, 295–305.
- Fossen, H., R. A. Schultz, Z. K. Shipton, and K. Mair (2007), "Deformation bands in sandstone: a review." *Journal of the Geological Society*, 164, 1–15.

- Fossen, Haakon (2010), *Structural Geology*. Cambridge University Press, Cambridge, URL <http://ebooks.cambridge.org/ref/id/CB09780511777806>.
- Freeman, Brett, David J Quinn, Cathal G Dillon, Michael Arnhild, and Bastiaan Jaarsma (2015), "Predicting subseismic fracture density and orientation in the Gorm Field, Danish North Sea." *Geological Society, London, Special Publications*, 421, 231–244, URL <http://sp.lyellcollection.org/content/421/1/231.abstract>.
- Gale, Julia F W, Robert H. Lander, Robert M. Reed, and Stephen E. Laubach (2010), "Modeling fracture porosity evolution in dolostone." *Journal of Structural Geology*, 32, 1201–1211.
- Gale, Julia F W, Stephen E. Laubach, Jon E. Olson, Peter Eichhubl, and András Fall (2014), "Natural fractures in shale: A review and new observations." *AAPG Bulletin*, 98, 2165–2216.
- Gale, Julia F.W., Robert M. Reed, and Jon Holder (2007), "Natural fractures in the Barnett Shale and their importance for hydraulic fracture treatments." *AAPG Bulletin*, 91, 603–622.
- Geluk, Mark (2005), *Stratigraphy and tectonics of Permo- Triassic basins in the Netherlands and surrounding areas*. Utrecht University, URL <http://natuurtijdschriften.nl/download?type=document;docid=568360>.
- Genter, Albert, Clément Baujard, Nicolas Cuenot, Chrystel Dezayes, Thomas Kohl, Bernard Sanjuan, Julia Scheiber, Eva Schill, Jean Schmittbuhl, and Jeanne Vidal (2016), "Geology , Geophysics and Geochemistry in the Upper Rhine Graben : the frame for geothermal energy use." In *European Geothermal Congress 2016*, February 2017.
- Germanovich, Leonid N and Dk Astakhov (2004), "Fracture closure in extension and mechanical interaction of parallel joints." *Journal of Geophysical Research*, 109, 1–22.
- Goodman, R.E. (1989), *Introduction to Rock Mechanics Second Edition*. Wiley.
- Griffith, A.A. (1921), "The Phenomena of Rupture and Flow in Solids." *The Royal Society: Mathematical, Physical and Engineering Sciences*, 221, 163–198.
- Gross, Michael R. (1993), "The origin and spacing of cross joints: examples from the Monterey Formation, Santa Barbara Coastline, California." *Journal of Structural Geology*, 15, 737–751.
- Gudmundsson, Agust, Trine H. Simmenes, Belinda Larsen, and Sonja L. Philipp (2010), "Effects of internal structure and local stresses on fracture propagation, deflection, and arrest in fault zones." *Journal of Structural Geology*, 32, 1643–1655, URL <http://dx.doi.org/10.1016/j.jsg.2009.08.013>.
- Guimaraes, J.T., A. Misi, A.J. Pedreira, and J.M.L. Dominguez (2011), "The Bebedouro Formation, Una Group, Bahia (Brazil)." *Geological Society, London, Memoirs*, v. 36, p. 503–508.
- Guo, Liwei (2014), *Development of a Three-dimensional Fracture Model for the Combined Finite-Discrete Element Method*. Imperial College London, URL <http://hdl.handle.net/10044/1/25120>.
- Guo, Liwei, John-Paul Latham, and Jiansheng Xiang (2017), "A numerical study of fracture spacing and through-going fracture formation in layered rocks." *International Journal of Solids and Structures*, 110–111, 44–57, URL <http://linkinghub.elsevier.com/retrieve/pii/S0020768317300574>.

- Hale, Dave (2013), "Methods to compute fault images, extract fault surfaces, and estimate fault throws from 3D seismic images." *Geophysics*, 78.
- Hanke, John R., Mark P. Fischer, and Ryan M. Pollyea (2018), "Directional semivariogram analysis to identify and rank controls on the spatial variability of fracture networks." *Journal of Structural Geology*, 108, 34–51, URL <https://doi.org/10.1016/j.jsg.2017.11.012>.
- Hantschel, Thomas and Armin I. Kauerauf (2009), *Fundamentals of basin and petroleum systems modeling*.
- Hardebol, N. J. and G. Bertotti (2013), "DigiFract: A software and data model implementation for flexible acquisition and processing of fracture data from outcrops." *Computers and Geosciences*, 54, 326–336, URL <http://dx.doi.org/10.1016/j.cageo.2012.10.021>.
- Hardebol, N. J., C. Maier, H. Nick, S. Geiger, G. Bertotti, and H. Boro (2015), "Multiscale fracture network characterization and impact on flow: A case study on the Latemar carbonate platform." *Journal of Geophysical Research B: Solid Earth*, 120, 8197–8222.
- Healy, David, Roberto E. Rizzo, David G. Cornwell, Natalie J.C. Farrell, Hannah Watkins, Nick E. Timms, Enrique Gomez-Rivas, and Michael Smith (2017), "FracPaQ: A MATLAB™ toolbox for the quantification of fracture patterns." *Journal of Structural Geology*, 95, 1–16.
- Heidbach, O., M. Rajabi, K. Reiter, and M. Ziegler (2016), "World Stress Map 2016, GFZ Data Service." Technical report, GFZ Data Services.
- Heidbach, Oliver, Mojtaba Rajabi, Xiaofeng Cui, Karl Fuchs, Birgit Müller, John Reinecker, Karsten Reiter, Mark Tingay, Friedemann Wenzel, Furen Xie, Moritz O. Ziegler, Mary-Lou Zoback, and Mark Zoback (2018), "The World Stress Map database release 2016: Crustal stress pattern across scales." *Tectonophysics*, 744, 484–498, URL <https://linkinghub.elsevier.com/retrieve/pii/S0040195118302506>.
- Hoek, E. and E. T. Brown (1997), "Practical estimates of rock mass strength." *International Journal of Rock Mechanics and Mining Sciences*, 34, 1165–1186.
- Holder, Jon, Jon E. Olson, and Zeno Philip (2001), "Experimental determination parameters in sedimentary rock of subcritical crack growth." *Geophysical Research Letters*, 28, 599–602.
- Holdsworth, R. E., R. Trice, K. Hardman, K. J. W. McCaffrey, A. Morton, D. Frei, E. Dempsey, A. Bird, and S. Rogers (2019), "The nature and age of basement host rocks and fissure fills in the Lancaster field fractured reservoir, West of Shetland." *Journal of the Geological Society*, jgs2019–142.
- Hooker, J. N., L. A. Gomez, S. E. Laubach, J. F. W. Gale, and R. Marrett (2012), "Effects of diagenesis (cement precipitation) during fracture opening on fracture aperture-size scaling in carbonate rocks." *Geological Society, London, Special Publications*, 370, 187 LP – 206, URL <http://sp.lyellcollection.org/content/370/1/187.abstract>.
- Hooker, J. N., S. E. Laubach, and R. Marrett (2013), "Fracture-aperture sizedfrequency, spatial distribution, and growth processes in strata-bounded and non-strata-bounded fractures, Cambrian mesón group, NW Argentina." *Journal of Structural Geology*, 54, 54–71, URL <http://dx.doi.org/10.1016/j.jsg.2013.06.011>.
- Hooker, J. N., S. E. Laubach, and R. Marrett (2014), "A universal power-law scaling exponent for fracture apertures in sandstones." *GSA Bulletin*, 126, 1340–1362.

- Houben, M. E., N. J. Hardebol, A. Barnhoorn, Q. D. Boersma, A. Carone, Y. Liu, D. A.M. de Winter, C. J. Peach, and M. R. Drury (2017), "Fluid flow from matrix to fractures in Early Jurassic shales." *International Journal of Coal Geology*, 175, 26–39, URL <http://dx.doi.org/10.1016/j.coal.2017.03.012>.
- Imber, Jonathan, Howard Armstrong, Sarah Clancy, Susan Daniels, Liam Herringshaw, Ken McCaffrey, Joel Rodrigues, Joao Trabucho-Alexandre, and Cassandra Warren (2014), "Natural fractures in a United Kingdom shale reservoir analog, Cleveland Basin, northeast England." *AAPG Bulletin*, 98, 2411–2437.
- Irwin, G.R. (1957), "Analysis of Stresses and Strains Near the End of a Crack Traversing a Plate."
- Jaeger, J.C., N.G.W Cook, and R.W. Zimmerman (2007), *Fundamentals of Rock Mechanics*, 4th edition. Blackwell Publishing.
- Jaglan, Hardeep and Farrukh Qayyum (2015), "Unconventional seismic attributes for fracture characterization." *First Break*, 33, 101–109.
- Josnin, Jean-Yves, Hervé Jourde, Pascal Fénart, and Pascal Bidaux (2002), "A three-dimensional model to simulate joint networks in layered rocks." *Canadian Journal of Earth Sciences*, 39, 1443–1455, URL <http://www.nrcresearchpress.com/doi/10.1139/e02-043>.
- Kahrobaei, S, R M Fonseca, C J L Willems, F Wilschut, and J D Van Wees (2019), "Regional Scale Geothermal Field Development Optimization under Geological Uncertainties." 11–14.
- Karimi-Fard, M., L.J. Durlofsky, and K. Aziz (2004), "An Efficient Discrete-Fracture Model Applicable for General-Purpose Reservoir Simulators." *SPE Journal*, 9, 227–236, URL <http://www.onepetro.org/doi/10.2118/88812-PA>.
- Karimi-Fard, M. and A Firoozabadi (2001), "Numerical Simulation of Water Injection in 2D Fractured Media Using Discrete-Fracture Model." *Society of Petroleum Engineers*.
- Kettermann, Michael and Janos L. Urai (2015), "Changes in structural style of normal faults due to failure mode transition: First results from excavated scale models." *Journal of Structural Geology*, 74, 105–116, URL <http://dx.doi.org/10.1016/j.jsg.2015.02.013>.
- Khait, M. (2019), *Delft Advanced Research Terra Simulator*. Ph.D. thesis, Delft University of Technology.
- Khait, Mark and Denis Voskov (2018), "Operator-based linearization for efficient modeling of geothermal processes." *Geothermics*, 74, 7–18, URL <https://doi.org/10.1016/j.geothermics.2018.01.012>.
- Klimchouk, Alexander (2009), "Morphogenesis of hypogenic caves." *Geomorphology*, 106, 100–117, URL <http://dx.doi.org/10.1016/j.geomorph.2008.09.013>.
- Klimchouk, Alexander, Augusto S. Auler, Francisco H R Bezerra, Caroline L. Cazarin, Fabrizio Balsamo, and Yuri Dublyansky (2016), "Hypogenic origin, geologic controls and functional organization of a giant cave system in Precambrian carbonates, Brazil." *Geomorphology*, 253, 385–405, URL <http://dx.doi.org/10.1016/j.geomorph.2015.11.002>.
- Ko, Tae Young and John Kemeny (2011), "Subcritical crack growth in rocks under shear loading." *Journal of Geophysical Research: Solid Earth*, 116.

- Koehn, Daniel, François Renard, Renaud Toussaint, and Cees W. Passchier (2007), "Growth of stylolite teeth patterns depending on normal stress and finite compaction." *Earth and Planetary Science Letters*, 257, 582–595.
- Kombrink, H., J. C. Doornenbal, E. J.T. Duin, M. Den Dulk, J. H. Ten Veen, and N. Witmans (2012), "New insights into the geological structure of the Netherlands; Results of a detailed mapping project." *Geologie en Mijnbouw/Netherlands Journal of Geosciences*, 91, 419–446.
- Kramers, L., J. D. Van Wees, M. P.D. Pluymaekers, A. Kronimus, and T. Boxem (2012), "Direct heat resource assessment and subsurface information systems for geothermal aquifers; The Dutch perspective." *Geologie en Mijnbouw/Netherlands Journal of Geosciences*, 91, 637–649.
- Lamarche, Juliette, Arthur P C Lavenu, Bertrand D M Gauthier, Yves Guglielmi, and Oc??ane Jayet (2012), "Relationships between fracture patterns, geodynamics and mechanical stratigraphy in Carbonates (South-East Basin, France)." *Tectonophysics*, 581, 231–245, URL <http://dx.doi.org/10.1016/j.tecto.2012.06.042>.
- Lander, R. H. and S. E. Laubach (2014), "Insights into rates of fracture growth and sealing from a model for quartz cementation in fractured sandstones." *Bulletin of the Geological Society of America*, 127, 516–538.
- Lander, Robert H., Richard E. Larese, and Linda M. Bonnell (2008), "Toward more accurate quartz cement models: The importance of euhedral versus noneuhedral growth rates." *American Association of Petroleum Geologists Bulletin*, 92, 1537–1563.
- Larsen, Belinda and Agust Gudmundsson (2010), "Linking of fractures in layered rocks: Implications for permeability." *Tectonophysics*, 492, 108–120, URL <http://dx.doi.org/10.1016/j.tecto.2010.05.022>.
- Laubach, S.E., R.H. Lander, L.J. Criscenti, L.M. Anovitz, J.L. Urai, R.M. Pollyea, J.N. Hooker, W. Narr, M.A. Evans, S.N. Kerisit, J.E. Olson, T. Dewers, D. Fisher, R. Bodnar, B. Evans, P. Dove, L.M. Bonnell, M.P. Marder, and L. Pyrak-Nolte (2019), "The Role of Chemistry in Fracture Pattern Development and Opportunities to Advance Interpretations of Geological Materials." *Reviews of Geophysics*, 1–47.
- Laubach, Stephen E., Jon E. Olson, and Michael R. Cross (2009), "Mechanical and fracture stratigraphy." *AAPG Bulletin*, 93, 1413–1426.
- Lepillier, Baptiste, Alexandros Daniilidis, Nima Doonechalay Gholizadeh, Pierre Olivier Bruna, Juliane Kummerow, and David Bruhn (2019), "A fracture flow permeability and stress dependency simulation applied to multi-reservoirs, multi-production scenarios analysis." *Geothermal Energy*, 7, URL <https://doi.org/10.1186/s40517-019-0141-8>.
- Li, J. Z., S. E. Laubach, J. F.W. Gale, and R. A. Marrett (2018), "Quantifying opening-mode fracture spatial organization in horizontal wellbore image logs, core and outcrop: Application to Upper Cretaceous Frontier Formation tight gas sandstones, USA." *Journal of Structural Geology*, 108, 137–156.
- Libby, S., L. Hartley, R. Turnbull, M. Cottrell, T. Bym, N. Josephson, R. Munier, J.O. Selroos, and D. Mas Ivars (2019), "Dynamic Fracture Network Generation : a new method for growing fractures according to their deformation history." In *53 rd US ROCK MECHANICS / GEOMECHANICS SYMPOSIUM*, June.

- Liu, Xiaolong, Andreas Eckert, and Peter Connolly (2016), "Stress evolution during 3D single-layer visco-elastic buckle folding: Implications for the initiation of fractures." *Tectonophysics*, 679, 140–155, URL <http://dx.doi.org/10.1016/j.tecto.2016.04.042>.
- Loucks, Robert G (1999), "Paleocave Carbonate Reservoirs : Origins , Burial-Depth Modifications , Spatial Complexity , and Reservoir Implications." *AAPG Bulletin*, 83, 1795–1834.
- Loucks, Robert G., Paul K. Mescher, and George A. McMechan (2004), "Three-dimensional architecture of a coalesced, collapsed-paleocave system in the Lower Ordovician Ellenburger Group, central Texas." *American Association of Petroleum Geologists Bulletin*, 88, 545–564.
- Luthi, Stepan M. and Philippe Souhaite (1990), "Fracture apertures from electrical borehole scans." *Geophysics*, 55, 821–833.
- Maerten, Laurent, Paul Gillespie, and Jean Marc Daniel (2006), "Three-dimensional geomechanical modeling for constraint of subseismic fault simulation." *AAPG Bulletin*, 90, 1337–1358.
- Maerten, Laurent, Xavier Legrand, Claire Castagnac, Marie Lefranc, Jean-Pierre Joonnekindt, and Frantz Maerten (2019), "Fault-related fracture modeling in the complex tectonic environment of the Malay Basin, offshore Malaysia: An integrated 4D geomechanical approach." *Marine and Petroleum Geology*, 105, 222–237, URL <http://www.sciencedirect.com/science/article/pii/S0264817219301758>.
- Maerten, Laurent, Frantz Maerten, Mostfa Lejri, and Paul Gillespie (2016), "Geomechanical paleostress inversion using fracture data." *Journal of Structural Geology*, 89, 197–213, URL <http://dx.doi.org/10.1016/j.jsg.2016.06.007><http://linkinghub.elsevier.com/retrieve/pii/S0191814116300839>.
- Mandl, Georg (2005), *Rock Joints: The Mechanical Genesis*. Springer.
- Matev, P.S. (2011), *Comprehensive reservoir quality assessment of Buntsandstein sandstone reservoirs in the West Netherlands Basin for geothermal applications in Zuid Holland province area*. Ph.D. thesis, Delft University of Technology, URL <http://resolver.tudelft.nl/uuid:1b6c1430-42b6-4630-8fa8-4f0eb9e8e280>.
- Matthäi, S. K., S. Geiger, S. G. Roberts, A. Paluszny, M. Belayneh, A. Burri, A. Mezentsev, H. Lu, D. Coumou, T. Driesner, and C. A. Heinrich (2007), "Numerical simulation of multi-phase fluid flow in structurally complex reservoirs." *Geological Society Special Publication*, 292, 405–429.
- Matthäi, Stephan K. and Mandefro Belayneh (2004), "Fluid flow partitioning between fractures and a permeable rock matrix." *Geophysical Research Letters*, 31, 1–5.
- Mavko, Gary, Tapan Mukerji, and Jack Dvorkin (2009), *The Rock Physics Handbook*. Cambridge University Press, Cambridge, URL <http://ebooks.cambridge.org/ref/id/CB09780511626753>.
- McCrack, Jason, Don Lawton, and Cheran Mangat (2009), "Geostatistical Inversion of Seismic Data from Thinly Bedded Ardley Coals." In *Frontiers & Innovation GeoConvention*, 649–652.
- McGinnis, Ronald N., David A. Ferrill, Alan P. Morris, Kevin J. Smart, and Daniel Lehrmann (2017), "Mechanical stratigraphic controls on natural fracture spacing and penetration." *Journal of Structural Geology*, 95, 160–170.

- McGinnis, Ronald N., David A. Ferrill, Kevin J. Smart, Alan P. Morris, Camilo Higuera-Diaz, and Daniel Prawica (2015), "Pitfalls of using entrenched fracture relationships: Fractures in bedded carbonates of the hidden valley fault zone, Canyon Lake Gorge, Comal County, Texas." *AAPG Bulletin*, 99, 2221–2245.
- Misi, A., A. J. Kaufman, K. Azmy, M. A. Dardenne, A. N. Sial, and T. F. de Oliveira (2011), "Chapter 48 Neoproterozoic successions of the Sao Francisco Craton, Brazil: the Bambui, Una, Vazante and Vaza Barris/Miaba groups and their glaciogenic deposits." *Geological Society, London, Memoirs*, 36, 509–522, URL <http://mem.lyellcollection.org/cgi/doi/10.1144/M36.48>.
- Munjiza, Ante (2004), *The Combined Finite-Discrete Element Method*. John Wiley & Sons, Ltd, URL <https://onlinelibrary.wiley.com/doi/abs/10.1002/0470020180>.
- Nara, Y. and K. Kaneko (2005), "Study of subcritical crack growth in andesite using the Double Torsion test." *International Journal of Rock Mechanics and Mining Sciences*, 42, 521–530.
- Nara, Yoshitaka, Kazuya Morimoto, Naoki Hiroyoshi, Tetsuro Yoneda, Katsuhiko Kaneko, and Philip M. Benson (2012), "Influence of relative humidity on fracture toughness of rock: Implications for subcritical crack growth." *International Journal of Solids and Structures*, 49, 2471–2481.
- Nelson, R.a. (2001), *Geologic Analysis of Naturally Fractured Reservoirs*. Gulf Professional Publishing, URL <http://www.sciencedirect.com/science/article/pii/B9780884153177500051>.
- Neves, Benjamim Bley de Brito, Reinhardt Adolfo Fuck, and Marcio Martins Pimentel (2014), "The Brasiliano collage in South America: a review." *Brazilian Journal of Geology*, 44, 493–518, URL http://www.scielo.br/scielo.php?script=sci_arttext&pid=S2317-48892014000200493&lng=en&nrm=iso&tlng=en.
- Nguyen, S. H., A. I. Chemenda, and J. Ambre (2011), "Influence of the loading conditions on the mechanical response of granular materials as constrained from experimental tests on synthetic rock analogue material." *International Journal of Rock Mechanics and Mining Sciences*, 48, 103–115, URL <http://dx.doi.org/10.1016/j.ijrmms.2010.09.010>.
- Nick, H. M. and S. K. Matthäi (2011), "Comparison of Three FE-FV Numerical Schemes for Single- and Two-Phase Flow Simulation of Fractured Porous Media." *Transport in Porous Media*, 90, 421–444.
- Nyberg, Björn, Casey W. Nixon, and David J. Sanderson (2018), "NetworkGT: A GIS tool for geometric and topological analysis of two-dimensional fracture networks." *Geosphere*, URL <https://pubs.geoscienceworld.org/gsa/geosphere/article/531129/NetworkGT-A-GIS-tool-for-geometric-and-topological>.
- Oda, M. (1985), "Permeability Tensor for Discontinuous Rock Masses." *Géotechnique*, 483–495.
- Odling, N. E., P. Gillespie, B. Bourguine, C. Castaing, J. P. Chiles, N. P. Christensen, E. Fillion, a. Genter, C. Olsen, L. Thrane, R. Trice, E. Aarseth, J. J. Walsh, and J. Watterson (1999), "Variations in fracture system geometry and their implications for fluid flow in fractures hydrocarbon reservoirs." *Petroleum Geoscience*, 5, 373–384.
- Olson, J. (2008), "Multi-fracture propagation modeling : Applications to hydraulic fracturing in shales and tight gas sands." *Conference Paper*.

- Olson, J. E. (2007), "Fracture aperture, length and pattern geometry development under biaxial loading: a numerical study with applications to natural, cross-jointed systems." *The Relationship between Damage and Localization*, 289, 123–142.
- Olson, Jon E. (1993), "Joint pattern development: Effects of subcritical crack growth and mechanical crack interaction." *Journal of Geophysical Research*, 98, 12251–12265.
- Olson, Jon E. (2003), "Sublinear scaling of fracture aperture versus length: An exception or the rule?" *Journal of Geophysical Research*, 108, 2413, URL <http://doi.wiley.com/10.1029/2001JB000419>.
- Olson, Jon E. (2004), "Predicting fracture swarms — the influence of subcritical crack growth and the crack-tip process zone on joint spacing in rock." *Geological Society, London, Special Publications*, 231, 73–88, URL <http://sp.lyellcollection.org/lookup/doi/10.1144/GSL.SP.2004.231.01.05>.
- Olson, Jon E., Stephen E. Laubach, and Robert H. Lander (2009), "Natural fracture characterization in tight gas sandstones: Integrating mechanics and diagenesis." *AAPG Bulletin*, 93, 1535–1549.
- Olsson, R. and N. Barton (2001), "An improved model for hydromechanical coupling during shearing of rock joints." *International Journal of Rock Mechanics and Mining Sciences*, 38, 317–329.
- Ouraga, Zady, Nicolas Guy, and Amade Pouya (2018), "Effect of hydro mechanical coupling on natural fracture network formation in sedimentary basins." *Geophysical Journal International*, 213, 798–804, URL <https://academic.oup.com/gji/article/213/2/798/4828336>.
- Paluszny, Adriana and Stephan K. Matthäi (2009), "Numerical modeling of discrete multi-crack growth applied to pattern formation in geological brittle media." *International Journal of Solids and Structures*, 46, 3383–3397, URL <http://dx.doi.org/10.1016/j.ijsolstr.2009.05.007>.
- Philip, Zeno G., James W. Jennings, Jon E. Olson, Stephen E. Laubach, and Jon Holder (2005), "Modeling Coupled Fracture-Matrix Fluid Flow in Geomechanically Simulated Fracture Networks." *SPE Reservoir Evaluation & Engineering*, 8, 300–309, URL <http://www.onepetro.org/doi/10.2118/77340-PA>.
- Philipp, Sonja L., Filiz Afşar, and Agust Gudmundsson (2013), "Effects of mechanical layering on hydrofracture emplacement and fluid transport in reservoirs." *Frontiers in Earth Science*, 1, 4, URL <http://journal.frontiersin.org/article/10.3389/feart.2013.00004/abstract>.
- Phillip, S. L. (2008), "Geometry and formation of gypsum veins in mudstones at Watchet, Somerset, SW England." *Geological Magazine*, 145, 831–844, URL http://www.journals.cambridge.org/abstract/_j_S0016756808005451.
- Pichel, Leonardo, Emma Finch, and Rob L. Gawthorpe (2019), "The Impact of Pre-Salt Rift Topography on Salt Tectonics: A Discrete-Element Modeling Approach." *Tectonics*, 38, 1466–1488.
- Pluymaekers, M. P.D., L. Kramers, J. D. Van Wees, A. Kronimus, S. Nelskamp, T. Boxem, and D. Bonté (2012), "Reservoir characterisation of aquifers for direct heat production: Methodology and screening of the potential reservoirs for the Netherlands." *Geologie en Mijnbouw/Netherlands Journal of Geosciences*, 91, 621–636.

- Pollard, David D. and Paul Segall (1987), *Theoretical displacements and stress near fractures in rock: with applications to faults, joints, veins, dikes, and solution surfaces*.
- Prabhakaran, Rahul, Pierre-Olivier Bruna, Giovanni Bertotti, and David Smeulders (2019), "Automated fracture trace detection technique using the complex shearlet transform." *Solid Earth Discussions*, 1–40.
- Purvis, K and J A Okkerman (1996), "Inversion of reservoir quality by early diagenesis: an example from the Triassic Buntsandstein, offshore the Netherlands." In *Geology of Gas and Oil under the Netherlands: Selection of papers presented at the 1983 International Conference of the American Association of Petroleum Geologists, held in The Hague* (H E Rondeel, D A J Batjes, and W H Nieuwenhuijs, eds.), 179–189, Springer Netherlands, Dordrecht, URL https://doi.org/10.1007/978-94-009-0121-6_{ }16.
- Quinn, D, B Freeman, C.G Dillon, M Arnhild, and B Jaarsma (2014), "Building a robust framework model for geomechanical prediction of fracture density, orientation and likely hydraulic signature: Leading-edge technology in the Gorm field Danish Central Graben." *SEG Technical Program Expanded Abstracts 2014*, 1528–1532, URL <http://library.seg.org/doi/abs/10.1190/segam2014-0148.1>.
- Ramsey, Jonathan M and Frederick M Chester (2004), "Hybrid fracture and the transition from extension fracture to shear fracture." *Nature*, 428, 63–66, URL <https://doi.org/10.1038/nature02333>.
- Riccomini, Claudio and Marcelo Assumpção (1999), "Quaternary tectonics in Brazil." *Episodes*, 22, 221–225.
- Rijken, M.C.M. (2005), *Modeling naturally fractured reservoirs: From experimental rock mechanics to flow simulation*. URL <http://adsabs.harvard.edu/abs/2005PhDT.....79R>.
- Rijken, Peggy and Michele L. Cooke (2001), "Role of shale thickness on vertical connectivity of fractures: Application of crack-bridging theory to the Austin Chalk, Texas." *Tectonophysics*, 337, 117–133.
- Rives, T., M. Razack, J.-P. Petit, and K D Rawnsley (1992), "Joint spacing: analogue and numerical simulations." *Journal of Structural Geology*, 14, 925–937.
- Roche, V., C. Homberg, and M. Rocher (2013), "Fault nucleation, restriction, and aspect ratio in layered sections: Quantification of the strength and stiffness roles using numerical modeling." *Journal of Geophysical Research: Solid Earth*, 118, 4446–4460.
- Roche, V and M van der Baan (2015), "The role of lithological layering and pore pressure on fluid-induced microseismicity." *Journal of Geophysical Research: Solid Earth*, 120, 923–943.
- Ruf, Jason C, Kelly a Rust, and Terry Engelder (1998), "Investigating the effect of mechanical discontinuities on joint spacing." *Tectonophysics*, 295, 245–257, URL <http://linkinghub.elsevier.com/retrieve/pii/S0040195198001231>.
- Sams, Mark, Ian Millar, Wawan Satriawan, Denis Saussus, and Sumon Bhattacharyya (2011), "Integration of geology and geophysics through geostatistical inversion: A case study." *First Break*, 29, 47–56.

- Sanderson, David J. and Casey W. Nixon (2015), "The use of topology in fracture network characterization." *Journal of Structural Geology*, 72, 55–66, URL <http://dx.doi.org/10.1016/j.jsg.2015.01.005>.
- Schill, E., A. Genter, N. Cuenot, and T. Kohl (2017), "Hydraulic performance history at the Soultz EGS reservoirs from stimulation and long-term circulation tests." *Geothermics*, 70, 110–124, URL <http://dx.doi.org/10.1016/j.geothermics.2017.06.003>.
- Schmittbuhl, J., F. Renard, J. P. Gratier, and R. Toussaint (2004), "Roughness of stylolites: Implications of 3D high resolution topography measurements." *Physical Review Letters*, 93, 1–4.
- Schöpfer, Martin P J, Arzu Arslan, John J. Walsh, and Conrad Childs (2011), "Reconciliation of contrasting theories for fracture spacing in layered rocks." *Journal of Structural Geology*, 33, 551–565, URL <http://dx.doi.org/10.1016/j.jsg.2011.01.008>.
- Schultz, Richard A. and Haakon Fossen (2002), "Displacement-length scaling in three dimensions: The importance of aspect ratio and application to deformation bands." *Journal of Structural Geology*, 24, 1389–1411.
- Shen, B and M Rinne (2007), "A fracture mechanics code for modelling sub-critical crack growth and time dependency." *Rock Mechanics: Meeting Society's Challenges and Demands*, 591—598.
- Smart, Kevin J., Goodluck I. Ofoegbu, Alan P. Morris, Ronald N. McGinnis, and David A. Ferrill (2014), "Geomechanical modeling of hydraulic fracturing: Why mechanical stratigraphy, stress state, and pre-existing structure matter." *AAPG Bulletin*, 98, 2237–2261.
- Strijker, Geertje, Giovanni Bertotti, and Stefan M. Luthi (2012), "Multi-scale fracture network analysis from an outcrop analogue: A case study from the Cambro-Ordovician clastic succession in Petra, Jordan." *Marine and Petroleum Geology*, 38, 104–116, URL <http://dx.doi.org/10.1016/j.marpetgeo.2012.07.003>.
- Tang, C. A., Z. Z. Liang, Y. B. Zhang, X. Chang, X. Tao, D. G. Wang, J. X. Zhang, J. S. Liu, W. C. Zhu, and D. Elsworth (2008), "Fracture spacing in layered materials: A new explanation based on two-dimensional failure process modeling." *American Journal of Science*, 308, 49–72.
- Teufel, Lawrence W. and James A. Clark (1984), "Hydraulic Fracture Propagation in Layered Rock: Experimental Studies of Fracture Containment." *Society of Petroleum Engineers Journal*, 24, 19–32, URL <http://www.onepetro.org/doi/10.2118/9878-PA>.
- Teufel, Lawrence W and Helen E Farrell (1990), "In Situ Stress and Natural Fracture Distribution in the Ekofisk Field, North Sea." In *AAPG Annual Conference (1990)*, 1–33.
- Tingay, Mark R. P., John Reinecker, and Birgit Müller (2008), "Borehole breakout and drilling-induced fracture analysis from image logs." *World Stress Map Project*, 8.
- Toublanc, A, S Renaud, J E Sylte, C K Clausen, T Eiben, and G Nådland (2005), "Ekofisk Field: fracture permeability evaluation and implementation in the flow model." *Petroleum Geoscience*, 11, 321–330, URL <http://pg.lyellcollection.org/content/11/4/321.abstract>.
- Toussaint, R., E. Aharonov, D. Koehn, J. P. Gratier, M. Ebner, P. Baud, A. Rolland, and F. Renard (2018), "Stylolites: A review." *Journal of Structural Geology*, 114, 163–195.

- Ukar, Estibalitz, Ramiro G Lopez, Stephen E Laubach, and Julia F W Gale (2017), "Microfractures in bed-parallel veins (beef) as predictors of vertical macrofractures in shale: Vaca Muerta Formation, Agrio Fold-and-Thrust Belt, Argentina." *Journal of South American Earth Sciences*, 79, 152–169.
- Ukar, Estibalitz, Canalp Ozkul, and Peter Eichhubl (2016), "Fracture abundance and strain in folded Cardium Formation, Red Deer River anticline, Alberta Foothills, Canada." *Marine and Petroleum Geology*, 76, 210–230, URL <http://dx.doi.org/10.1016/j.marpetgeo.2016.05.016>.
- Van Balen, R. T., F Van Bergen, C. De Leeuw, H. Pagnier, E. Simmelink, J. D. Van Wees, and H. Verweij (2000), "Modelling the evolution of hydrocarbon systems in the inverted West Netherlands Basin, the Netherlands." *Journal of Geochemical Exploration*, 69-70, 685–688.
- van Dalssen, Wim, J. C. Doornenbal, S. Dortland, and J. L. Gunnink (2006), "A comprehensive seismic velocity model for the Netherlands based on lithostratigraphic layers." *Geologie en Mijnbouw/Netherlands Journal of Geosciences*, 85, 277–292.
- Van Wees, J. D., A. Kronimus, M. Van Putten, M. P.D. Pluymaekers, H. Mijnlief, P. Van Hoeff, A. Obdam, and L. Kramers (2012), "Geothermal aquifer performance assessment for direct heat production-Methodology and application to Rotliegend aquifers." *Geologie en Mijnbouw/Netherlands Journal of Geosciences*, 91, 651–665.
- Vermilye, Jan M. and Christopher H. Scholz (1995), "Relation between vein length and aperture." *Journal of Structural Geology*, 17, 423–434.
- Vidal, J., A. Genter, and F. Chopin (2017), "Permeable fracture zones in the hard rocks of the geothermal reservoir at Rittershoffen, France." *Journal of Geophysical Research: Solid Earth*, 122, 4864–4887.
- Vidal, Jeanne and Albert Genter (2018), "Overview of naturally permeable fractured reservoirs in the central and southern Upper Rhine Graben: Insights from geothermal wells." *Geothermics*, 74, 57–73, URL <https://doi.org/10.1016/j.geothermics.2018.02.003>.
- Voskov, Denis Viktorovich, Hamdi A. Tchelepi, and Rami Younis (2009), "General Nonlinear Solution Strategies for Multiphase Multicomponent EoS Based Simulation." *SPE Reservoir Simulation Symposium*, 2–4.
- Vrijlandt, M A W, E L M Struijk, L G Brunner, J G Veldkamp, N Witmans, D Maljers, and J D Van Wees (2019), "ThermoGIS update : a renewed view on geothermal potential in the Netherlands." *European Geothermal Congress 2016*, 11–14.
- Wang, Weihong, Kan Wu, and Jon Olson (2019), "Characterization of hydraulic fracture geometry in shale rocks through physical modeling." *International Journal of Fracture*, 216, 71–85, URL <https://doi.org/10.1007/s10704-019-00343-3>.
- Wang, Yang, Denis Voskov, Mark Khait, and David Bruhn (2020), "An efficient numerical simulator for geothermal simulation: A benchmark study." *Applied Energy*, 264.
- Warpinski, N R (2009), "Integrating Microseismic Monitoring With Well Completions, Reservoir Behavior, and Rock Mechanics." *SPE Tight Gas Completions Conference*, 15–17.

- Warpinski, N R, J A Clark, R A Schmidt, and C W Huddle (1981), "Laboratory Investigation on the Effect of In Situ Stresses on Hydraulic Fracture Containment." In *Joint SPE/DOE symposium, Denver, CO, USA, 27 May 1981*.
- Warpinski, Norman, Mike Mayerhofer, Eric Davis, and Eric Holley (2014), "Integrating Fracture Diagnostics for Improved Microseismic Interpretation and Stimulation Modeling." *Proceedings of the 2nd Unconventional Resources Technology Conference*, 1–19, URL <http://search.datapages.com/data/doi/10.15530/urtec-2014-1917906>.
- Watkins, Hannah, Robert W.H. Butler, Clare E. Bond, and Dave Healy (2015), "Influence of structural position on fracture networks in the Torridon Group, Achnashellach fold and thrust belt, NW Scotland." *Journal of Structural Geology*, 74, 64–80, URL <http://dx.doi.org/10.1016/j.jsg.2015.03.001>.
- Watkins, Hannah, David Healy, Clare E. Bond, and Robert W.H. Butler (2018), "Implications of heterogeneous fracture distribution on reservoir quality; an analogue from the Torridon Group sandstone, Moine Thrust Belt, NW Scotland." *Journal of Structural Geology*, 108, 180–197, URL <https://doi.org/10.1016/j.jsg.2017.06.002>.
- Willems, C. J.L. and H. Nick (2019), "Towards optimisation of geothermal heat recovery: An example from the West Netherlands Basin." *Applied Energy*, 247, 582–593, URL <https://doi.org/10.1016/j.apenergy.2019.04.083>.
- Willems, C.J.L. (2017), *Doublet deployment strategies for geothermal Hot Sedimentary Aquifer exploitation: Application to the Lower Cretaceous Nieuwerkerk Formation, West Netherlands Basin*. TUDelft.
- Williams, Ryan Michael, Enric Pascual-Cebrian, Jon Charles Gutmanis, and Gaynor Suzanne Paton (2017), "Closing the seismic resolution gap of fractures through seismic and image-log analysis, a North Sea case study." *Interpretation*, 5, SJ21–SJ30, URL <http://library.seg.org/doi/10.1190/INT-2016-0163.1>.
- Wong, Th E., D.A. Batjes, and J. de Jager (2007), *The Geology of The Netherlands*. Royal Netherlands Academy of Arts and Sciences, URL [notfound](#).
- Worum, Geza, Laurent Michon, Ronald T. Van Balen, Jan Diederik Van Wees, Sierd Cloetingh, and Henk Pagnier (2005), "Pre-Neogene controls on present-day fault activity in the West Netherlands Basin and Roer Valley Rift System (southern Netherlands): Role of variations in fault orientation in a uniform low-stress regime." *Quaternary Science Reviews*, 24, 473–488.
- Zoback, Mark D. (2007), *Reservoir Geomechanics*. Cambridge University Press.
- Zou, Yushi, Shicheng Zhang, Xinfang Ma, Tong Zhou, and Bo Zeng (2016), "Numerical investigation of hydraulic fracture network propagation in naturally fractured shale formations." *Journal of Structural Geology*, 84, 1–13, URL <http://dx.doi.org/10.1016/j.jsg.2016.01.004>.

ACKNOWLEDGEMENTS

This project PhD has been funded by the Dutch Upstream Gas Top-sector Initiative (project no. TKIG01020IG) and industry partners Energie Beheer Nederland, Neptune Energy Netherlands, and Wintershall Noordzee. Additional support was given by the Brazilian Agency of Oil and Gas (ANP) and the MolenGraaff Fund (Stichting Molengraaff Fonds).

The field trips to Brazil would not have been possible without the collaboration with Universidade Federal do Rio Grande do Norte (UFRN). My thanks to all the staff and students supporting us during our time in Brazil. I am particularly grateful to Hilario Bezerra who set up the collaboration between TUDelft and UFRN and guided us to all field locations. I would also like to thank Hilario for the warm welcomes he gave me. I very much enjoyed my stays in Brazil.

I want to thank the entire team of Schlumberger Stavanger Research (SSR) for their support and welcoming me in to their team. You have made me feel welcome from the moment I had arrived. My thanks go to Jarle, Trond, Martin, Michael, Jane, Geir, Knut, Massimo, Pierre, Aicha and all the rest. My special thanks go to Wiebke Athmer who started the collaboration between the TUDelft and SSR. You were a wonderful mentor from whom I have learned a lot. It is unfortunate that our work on the Ekofisk did not make in to this Thesis, but I have implemented most of what I have learned chapter 7. That being sad, we have managed to publish our findings in JSG, so that is really nice.

Special thanks go one of my BSc students, Cindy Dubbeld who did a great job in interpreting the Brejoes Cliff Outcrops.

I would like to thank Bill Rossen and Gerhard Diephuis, Jan-Kees Blom, Femke Vossepoel, Kees Weemstra, Joep Storms, Pierre-Olivier, Auke Barnhoorn Bruna and Giovanni Bertotti for involving in the courses Field Development Project, Geological Modelling, Simulation and Building of Stratigraphy, Seismic Interpretation and Geo-Energy Exploration Project. Teaching and preparing classes has been something I really enjoyed during my time at TUDelft. It kept me motivated throughout my PhD cycle. Doing a PhD is not only about conducting research.

I would also like to show my appreciation to the wonderful support staff of geoscience and engineering who were always happy and ready to help. My thanks go to Marlijn, Lydia, Margot, Ralf, Marja, Marijke and Anke.

I would like to thank CGG, Dassault Systemes, Schlumberger and dGB Earth Sciences for providing the software and tools used in this thesis. The Geological Survey of the Netherlands (part of TNO) is thanked for providing the reprocessed seismic dataset shown in chapter-7. Mourad Kourta (Schlumberger) is thanked for his technical support in the image-log analysis (chapter-7). PanTerra Geoconsultants is thanked for conducting the core interpretation shown in chapter-7. Furthermore, I would like to thank Harmen Mijnlief and Rick Donselaar for discussions which have led to the realisation of

the Naaldwijk project. Kevin Bisdom and Wouter van der Zee are thanked for their initial support in the Abaqus FEM software (chapters 2,3 and 4). I also want to thank Rahul Prabhakaran and Stephan de Hoop for their help and technical support in the aperture in fluid-flow computations (chapters 5, 6 and 7), which wouldn't have been possible without your help. Finally, I would like to thank Shervin Rasoulzadeh and Ali Moradi Tehrani (CGG) for their technical support regarding the seismic wavelet generation, synthetic seismic generation and geostatistical inversion (chapter-7).

Special thanks go to Nico Hardebol who has introduced me to the amazing world of natural fractures, modelling, python coding and outcrop analysis. By bringing me to the TUDelft, you had ignited my interest in applied geosciences, which ultimately resulted in me applying for this PhD position. I have learned a lot from your guidance and support during the initial phases of the PhD. I hope we can continue our collaboration. I would also like to thank Auke Barnhoorn for his support, supervision and guidance throughout my PhD. It has meant a lot for me.

This Thesis would never have existed if it wasn't for Giovanni Bertotti. I have always appreciated your guidance, patience, critical second opinions and writing advice. We may have had a rocky start but it has turned out great in the end! Working with you has meant a lot, many thanks!

Doing a PhD is not only about the content, it is also about fun and making friends. For that I want to thank my friends and (former) colleagues in the Applied Geology and Applied Geophysics sections. Thank you: Remi, Max, Joeri, Cees, Koen, Kevin, Lisanne, Myrna, Reuben, Emilio, Tim, Stephan, Rahul, Sixue, Siddarth, Ranjani, Florencia, Pierre-Olivier, Musab, Jonho, Matteo, Chris, Akeel, Santosh, Martha, Baptiste, Billy, Jan-Willem and Youwei. Thanks for all the drinks, coffees, cakes, pastas (Emilio), dog petting (Emilio and Remi), discussions (Max and Remi), board-game nights (Remi, Joeri, Tim, Stephan, Max and Jonho) and other fun events.

Special thanks go out to Remi and Emilie, you have become great friends! Thanks for all the nice coffees, endless discussions, occasional board-game and for letting me become the pet sitter of Monsieur Berlioz and Croquette. Have a great journey in the van and we will definitely see each other in the future.

I would also like show my appreciation for all my friends who have personally supported me throughout the last decade. Thanks you: Joost, Michiel, Ward, Rick, Rob, Esra, Yaro, Wieke, Chris, Daniel, Jacob, Kees, Monique, Nikki, Sabine, Mathijs, Mayke, Harry, Erik, Jasmijn, Ilse, Cas, Guus, Erik, Daniel, David and Carlijn. Finishing this PhD would not have been possible without your friendship and support.

Tot slot ga ik over in het Nederlands. Pa bedankt voor al je steun, ook kon je er de laatste tien jaar niet helemaal meer bij zijn. Ik hoop dat je dit nog een beetje begrijpt. Ik houd van je. Ma en Jens, bedankt dat jullie me altijd hebben gesteund en me de vrijheid hebben gegeven om te worden wil ik wil zijn. Jullie zijn de beste moeder en grote broer die ik me had kunnen wensen! En als laatste Simone, bedankt voor al je steun, liefde en geduld, het was niet gelukt zonder jou. Dankzij jou zijn de laatste twee jaren van mijn PhD de gelukkigste jaren van mijn leven geworden. Ik houd van je.

CURRICULUM VITÆ

Quinten Diede BOERSMA

30-04-1991 Born in Utrecht, The Netherlands.

Education

2003–2010 Pre-university education (Science and Technology)
Marnix College, Ede

2010–2013 BSc in Earth Sciences
Utrecht University

2013–2015 MSc in Earth Structure and Dynamics, focus: Earth Materials
Utrecht University

2016–2020 PhD. Applied Geology
Delft University of Technology
Thesis: Natural Fracture Network Characterisation
Promotor: Prof. dr. G. Bertotti
Co- dr. A. Barnhoorn
Promotor:

LIST OF PUBLICATIONS

Journal Publications

7. **Q. Boersma**, P.O. Bruna, S. De Hoop, F. Vinci, A.M. Tehrani, G. Bertotti, *The impact of natural fractures on heat extraction from tight Triassic sandstones in the West Netherlands Basin: A case study combining well, seismic, and numerical data*, Netherlands Journal of Geosciences (2020) (SUBMITTED).
6. **Q. Boersma**, W. Athmer, M. Heage, M. Etchebes, J. Haukas, G. Bertotti, *Natural fault and fracture network characterization for the Southern Ekofisk Field: A case study integrating seismic attribute analysis with image log interpretation*, *Journal of Structural Geology*, (2020).
5. **Q. Boersma**, L.A.N.R. Douma, G. Bertotti, A. Barnhoorn, *Mechanical controls on horizontal stresses and fracture behaviour in layered rocks: A numerical sensitivity analysis*, *Journal of Structural Geology* **130**, (2020).
4. L.A.N.R. Douma, J.A. Regelink, G. Bertotti, **Q. Boersma**, A. Barnhoorn, *The mechanical contrast between layers controls fracture containment in layered rocks*, *Journal of Structural Geology* **127**, (2019).
3. **Q. Boersma**, R. Prabhakaran, F. H. Bezerra, G. Bertotti, *Linking natural fractures to karst cave development: A case study combining drone imagery, a natural cave network and numerical modelling*, *Petroleum Geoscience* **25**, 4 (2019).
2. **Q. Boersma**, N. Hardebol, A. Barnhoorn, G. Bertotti, *Mechanical Factors Controlling the Development of Orthogonal and Nested Fracture Network Geometries*, *Rock Mechanics and Engineering* **51**, 11, pp 3455-3569 (2018).
1. M. Houben, N. Hardebol, A. Barnhoorn, **Q. Boersma**, A. Carone, Y. Liu, M. De Winter, C. Peack, M. Drury, *Fluid flow from matrix to fractures in Early Jurassic shales*, *International Journal of Coal Geology* **175**, pp 26-39 (2017).

*A detailed list of the **conference proceedings** published during my PhD can be found on my researchgate page: https://www.researchgate.net/profile/Quinten_Boersma/research